



HAL
open science

Coherent structures and wall-pressure fluctuations modeling in turbulent boundary layers subjected to pressure gradients

Miloud Alaoui

► **To cite this version:**

Miloud Alaoui. Coherent structures and wall-pressure fluctuations modeling in turbulent boundary layers subjected to pressure gradients. Mechanics of materials [physics.class-ph]. Ecole nationale supérieure d'arts et métiers - ENSAM, 2016. English. NNT : 2016ENAM0077 . tel-01540940

HAL Id: tel-01540940

<https://pastel.hal.science/tel-01540940>

Submitted on 16 Jun 2017

HAL is a multi-disciplinary open access archive for the deposit and dissemination of scientific research documents, whether they are published or not. The documents may come from teaching and research institutions in France or abroad, or from public or private research centers.

L'archive ouverte pluridisciplinaire **HAL**, est destinée au dépôt et à la diffusion de documents scientifiques de niveau recherche, publiés ou non, émanant des établissements d'enseignement et de recherche français ou étrangers, des laboratoires publics ou privés.

2016-ENAM-0077

École doctorale n° 432 : Science des Métiers de l'ingénieur

Doctorat ParisTech

A thesis submitted in fulfilment of the requirements

for the degree of Doctor of Philosophy

to

l'École Nationale Supérieure des Arts et Métiers

Spécialité " Mécanique et Matériaux "

By

Miloud ALAOUI

December 19th 2016

Coherent structures and wall-pressure fluctuations modeling in turbulent boundary layers subjected to pressure gradients

Advisor : **Xavier GLOERFELT**

Thesis Committee

Pr. Jean-Marc FOUCAULT, Professor, École Centrale de Lille, France

Pr. Christophe BAILLY, Professor, LMFA, École Centrale de Lyon, France

Pr. Jan DELFS, Professor, DLR Braunschweig, Germany

Pr. Xavier GLOERFELT, Professor, DynFluid, Art et Métiers ParisTech, Paris, France

Pr. William GRAHAM, Professor, Cambridge University, UK

Pr. Laurent JOLY, Professor, ISAE Toulouse, France

Dr. Alois SENGISSSEN, Research Engineer, Airbus Operations, Toulouse, France

Chairman

Examiner

Reviewer

Thesis Advisor

Reviewer

Examiner

Industrial Advisor

T
H
E
S
I
S

Contents

Contents	ii
List of Figures	iv
List of Tables	ix
Nomenclature	xi
1 Introduction	1
1.1 Introduction	1
1.2 Context and motivations	1
1.3 Objectives	2
1.4 Organization of the thesis	3
2 Turbulent boundary layer : literature review	5
2.1 Boundary layer : state of the art	5
2.1.1 Laminar boundary layer	5
2.1.2 Turbulent boundary layer	7
2.1.3 Effect of pressure gradient	9
2.1.4 Effect of wall curvature	10
2.1.5 Equilibrium and non-equilibrium boundary layers	11
2.2 Coherent structures in the turbulent boundary layer flow	12
2.2.1 General definition	12
2.2.2 Near-wall structures	12
2.2.3 Outer-region structures	14
2.2.4 Hairpin vortices and hairpin packets	15
2.2.5 Visualization, identification and analysis methods	21
2.3 Turbulent boundary layer wall-pressure spectrum	27
2.3.1 Global definition and features	28
2.3.2 Effect of pressure gradient on pressure spectrum	32
2.3.3 Fluid-structure coupling	34
2.3.4 Wall-pressure spectrum models	38
3 Analysis of turbulent structures in flows subjected to zero and non-zero pressure gradients	48
3.1 Numerical database	48
3.1.1 Equations and numerical methods	48
3.1.2 Grid design	50
3.1.3 Flow parameters	53
3.1.4 Available database summary	55

3.1.5	Mean profiles and equilibrium state validation	56
3.2	Instantaneous velocity fields analysis	56
3.2.1	Analysis and identification tools in two-dimensional planes	57
3.2.2	Effect of pressure gradient on the coherent structures	59
3.2.3	Analysis of a three-dimensional database	61
3.3	Statistical analysis of velocity fields	62
3.3.1	Conditionally averaged velocity fields	62
3.3.2	Two-points correlations	68
3.3.3	Angle of structures	71
3.3.4	Statistical analysis of three-dimensional database	72
4	A stochastic model for wall-pressure spectrum	78
4.1	Definition of the model	78
4.1.1	Ahn's horseshoe model	78
4.1.2	Introducing large-scale structures	88
4.1.3	Introducing pressure gradient effect	90
4.1.4	Coupling with autospectrum model and frequency dependency	92
4.2	Comparison with SONOBL database	94
4.3	Coupling with vibro-acoustics code	95
5	Conclusions and perspectives	101
	Bibliography	104

List of Figures

1.1	Sound pressure levels and noise sources in an A380 cockpit - Airbus document.	2
1.2	Flow-generated-noise mechanism.	2
2.1	Boundary layer representation with free stream velocity U_∞ showing transition between laminar and turbulent regimes.	6
2.2	Velocity defect caused by the presence of the boundary layer in comparison to ideal fluid - this is quantified by the displacement thickness δ^*	6
2.3	Typical velocity profiles on a flat plate for laminar and turbulent boundary layers showing the increase in wall-shear for the turbulent case - after Young (1989).	7
2.4	Typical velocity profile for a turbulent boundary layer showing the different sub-layers with respect to the wall-normal distance for different Reynolds numbers. The logarithmic regions increases as the Reynolds number increases - after Delery (2007), the text in the figure was translated from french to english.	8
2.5	Different layers in the turbulent boundary layer flow - after Pope (2000)	9
2.6	Mean velocity profiles $u^+ = U/u_\tau$ (left) and streamwise component of turbulent intensity u_{rms}/U_e (right) for favorable (— — —), zero (— — —), adverse weak (— — —) and adverse strong (— — —) pressure gradients - after Cohen and Gloerfelt (2015).	10
2.7	A pair of counter-rotating streamwise vortices with the resulting low-speed streak (dark region) - after Blackwelder (1979).	13
2.8	The quadrant splitting scheme showing the probability density function in the (u', v') plane.	14
2.9	Outer region model showing large scale motions and typical eddies - after smoke visualization by Falco (1977)	15
2.10	Conceptual model of interaction between the near-wall region and the outer flow motions - after Praturi and Brodkey (1978).	16
2.11	Theodorsen (1952) hairpin-like vortex.	17
2.12	Hairpin packets organization in the turbulent boundary layer flow - (left) Instantaneous velocity field in Galilean frame convecting at $U_c = 0.55U_e$ after Mayam (2009) and (right) idealized model of nested hairpin packets travelling at different convection velocities after Adrian et al. (2000).	17
2.13	Effect of Reynolds number on the geometry of hairpin-like eddies - after Head and Bandyopadhyay (1981).	18
2.14	Sideview of hairpin-vortex - idealized linear representation (left) and "realistic" hairpin geometry (right).	19
2.15	Different parts of the hairpin vortex with the corresponding angles to the wall - after Robinson (1991b)	19
2.16	Evidence of streamwise aligned vortices along a line inclined to the wall - flow is from right to left - after Head and Bandyopadhyay (1981).	20

2.17	Example of non-monotonically increasing hairpin packet represented by the lower dashed line - after Adrian et al. (2000)	21
2.18	Vorticity contours showing von Kármán vortex street behind a cylinder at $Re \simeq 3000$ - Marine Ecosystem Dynamics Modelling lab.	22
2.19	Isosurface of Q -criterion colored by velocity magnitude showing near-wall structures in boundary layer transition - Mech. Eng. Dept, Stanford Univ.	23
2.20	LES of spatially developing TBL at Mach 0.5, isosurface of λ_2 criterion colored by streamwise velocity - after Gloerfelt and Marnat (2014).	23
2.21	Wavenumber-frequency spectrum $\Phi_{pp}(\mathbf{k}, \omega)$ for a frequency $\omega\delta^*/U_\infty=500$, where $M_\infty=0.1$ and $\delta=2$ cm. The model of Chase (1987) is used for illustration: $\Phi_{pp}(\mathbf{k}, \omega) = \frac{\rho_0^2 u_\tau^3 \delta^3}{[(k_+ \delta)^2 + 1/b^2]^{\frac{5}{2}}} \left[\frac{C_M (k_1 \delta)^2 k^2}{ k^2 - k_0^2 + \epsilon^2 k_0^2} + C_T (k\delta)^2 \times \mathcal{F} \right]$ with $k_+^2 = (\omega - U_c k_1)^2 / (hu_\tau)^2 + k^2$, and $\mathcal{F} = \frac{(k_+ \delta)^2 + 1/b^2}{(k\delta)^2 + 1/b^2} \left(c_1 + \frac{c_2 k^2 - k_0^2 }{k^2} + \frac{c_3 k^2}{ k^2 - k_0^2 + \epsilon^2 k_0^2} \right)$. We set $C_M=0.1553$, $C_T=0.0047$, $b=0.75$, $h=3$, $c_1=2/3$, $c_2=0.005$, $c_3=1/6$, and $\epsilon=0.2$. $k_0 = \omega/c_0$ is the acoustic wavenumber.	29
2.22	Wavenumber-frequency spectrum $10 \log_{10} \Phi_{pp}(\mathbf{k}, \omega)$ of wall pressure beneath a ZPG Mach 0.5 turbulent boundary layer in the (a) $k_x - k_z$ plane at $\omega\delta/U_e = 5.9$, (b) $k_x - \omega$ plane at $k_z = 0$ and (c) $k_z - \omega$ plane at $k_x = 0$ - The white dashed circle in (a) as well as the plain white lines in (b) and (c) represent the acoustic domain defined by equation 2.31, the dashed line in (b) corresponds to a theoretical convective velocity $U_c = 0.7U_e$ - after Cohen (2015).	30
2.23	Streamwise pressure gradient over front region of a typical long range aircraft. Arbitrary units - Airbus document.	33
2.24	One-point frequency spectra for different cases of pressure gradient measured on a rotatable NACA 0012 airfoil - angles indicate the angle of attack of the airfoil - after Hu and Herr (2016).	33
2.25	Wavenumber-frequency spectra $10 \log_{10} \Phi_{pp}(\mathbf{k}, \omega)$ for favorable (FPG), zero (ZPG), adverse weak (APGw) and adverse strong (APGs) pressure gradients in the $k_x - k_z$ plane at frequencies $\omega\delta/U_e = 2.7$ (FPG), 3 (ZPG), 4.3 (APGw) and 5.2 (APGs) after Cohen (2015). Refer to section 3.1 for description of the pressure gradients.	34
2.26	Flat plate model for TBL-structure coupling.	35
2.27	$\Phi_{pp}(\mathbf{k}, \omega)$ spectra in the $k_x - \omega$ plane at constant k_z and bending wavenumber for an infinite plate (black line). The dashed circles show regions of acoustic and hydrodynamic coincidence between the TBL excitation and the structure.	37
2.28	$\Phi_{pp}(\mathbf{k}, \omega)$ spectra at constant frequency with (left) low coupling $c_b > U_c$ and (right) high coupling $c_b < U_c$. Black line shows the bending wavenumber for an infinite plate.	37
3.1	Sketch of the computational domain for the non-zero-pressure-gradient computations - Mean streamwise velocity \bar{u} and streamlines from a 2D simulation with the backward-facing step of height h . The mean flow a few points after the step is used as inlet for the 3D domain - from Gloerfelt and Marnat (2014).	50
3.2	Top view close to the wall ($y^+ \simeq 25$) of the streamwise velocity for the ZPG case showing the transition zone. A fully turbulent state is reached after the solid line for $x/h \simeq 900$	50

3.3 Computation domain in the streamwise/wall-normal plane (x_1, x_2) : strong adverse APGs (a), weak adverse APGw (b), zero gradient ZPG (c), and favorable FPG (d). The zone of interest for the velocity and wall-pressure analyses is delimited with the dashed rectangle. Parameter h is the height of the backward-facing step located upstream of the domain involved in the turbulence transition process. 52

3.5 (a) Clauser pressure gradient parameter β_C , (b) acceleration parameter K and (c) viscous scaled pressure parameter Δ_p for FPG (— — —), APGw (— — —) and APGs (— — —) - after Cohen (2015). 56

3.6 Instantaneous streamwise velocity u in the streamwise/wall-normal plane for APGs (a), APGw (b), ZPG (c) and FPG (d). x_{min} and x_{max} denote the streamwise boundaries of the zone of interest. Black line corresponds to $u = 140\text{m/s}$ and highlights thickening of the boundary layer from FPG to APGs - scale is from 10 m/s (blue) to 260 m/s (red) - Provided by X. Gloorfelt. 57

3.7 Single hairpin-like vortex signature in streamwise/wall-normal plane - Velocity vector field in a frame of reference moving with the structure - after Mayam (2009). 58

3.8 Instantaneous views of streamwise/wall-normal vector fields showing hairpin vortex signatures, viewed in a frame of reference moving at $U_c = 0.72U_e$ for the APGs (a), APGw (b), ZPG (c) and FPG (d) configurations - Streamwise and wall normal axes (x, y) are made non-dimensional using the boundary layer thickness δ 58

3.9 Contours of swirling strength λ_{ci} for APGs (a), APGw (b), ZPG (c) and FPG (d). 60

3.10 Number of prograde and retrograde spanwise vortices for the four pressure gradient cases along the TBL thickness. The number of vortices is measured over 8000 snapshots with a threshold $|\lambda_{ci}| > 1.5\lambda_{ci}^{rms}$ 61

3.11 Isosurface of instantaneous streamwise velocity u' revealing presence of low speed streaks $u'/U_e = -0.058$ (blue) and high speed streaks $u'/U_e = 0.058$ (yellow) in the near-wall region. 62

3.12 Isosurface of swirling strength criterion $\lambda_{ci} = 4.2\lambda_{ci}^{rms}$ colored with fluctuating streamwise velocity u'/U_e showing (a) hairpin forest in the outer part of the boundary layer $y/\delta > 0.39$ and isolated hairpin with axes scaled with (b) inner variables x_i^+ and (c) outer variables x_i/δ 63

3.13 Estimated velocity field \hat{u}_i using a negative swirling strength condition $\lambda_{ci} < 0$ for the APGs (a), APGw (b), ZPG (c) and FPG (d) configurations with reference point at $y/\delta = 0.2$ - Black circles indicate positions of prograde vortices (biggest circle indicates vortex at the reference point) - Streamwise and wall-normal axes (x, y) are made non-dimensional using δ 64

3.14 Estimated velocity field using a negative swirling strength condition $\lambda_{ci} < 0$ for (a) APGs, (b) APGw and (c) ZPG configurations with reference point at $y/\delta = 0.15$ - Black circles indicate positions of prograde vortices. Horizontal lines are plotted to highlight hairpin structures within a same subpacket. Streamwise and wall-normal axes (x, y) are made non-dimensional using δ 66

3.15 Estimated velocity field in the streamwise/spanwise (x, z) plane using a negative swirling strength condition $\lambda_{ci} < 0$ for the (a) APGs $y/\delta = 0.10$, (b) APGw $y/\delta = 0.11$, (c) ZPG $y/\delta = 0.16$ and (d) FPG $y/\delta = 0.14$ - Circles indicate positions of vortices (biggest circle indicates vortex at the reference point) - Red line is the loci of $\bar{u} = 0$ 67

3.16 Spanwise separation of hairpin vortices legs $\lambda_{z,\delta}^{hp}$ with respect to wall-normal distance. 67

3.17	Contours of R_{uu} correlation superimposed to estimated velocity field with reference point at $y/\delta = 0.2$ for the APGs (a), APGw (b), ZPG (c) and FPG (d) configurations - Contour levels range from 0.2 to 1.0 with a step of 0.2 - Streamwise and wall-normal axes (x, y) are made non-dimensional using δ	69
3.18	Comparison of correlation R_{uu} streamwise extent Lx_{uu} - Based on $R_{uu} = 0.5$ contour level (top) and comparison between Lx_{uu} based on $R_{uu} = 0.5$ vs $R_{uu} = 0.6$ (bottom).	70
3.19	Contours of $R_{uu} = 0.2$ correlation at all reference points $y/\delta = 0.1, 0.15, 0.2, 0.3, 0.4, 0.5, 0.6, 0.7, 0.8, 0.9$ for the APGs (a), APGw (b), ZPG (c) and FPG (d) configurations - Streamwise and wall-normal axes (x, y) are made non-dimensional using δ	71
3.20	Growth angle of hairpin packets given by the streamwise velocity correlation R_{uu}	72
3.21	Linear stochastic estimation of 3D velocity field reveals hairpin-like structure over a low momentum region - Isosurfaces of λ_{ci} colored with u' and isosurface of negative fluctuating velocity u' (blue) - condition location is $y/\delta = 0.2$	73
3.22	Vector field of estimated velocity field shown in figure 3.21 in (a) the streamwise/wall-normal plane and (b) the streamwise/spanwise plane. Condition location is $y/\delta = 0.2$, big circles indicate vortices corresponding to the main hairpin structure and the small circles to the secondary structures.	73
3.23	Linear stochastic estimation of 3D velocity field with events locations between $0.2 < y/\delta < 0.9$ with a step of 0.1 - axes are made non-dimensional using δ	75
3.24	Linear stochastic estimation of 3D velocity field with event located at $y/\delta = 0.3$ - Estimation based on (left) velocity field \mathbf{u} and (right) normalized velocity field $\mathbf{u}/\ \mathbf{u}\ $ - Isocontours of swirling strength λ_{ci} colored with streamwise velocity and negative streamwise velocity $u' < 0$	76
3.25	Linear stochastic estimation of 3D velocity field with event located at $y/\delta = 0.3$ - Velocity vector field in plane (y, z) shows two counter-rotating vortices downstream and above main hairpin structure - Isocontours of λ_{ci} are different between left and right representations.	76
3.26	Conceptual model for the generation of the inverse hairpin structure - side, front and 3D views.	77
4.1	Ahn's horseshoe-vortex representation. Each straight-line element has a constant circulation Γ and is modeled by a cylinder - after Ahn et al. (2010).	78
4.2	Methodology to obtain the eddy pressure field - Figure 3 is extracted from Ahn et al. (2010).	79
4.3	Definition of local coordinate system attached to the hairpin structure.	80
4.4	Streamlines around a single hairpin in a uniform streamwise mean flow.	81
4.5	Scheme of the integration of the wavenumber spectrum method through each sublayer to model a continuous distribution of hairpin eddies.	83
4.6	Wavenumber spectrum in the (k_x, k_z) plane (a) without continuous distribution and (b) with continuous distribution of hairpin eddies - only the first sublayer (logarithmic region) is considered here.	84
4.7	Streamwise wavenumber spectrum for each of the six hairpin sublayers. Legend indicates the wall-normal position y/δ of the heads of the hairpin eddies.	85
4.8	Influence of the upper limit position of the hairpin eddy field to the wavenumber spectrum. For each case, the legend indicates the upper limit y/δ of the highest sublayer.	85
4.9	Influence of the velocity induced field calculation method on the wavenumber spectrum.	86

4.10	Local velocity field around a hairpin-like vortex with neck/legs geometry located in the logarithmic region (left) and a pair of outward-spinning counter rotating quasi-streamwise vortices at an angle of 5° to the wall located in the buffer region (right) - Isosurfaces of wall-normal velocity $v' < 0$ (blue) and $v' > 0$ (red). . . .	87
4.11	Local velocity field around a horseshoe-like vortex with head (top) and without head (bottom) located in the logarithmic region - Isosurfaces of fluctuating streamwise velocity $u' < 0$ (blue) and $u' > 0$ (red).	87
4.12	Streamwise wavenumber spectra predicted by the model for different shapes of the coherent structures.	88
4.13	Low-momentum region developing under a packet of five hairpin-like eddies - Isosurface of negative fluctuating velocity $u' < 0$ in blue.	89
4.14	Model prediction of wavenumber-frequency spectrum in the (k_x, k_z) plane for (a) single hairpin and (b) for packets of five hairpin structures. The black cross indicates the position of the peak.	89
4.15	Mean velocity profiles for favorable (— — —), zero (— — —), adverse weak (— — —) and adverse strong (— — —) pressure gradients. Dashed black lines correspond to the theoretical linear law $U^+ = y^+$ and logarithmic law $U^+ = \ln(y^+)/0.41 + 5.1$	91
4.16	Streamwise wavenumber spectrum for hairpin structures at different angles to the wall. Hairpin structures at 20° , 45° and 75° are illustrated on the right.	91
4.17	Streamwise wavenumber spectra $S_{pp}(k_x, k_z = 0, \omega)$ for the ZPG case of the LES computation for different frequencies $\omega\delta_{ref}^*/U_e$ \circ — 1.1, \triangle — 5.2, \square — 10.4, \ast — 12, ∇ — 20.9, and \diamond — 31.1 - after Cohen (2015).	92
4.18	Comparison of streamwise wavenumber spectra between (+) LES database and (— — —) the hairpin packet model for first frequency $\omega\delta/U_e = 0.06$ (FPG), 0.09 (APGw) and 0.10 (APGs). Dashed vertical lines indicate the cut-off wavenumbers for the LES computations.	94
4.19	Comparison of streamwise wavenumber spectra between (+) LES database and (— — —) the hairpin packet model at three frequencies for (left) APGw [0.09, 0.86, 1.72] and (right) APGs [0.10, 1.04, 2.08]. Frequencies $\omega\delta/U_e$ are given inside brackets.	95
4.20	ATRA aircraft from the DLR. The colors indicate the areas where measurements of panels accelerations have been performed: front cabin (blue), mid cabin (red) and aft cabin (green) - after Klabas et al. (2015).	95
4.21	SEA model for the front cabin area. The panels mentioned here are used for SEA computation using the TBL models.	96
4.22	Comparison between the SEA predictions submitted to the hairpin model and the flight test measurements on roof panel of the front cabin - acceleration vs 1/3 octave band frequencies - (a) Direct predictions, (b) predictions are rescaled to match measurement point at 2000Hz. Measurements, Cockburn-Jolly, Efimtsov and FRPM data have been communicated by A. Klabas.	97
4.23	Comparison between the SEA predictions submitted to the hairpin model and the flight test measurements on window panel of the front cabin - acceleration vs 1/3 octave band frequencies - (a) Direct predictions, (b) predictions are rescaled to match measurement point at 2000Hz. Measurements, Cockburn-Jolly, Efimtsov and FRPM data have been communicated by A. Klabas.	98
4.24	Comparison between the SEA predictions submitted to the hairpin model and the flight test measurements on lower side-wall panel of the front cabin - acceleration vs 1/3 octave band frequencies - (a) Direct predictions, (b) predictions are rescaled to match measurement point at 2000Hz. Measurements, Cockburn-Jolly, Efimtsov and FRPM data have been communicated by A. Klabas.	99

List of Tables

3.1	Summary of meshes parameters for the simulated cases at Mach 0.5 with pressure gradients. The two values for Δy^+ indicate the mesh spacing at the wall (subscript w) and at the boundary layer edge (subscript e).	51
3.2	Free flow properties for the LES computation	53
3.3	Boundary layer properties for the four pressure gradient cases. Subscript ref denotes values taken at the middle of the domain of interest.	54
3.4	Parameters quantifying the pressure gradient for the different cases (α is the angle of the slanted wall used to impose a prescribed pressure gradient.	54
3.5	Summary of mesh parameters for the Mach 0.5 ZPG 3D database. The two values for Δy^+ indicate the mesh spacing at the wall (subscript w) and at the boundary layer edge (subscript e).	55
3.6	Boundary layer properties for the zero pressure gradient 3D database. Subscript ref denotes values taken at the middle of the domain of interest.	55
3.7	Use of the different databases for each step of the analysis.	56
4.1	Parameters for the mean velocity profiles extracted from the LES computations.	90
4.2	Boundary layer parameters for front cabin region - A. Klabas personal communication.	96

Nomenclature

α_l	Hairpin leg angle
α_n	Hairpin neck angle
α_p	Hairpin packet angle
α_{hp}	Hairpin-vortex angle
β_C	Clauser's pressure gradient parameter
$\boldsymbol{\omega}$	Vorticity $\boldsymbol{\omega} = (\omega_x, \omega_y, \omega_z)$
\mathbf{k}	Wall wavenumber vector (k_x, k_z)
\mathbf{u}	3D velocity vector (u, v, w)
δ	Boundary layer thickness
δ^*	Displacement thickness
ϵ	Dissipation of turbulence
Γ	Circulation
γ	Ratio of specific heats
κ	von Kárám constant $\kappa = 0.41$
κ_R	Wall curvature
λ	Length of hairpin-eddy head for the hairpin model
λ_{ci}	Swirling strength
\mathcal{P}	Production of turbulence
μ	Dynamic viscosity
ν	Kinematic viscosity
ω	Angular frequency $\omega = 2\pi f$
Ω_{ij}	Rotation term of the velocity gradient tensor
$\Phi(\omega)$	Wall-pressure autospectrum
Π	Cole's wake parameter

$\Psi_{pp}(\mathbf{k}, \omega)$	Wall-pressure wavenumber-frequency spectrum - notation in literature review section
ρ	Air density
ρ_e	Air density at the edge of the boundary layer
τ_w	Wall-shear
τ_{ij}	Viscous shear stress tensor
θ	Momentum thickness
c_0	Celerity of sound waves in air
C_f	Friction coefficient
c_p	Specific heat at constant pressure
f	Frequency
G	Clauser's factor for pressure gradient
$G(\mathbf{x}'; \mathbf{x})$	Green's function
H	Shape factor $H = \delta^*/\theta$
h, L	Length of hairpin-eddy legs for the hairpin model h is the height of the backward facing step for turbulence transition in the numerical database presentation section
K	Acceleration parameter
k	Turbulent kinetic energy
k_b	Plate bending wavenumber
k_c	Convective wavenumber
k_x	Streamwise wavenumber
k_z	Spanwise wavenumber
M	Mach number
N_k	Kinematic vorticity number
P	Mean pressure
p	Instantaneous pressure
p_e	Pressure at the edge of the boundary layer
Pr	Prandtl number - $Pr = 0.72$ for air
q	Dynamic pressure
r	Gas constant $r = 287 \text{ J.kg}^{-1}.\text{K}^{-1}$
r_c	Radius of hairpin-eddy legs and head for the hairpin model

LIST OF TABLES

$Re^+ = \delta u_\tau / \nu$	Reynolds number based on the friction velocity u_τ
$Re_\delta = \delta U_e / \nu$	Reynolds number based on the boundary layer thickness δ
$Re_\theta = \theta U_e / \nu$	Reynolds number based on the momentum thickness θ
$Re_{\delta^*} = \delta^* U_e / \nu$	Reynolds number based on the displacement thickness δ^*
S_{ij}	Shear stress tensor
$S_{pp}(\mathbf{k}, \omega)$	Wall-pressure wavenumber-frequency spectrum
T	Temperature
U	Mean streamwise velocity
u	Instantaneous streamwise velocity
u'	Fluctuating streamwise velocity
u^+	Instantaneous streamwise velocity in wall units $u^+ = u/u_\tau$
U_c	Convection velocity
U_e	Streamwise edge velocity
u_τ	Wall friction velocity
V	Mean wall-normal velocity
v	Instantaneous wall-normal velocity
v'	Fluctuating wall-normal velocity
W	Mean spanwise velocity
w	Instantaneous spanwise velocity
w'	Fluctuating spanwise velocity
x	Streamwise coordinate
x^+	Streamwise distance in wall units $y^+ = y u_\tau / \nu$
y	Wall-normal coordinate
y^+	Wall-normal distance in wall units $y^+ = y u_\tau / \nu$
z	Spanwise coordinate
z^+	Spanwise distance in wall units $y^+ = y u_\tau / \nu$

Chapter 1

Introduction

1.1 Introduction

This thesis focuses on the coherent structures in turbulent boundary layers subjected to pressure gradients and their role in aircraft structure excitation due to wall-pressure fluctuations. Flow-generated noise has become a non-negligible technological issue for the transport industry since great efforts have been made in reducing the propulsion generated noise.

This chapter aims at describing the context and motivations of this study by focusing on the flow-generated noise mechanisms. Due to the smooth curvature of aircraft fuselage, the importance of developing a precise knowledge of the turbulent properties of the flow when subjected to pressure gradients will be highlighted. The objectives and outline of this study will also be presented hereafter.

1.2 Context and motivations

Since the engine noise levels have considerably reduced since the past 60 years, the turbulent boundary layer (TBL) has become one of the main sources of aircraft interior noise over a large frequency range (see figure 1.1), driving insulation concept design in the cabin and flight deck area. As a driver of the crew and passenger comfort it is a subject of interest since years and several contributions on flight tests data and/or modeling approaches can be found in the literature (Bhat, 1971; Collery, 2010; Collery et al., 2013; Rackl and Weston, 2005; Rizzi et al., 2000). In fact, the pressure fluctuations within a turbulent boundary layer are responsible for structural vibrations (Blake, 1986) that are transmitted through the structure and radiate into the vehicle as can be seen in the scheme in figure 1.2. The aim of this research field has always been to increase confidence in excitation models to improve design concepts for aircraft insulation. Nevertheless, these models are usually not adapted to characterize pressure gradient areas, such as the flight deck and the wing/fuselage junction, and need strong improvements. Nowadays, with improvements of numerical capabilities, investigations of turbulent structures properties and their organization in the vicinity of walls at representative Mach numbers are accessible.

In fact, the pressure fluctuations which are responsible for the excitation of the aircraft's cockpit and fuselage panels are the imprint of the turbulent motions living within the flow. Therefore it is crucial to investigate these coherent structures in order to understand the mechanism of noise generation from flow vibrating panels and build more reliable noise prediction tools.

Many authors have worked on turbulent boundary layers subjected to zero and non-zero pressure gradients (Bradshaw, 1967b; Burton, 1973; Clauser, 1954; Dixit and Ramesh, 2010; Hu and Herr,

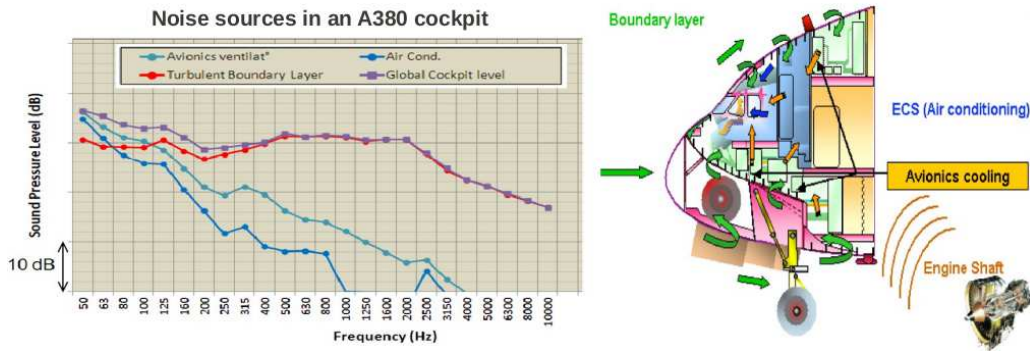


Figure 1.1 – Sound pressure levels and noise sources in an A380 cockpit - Airbus document.

2016; Kline et al., 1967; Lee and Sung, 2009; McGrath and Simpson, 1988; Salze et al., 2014; Schloemer, 1967; Spalart and Watmuff, 1993). Apart from the canonical zero pressure gradient flow which gathers the majority of the research, focus has been put on adverse pressure gradient flows, since this type of pressure gradient can be critical in several engineering applications such as separation of the turbulent boundary layer over the wing when the critical angle of attack is reached or pumping effect in turbomachinery. Favorable pressure gradient turbulent boundary layers would come in last position in terms of amount of research papers.

Nevertheless, even though turbulent boundary layer flows have gathered the interest of many authors, there is little information concerning the coherent turbulent structures when the flow is subjected to pressure gradients. It is well known that the turbulent eddies play an important role in turbulence production and mass and momentum transport, but very little is known on their contribution to wall-pressure fluctuations. In this study, an attempt to correlate these structures to the wall-pressure fluctuations is undergone.

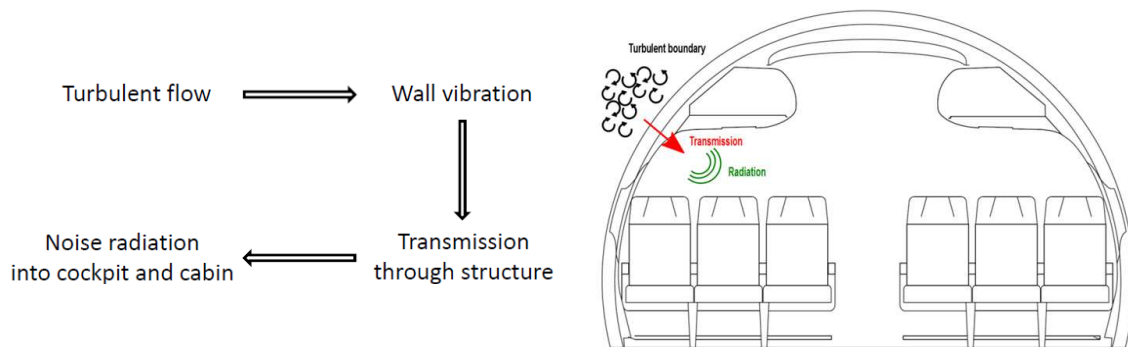


Figure 1.2 – Flow-generated-noise mechanism.

1.3 Objectives

Aircraft manufacturers show increasing interest in noise generated by the turbulent boundary layer flow over the fuselage and cockpit. The noise predicting tools which are used in industry today rely on analytic wall-pressure models which lack precision especially in areas where the flow is subjected to pressure gradients.

The aims of the thesis are

- From a phenomenological point of view, to understand the effect of pressure gradient on

the turbulent boundary layer excitation by investigating the turbulent coherent structures existing within the flow. Many authors have showed that the hairpin vortex, which refers to hairpin, cane, horseshoe or omega vortex, is one of the most frequently encountered coherent structure in the turbulent boundary layer flow and it is believed that this type of vortex has a significant influence on the wall-pressure fluctuations.

- From a modelling point of view, to develop based upon these observations a stochastic wall-pressure spectrum model. This model is designed to improve the reliability of the current turbulent boundary layer excitation by explicitly taking into account turbulent features of the flow. Indeed, the majority of the models used by transport manufacturers nowadays rely only on averaged quantities since these model are very easy to implement and require very low computation time.

This work has been conducted in the frame of the SONOBL project (Sources of NOise from Boundary Layers over vehicules) which was coordinated by the fluid mechanics laboratory DynFluid from Ecole Nationale Supérieure des Arts et Métiers located in Paris, and in collaboration with the Laboratoire de Mécanique des Fluides et d'Acoustique (LMFA) from Ecole Centrale de Lyon, as well as three industrial partners, Airbus, Renault and Dassault. Among the main outcomes of SONOBL, an extensive numerical Large Eddy Simulation (LES) database of turbulent boundary layers flows subjected to favorable (FPG), zero (ZPG) and adverse (APG) pressure gradients has been generated by DynFluid, and compared with wind tunnel measurements from LMFA. The current thesis is built on these roots and greatly acknowledges them. Therefore, a particular effort will be put on analyzing this database to characterize the features of the flow, and more specifically quantify hairpin vortices evolution prior to modelling them as vibroacoustic excitation input. However, the various vibroacoustic approaches themselves (Analytical, FEM, SEA, ...) and their properties are out of the scope and will not be discussed in the current manuscript.

1.4 Organization of the thesis

This thesis is divided into five parts.

The first chapter contains the introduction in which the motivations, objectives and organization of the manuscript are presented.

The second chapter is a literature review of boundary layer flows along with the effects of pressure gradients. This chapter also provides detailed phenomenology on the coherent structures in turbulent boundary layer flows with a specific focus on hairpin vortex type. An overview of the common visualization and identification methods and criteria will also be provided. This chapter ends with a review of the existing wall-pressure models, and their way to couple the wall-pressure spectrum with the structure.

The third chapter deals with the instantaneous and statistical analysis of the velocity fields for turbulent boundary layers subjected to zero and non-zero pressure gradients. The numerical simulation providing the database used for this study will be presented in this chapter, along with description of the numerical tools and methods used for the study. The effect of pressure gradients on the turbulent vortices will be highlighted.

The fourth chapter focuses on the stochastic wall-pressure spectrum model. In this section the model as well as the methodology of enhancement of the model are described. Results from a first coupling with an aircraft structure using a vibroacoustic simulation tool will also be shown.

The conclusions of this study are summarized in the last chapter where perspectives for future work are also proposed.

Chapter 2

Turbulent boundary layer : literature review

The boundary layer is a well known concept in mechanical, aeronautical, naval as well as civil engineering and has undergone increasing interest from the scientific community as a result of rapidly growing use of powerful computation methods and tools. This concept came into the mind of Prandtl (1904) in the beginning of the past century where he built a bridge between the two major disciplines of fluid dynamics at that moment, hydrodynamics which had developed from Euler's theory of inviscid flows and hydraulics which relied on a large amount of experimental data to tackle practical engineering problems. In his 1904 paper, Prandtl stated that however small the viscosity of a fluid in motion may be, it cannot be ignored. Over the years, this had an outstanding impact on the competitiveness-driven industry of transport by introducing a theoretical background to the concept of drag for fluid-immersed bodies. A simple definition of the boundary layer would be :

"The boundary layer is a region of the flow with non-negligible effects of viscosity separating a solid body and a free flow which corresponds to the inviscid limiting solution."

Due to viscosity effects, the flow within the boundary layer can be considered laminar or turbulent depending on the Reynolds number Re_x defined hereafter :

$$Re_x = \frac{Ux}{\nu} \quad (2.1)$$

where U and x are respectively a characteristic streamwise velocity and the distance from the leading edge of the surface and ν is the kinematic viscosity of the fluid. When the Reynolds number increases, the regime transitions from laminar to turbulent leading to much more complex flow pattern and a thickening of the boundary layer as shown in figure 2.1.

2.1 Boundary layer : state of the art

2.1.1 Laminar boundary layer

The laminar flow is characterized by smooth streamlines approximately parallel to the wall over which the boundary layer develops. The boundary layer is likely to be laminar (at least for a short time before transitioning) in the range $1000 < Re_x < 10^6$ (White, 1991) which is coherent with the critical Reynolds number defined in the next section. If we consider a flow over a flat plate with its leading edge at $x = 0$, the thickness of the boundary layer δ is a monotonically

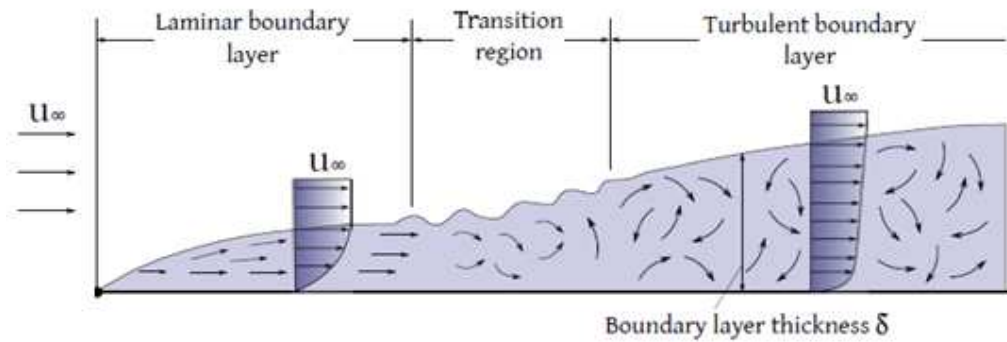


Figure 2.1 – Boundary layer representation with free stream velocity U_∞ showing transition between laminar and turbulent regimes.

increasing function of x . The transition from boundary layer flow to outer flow for laminar regime takes place continuously so that the boundary cannot be given precisely. Thus, the most straightforward definition of boundary layer thickness is given by the point where the velocity reaches 99% of the free stream velocity and is therefore often denoted δ_{99} .

A correct and reliable measure for the thickness of the boundary layer is the displacement thickness δ^* (also denoted δ_1), which, under hypothesis of incompressible flow, is defined by:

$$\delta^*(x) = \int_0^{\delta(x)} \left(1 - \frac{U}{U_e}\right)(x, y) dy \quad (2.2)$$

where U_e is the edge velocity, i.e. the velocity at the outer edge of the boundary layer, U is the mean flow velocity and y is the wall-normal distance. The displacement thickness tells us how far the streamlines of the outer flow are displaced by the boundary layer (Schlichting and Gersten, 2000) as depicted in figure 2.2 and is about 1/3 of the boundary layer thickness for laminar flow over flat plate.

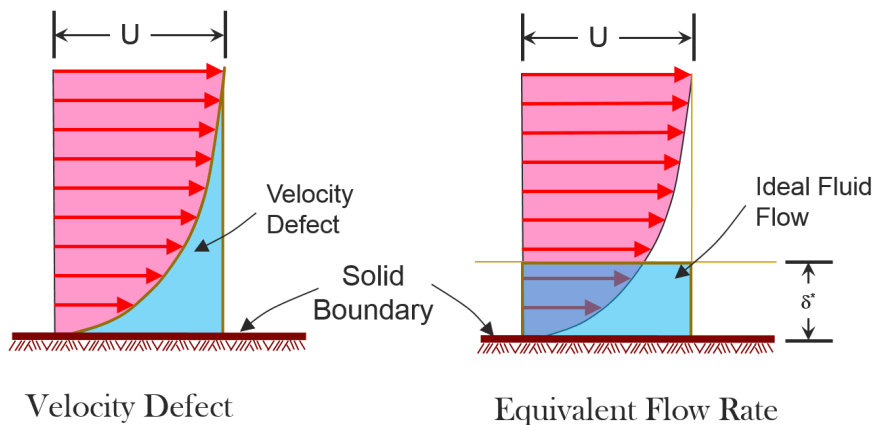


Figure 2.2 – Velocity defect caused by the presence of the boundary layer in comparison to ideal fluid - this is quantified by the displacement thickness δ^* .

One can also define the following integral quantity referred to as the momentum thickness θ (also denoted δ_2) defined by:

$$\theta(x) = \int_0^{\delta(x)} \frac{u}{U_e} \left(1 - \frac{U}{U_e}\right)(x, y) dy \quad (2.3)$$

The momentum thickness is a distance indicative of the boundary layer momentum deficit relative to a mean flow. The displacement and momentum thickness are related through the shape factor H given by:

$$H = \frac{\delta^*}{\theta} > 1 \quad (2.4)$$

Notice how the shape of the mean velocity profile is flatter away from the wall in the case of a turbulent boundary layer (see figure 2.3). This "flatness" is characterized by the shape factor H . The shape factor is around $5/2$ for a laminar boundary layer over a flat plate (White, 1991); for instance $H = 2.6$ for the Blasius (1908) profile. In comparison, the shape factor is lower for the turbulent boundary layer - $H = 1.3$ for the zero pressure gradient Klebanoff (1954) boundary layer.

2.1.2 Turbulent boundary layer

As was already mentioned, the boundary layer does not remain laminar and transitions towards a turbulent regime at a certain critical Reynolds number. The numerical value of the critical Reynolds number Re_{crit} is strongly dependent on the level of perturbations in the outer flow. Considering a turbulent boundary layer developing over a flat plate, this number ranges within $3 \cdot 10^5 < Re_{x,crit} < 3 \cdot 10^6$, where x is the distance from the leading edge of the plate. The turbulent boundary layer (TBL) is characterized, from a very basic point of view, by a great increase in its thickness and wall-shear stress leading to a change in the shape of the mean velocity profile as can be seen in figure 2.3.

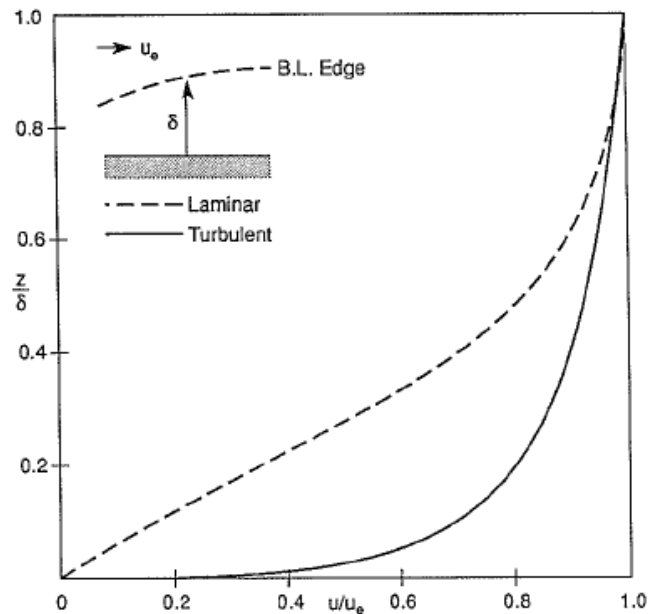


Figure 2.3 – Typical velocity profiles on a flat plate for laminar and turbulent boundary layers showing the increase in wall-shear for the turbulent case - after Young (1989).

Unlike the laminar boundary layer where the entire region of the boundary layer is affected by viscosity, the first turbulent boundary layer studies (Klebanoff, 1954; Kovaszny, 1967; Laufer, 1954; Townsend, 1951) show that it can be divided into two regions:

- a very thin layer directly at the wall called the viscous sublayer or viscous wall layer where the effects of viscosity are dominant
- a larger region away from the wall which can be referred to as the frictional layer because only the "apparent friction" due to the turbulent fluctuating motions, and which is unaffected by viscosity, is driving the flow.

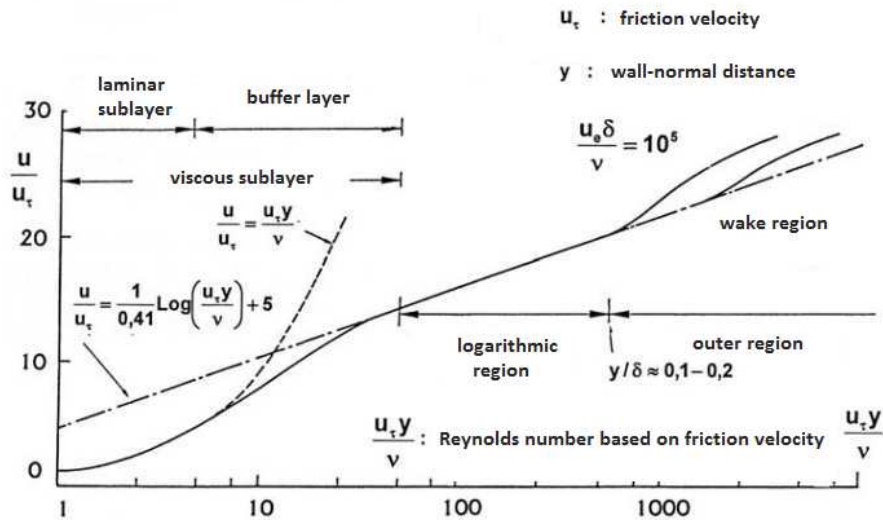


Figure 2.4 – Typical velocity profile for a turbulent boundary layer showing the different sub-layers with respect to the wall-normal distance for different Reynolds numbers. The logarithmic regions increases as the Reynolds number increases - after Delery (2007), the text in the figure was translated from french to english.

This leads to the fact that there is no global scaling for the entire turbulent boundary layer. For instance, the profile of the mean velocity close to the wall is dictated by inner variables such as the wall-shear $\tau_w = \mu dU/dy$ (where μ is the dynamic viscosity), the friction velocity $u_\tau = \sqrt{\tau_w/\rho}$, and the kinematic viscosity ν , whereas the outer profile can be scaled with outer variables such as the edge velocity U_e and the TBL thickness δ . A detailed description of the different layers within the TBL scaled with inner $y^+ = yu_\tau/\nu$ and outer y/δ variables is given in figure 2.5.

An important characteristic of the turbulent boundary layer mean velocity profile is the logarithmic law, first introduced by von Kármán (1930), which lays within the logarithmic region as shown in figures 2.4 and 2.5. This region is believed to play a major role in wall turbulence. In fact, most of the kinetic energy from the outer flow is contained in large-scale structures and this energy "cascades" from these structures to smaller scale structures. This process creates structures that are small enough that molecular diffusion becomes important and viscous dissipation of energy takes place; the scale at which this happens is the Kolmogorov scale (Kolmogorov, 1941a,b). The logarithmic region is the bridge between the highly energetic outer structures and the very small ones near the wall and gathers universal properties. For instance, the production to dissipation ratio \mathcal{P}/ϵ as well as the normalized Reynolds shear stress $-\langle uv \rangle/k$ are almost

constant within this region. Consequently, when the Reynolds number increases, disparities of scales between the larger structures (integral scale, where most of the energy is contained) and the smallest structures (from Taylor scale down to Kolmogorov scale) increase and thus widens the logarithmic region of the TBL.

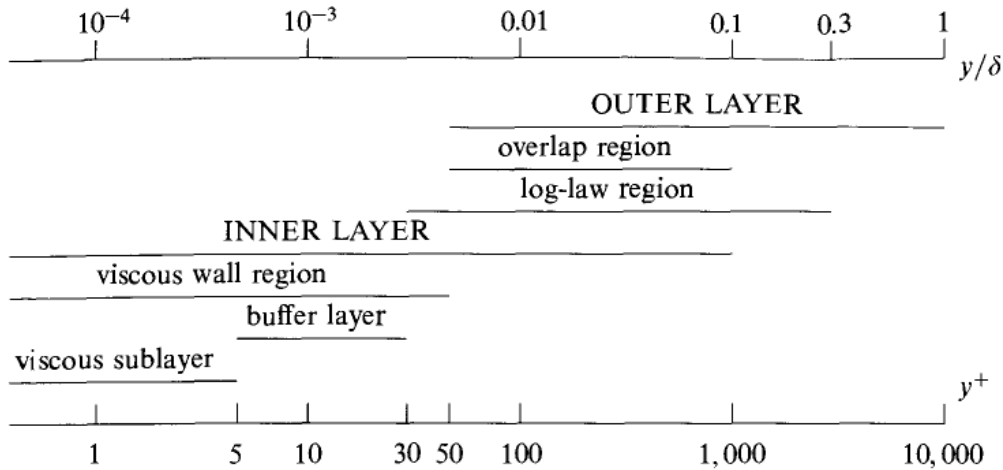


Figure 2.5 – Different layers in the turbulent boundary layer flow - after Pope (2000)

For the remainder of the study, one should keep in mind that the turbulent boundary layer can be separated into an outer and an inner region, each of which behave with respect to different scaling properties. Moreover, the flow can be viewed as made of a hierarchy of eddies over a wide range of length scales with their intensity described by the energy spectrum of velocity fluctuations for each length scale; these eddies are then convected by a mean flow characterized by a logarithmic law which is the link between near wall flow and outer flow.

2.1.3 Effect of pressure gradient

Presence of a mean pressure gradient is widely encountered in industrial flows, may they be outer flows or internal flows and may have a significant impact on the properties of the flow. Apart from the zero-pressure gradient case, two cases of pressure gradients may exist (here only streamwise pressure gradients are considered):

- favorable pressure gradient (FPG) $dp_e/dx < 0$: corresponds to an acceleration of the flow ($dU_e/dx > 0$) and a thinner boundary layer. This occurs for example on the forward part of an airfoil or the major part of a cockpit
- adverse pressure gradient (APG) $dp_e/dx > 0$: corresponds to a decelerating flow ($dU_e/dx < 0$) and a thickening of the boundary layer. This occurs in a diffuser or the aft part of an airfoil.

In this study, the "intensity" of the pressure gradient is quantified by the Clauser (1954) parameter β_C :

$$\beta_C = \frac{\delta^*}{\tau_w} \frac{dp_e}{dx} \quad (2.5)$$

where δ^* , τ_w and dp_e/dx are respectively the TBL displacement thickness, the shear stress at the wall and the streamwise pressure gradient. This parameter can be interpreted as the ratio

between the pressure forces and the shear stress. Other pressure gradient parameters can be found in the literature such as the acceleration parameter K introduced by Kline et al. (1967), Clauser's defect shape factor G , Castillo and George (2001) parameter Λ and the viscous-scaled pressure gradient Δ_p :

$$K = \frac{\nu}{U_e^2} \frac{dU_e}{dx} \quad (2.6a)$$

$$G = \frac{H-1}{H\sqrt{C_f/2}} \quad (2.6b)$$

$$\Lambda = \frac{\delta}{\rho U_e^2 (d\delta/dx)} \frac{dp_e}{dx} \quad (2.6c)$$

$$\Delta_p = \frac{\nu}{\rho u_\tau^3} \frac{dp_e}{dx} \quad (2.6d)$$

The effect of the pressure gradient on the mean velocity profile is visible in the wake region (wake law) where departure from the logarithmic behavior is steeper in the case of an adverse pressure gradient and smoother in the case of a favorable pressure gradient. Regarding turbulent intensities $u_i^{rms} = \sqrt{u_i'^2}$, a secondary peak is visible in the outer region for adverse pressure gradient flows. These effects are visible in figure 2.6 ($u^+ = U/u_\tau$ in this figure corresponds to the mean streamwise velocity expressed in terms of wall units). One can refer to section 3.1 for details on the pressure gradient cases that are shown here.

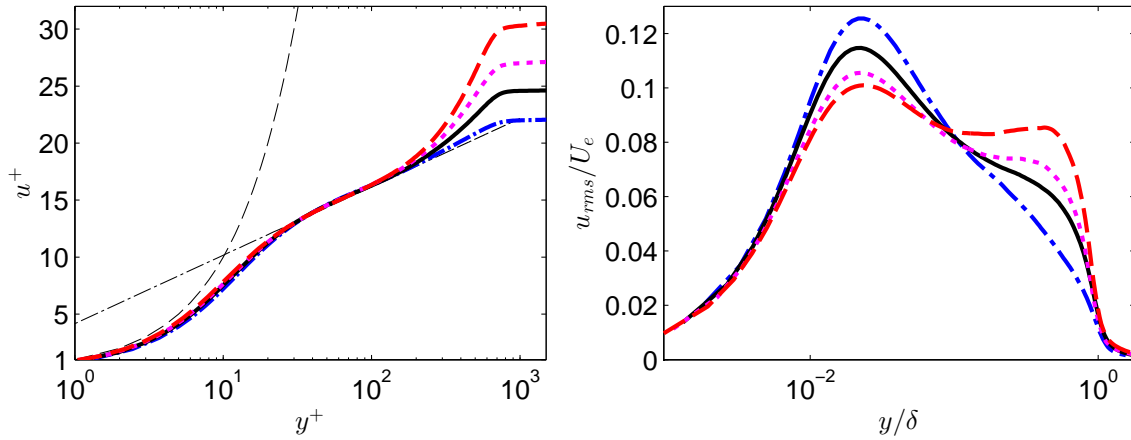


Figure 2.6 – Mean velocity profiles $u^+ = U/u_\tau$ (left) and streamwise component of turbulent intensity u_{rms}/U_e (right) for favorable (— — —), zero (—), adverse weak (— — —) and adverse strong (— — —) pressure gradients - after Cohen and Gloerfelt (2015).

2.1.4 Effect of wall curvature

As for the pressure gradient, curved surfaces are encountered in many industrial flows, such as the flow over an airfoil or in pipes. Usually, an additional dimensionless parameter R/δ , where R is the radius of the curved surface, is used to characterize the influence of the curvature to which the flow is subjected. Curvature of the wall generates centrifugal forces which are compensated by a wall-normal pressure gradient so that:

$$\frac{\partial p}{\partial n} = K_R \rho u^2 \quad (2.7)$$

where n denotes the normal coordinate and $K_R = 1/R$ is the surface curvature. According to Muck et al. (1985) and Hoffmann et al. (1985), a convex surface has a stabilizing effect whereas a concave curvature has a destabilizing effect on boundary layers, and presumably on other shear flows. A mild convex curvature, with a radius of curvature of the order of 100 times the boundary-layer thickness, tends to attenuate the pre-existing turbulence, apparently without producing large changes in statistical-average eddy shape, while concave curvature results in the quasi-inviscid generation of longitudinal Taylor-Görtler vortices, together with significant changes in the turbulence structure induced directly by the curvature and indirectly by the vortices. For a constant pressure flow over both convex and concave walls, Meroney and Bradshaw (1975) found that for $R/\delta \simeq 100$, skin friction differs from its corresponding plane-wall value by as much as 10% while the boundary layer thickness is halved on the convex surface. The effect of transverse curvature was studied by authors such as Landweber (1949), Eckert (1952) and Yu (1958). Their main results suggest that transverse curvature involves lower boundary layer thickness and displacement thickness, higher momentum thickness and local and mean wall shearing stress. These results were obtained from measurements for flows over axial cylinders, which is the basic shape of an aircraft. For the latter however, the ratio of surface radius to boundary layer thickness R/δ is so high that the effects of transverse curvature can be neglected.

2.1.5 Equilibrium and non-equilibrium boundary layers

It is hard to give a unique definition of an equilibrium boundary layer. The most commonly found in the literature is that provided by Clauser (1954), postulating that a boundary layer is in equilibrium state if the pressure gradient parameter β_C (see equation 2.5) is constant along the streamwise direction. He concluded that equilibrium flows are very hard to generate and maintain and that most flows are non-equilibrium flows. In fact, a strict equilibrium can never be reached except for sink-flows, where the strength of the favorable pressure gradient leads to the mean velocity profiles approaching the pure wall profile (Dixit and Ramesh, 2010; Jones et al., 2001). Bradshaw (1967b) showed that a necessary condition for a turbulent boundary layer to maintain equilibrium was that the contribution of the pressure gradient to the growth of the momentum deficit should be a constant multiple of the contribution from the surface shear stress, which was shown to be equivalent to the condition on Clauser's pressure parameter β_C . A boundary layer is in equilibrium state if the local rates of kinetic energy production and dissipation are balanced and if the free stream velocity varies as a power of distance downstream with an exponent greater than $-1/3$ according to Townsend (1976b). Castillo and George (2001) showed that an equilibrium boundary layer was found to exist only when the pressure parameter Λ (see equation 2.6) was constant and surprisingly found that this was the case for most of flows subjected to pressure gradients and the exceptions were non-equilibrium flows, contrary to what Clauser postulated. For Kameda et al. (2008), equilibrium is characterized by the local skin friction coefficient being independent of two parameters, both the streamwise distance and the Reynolds number based on momentum thickness Re_θ , whereas for the non-equilibrium boundary layer, the skin friction coefficient depends on these parameters.

2.2 Coherent structures in the turbulent boundary layer flow

2.2.1 General definition

Over half a century ago, it was observed that some kind of organized motions populated the random turbulent field in wall-bounded flows. The first studies concerned the outer region of the boundary layer with investigations on intermittency in the turbulent/potential interface at the edge of turbulent flows (Corrsin, 1943; Corrsin and Kistler, 1954), followed by the large eddy motions populating the outer layer (Favre et al., 1957; Grant, 1958; Townsend, 1976a). At the same time, people started looking at the structure of the near-wall region, such as Einstein and Li (1956) and Kline and Runstadler (1959). Since then, great effort has been undergone to characterize these coherent regions and this field of study is still a very active research topic nowadays. This is partly due to the fact that until now, fluid dynamicists still struggle giving a generally accepted definition of a coherent motion in turbulent flows. For example, Robinson (1991a) gives the following definition:

"a coherent motion is a three-dimensional region of the flow over which at least one fundamental flow variable (velocity component, density, temperature, etc.) exhibits significant correlation with itself or with another variable over a range of space and/or time that is significantly larger than the smallest local scales of the flow."

Pope (2000) defines turbulent structures as:

"regions of space and time (significantly larger than the smallest flow or turbulence scales) within which the flow field has a characteristic coherent pattern".

Vortices are part of the vast population of coherent motions in turbulent flows but have a specific property in addition. According to Robinson (1991a):

"A vortex exists when instantaneous streamlines mapped onto a plane normal to the vortex core exhibit roughly circular or spiral pattern, when viewed from a reference frame moving with the center of the vortex core."

Hussain (1986) postulates that the coherent vorticity is the primary identifier of coherent structures; coherent vorticity being designated as *"instantaneously space- and phase-correlated vorticity"*. The vast majority of turbulent structures investigation has resulted from low Reynolds numbers experiments since it is more effective for flow visualization and numerical simulation. Hereafter, a summarized overview of the most known coherent motions present in the turbulent boundary layer flow is provided. The literature on this topic is extensive and the reader can refer to reviews by Robinson (1991a), Cantwell (1981), Kline and Falco (1979), Kline (1978), Townsend (1976b) and Willmarth (1975).

2.2.2 Near-wall structures

In the late 1950s, a series of flow visualization experiments was begun in Stanford to study boundary layers. The next decade, Kline et al. (1967) revealed new features of the near-wall region through hydrogen bubble visualization of a low Reynolds-number turbulent boundary layer. They found that very close to the wall, in the viscous sublayer at $y^+ = 2.7$ and up to $y^+ = 10$, the bubbles accumulated in high- and low-speed regions called streaks. They observed that the streaks interacted with the outer region of the flow through a sequence of four events:

gradual outflow, liftup, sudden oscillation and breakup, and defined the sequence of the three last events as "bursting". They could deduce that the average spanwise spacing of streaks λ_z^+ for smooth walls and all pressure gradients was approximately 100 wall units, e.g. $100\delta_\nu$ where $\delta_\nu = \nu/u_\tau$ is the viscous lengthscale. Subsequent experiments (Kim et al., 1971) confirmed that the spanwise spacing is between $80 < \lambda_z^+ < 120$, independent of the Reynolds number. Smith and Metzler (1983) observed that this spacing increases away from the wall. In the streamwise direction, the length of the streaks can exceed $\lambda_x^+ = 1000$ (Blackwelder, 1979).

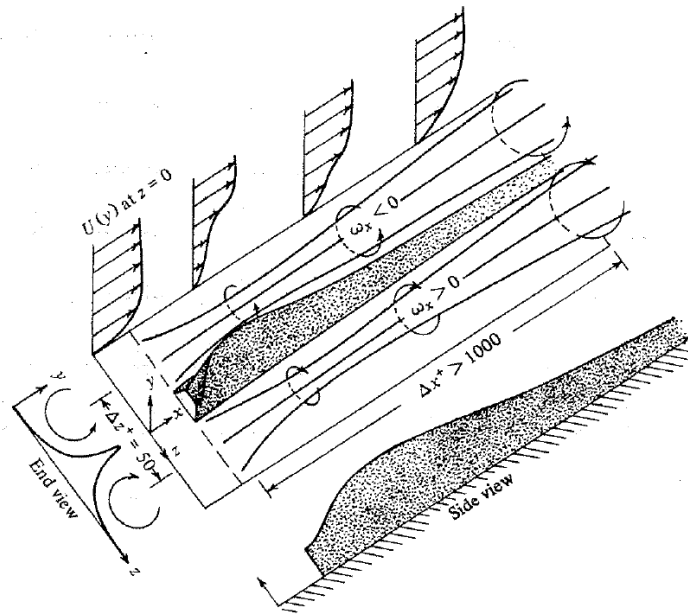


Figure 2.7 – A pair of counter-rotating streamwise vortices with the resulting low-speed streak (dark region) - after Blackwelder (1979).

Kim et al. (1971) observed near the wall a rotational motion which they interpreted as streamwise vortices. Later on, Blackwelder (1979) inferred that these streamwise vortices evolve by counter-rotating pairs, based on hot-film signals. He suggested that the low-speed streaks come from counter-rotating pairs of streamwise vortices, which lift-up low-momentum fluid from the wall. This leads to the velocity profiles having an inflection point as shown in figure 2.7. Another explanation is that the low-speed streaks are the trace of one or several stacked hairpin vortices (which will be detailed later, see figures 2.11 and 2.12), convecting over the wall and which lift-up between their legs and heads low-speed fluid. This has been recently supported by the work of Zhou et al. (1999) who carried out DNS of the evolution of one hairpin vortex in a turbulent channel flow. They showed that the initial hairpin persists in time and induces, upstream and downstream, other hairpin vortices associated with ejections. This system of hairpin vortices generates then progressively a low-speed streak. However, these two proposals may agree if it is considered that the counter-rotating pairs of streamwise vortices are legs near the wall of hairpin vortices.

Corino and Brodkey (1969) observed what they called ejections in the region $5 < y^+ < 15$ consisting of low speed fluid being lifted up away from the wall, and it was noticed that ejections were followed by a sweep event where an axial movement upstream of the ejection sweeps high-speed fluid $u' > 0$ towards the wall. It has been demonstrated that ejections and sweeps have a significant role in turbulence production. The (u', v') sample space of fluctuating velocities

is divided in four quadrants as shown in figure 2.8. In quadrants 2 and 4, which correspond respectively to ejections ($u' < 0, v' > 0$) and sweeps ($u' > 0, v' < 0$), the product uv is negative and consequently events in this region correspond to positive production $\mathcal{P} = -\langle uv \rangle \partial U / \partial y > 0$. Studies focusing on the contribution of each quadrant to $\langle uv \rangle$ (Comte-Bellot et al., 1978; Wallace et al., 1972; Willmarth and Lu, 1972) provided evidence for the importance of ejections and sweeps to production and that the correlation coefficient $R_{u'v'}$ suggests that quadrant-2 and -4 events are twice as likely as quadrant-1 and -3 events irrespective to the turbulence structure. Wallace et al. (1972) showed that at $y^+ \simeq 15$, the contributions of the ejections and sweeps to the Reynolds stress are equivalent. Ejections dominate in the region $y^+ > 15$, while sweeps are the major contributor close to the wall $y^+ < 15$.

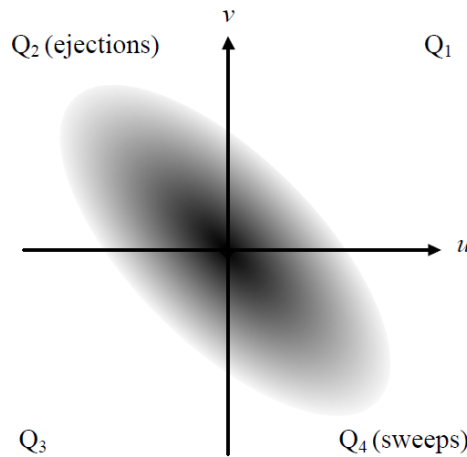


Figure 2.8 – The quadrant splitting scheme showing the probability density function in the (u', v') plane.

Finally, the existence of shear zones was observed in the near wall region between low-speed and high-speed streaks. Studies by Johansson et al. (1987) and Johansson et al. (1991) showed that these structures are inclined by around 5° to the wall in the near wall region $y^+ < 10$ and 18° above. Intense shear zones develop between the ejected fluid and the low-speed fluid surrounding it. Results from Johansson et al. (1991) gave evidence that shear regions generate strong positive pressure fluctuations and are in average located upstream of a very intense ejection. Instantaneous velocity and vorticity field from DNS (Robinson, 1991b) showed that for $30 < y^+ < 80$ shear zones are rolled forming transverse vortices that generate strong ejections.

2.2.3 Outer-region structures

In the outermost part of the boundary layer the flow is intermittent. There is a thin turbulence front, referred to as the viscous super-layer, separating the turbulent boundary layer from the irrotational free-stream fluid. Figure 2.9 shows that "valleys" of non-turbulent fluid penetrate deep into the boundary layer and that they separate large eddies or bulges that are inclined at a characteristic angle of 25° . Therefore, shear layers are observed in the "valleys" since relatively high velocity fluid impacts the upstream side of the bulges. Kovasznay et al. (1970) showed that these bulges have a typical length δ to 3δ in the stream direction and are about half as wide in the spanwise direction. The large eddies and the super-layer also contain smaller structures referred to as typical eddies by Falco (1977), which appear at the trailing of the large scale eddies (see figure 2.9). Head and Bandyopadhyay (1981) support that they are tips of hairpin

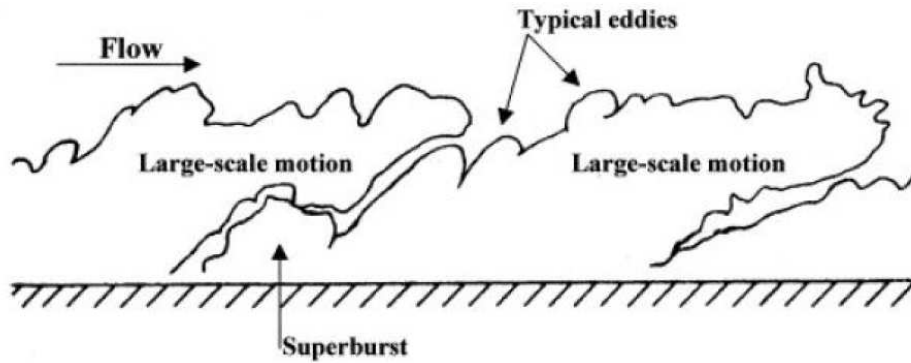


Figure 2.9 – Outer region model showing large scale motions and typical eddies - after smoke visualization by Falco (1977) .

vortices inclined at 45° to the wall.

Since organized motions were also present in the outer layer, a relationship between the inner events and the outer region received scrutiny. Kovaszny et al. conjectured that the bulges become inactive and that only the birth of new ejected "lumps" (presumably from the wall) is the mechanism that maintains the Reynolds stress of the outer layer. They also suggest that the bursts observed by Kline et al. (1967) near the wall are responsible for the large-scale motions in the outer flow. Blackwelder and Kovaszny (1972) found that the intense motions in the near wall region remained strongly correlated out to $y/\delta \simeq 0.5$. Using turbulent pipe and boundary layer flow visualizations, Praturi and Brodkey (1978) came up with an elegant model which relates the coherent motions in the outer region to the near-wall turbulence production as shown on figure 2.10. In their model, the near-wall transverse vortices are lifted up from the wall due to the ejection process in the buffer layer and transported in the outer layer where they induce shear layers and form the large scale bulges. However, the question of mass and momentum transfer between the inner and outer part of the boundary layer still remains controversial.

2.2.4 Hairpin vortices and hairpin packets

Global definition

The first hairpin model was first introduced by Theodorsen (1952) (see figure 2.11). The common definition stipulates that hairpin structures can be divided into three parts: legs, neck and head as shown in figures 2.13 and 2.15. More generally, hairpin vortices refer to hairpin-, horseshoe-, cane-, arch-, omega-shaped vortices or any deformed version of these, and can be symmetric or asymmetric. In his conceptual model, since the layer farther from the wall has higher mean flow velocity in comparison to the layer close to the wall, as the structures move downstream, as well as experiencing a high degree of stretching, the head (spanwise part) undergoes a lifting movement from the wall. This motion results in the head of the vortex lifting upward toward the free stream allowing higher velocities to carry the head downstream faster than the legs. This action leads to a stretching of the legs as the hairpin vortices are convected downstream. This motion of vortices transports low-speed fluid away from the wall and produces Reynolds stresses. Theodorsen (1952) argues that the hairpin structures are the primary element of wall-bounded turbulence.

Hairpin-like vortices were first observed by Head and Bandyopadhyay (1981) in a zero pressure gradient turbulent boundary layer using flow visualization. It was shown that hairpins are

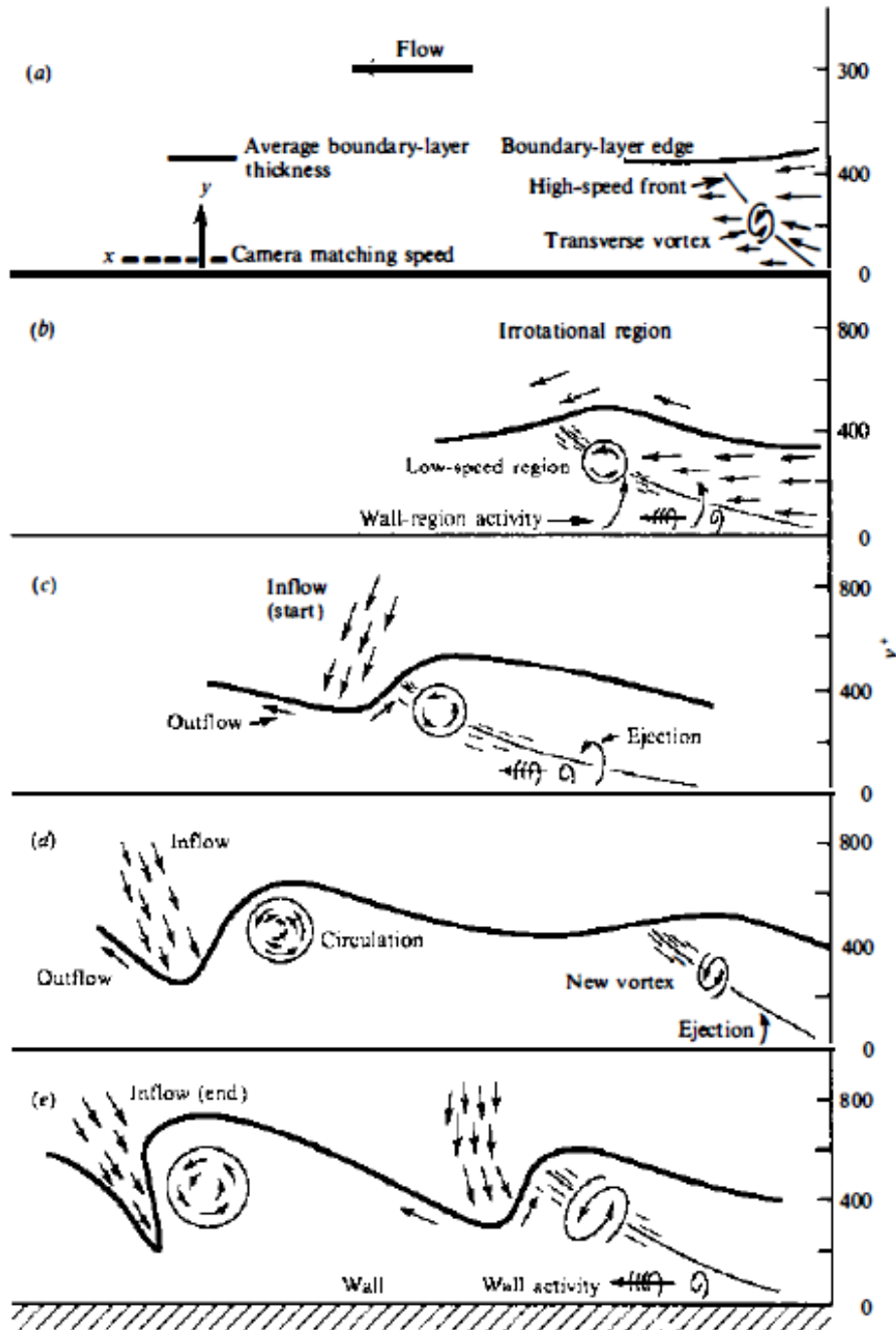


Figure 2.10 – Conceptual model of interaction between the near-wall region and the outer flow motions - after Praturi and Brodkey (1978).

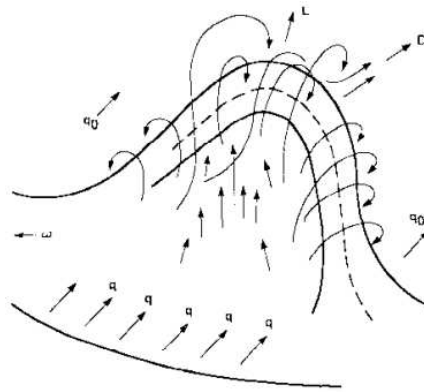


Figure 2.11 – Theodorsen (1952) hairpin-like vortex.

a major constituent of TBLs over a wide range of Reynolds numbers and that they are produced in a relatively regular sequence so that the locus of their tips presents a more or less straight line with a certain angle to the surface which is less than that of the individual hairpin. This last observation is the evidence of the existence of hairpin packets, which correspond to a sequence of individual hairpin vortices aligned along the streamwise direction. As can be seen in figure 2.12, hairpin packets exist at different wall-normal distances. They have different length scales and convection velocities. According to Adrian et al. (2000), hairpin vortices within a same packet have very low velocity dispersion such that the relative spacing and arrangement of the hairpins remain coherent for a long time. Figure 2.12 also shows that the packets lay over a region of low momentum due to the backward induced motion between the legs of the hairpin sequence. This region is referred to as a Low Momentum Region (LMR) and was also observed by Lee and Sung (2009), Mayam (2009), Dennis and Nickels (2011), Ganapathisubramani et al. (2005) and many others.

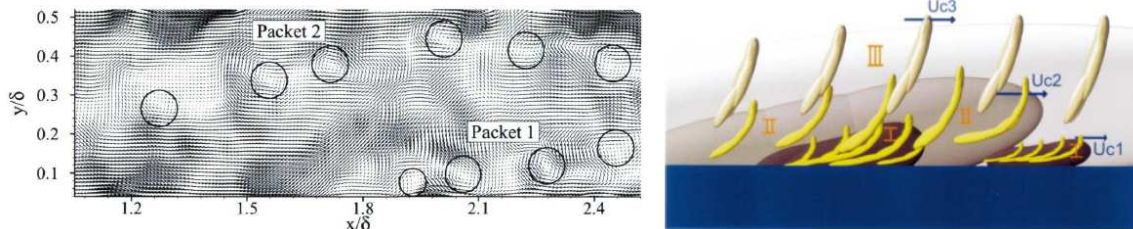


Figure 2.12 – Hairpin packets organization in the turbulent boundary layer flow - (left) Instantaneous velocity field in Galilean frame convecting at $U_c = 0.55U_e$ after Mayam (2009) and (right) idealized model of nested hairpin packets travelling at different convection velocities after Adrian et al. (2000).

Figure 2.12 also shows that small newly formed packets exist within larger older packets. Measurements of convection velocities reveal that the small packets located near the wall propagate more slowly than the older ones. This has two combined reasons:

- the flow surrounding large packets has a higher velocity since they are located in the outer region of the boundary layer
- in the small young packets, the individual hairpin vortices are closer to each other, therefore producing higher back-induced velocities and even lower momentum regions.

Reynolds number effect

Some authors were interested in the effect of the Reynolds number on the coherent motions. Head and Bandyopadhyay (1981) focused on the hairpin-like vortices in a zero pressure gradient turbulent boundary layer in a Reynolds number range $500 < Re_\theta < 17500$. They observed that at high Reynolds number ($Re_\theta > 2000$), the structures consist of elongated hairpin vortices pairs, originating in the wall region and extending through a large part of the boundary layer thickness or beyond it. At low Reynolds numbers ($Re_\theta < 500$) however, the hairpin vortices are much less elongated and would be better defined as horseshoe vortices or vortex loops. This Reynolds number effect on the topology of the hairpin-like vortices is illustrated in figure 2.13. Authors such as Schlatter and Örlü (2010) suggest that at even higher Reynolds number, the hairpins vortices break and become asymmetric cane-shaped structures.

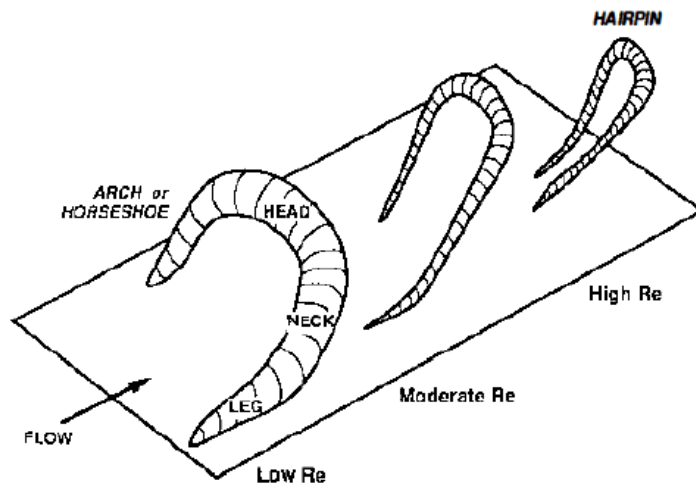


Figure 2.13 – Effect of Reynolds number on the geometry of hairpin-like eddies - after Head and Bandyopadhyay (1981).

Adrian et al. (2000) also suggest that packets contain fewer individual hairpins at low Reynolds numbers than at high Reynolds numbers in the outer region of the boundary layer. This result is based on the fact that the hairpin packets present in the very outer region define the instantaneous boundary layer edge which is highly corrugated at low Reynolds numbers and may therefore be assimilated to bulges. Since the length of the bulges is about 2δ (Kovaszny et al., 1970), while the distance between hairpins scales roughly with viscous wall variables at about 100-200 viscous wall units, the number per packet increases with increasing Reynolds number.

Angle of hairpin vortices

Since the hairpin-like structure can be divided into three parts, it is possible to define the angle of the hairpin α_{hp} (which is an average angle of the structure), the angle of the legs of the hairpin α_l and the angle of the neck of the hairpin α_n as can be seen on the schemes in figures 2.14 and 2.15.

Head and Bandyopadhyay (1981) found an average hairpin angle of $45^\circ - 50^\circ$ from flow visualization of a zero-pressure gradient turbulent boundary layer. Mayam (2009) performed Particle Image Velocimetry (PIV) measurements of a turbulent boundary layer subjected to a severe adverse pressure gradient for Reynolds numbers ranging within $5300 < Re_\theta < 12000$

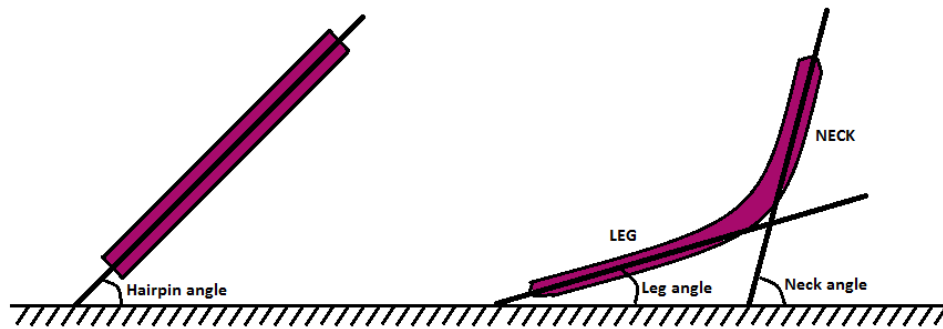


Figure 2.14 – Sideview of hairpin-vortex - idealized linear representation (left) and "realistic" hairpin geometry (right).

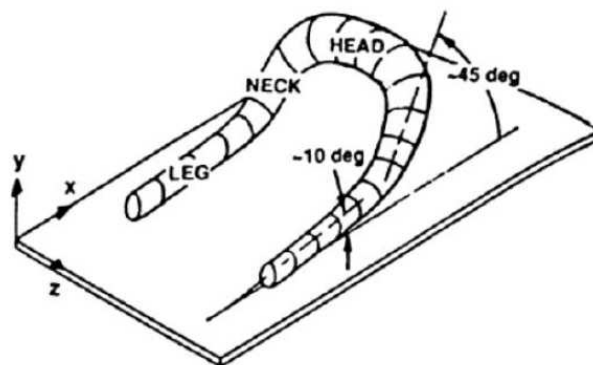


Figure 2.15 – Different parts of the hairpin vortex with the corresponding angles to the wall - after Robinson (1991b) .

along the streamwise direction and compared his results to a zero pressure gradient flow. He found that the neck angles of the hairpin vortices are rather close for both flows in the inner layers whereas the angle is up to 18% higher for the APG case for the upper region of the boundary layer. Lee and Sung (2009) performed Direct Numerical Simulation (DNS) of ZPG and APG turbulent boundary layers. For the APG case, $\beta_C = 1.68$ and $Re_\theta = 1200 - 1400$ (for the ZPG flow, only the Reynolds number $Re_\theta^{in} = 1410$ at the inlet of the computation domain is mentioned). Lee and Sung (2009) were able to measure both the leg angle and neck angle of the hairpin structures based on conditionally averaged velocity fields at $y^+ = 50$. They found leg angles around 9.2° for the APG case and 8.8° for the ZPG flow, and neck angles around 28.8° and 21.3° respectively for the APG and ZPG cases.

Angle of hairpin packets

Evidence of streamwise aligned hairpin vortices in the turbulent boundary layer flow was shown at early stages by Head and Bandyopadhyay (1981). They were able to directly visualize tips of hairpin vortices lying in a line inclined at an angle around $\alpha_p = 20^\circ$ to the wall as can be seen in figure 2.16. Mayam (2009) measured a hairpin packets average growth angle close to 11° for the adverse pressure gradient case from instantaneous velocity fields visualization. For this flow, he was also able to observe that the hairpin vortices within the same packet are more closely spaced along the streamwise direction in comparison to the ZPG flow.

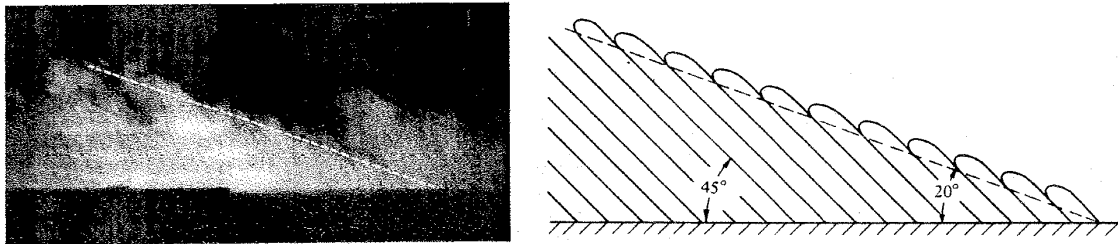


Figure 2.16 – Evidence of streamwise aligned vortices along a line inclined to the wall - flow is from right to left - after Head and Bandyopadhyay (1981).

Adrian et al. (2000) observed angles ranging from 3° to 35° from instantaneous velocity fields of a channel flow, with a 12° mean angle which agrees well with the simulations of Zhou et al. (1999). From the same measurement data, they could also identify packets of hairpins with non monotonous angles, i.e. a positive ramp angle followed by a negative angle (see figure 2.17). This was also observed by Mayam (2009) and it is suggested that this could be due to the formation of hairpins downstream of the primary hairpin (Zhou et al., 1999). However, statistical analyses reveal that the most common feature consists in packets with a positive angle.

Lee and Sung (2009) reported angles around $\alpha_p = 13^\circ$ for the ZPG flow and $\alpha_p = 18.5^\circ$ for the APG by estimating the angle of the packet line from linear stochastic estimation of the velocity field (see section 2.2.5) with event location at $y/\delta = 0.2$. Similarly, Christensen and Adrian (2001) measured $\alpha_p = 13^\circ$ and $\alpha_p = 14^\circ$ growth angles for a turbulent channel flow with $Re_\tau = 547$ ($y_{ref}^+ = 83.6$, $y/h = 0.16$) and $Re_\tau = 1734$ ($y_{ref}^+ = 256$, $y/h = 0.15$) respectively, where $Re_\tau = u_\tau h/\nu$ is the Reynolds number based on the friction velocity u_τ and the channel half height h . Volino et al. (2007) determined angles around $13.2^\circ \pm 2.5^\circ$ for $0.2 < y/\delta < 0.7$ with angles decreasing above $y/\delta = 0.7$.

It will be shown in section 3.3.2 that the angle of the two-points spatial correlation of the streamwise velocity R_{uu} is correlated with the angle of the hairpin packets. Liu et al. (2001) measured an angle of R_{uu} around $6^\circ - 8^\circ$ at reference point $y/h = 0.24$ in a turbulent channel

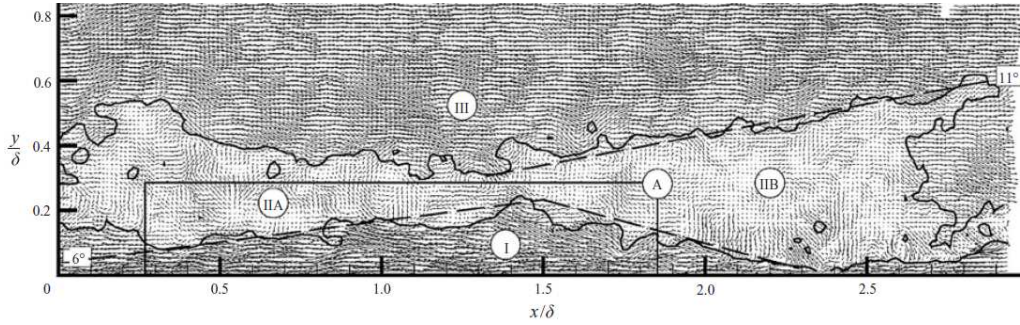


Figure 2.17 – Example of non-monotonically increasing hairpin packet represented by the lower dashed line - after Adrian et al. (2000) .

flow at $Re_h = 3 \times 10^4$. Similarly, Nakagawa and Hanratty (2001) measured an inclination angle of the correlation around 9° in a channel flow with wavy boundaries at a reference point $y/h = 0.23$ and $Re_h = 4.6 \times 10^4$. Tay et al. (2009) looked at the streamwise extent and angle of the correlation when studying the effect of surface roughness on turbulent boundary layers subjected to pressure gradients with Reynolds numbers $Re_\theta = 914$ for the ZPG case and $Re_\theta = 2182$ for the APG (deceleration parameter $K = -4.45 \times 10^{-7}$). For the smooth surface case, they measured inclination angles of 10.1° for the FPG and 17.3° for the APG at reference point around $y/\delta \simeq 0.25$. Krogstad and Antonia (1994) found an angle around 10° based on the inclination of the $R_{uu} = 0.3$ contour in the range $0.1 < y/\delta < 0.4$ from X-wire measurements of a $Re_\theta = 6030$ ZPG turbulent boundary layer.

2.2.5 Visualization, identification and analysis methods

As already mentioned, fluid dynamicists still struggle giving a generally accepted definition of coherent motions in turbulent flows. Indeed, the definition and identification of a vortex in unsteady flows is difficult since streamlines and pathlines are not invariant with respect to Galilean and rotational transformations as emphasized by Lugt (1979).

Vorticity has long been the most accepted candidate for vortex identification, but Jeong and Hussain (1995) along with other authors such as Kida and Miura (1998) and Cucitore et al. (1999) showed that vorticity is not able to distinguish between regions of shear flow and real spinning motions. More complex methods based on invariants of the velocity gradient tensor $\nabla \mathbf{u}$ have been developed. Chong et al. (1990) propose that a vortex core is a region with complex eigenvalues of $\nabla \mathbf{u}$ as a complex eigenvalue implies that the local streamline pattern is closed or spiral in a reference frame moving with the point of calculation. Hunt et al. (1988) defined an eddy as a region with positive second invariant of the velocity gradient tensor. More recently, an identification method based on the concept of Lagrangian Coherent Structures (LCS) was proposed (Haller, 2002, 2005; Haller and Beron-Vera, 2013).

Vortex identification criteria still remain a subject of interest and debate due to their arbitrary threshold which provides information on presence of a vortex and its boundaries. Authors such as Cucitore et al. (1999), Chakraborty et al. (2005) and Vollmers (2001) performed a comparison of some of these criteria. Hereafter, an overview of visualization, identification as well as analysis methods is provided.

Pressure

Pressure can be used for vortical structures identification since the center of a vortex is a region of local minimum of pressure. In this case, the criteria would be:

$$p \leq p_{thresh} \quad (2.8)$$

This method is based on the idea that centripetal force induces pressure gradient. It is very simple to implement but the threshold is purely arbitrary and the pressure can vary greatly along the vortex.

Vorticity

Vorticity is defined as the curl of the velocity field and often denoted ω :

$$\omega = \nabla \times \mathbf{u} \quad (2.9)$$

It describes the local spinning motion of the fluid near some point as would be seen by an observer located at that point and travelling along with the fluid. It is therefore related to the moment of momentum of a small particle about its own center of mass, as defined in Shapiro (1969). For example, for rigid body, every line perpendicular to the axis of rotation has the same angular velocity; therefore vorticity is the same at every point and is twice the angular velocity.

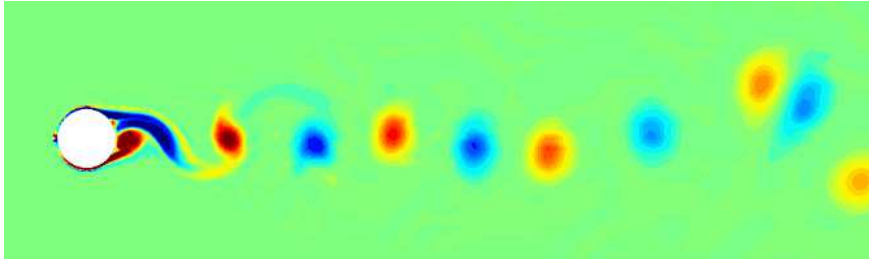


Figure 2.18 – Vorticity contours showing von Kármán vortex street behind a cylinder at $Re \simeq 3000$ - Marine Ecosystem Dynamics Modelling lab.

Vorticity can be used to visualize and identify vortical structures since the center of a vortex corresponds to a local maximum of the vorticity modulus. In figure 2.18, a Kármán vortex street is revealed using vorticity.

Q criterion

The quantity Q used here is the second invariant of the Jacobian of the velocity field and can be defined as:

$$Q = \frac{1}{2}(\overline{\Omega_{ij}\Omega_{ij}} - \overline{S_{ij}S_{ij}}) \quad (2.10)$$

where S_{ij} is the shear stress tensor and Ω_{ij} the rotation term of the velocity gradient tensor, e.g.:

$$S_{ij} = \frac{1}{2} \left(\frac{\partial u_i}{\partial x_j} + \frac{\partial u_j}{\partial x_i} \right) \quad (2.11a)$$

$$\Omega_{ij} = \frac{1}{2} \left(\frac{\partial u_i}{\partial x_j} - \frac{\partial u_j}{\partial x_i} \right) \quad (2.11b)$$

The criterion, introduced by Hunt et al. (1988), consists in looking for regions where this quantity is positive since $Q > 0$ implies local pressure smaller than the surrounding pressure. This method

is commonly used in flow visualization. Figure 2.19 shows near-wall structure at turbulent boundary layer transition using this method.

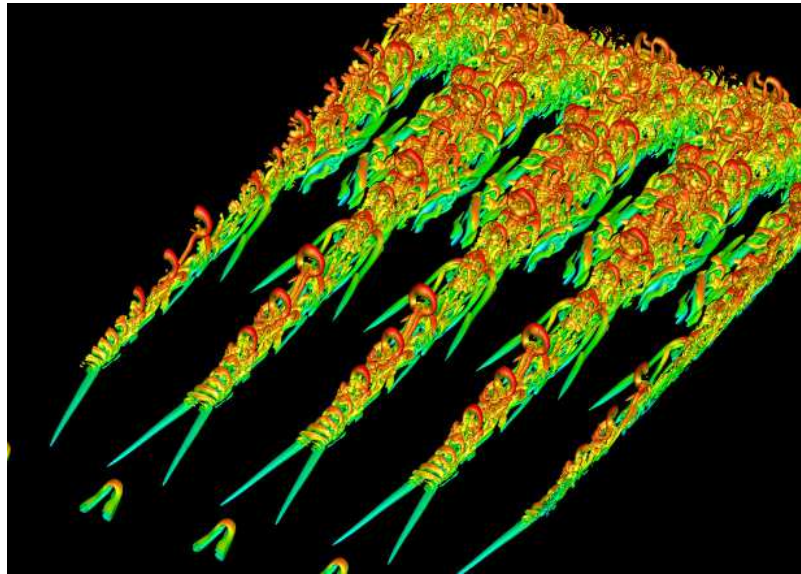


Figure 2.19 – Isosurface of Q -criterion colored by velocity magnitude showing near-wall structures in boundary layer transition - Mech. Eng. Dept, Stanford Univ.

λ_2 criterion

The quantity λ_2 is defined as the second largest eigenvalue of the tensor $S^2 + \Omega^2$ (where S and Ω are the two tensors introduced in equation 2.11). The criterion was introduced by Jeong and Hussain (1995) and consists in identifying regions where $\lambda_2 < 0$ since they correspond to local pressure minimum. This criterion is widely used among fluid dynamicists, but is sensitive to high shear. Gloerfelt and Margnat (2014) used the λ_2 criterion to reveal structures between transition and fully turbulent flow as shown in figure 2.20.

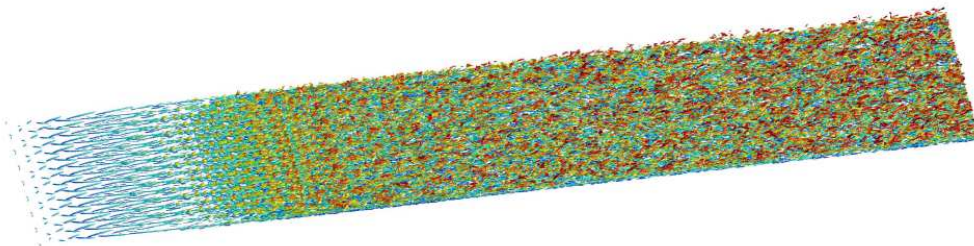


Figure 2.20 – LES of spatially developing TBL at Mach 0.5, isosurface of λ_2 criterion colored by streamwise velocity - after Gloerfelt and Margnat (2014).

Δ criterion

Chong et al. (1990) define a vortex core as a region where $\nabla \mathbf{u}$ has complex eigenvalues. The characteristic equation for $\nabla \mathbf{u}$ is given by:

$$\lambda^3 + P\lambda^2 + Q\lambda + R = 0 \quad (2.12)$$

where P , Q , and R are the three invariants of the velocity gradient tensor. The discriminant for eq. (2.12) is (for incompressible case, i.e $P = 0$):

$$\Delta = \left(\frac{1}{2}R\right)^2 + \left(\frac{1}{3}Q\right)^3 \quad (2.13)$$

The condition $\Delta > 0$ implies that $\nabla \mathbf{u}$ has complex eigenvalues. From Eq. (2.13) it can be seen that $Q > 0$ criterion is more restrictive than the $\Delta > 0$ criterion. Cucitore et al. (1999) used this criterion along with an empirical Galilean invariant non-local criterion. The latter is based on the intuitive notion that the change in the relative distance between particles inside a vortex structure is small and therefore introduces a ratio to quantify this change.

Kinematic vorticity number

Truesdell (1953) introduced the kinematic vorticity number N_k to measure 'the quality of rotation', instead of the local rotation rate given by $\|\boldsymbol{\Omega}\|$.

$$N_k = \left(\frac{|\boldsymbol{\omega}|^2}{2S_{ij}S_{ij}}\right)^{1/2} = \frac{\|\boldsymbol{\Omega}\|}{\|\mathbf{S}\|} = \left(1 + \frac{2Q}{S_{ij}S_{ij}}\right)^{1/2} \quad (2.14)$$

Thus, N_k is a pointwise measure of $|\boldsymbol{\omega}|$ non-dimensionalized by the norm of the strain rate, which gives the quality of rotation regardless of the vorticity magnitude. For example, $N_k = \infty$ and $N_k = 0$ correspond to solid-body rotation and irrotational motion respectively. Melander and Hussain (1993) used this quantity to identify the core of an axisymmetric vortex column as "a maximally connected spatial region with $N_k > 1$ ". However, the kinematic vorticity number does not discriminate between vortices with small and large vorticity (or circulation) as long as the quality of the rotation is the same for both.

Swirling strength λ_{ci}

The swirling strength λ_{ci} is the imaginary part of the complex eigenvalue of the velocity gradient tensor which can be expressed as:

$$\nabla \mathbf{u} = \begin{pmatrix} \mathbf{v}_r & \mathbf{v}_{cr} & \mathbf{v}_{ci} \end{pmatrix} \begin{pmatrix} \lambda_r & & \\ & \lambda_{cr} & \lambda_{ci} \\ & -\lambda_{ci} & \lambda_{cr} \end{pmatrix} \begin{pmatrix} \mathbf{v}_r & \mathbf{v}_{cr} & \mathbf{v}_{ci} \end{pmatrix}^{-1} \quad (2.15)$$

where $(\mathbf{v}_r, \mathbf{v}_{cr}, \mathbf{v}_{ci})$ are the eigenvectors of the tensor. This method automatically eliminates regions having vorticity but no spiralling motion such as shear layers (refer to Zhou et al. (1999) for more details). For this reason, but also because the λ_{ci} criterion has been the last developed and therefore is believed to be more advanced, this criterion will be used hereafter. Recently, several authors which use the linear stochastic estimation (LSE) method to investigate vortical structures in turbulent flows use this criterion.

Enhanced swirling strength criterion

The common factors to most of the criteria are that an identification criterion should be Galilean invariant and that the local flow in the frame of reference translating with the vortex should be swirling. Chakraborty et al. (2005) added a third requirement which is that the separation between the swirling material points inside the vortex core should remain small, i.e. the orbits of the material points are compact. Therefore, they introduced the spiralling inverse compactness given by:

$$\frac{\lambda_{cr}}{\lambda_{ci}} \quad (2.16)$$

This ratio measures the spatial extent of the local spiralling motion. A value of $\lambda_{cr}/\lambda_{ci} = 0$ results in a perfectly circular path, while a positive (or negative) value corresponds to a path

that spirals outward (or inward) in the plane of the vortex.

Γ_1 and Γ_2

These methods have been developed for two-dimensional cases only and therefore can be applied to PIV plane measurements. They allow to determine both the center and boundaries of a vortical structure.

Let P be a fixed point in the measurement domain. Graftieaux et al. (2001) define the dimensionless scalar function Γ_1 at P as :

$$\Gamma_1(P) = \frac{1}{S} \int_{M \in S} \frac{(\mathbf{PM} \times \mathbf{u}_M) \cdot \mathbf{n}}{\|\mathbf{PM}\| \cdot \|\mathbf{u}_M\|} dS \quad (2.17)$$

where S is a 2D-area surrounding P , M lies in S and \mathbf{n} is the unit vector normal to the measurement plane. Γ_1 is a dimensionless scalar, with Γ_1 bounded by 1. It can be shown that this bound is reached at the location of the vortex centre if the vortex is axisymmetrical. Thus, the scalar function Γ_1 provides a way to quantify the streamline topology of the flow in the vicinity of P and the rotation sign of the vortex.

Graftieaux et al. (2001) improved this method by introducing the quantity Γ_2 which takes into account a local convection velocity $\tilde{\mathbf{u}}_P$ around P :

$$\Gamma_2(P) = \frac{1}{S} \int_{M \in S} \frac{[\mathbf{PM} \times (\mathbf{u}_M - \tilde{\mathbf{u}}_P)] \cdot \mathbf{n}}{\|\mathbf{PM}\| \cdot \|\mathbf{u}_M - \tilde{\mathbf{u}}_P\|} dS \quad (2.18)$$

where $\tilde{\mathbf{u}}_P = \frac{1}{S} \int_S \mathbf{u} dS$. Note that in contrast to Γ_1 , Γ_2 is Galilean invariant.

Proper Orthogonal Decomposition (POD)

The Proper Orthogonal Decomposition (POD) method for vortex identification is based on the idea that regions of high vorticity correspond to energetic modes. It identifies the set of orthogonal modes that best reconstruct a dataset. Graftieaux et al. (2001) used this method along with the Γ_2 for vortex identification from PIV measurements in a highly turbulent swirling flow. Lumley (1981), Holmes et al. (1996), Baltzer et al. (2010) and more recently He et al. (2016) also use POD to identify coherent structures such as low-speed streaks and hairpin-like vortices. Liu et al. (2001) and Rempfer and Fasel (1994) used also this method to study Large Scale Motions (LSMs) and structures in turbulence transition respectively. Due to success of the method, it has spawned a number of variants including double POD (Siegel et al., 2008; Tubino and Solari, 2005), observer-inferred decomposition (OID) (Schlegel et al., 2012), temporal POD (Gordeyev and Thomas, 2013), spectral POD (Sieber et al., 2016), etc.

Dynamic Mode Decomposition (DMD)

Recently dynamic mode decomposition has gained popularity as a tool for analyzing the dynamics of nonlinearity evolving fluid flows and is actually the only modal decomposition method developed for this task. For instance, POD can be applied to flows with nonlinear dynamics, but the POD modes are not necessarily optimal for those dynamics. This method was first introduced at a conference by Schmid and Sesterhenn (2008) and followed one year later by a paper published by Rowley et al. (2009). The latter introduces a method based on Koopman theory (Koopman, 1931) which states that there exists a set of modes, the "Koopman modes", that completely characterizes the dynamics of a nonlinear system. On the other hand, Schmid and Sesterhenn (2008) presents the DMD as a method analyzing a "linear tangent approximation" to the underlying flow. They also explored the connections between DMD and POD, leading to an SVD-based algorithm which has become the standard for DMD users.

In terms of coherent structures analysis, Zhang et al. (2014) used DMD along with POD to

identify coherent structures behind a single cylinder and two side-by-side cylinders, Tang and Jiang (2012) applied DMD for the analysis of hairpin vortices generated by a hemisphere protuberance using PIV measurements in a water channel, Hyhlík and Netrebská (2016) evaluated the travelling vortex speed in a synthetic jet flow.

Variable Interval Time Average (VITA)

The VITA method introduced by Blackwelder and Kaplan (1976) is a statistical method which can be seen as a low-pass filter giving a localized temporal measure of a quantity. The simple criteria used allow to detect the events associated with the sudden variations of the signal under study, both in the time and space domains. For a turbulent signal $Q(\mathbf{x}, t)$ the variable interval time average $\hat{Q}(\mathbf{x}, t)$ is defined by:

$$\hat{Q}(\mathbf{x}, t, T) = \frac{1}{T} \int_{t-T/2}^{t+T/2} Q(\mathbf{x}, \tau) d\tau \quad (2.19)$$

where \mathbf{x} is the location where the sample has been taken and T is the averaging time. As T becomes large, the conventional time averaging results:

$$\lim_{T \rightarrow \infty} \hat{Q}(\mathbf{x}, t, T) = \overline{Q}(\mathbf{x}) \quad (2.20)$$

which is independent of t because of stationarity. In order to obtain a local average of some phenomenon, the average time T must be of the order of timescale of the phenomenon under study. Therefore, as already mentioned, the VITA method can be assimilated to a low-pass filter with $1/T$ representing the cut-off frequency and gives a localized temporal measure of the quantity Q .

Blackwelder and Kaplan (1976) could examine the vortex structures associated with the bursting phenomenon in the near wall region which is characterized by low-speed fluid being "pumped" away from the wall. Morrison et al. (1988) applied the VITA algorithm to a variety of turbulent boundary layers where they were able to capture length-scale statistics within the flow.

Window Average Gradient (WAG)

The window average gradient detection scheme (Antonia and Fulachier, 1989; Antonia et al., 1990) searches for changes in the average signal level over a certain time interval. This interval is selected so that the corresponding length scale is comparable to the event of interest. For instance, if a window of $2\tau + 1$ samples is moved through the data, the quantity:

$$\text{WAG}_i = \frac{\text{sign}}{2\tau} \left(\sum_{j=i+1}^{i+\tau} u_j - \sum_{j=i-\tau}^{i-1} u_j \right) \quad (2.21)$$

is computed at every point and the detection begins when WAG_i first exceeds a certain threshold. This method was used by Krogstad and Antonia (1994) to study large-scale motions in turbulent boundary layers on smooth and rough walls since it is well suited to detect discontinuities in the velocity signal which characterizes large-scale motions.

Linear Stochastic Estimation (LSE)

Linear stochastic estimation is a statistical tool first introduced by Adrian (1975). The method uses a two-point second order correlation in terms of conditional flow pattern. The idea is to reconstruct a certain quantity, for instance the velocity, based on a chosen condition at one position of the flow field. In comparison to the previous analysis methods, the LSE method will be detailed further hereafter since it is often used in the present study. The following equations and nomenclature are taken from Adrian (1994) review on LSE.

Let $\mathbf{u}' = \mathbf{u}(x', t')$ be the quantity that we want to estimate for some domain of positions and times, based on a certain condition or event grouped in an *event data vector* \mathbf{E} . The estimate of \mathbf{u}' is denoted $\hat{\mathbf{u}}'$. The best mean square estimate of \mathbf{u}' given the data \mathbf{E} is the conditional average of \mathbf{u}' given \mathbf{E} , $\langle \mathbf{u}' | \mathbf{E} \rangle$.

The idea is then to expand $\langle \mathbf{u}' | \mathbf{E} \rangle$ in a Taylor series about $\mathbf{E} = 0$ and truncate at some level. When the series is truncated at the first term, the method is referred to as linear stochastic estimation, if it is truncated at the second term, the method is called quadratic stochastic estimation, and so on. The equations for LSE of the i th component of \mathbf{u}' are:

$$\hat{u}'_i \simeq \langle u'_i | \mathbf{E} \rangle = \sum_{j=1}^M L_{ij} E_j \quad (2.22)$$

where M is the number of event data and $L_{ij} = L_{ij}(\mathbf{x}, \mathbf{x}')$. The estimation coefficients L_{ij} are chosen so that the mean square error

$$\langle [\langle \mathbf{u}' | \mathbf{E} \rangle - \sum_j L_{ij} E_j]^2 \rangle = \text{minimum} \quad (2.23)$$

A necessary condition for minimization is the orthogonality principle which states that the errors $\hat{\mathbf{u}}' \simeq \langle \mathbf{u}' | \mathbf{E} \rangle - \sum_j L_{ij} E_j$ are statistically orthogonal to the data:

$$\langle [\hat{\mathbf{u}}' \simeq \langle \mathbf{u}' | \mathbf{E} \rangle - \sum_j L_{ij} E_j] E_k \rangle = 0 \quad i = 1, 2, 3 \quad \text{and} \quad j, k = 1, \dots, M. \quad (2.24)$$

From here, the problem consists in finding the coefficients L_{ij} by solving an $M \times M$ linear algebraic system whose coefficients are the correlations between each event datum and every other event datum. The quantity is then estimated by:

$$\sum_j \langle E_j E_k \rangle L_{ij} = \langle E_k u'_i \rangle \quad (2.25)$$

If the data consist of velocity vectors $\mathbf{u}_\alpha = \mathbf{u}(x_\alpha, t_\alpha)$, then $\langle E_j E_k \rangle$ involves only the second-order two-point space-time correlation $R_{jk}(x_\alpha, x_\beta, t_\alpha, t_\beta)$ and $\langle E_k u'_i \rangle$ reduces to $R_{ki}(x_\alpha, x', t_\alpha, t')$. Linear stochastic estimation has been widely used over the past years to study coherent structures in turbulent boundary layers (Dennis and Nickels, 2011; Elsinga et al., 2010; Juan et al., 2006; Kan et al., 2013; Lee and Sung, 2009; Natrajan et al., 2007), channel flows (Christensen and Adrian, 2001; Moin et al., 1987; Moser, 1990; Zhou et al., 1999), jet and mixing layers (Bonnet et al., 1994; Gutmark et al., 2006). Druault et al. (2011) used quadratic stochastic estimation (QSE) along with POD to reconstruct the acoustic pressure field in a flow over a cavity.

2.3 Turbulent boundary layer wall-pressure spectrum

The noise induced by a turbulent boundary layer for aero-moving vehicles is of two natures. For a turbulent flow over a surface, there will be two acoustic contributions, one referred to as the direct contribution which corresponds to the acoustic pressure generated within the flow and which radiates in the same half space as the flow, and an indirect contribution corresponding to the acoustic field generated by the vibrations of the flow-excited surface and which radiates in the half-space opposite to the flow (referred to interior domain in figure 2.26). Turbulent boundary layer noise issues for passenger comfort are related to the indirect contribution. Indeed, the direct acoustic contribution is of very low energy (Cohen, 2015; Cohen and Gloerfelt, 2015;

Gloerfelt and Margnat, 2014) and is not of interest in the present study. According to Powell's theorem (Powell, 1960), turbulent flow homogeneous in the plane of a flat, rigid infinite surface can radiate only as quadrupole or higher-order acoustic sources which are acoustically inefficient. Spatial inhomogeneities of the surface such as stiffeners or ribs or abrupt termination such as a trailing edge would be needed to generate sources with lower orders and generate additional radiation (Blake, 1986, Chapter 8).

2.3.1 Global definition and features

According to Lighthill's theory (Lighthill, 1952, 1954), the instantaneous pressure resulting from turbulent fluctuating motions obeys the wave equation:

$$\frac{1}{c_0^2} \frac{\partial^2 p}{\partial t^2} - \nabla^2 p = \frac{\partial^2 \rho_0 (u_i u_j - \overline{u_i u_j})}{\partial x_i \partial x_j} \quad (2.26)$$

where $\overline{u_i u_j}$ is the temporal average of $u_i u_j$. The source term on the right hand side is an approximation including only incompressible Reynolds stresses but still represents both aerodynamic and acoustic contributions to pressure. If the boundary layer is assumed to exist over a rigid flat surface, i.e. $u_n = u_2 = 0$, the pressure field at a wall location \mathbf{x}_w is given by (Blake, 1986, Chapter 8):

$$p(\mathbf{x}_w, t) = \frac{1}{2\pi} \iiint_V \frac{\partial^2 \rho_0 (u_i u_j - \overline{u_i u_j})}{\partial x_i \partial x_j} \frac{dV}{|\mathbf{x}_w - \mathbf{x}|} - \frac{1}{2\pi} \iint_S \frac{\partial \tau_{i2}}{\partial x_i} \frac{dS}{|\mathbf{x}_w - \mathbf{x}|} \quad i \neq 2 \quad (2.27)$$

The surface integral is over the entire wall-plane $y = 0$ as well as a control surface assumed to be a hemispherical dome at a large distance from the wall. Burton (1974) and Kraichnan (1956) provide convincing evidence that the surface integral has negligible contribution to the wall pressure. In fact, using measurements of fluctuating wall-shear stress, Burton (1974) could show that the contribution of the integral to the total root mean square wall pressure fluctuation is only on the order of at most 6%. Thus, equation (2.27) reduces to:

$$p(\mathbf{x}_w, t) = \iiint_V \left[\frac{\partial^2 \rho_0 (u_i u_j - \overline{u_i u_j})}{\partial x_i \partial x_j} \right] \frac{dV}{|\mathbf{x}_w - \mathbf{x}|} \quad (2.28)$$

where the brackets denote retardation, that is to say source terms are evaluated at the retarded time $t - r/c_0$, with $r = |\mathbf{x}_w - \mathbf{x}|$. Let \tilde{p} be the Fourier transform of the pressure at the wall:

$$\tilde{p}(\mathbf{k}, \omega) = \frac{1}{(2\pi)^3} \iiint_{-\infty}^{\infty} e^{-i(\mathbf{k} \cdot \mathbf{X} - \omega t)} p(\mathbf{x}_w, t) d^2 \mathbf{X} dt \quad (2.29)$$

with \mathbf{k} being the wave vector and \mathbf{X} a space vector in the plane of the wall. The wavenumber-frequency spectrum of wall-pressure $\Phi_{pp}(\mathbf{k}, \omega)$ is then given by:

$$\Phi_{pp}(\mathbf{k}, \omega) \delta(\mathbf{k} - \mathbf{k}') \delta(\omega - \omega') = \langle \tilde{p}(\mathbf{k}, \omega) \tilde{p}(\mathbf{k}', \omega') \rangle \quad (2.30)$$

where the angle brackets denote the ensemble average and $\delta(\cdot)$ the Dirac function.

Figure 2.22 provides the reader with information on the shape of the three-dimensional wavenumber-frequency spectrum $\Phi_{pp}(\mathbf{k}, \omega)$. In the $k_x - k_z$ plane (figure 2.22(a)), which corresponds to the top illustration in figure 2.21, the convective ridge and the acoustic domain have respectively "elliptical" and "circular" shapes. The acoustic domain is the region of supersonic wavenumbers enclosed in the circle $|\mathbf{k}| < k_0$ where k_0 is the acoustic wavenumber. In presence of a mean flow

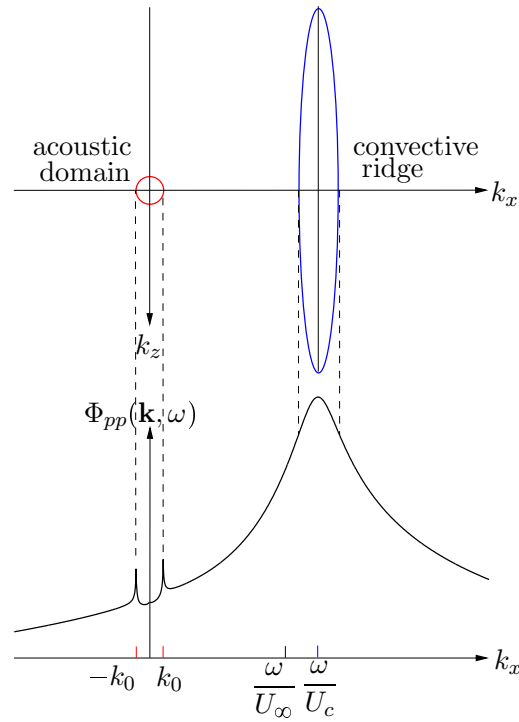


Figure 2.21 – Wavenumber-frequency spectrum $\Phi_{pp}(\mathbf{k}, \omega)$ for a frequency $\omega\delta^*/U_\infty=500$, where $M_\infty=0.1$ and $\delta=2$ cm. The model of Chase (1987) is used for illustration: $\Phi_{pp}(\mathbf{k}, \omega) = \frac{\rho_0^2 u_\tau^3 \delta^3}{[(k_+ \delta)^2 + 1/b^2]^{\frac{5}{2}}} \left[\frac{C_M (k_1 \delta)^2 k^2}{|k^2 - k_0^2| + \epsilon^2 k_0^2} + C_T (k\delta)^2 \times \mathcal{F} \right]$ with $k_+^2 = (\omega - U_c k_1)^2 / (h u_\tau)^2 + k^2$, and $\mathcal{F} = \frac{(k_+ \delta)^2 + 1/b^2}{(k\delta)^2 + 1/b^2} \left(c_1 + \frac{c_2 |k^2 - k_0^2|}{k^2} + \frac{c_3 k^2}{|k^2 - k_0^2| + \epsilon^2 k_0^2} \right)$. We set $C_M=0.1553$, $C_T=0.0047$, $b=0.75$, $h=3$, $c_1=2/3$, $c_2=0.005$, $c_3=1/6$, and $\epsilon=0.2$. $k_0 = \omega/c_0$ is the acoustic wavenumber.

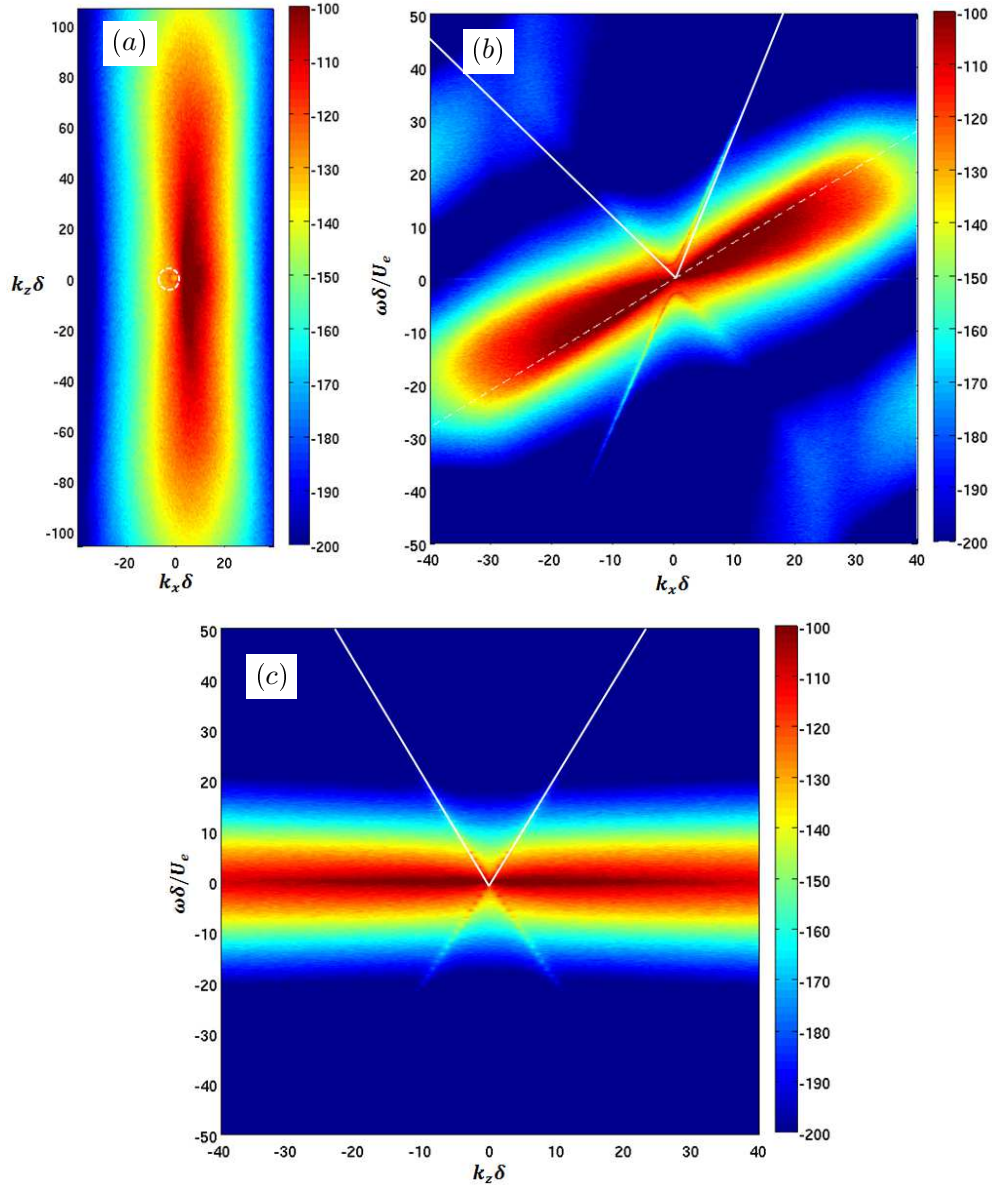


Figure 2.22 – Wavenumber-frequency spectrum $10 \log_{10} \Phi_{pp}(\mathbf{k}, \omega)$ of wall pressure beneath a ZPG Mach 0.5 turbulent boundary layer in the (a) $k_x - k_z$ plane at $\omega \delta / U_e = 5.9$, (b) $k_x - \omega$ plane at $k_z = 0$ and (c) $k_z - \omega$ plane at $k_x = 0$ - The white dashed circle in (a) as well as the plain white lines in (b) and (c) represent the acoustic domain defined by equation 2.31, the dashed line in (b) corresponds to a theoretical convective velocity $U_c = 0.7U_e$ - after Cohen (2015).

at Mach number M , the acoustic domain is theoretically delimited by an ellipse which equation is:

$$\frac{(k_x + k_0 M / \beta_p^2)^2}{(k_0 / \beta_p^2)^2} + \frac{k_z^2}{(k_0 / \beta_p)^2} = 1 \quad (2.31)$$

where $k_0 = \omega / c_0$ is the acoustic wavenumber and $\beta_p = \sqrt{1 - M^2}$ is the Prantdl-Glauert parameter. For low frequencies, the acoustic peak is hardly distinguishable since it overlaps the convective ridge. As the frequency increases, both acoustic and aerodynamic contributions separate due to small scale turbulent structures (e.g. high frequency structure) travelling at lower convection velocities. The elliptic shape of the convective ridge demonstrates the anisotropic topology of the coherent motions which have a privileged streamwise elongation in average. In the $k_x - \omega$ and $k_z - \omega$ planes, the acoustic domain is delimited by a cone. The $k_x - \omega$ representation in figure 2.22(b) gathers two pieces of information. The first one is that the inclination of the convective ridge provides a measure of the average convective velocity of the structures. The second result comes from the observation that the acoustic peak is more intense for positive wavenumbers $k_x > 0$ which translates in acoustic pressure preferably radiating in the same direction as the mean flow within the boundary layer, contrary to the exterior acoustic radiation which preferably propagates upstream (Cohen, 2015; Gloerfelt and Margnat, 2014).

The early studies on wall-pressure fluctuations were based on wind tunnel measurements or flight tests. The measurements techniques consist of microphones or kulites which provide the pressure time signal at one point in space $p(\mathbf{x}_0, t)$. The auto-correlation of this signal is:

$$R_{\mathbf{x}_0, pp}(\tau) = \frac{\langle p(\mathbf{x}_0, t)p(\mathbf{x}_0, t + \tau) \rangle}{p_{rms}^2} \quad (2.32)$$

One can define the one point pressure spectrum $\Phi_{pp}(x_0, \omega)$ by performing the Fourier transform of the auto-correlation function:

$$\Phi_{pp}(\mathbf{x}_0, \omega) = \frac{1}{2\pi} \int_{-\infty}^{\infty} R_{\mathbf{x}_0, pp}(\tau) e^{-i\omega\tau} d\tau \quad (2.33)$$

This provides information on the energy of the turbulent boundary layer excitation at one specific point over the surface. If we assume that the convected pressure is a statistically homogeneous field in the plane of the wall, this quantity can be obtained by integrating the wavenumber-frequency spectrum over the entire range of wavenumbers (k_x, k_z) :

$$\Phi_{pp}(\omega) = \int_{-\infty}^{\infty} \Phi_{pp}(\mathbf{k}, \omega) d\mathbf{k} \quad (2.34)$$

In order to obtain a smoother single point frequency spectrum, it is preferably computed from equation (2.34) since it corresponds to the averaged autospectrum of a small patch over the surface. Unlike experimental data, LES computational data allows this thanks to the sufficient discretization of the wall.

Consideration of the source term

Considering an incompressible flow, the source term in Lighthill's equation (2.27) can be written:

$$\text{Source} = T_{ij} = \frac{\partial^2 (u_i u_j - \overline{u_i u_j})}{\partial x_i \partial x_j} \quad (2.35)$$

Applying the Reynolds decomposition $u_i = U_i + u'_i$ to separate the mean and fluctuating quantities and then subtracting the mean pressure, one obtains:

$$T_{ij} = T_{ij}^{MS} + T_{ij}^{TT} = \left(2 \frac{\partial U_i}{\partial x_j} \frac{\partial u'_j}{\partial x_i} \right) + \left(\frac{\partial^2 (u'_i u'_j - \overline{u'_i u'_j})}{\partial x_i \partial x_j} \right) \quad (2.36)$$

The term T_{ij}^{MS} is the mean-shear (MS) source term ("linear" or "rapid") while T_{ij}^{TT} is the sum of turbulent-turbulent (TT) source terms ("non-linear" or "slow"). Assuming that the mean velocity in the boundary layer flow is $U_1 = U$ and invoking continuity for the TT term, the two contributions can be simplified:

$$T^{MS} = 2 \frac{\partial U}{\partial y} \frac{\partial v'}{\partial x} \quad (2.37a)$$

$$T_{ij}^{TT} = \frac{\partial u'_i}{\partial x_j} \frac{\partial u'_j}{\partial x_i} - \frac{\partial^2 \overline{u'_i u'_j}}{\partial x_i \partial x_j} \quad (2.37b)$$

It is interesting to consider such a decomposition of the source term in order to evaluate the contribution of each component to wall-pressure fluctuations. Assuming a Gaussian distribution for the turbulent statistics, Kraichnan (1956) evaluated the ratio between the contribution of mean-shear and turbulent-turbulent terms as $p_{rms}^{MS}/p_{rms}^{TT} \simeq 4/15C_f \gg 1$. Meecham and Travis (1980) calculated the value $p_{rms}^{MS}/p_{rms}^{TT} \simeq 10$ for a classical isotropic field with a Gaussian probability distribution. More recently, Hu et al. (2016) calculated the contributions of the MS and TT terms by solving the Poisson equation of pressure. The source term was obtained by a Fast Random Particle-Mesh method (FRPM, Ewert et al. (2000); Siefert and Ewert (2009)) based on a RANS calculation. When plotting the one-point spectra of wall-pressure, they found that most of the energy is contained in the MS term and that the TT term can be neglected, following the conclusions of Townsend (1976b). Chang et al. (1999) analyzed a DNS of low Reynolds number incompressible turbulent channel flow to study the relationship between wall-pressure and velocity field sources. Contrary to the results above, it appeared that the mean-shear and turbulent-turbulent partial pressures are the same order of magnitude close to the wall.

2.3.2 Effect of pressure gradient on pressure spectrum

Point-frequency spectrum

It is interesting to know the effect of the pressure gradient on wall-pressure fluctuations since the majority of flows in engineering applications are submitted to pressure gradients. On an aircraft for instance, adverse pressure gradient areas exist at the beginning of the windshield, over the fuselage/wing junction and on the aft fuselage, whereas favorable pressure gradient areas are found over the entire cockpit (see figure 2.23).

Many authors have tackled this particular aspect looking mainly at the one-point frequency spectrum (Bradshaw, 1967a,b; Burton, 1973; McGrath and Simpson, 1988; Schloemer, 1967) and two main results emerge: 1) absolute levels of energy increase with an adverse pressure gradient and 2) the mid-frequency slope becomes steeper as the pressure gradient moves from favorable to adverse. This is shown in figure 2.24 which compares the one-point frequency spectra for different pressure gradient cases and intensities measured over a rotating NACA 0012 airfoil (Hu and Herr, 2016).

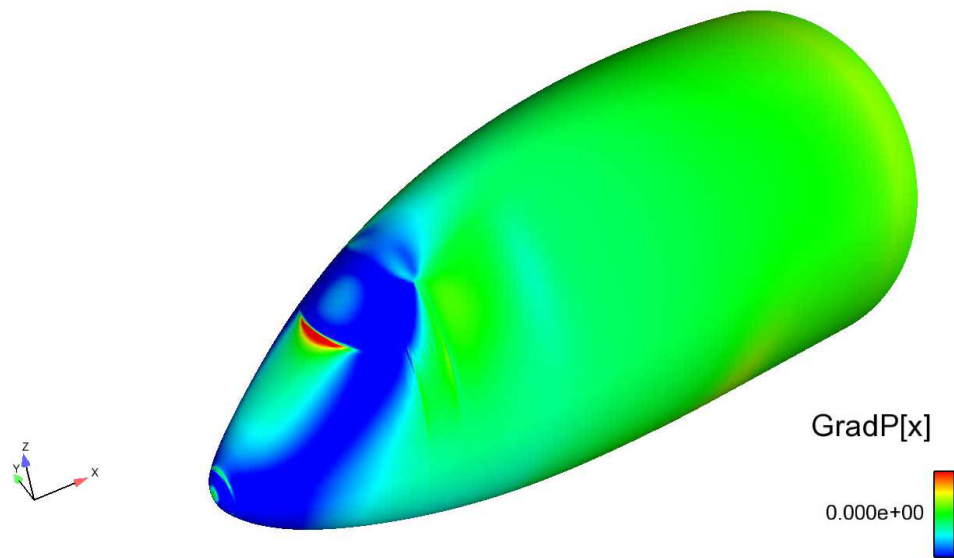


Figure 2.23 – Streamwise pressure gradient over front region of a typical long range aircraft. Arbitrary units - Airbus document.

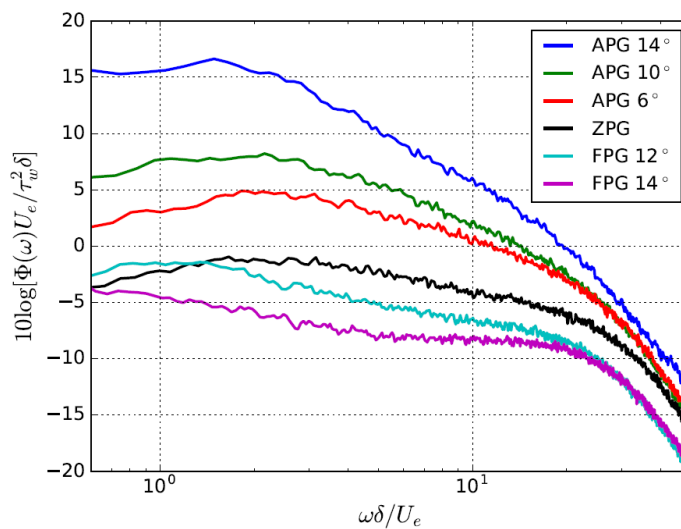


Figure 2.24 – One-point frequency spectra for different cases of pressure gradient measured on a rotatable NACA 0012 airfoil - angles indicate the angle of attack of the airfoil - after Hu and Herr (2016).

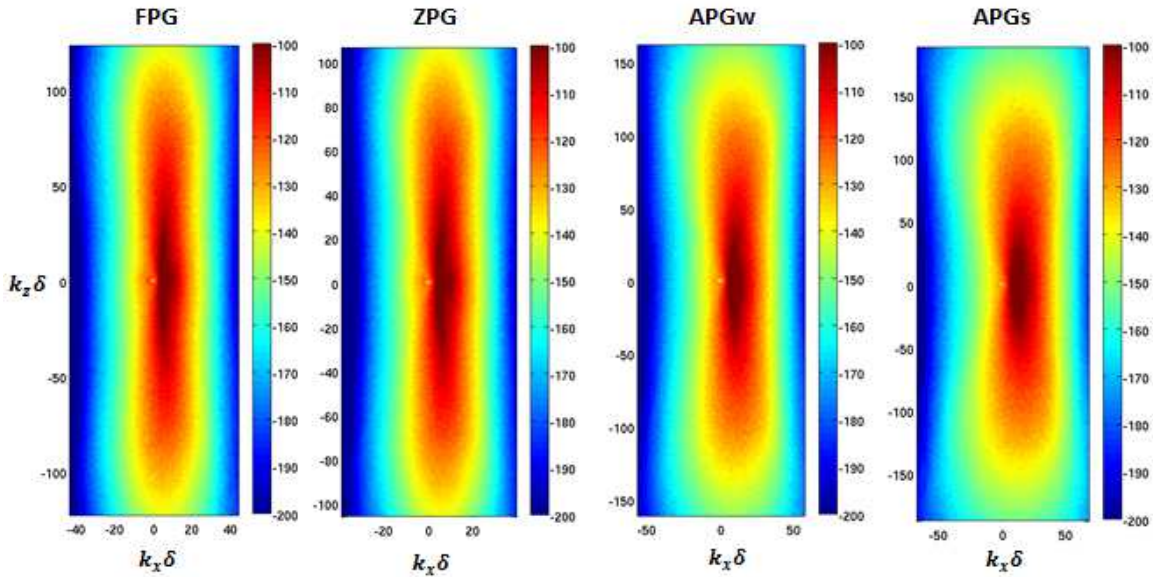


Figure 2.25 – Wavenumber-frequency spectra $10 \log_{10} \Phi_{pp}(\mathbf{k}, \omega)$ for favorable (FPG), zero (ZPG), adverse weak (APGw) and adverse strong (APGs) pressure gradients in the $k_x - k_z$ plane at frequencies $\omega\delta/U_e = 2.7$ (FPG), 3 (ZPG), 4.3 (APGw) and 5.2 (APGs) after Cohen (2015). Refer to section 3.1 for description of the pressure gradients.

Wavenumber-frequency spectrum

Figure 2.25 shows a direct effect of the pressure gradient on the wavenumber-frequency spectrum. By looking at the representation in the $k_x - k_z$ wavenumber plane for a given frequency, it can be seen that the convective ridge has a greater extent along k_x for the adverse pressure cases and a smaller one for the favorable pressure gradient case. This result has also been observed through experimental measurements of the wall-pressure cross-spectra in wind tunnels by Salze et al. (2014). This behaviour suggests that, for the adverse pressure gradient case, the wall-pressure is related to events (or structures) which have a smaller extent in the streamwise direction, and vice-versa for the favorable case.

2.3.3 Fluid-structure coupling

In this section, an overview of the theory behind fluid-structure coupling is given by developing the example of a flat plate under the weak coupling assumption. The weak coupling assumption assumes that the plate is linearly excited by the flow and that the influence of the motion of the panel on the flow is neglected. In fact, very few experiments tackled this problem; Mercer (1962) found no influence on the mean boundary layer quantities through measurements in a water channel with a vibrating wall, Izzo (1969) measured enhanced streamwise velocity fluctuations at frequencies of vibration for which $du_{\tau}/\nu > 3$, where d is the amplitude of the wall motion.

Moreover, it has been demonstrated (Junger and Feit, 1986; Timoshenko and Woinowsky-Krieger, 1959) that curved plates may be approximated as vibrating flat plates as long as the condition

$$k_b R \gg \sqrt[4]{12} \sqrt{R/h} \quad (2.38)$$

holds, where R is the radius of the curvature, h the thickness of the plate and k_b the plate

bending wavenumber. For a classical aircraft panel with $R = 1.94\text{m}$, $h = 1.4\text{mm}$, equation (2.38) is satisfied for the range of frequencies of the TBL excitation. The flat plate is then a simple example for fluid-structure coupling for aircraft panels.

This being said, consider a simply supported thin elastic plate of length a and breath b set in an infinite rigid baffle. The flat plate has bending stiffness B , membrane tensions N_x and N_z and mass per unit area M . The plate is bounded by a turbulent boundary layer flow of density and sound speed ρ_0 and c_0 on one side and a fluid at rest characterized by ρ_1 and c_1 , as illustrated in figure 2.26. Under the weak coupling assumption, the driving pressures consist of the perfect rigid wall boundary layer pressure p_t and the acoustic pressure fluctuations induced by the plate motion.

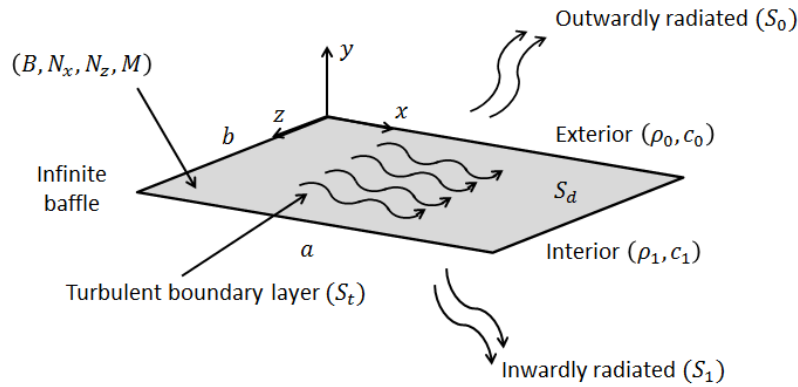


Figure 2.26 – Flat plate model for TBL-structure coupling.

Before going into the theoretical expressions, keep in mind that in the following equations, i refers to the index of the medium (0=turbulent boundary layer and 1=fluid at rest) whereas i is the imaginay number defined by $i^2 = -1$.

Let S_t be the power input from the TBL, S_0 and S_1 the powers radiated respectively to the exterior half space and interior half space and S_d the dissipated power. Therefore, the power balance writes:

$$S_t(\omega) = S_0(\omega) + S_1(\omega) + S_d(\omega) \quad (2.39)$$

The quantity of interest here is the power input $S_t(\omega)$. The harmonic normal velocity component for the plate $v_p(x, z, \omega)e^{-i\omega t}/2\pi$ satisfies

$$B\nabla^4 v_p - N_x \frac{\partial^2 v_p}{\partial x^2} - N_z \frac{\partial^2 v_p}{\partial z^2} - M\omega^2 v_p = i\omega[p_t + p_0 - p_1]_{x=0} \quad (2.40)$$

The acoustic pressures p_1 and p_0 obey the Helmholtz equation

$$(\nabla^2 + k_i^2)p_i = 0 \quad (2.41)$$

where $k_i = \omega/c_i$ is the acoustic wavenumber and are linked to the plate velocity via the boundary condition

$$\frac{1}{\rho_i} \frac{\partial p_i}{\partial x} = i\omega v_p \quad i = 0, 1 \quad (2.42)$$

which guarantees equal displacement for the fluid and the plate in the normal direction. It remains to include structural damping which shall be represented as a small imaginary component:

$$B = B_r(1 - i\epsilon_s) \quad N_x = N_{xr}(1 - i\epsilon_s) \quad N_z = N_{zr}(1 - i\epsilon_s) \quad (2.43)$$

The plate velocity can now be expressed as a sum of modal components:

$$v_p(x, z, \omega) = \sum_{mn} v_{p,mn}(\omega) \Psi_{mn}(x, z) \quad (2.44)$$

where $\Psi_{mn}(x, z)$ is the mode shape for a simply supported plate, i.e.:

$$\Psi_{mn}(x, z) = \frac{2}{\sqrt{ab}} \sin\left(\frac{m\pi x}{a}\right) \sin\left(\frac{n\pi z}{b}\right) \quad (2.45)$$

Let $S_{mn}(\mathbf{k})$ be the Fourier transform of the mode shape $\Psi_{mn}(y, z)$. Therefore, the modal excitation term Φ_{mn} can be written as the weighted contributions of the wall-pressure wavenumber-frequency spectrum $\Phi_{pp}(\mathbf{k}, \omega)$ over the spatial components of mode (m, n) :

$$\Phi_{mn} = \frac{1}{(2\pi)^2} \int_{-\infty}^{\infty} \Phi_{pp}(\mathbf{k}, \omega) |S_{mn}(\mathbf{k})|^2 d^2\mathbf{k} \quad (2.46)$$

It is now possible to calculate the normalized boundary layer input power $\tilde{S}_t(\omega)$ such as:

$$\tilde{S}_t(\omega) = 2 \sum_{m,n} \text{Re}(d_{mn}) \frac{\tilde{\Phi}_{mn}}{|d_{mn}|^2} \quad (2.47a)$$

$$\tilde{\Phi}_{mn} = \frac{\omega^2 u_\tau}{\tau_w^2 \delta U_c^2} \Phi_{mn} \quad (2.47b)$$

$$d_{mn} = i \left[\frac{B_r |\mathbf{k}|^2 + N_{xr} k_m^2 + N_{zr} k_n^2}{M\omega^2} (1 - i\epsilon_s) - 1 \right] + \epsilon_{f0} Z_{mnmn}^{0f} + \epsilon_{f1} Z_{mnmn}^{1f} \quad (2.47c)$$

$$\epsilon_{fi} = \frac{\rho_i c_i}{M\omega} \quad i = 0, 1 \quad (2.47d)$$

$$Z_{mnmn}^{if} = \frac{k_i}{2\pi^2} \int_{-\infty}^{\infty} \frac{S_{mn}^* S_{mn}}{(k_i^2 - |\mathbf{k}|^2)^{1/2}} d^2\mathbf{k} \quad i = 0, 1 \quad (2.47e)$$

where $\tilde{\Phi}_{mn}$ is the normalized modal excitation term and Z_{mnmn}^{if} and d_{mn} are dimensionless impedances. S_{mn}^* denotes the complex conjugate of S_{mn} .

It is important to keep in mind that the noise levels in an aero-moving vehicle are highly linked to the degree of coupling, i.e. the degree of power reception by the structure. This was found to be dependent on how well the structure filters the excitation wavenumbers. Boundary layer induced vibration is complicated because the wavenumber spectrum of wall-pressure is not independent of the wavenumber: high pressure levels are concentrated in a region near the convective wavenumber $k_c = \omega/U_c$ and the acoustic domain $|k| < k_0 = \omega/c_0$ as shown in figures 2.21 and 2.22. In figure 2.28(a), the speed of free bending waves of the plate is greater than the convective wavenumber $c_b > U_c$, so that the shape function and maximum of pressure spectrum do not overlap and leads to low coupling. This situation is more common in underwater applications. In the aeronautical field, the convective velocity increases and becomes greater than the phase speed of bending waves so that $k_m \approx k_c$ and fluid-structure coupling becomes efficient, as can be seen in figure 2.28(b). Finally, acoustic coincidence occurs when the convection velocity approaches the speed of sound c_0 ; this is shown in figure 2.27.

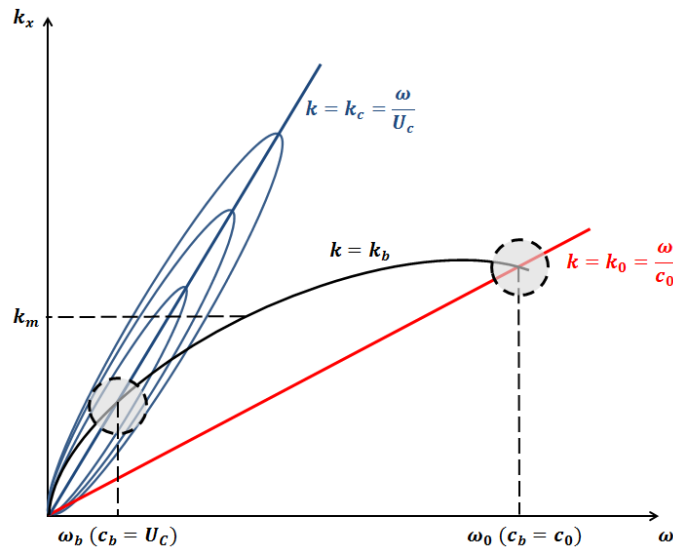


Figure 2.27 – $\Phi_{pp}(\mathbf{k}, \omega)$ spectra in the $k_x - \omega$ plane at constant k_z and bending wavenumber for an infinite plate (black line). The dashed circles show regions of acoustic and hydrodynamic coincidence between the TBL excitation and the structure.

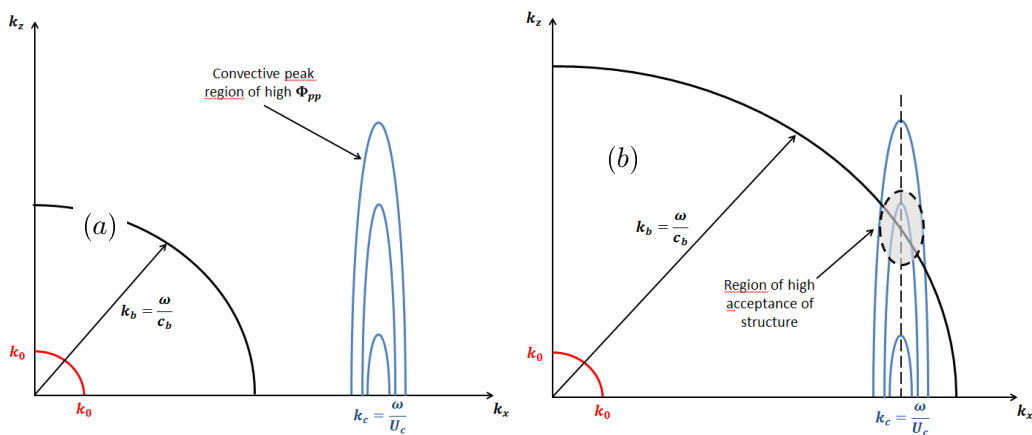


Figure 2.28 – $\Phi_{pp}(\mathbf{k}, \omega)$ spectra at constant frequency with (left) low coupling $c_b > U_c$ and (right) high coupling $c_b < U_c$. Black line shows the bending wavenumber for an infinite plate.

2.3.4 Wall-pressure spectrum models

A compendium of the main existing models is given. The list is exhaustive enough to provide a picture of the current state of the art concerning wall-pressure modeling and the underlying parameters.

Auto-correlation empirical models

ESDU

ESDU (1975) is a power spectrum model based on analysis and curve fitting of flight measurements.

Robertson

Robertson (1971) based his model on Lawson (1968) work and data from supersonic NASA-Ames measurements.

$$\Phi(\omega) = \frac{p_{ms}}{\omega_0 \left[1 + \left(\frac{\omega}{\omega_0} \right)^{0.9} \right]^{0.2}} \quad (2.48)$$

with $\omega_0 = 0.5U_e/\delta^*$ and using the definition of the mean square pressure fluctuations from Lawson (1968)

$$p_{ms} = \left(\frac{0.006q}{1 + 0.14M^2} \right)^2$$

where $q = \rho_0 U_e^2/2$ is the dynamic pressure and M the Mach number.

Willmarth-Amiet-Roos

Amiet (1976) proposed the following expression for the pressure spectrum underneath a turbulent boundary layer based on measurements by Willmarth and Roos (1965) over a flat plate.

$$\Phi(\omega) = \frac{q^2 \delta^*}{U_e} \frac{2 \times 10^{-5}}{1 + \bar{\omega} + 0.217\bar{\omega}^2 + 0.00562\bar{\omega}^4} \quad (2.49)$$

valid for $0.1 < \bar{\omega} = \omega\delta^*/U_e < 20$ and where $q = \rho_0 U_e^2/2$ is the dynamic pressure.

Chase

$$\Phi(\omega) = \frac{\tau_w^2}{\omega} \left[2\pi C_M \alpha^{-3} (1 + \mu^2 \alpha^2) + 3\pi C_T \alpha^{-1} (1 + \alpha^{-2}) \right] \quad (2.50)$$

with

$$\mu = \frac{h u_\tau}{U_c} \quad \alpha^2 = 1 + \left(\frac{b \omega \delta}{U_c} \right)^{-2}$$

Chase recommends to use the values $h = 3$, $C_M = 0.466/h$, $C_T = 0.014/h$ and $b = 0.75$.

Chase-Howe

Howe (1998) builds a simple model based on the Chase (1980) model. This model does not include the ω^{-5} decay that is sometimes measured at high frequencies.

$$\Phi(\omega) = 2 \left(\frac{\delta^*}{U_e} \right)^3 \frac{(\omega \tau_w)^2}{\left[\left(\frac{\omega \delta^*}{U_e} \right)^2 + 0.0144 \right]^{3/2}} \quad (2.51)$$

Goody

The Goody (2004) model is a modified Chase-Howe model based on 19 different experimental studies which cover a range of Reynolds numbers $1400 < Re_\theta < 23400$. These modifications give higher levels at low frequencies and make high frequencies decay more rapidly. The somewhat Reynolds number R_T in the denominator ensures a control on the mid frequencies bandwidth.

$$\Phi(\omega) = \frac{\tau_w^2 \delta}{U_e} \frac{3.0 \left(\frac{\omega \delta}{U_e} \right)^2}{\left[\left(\frac{\omega \delta}{U_e} \right)^{0.75} + 0.5 \right]^{3.7} + \left[1.1 R_T^{-0.57} \left(\frac{\omega \delta}{U_e} \right) \right]^7} \quad (2.52)$$

with

$$R_T = \frac{u_\tau^2 \delta}{U_e \nu}$$

Smol'yakov

Smol'yakov (2000) built his model to take into account the fact that the single point pressure spectra scales with different variables depending on the frequency band.

$$\Phi(\omega) = \frac{1.49 \times 10^{-5} \tau_w^2 \nu Re_\theta^{2.74} \omega_\nu^2}{u_\tau^2} (1 - 0.117 Re_\theta^{0.44} \omega_\nu^{1/2}) \quad \omega_\nu < \omega_\theta$$

$$\Phi(\omega) = \frac{2.75 \tau_w^2 \nu}{u_\tau^2 \omega_\nu^{1.11}} [1 - 0.82 \exp(-0.51(\frac{\omega_\nu}{\omega_\theta} - 1))] \quad \omega_\theta < \omega_\nu < 0.2$$

$$\Phi(\omega) = \frac{\tau_w^2 \nu}{u_\tau^2} (38.9 e^{-8.35 \omega_\nu} + 18.6 e^{-3.58 \omega_\nu} + 0.31 e^{-2.14 \omega_\nu}) [1 - 0.82 \exp(-0.51(\frac{\omega_\nu}{\omega_\theta} - 1))] \quad \omega_\nu > 0.2$$

where $\omega_\nu = \frac{\omega \nu}{u_\tau^2}$ and $\omega_\theta = 49.35 Re_\theta^{0.88}$.

Efimtsov 1

Efimtsov 1 model (Efimtsov, 1982) is based on multiple wall pressure measurements on aircraft fuselage during flight tests. The results cover Mach and Reynolds numbers domains ranging within $0.41 < M < 2.1$ and $0.5 \times 10^8 < Re_x < 4.85 \times 10^8$.

$$\Phi(\omega) = \frac{0.01 \tau_w^2 \delta}{u_\tau \left[1.0 + 0.02 \left(\frac{\omega \delta}{u_\tau} \right)^{2/3} \right]} \quad (2.53)$$

Efimtsov 2

Efimtsov 2 model (Efimtsov et al., 1999) is an updated model using data from TsAGI wind tunnel and flight measurements on supersonic aircraft TU-144LL.

$$\Phi(\omega) = \frac{2\pi \alpha u_\tau^3 \rho_\infty^2 \delta \beta}{\left[1 + 8\alpha^3 \left(\frac{\omega \delta}{u_\tau} \right)^2 \right]^{1/3} + \alpha \beta Re_\tau \left[\left(\frac{\omega \delta}{u_\tau} \right) Re_\tau^{-1} \right]^{10/3}} \quad (2.54)$$

where

$$\begin{aligned}
 Re_\tau &= \frac{\delta u_\tau}{\nu_w} & \gamma &= 0.905 \\
 Re_{\tau 0} &= 3000 & T_w &= T_\infty \left(1 + r \frac{\kappa - 1}{2} M^2\right) \\
 \beta &= \left[1 + \left(\frac{Re_{\tau 0}}{Re_\tau}\right)^3\right]^{1/3} & r &= 0.89 \\
 \alpha &= 0.01 & \kappa &= 1.4 \\
 \nu_w &= \nu_\infty \frac{\rho_\infty}{\rho_w} \left(\frac{T_w}{T_\infty}\right)^\gamma & \rho_w &= \rho \frac{T_w}{T_\infty}
 \end{aligned}$$

Rackl and Weston

Rackl and Weston (2005) used two functions to adjust Efimtsov 2 model in order to take into account the broadband spectral peak that appears near Strouhal number $Sh = 2\pi f \delta^* / U_e = 0.6$ and the lower high frequency negative slope compared to other models and measurements on the TU-144LL test data.

$$factor1 = 2.5 \exp \left[- \left(\ln \left(\frac{2\pi f \delta^*}{U_e} \right) - \ln(0.6) \right)^2 \right]$$

$$factor2 = \frac{1}{4} \left[\tanh \left(\log_{10} \left(\frac{f}{1000} \right) \right) + 1 \right] (M - 1.65) \log_{10}(f)$$

In order to do this properly, one has to convert the Efimtsov model to decibels, then add the Rackl and Weston factors, and finally convert the corrected model back into the original units.

Laganelli

Laganelli and Wolfe (1993) model is derived from experimental studies from AFWAL Mach3 facility, Blake, Laganelli, Raman, Coe and Bull and fluid dynamics principles. This model is an expansion of Robertson's model which takes into account compressibility effects.

$$\Phi(\omega) = 2.293 \frac{q^2 \delta^*}{U_e} \frac{10^{-5} F_C^{-0.5733}}{1 + F_C^{2.867} \left(\frac{\omega \delta^*}{U_e}\right)^2} \quad (2.55)$$

where F_C is a transformation from compressible to incompressible flow states :

$$F_C = \frac{C_{f_i}}{C_{f_c}} = \frac{h^*}{h_e} = 0.5 + \frac{h_w}{h_{aw}} \left(0.5 + r \frac{\gamma - 1}{2} M_e^2 \right) + 0.22r \frac{\gamma - 1}{2} M_e^2$$

with M_e , $r = 0.896$ and $\gamma = 1.4$ being respectively the Mach number at the edge of the boundary layer, the recovery factor and the ratio of constant heat capacity for air. h_w/h_{aw} is the ratio of enthalpy between normal and adiabatic wall conditions.

Goodwin

Goodwin (1994) built a model using flight test data on three supersonic aircraft: XB-70, A3J and Concorde. However only a few amount of data collected on the two first aircraft was usable and the measurement on Concorde seemed suspect due to the sensitivity of the Kulites to the flushness of the sensor's surface relatively to the surrounding surface.

$$\Phi(\omega) = \frac{2}{\pi} \left(\frac{p_{rms}}{q_e} \right)^2 \left(\frac{\rho_w(T_w, p_w)}{\rho_e} \right)^3 \frac{1.2 + 0.1 \left(\frac{n-7}{7} \right)^{0.45}}{1 + \left(\frac{1.2\theta\omega}{U_e} \right)^2} \quad (2.56)$$

where

$$n = 4.0 + 2.5 \log_{10} \left(\frac{Re_x}{6.31 \times 10^5} \right) \quad p_{rms}^2 = \frac{2}{\pi} \frac{A}{B} \frac{U_e}{\theta} \Phi(0)$$

$$A = \left(\frac{\rho_e}{\rho_w(T_w, p_e)} \right)^3 \frac{\theta}{\delta^*} \left(1 + 0.08 \left(\frac{n-7}{7} \right)^{0.45} \right) \quad B = 1.2$$

Kim-George (airfoil model)

Kim and George (2005) built a model by curve-fitting experimental data from Brooks and Hodgson (1981) and Yu and Joshi (1979) on a NACA0012 airfoil. Since they were interested in trailing edge noise for rotor application, the measurements they used were from a flow subjected to an adverse pressure gradient.

$$\Phi(\omega) = \frac{q^2 \delta^*}{2U_e} \frac{1.732 \times 10^{-3} \bar{\omega}}{1 - 5.489 \bar{\omega} + 36.7 \bar{\omega}^2 + 0.1505 \bar{\omega}^5} \quad \bar{\omega} < 0.06 \quad (2.57a)$$

$$\Phi(\omega) = \frac{q^2 \delta^*}{2U_e} \frac{1.4216 \times 10^{-3} \bar{\omega}}{0.3261 + 4.1837 \bar{\omega} + 22.818 \bar{\omega}^2 + 0.0013 \bar{\omega}^3 + 0.0028 \bar{\omega}^5} \quad 0.06 < \bar{\omega} < 20 \quad (2.57b)$$

where $q = 1/2 \rho_0 U_e^2$ is the dynamic pressure and $\bar{\omega} = \omega \delta^* / U_e$.

Rozenberg

Rozenberg (2007) based his model on Goody's model with a Strouhal number including the displacement thickness δ^* rather than the boundary layer thickness and fitting new parameters based on six different cases of adverse pressure gradient flows.

$$\Phi(\omega) = \frac{\tau_{max}^2 \delta^*}{U_e} \frac{[2.82 \Delta^2 (6.13 \Delta^{-0.75} + F_1)^{A_1}] [4.2 \left(\frac{\Pi}{\Delta} \right) + 1] \tilde{\omega}}{[4.7 \tilde{\omega}^{0.75} + F_1]^{A_1} + [C_3 \tilde{\omega}]^{A_2}} \quad (2.58)$$

where the maximum shear stress along the wall-normal τ_{max} is preferred to the shear stress τ_w as suggested by Simpson et al. (1987) and:

$$F_1 = 4.76 \left(\frac{1.4}{\Delta} \right)^{0.75} [0.375 A_1 - 1] \quad A_1 = 3.7 + 1.5 \beta_C$$

$$A_2 = \min(3, 19/\sqrt{R_T}) + 7 \quad \Delta = \frac{\delta}{\delta^*}$$

$$C_3 = 8.8 R_T^{-0.57} \quad \tilde{\omega} = \frac{\omega \delta^*}{U_e}$$

Catlett

Catlett et al. (2014) developed an empirical spectral model for wall-pressure beneath turbulent boundary layer subjected to an adverse pressure gradient. This model is derived version of the Goody model where the constants were calibrated based on wind tunnel measurements over the trailing edge region of an airfoil model with three interchangeable, symmetric trailing edge sections to obtain different intensities for the pressure gradient.

$$\Phi(\omega) = \frac{\tau_w^2 \delta}{U_e} \frac{a \left(\frac{\omega \delta}{U_e} \right)^b}{\left[\left(\frac{\omega \delta}{U_e} \right)^c + d \right]^e + \left[f R_T^g \left(\frac{\omega \delta}{U_e} \right) \right]^h} \quad (2.59)$$

with the deviations from Goody's standard model parameters are given by:

$$\begin{aligned}
 \ln(a - a_G) &= 4.735(\beta_\Delta Re_\Delta^{0.35})^{0.162} - 5.379 & b &= 2 \\
 c - c_G &= 2.210(\beta_\delta)^{0.559} - 0.069 & d - d_G &= 0.072(\beta_\Delta Re_\Delta^{0.35})^{0.552} - 0.069 \\
 e - e_G &= -0.138(\beta_\delta Re_\Delta^{0.35})^{0.310} - 0.155 & f - f_G &= 8.862(H Re_\Delta^{0.1})^{-1.414} - 1.241 \\
 g - g_G &= 1.103(\beta_\delta)^{0.690} - 0.038 & h - h_G &= 0.959(\beta_\Delta Re_\Delta^{0.35})^{0.052} - 0.207
 \end{aligned}$$

where β_δ and β_Δ are Clauser parameters defined respectively with the length scales δ and Δ , Re_Δ is the Reynolds number based on Δ and H the shape factor. The length scale Δ is the Rotta-Clauser parameter introduced by Rotta (1950) and Clauser (1954). These parameters are defined by:

$$\beta_\delta = \frac{\delta}{q} \frac{dp}{dx} \quad \beta_\Delta = \frac{\Delta}{q} \frac{dp}{dx} \quad Re_\Delta = \frac{\Delta U_e}{\nu} \quad H = \delta^*/\theta \quad \Delta = \delta^* \sqrt{\frac{2}{C_f}}$$

Klabes

Similarly to Catlett et al. (2014), Klabes et al. (2016) builds a variation of the Goody model using flight measurement data over the fuselage of the DLR's (Deutsches Zentrum für Luft- und Raumfahrt) A320 Advanced Technology Research Aircraft (ATRA) at different flight levels and Mach numbers. Therefore he was able to reevaluate the constants and exponents of the Goody model and proposed a new normalization based on the local value of the kinetic energy.

$$\begin{aligned}
 \Phi(\omega) &= \frac{\delta(\rho k)^2}{U_e} \frac{a \left(\frac{\omega\delta}{U_e}\right)^b}{\left[\left(\frac{\omega\delta}{U_e}\right)^c + d\right]^e + \left[f R_T^g \left(\frac{\omega\delta}{U_e}\right)\right]^h} & (2.60) \\
 a &= \left(\frac{k_{max}}{k_{ref}}\right)^\gamma & b &= 0.5 \\
 c &= 1.35 + 3\beta_\delta & d &= Re_\delta^{0.174} - 6.7 \\
 e &= -0.11428\beta_\Delta + 1.55 & f &= 1.1 \\
 g &= -0.57 & h &= 7.0
 \end{aligned}$$

with

$$\begin{aligned}
 \beta_\delta &= \frac{\delta}{q} \frac{dp}{dx} & \beta_{\Delta_\delta} &= \frac{\Delta_\delta}{q} \frac{dp}{dx} \\
 Re_{\Delta_\delta} &= \frac{\Delta_\delta U_e}{\nu} & \Delta_\delta &= \delta \sqrt{\frac{2}{C_f}} \\
 \gamma &= [-592.71C_f + 1.74] Re_{\Delta_\delta}^{0.01}
 \end{aligned}$$

Hu

Hu and Herr (2016) measured wall-pressure fluctuations beneath a zero, favorable and adverse pressure gradient turbulent boundary layer in a wind tunnel. Various intensities of adverse

pressure gradient were obtained using a rotated NACA 0012 airfoil with incidence over a flat plate. Results from one-point spectra measurements showed that for both pressure gradient cases, fairly good collapse for the spectral maxima is found by scaling with outer variables $u_\tau/(q^2\theta)$ and $\omega\theta/U_e$. Once again, the Goody model was a good candidate with the new scaling parameters:

$$\Phi(\omega) = \frac{q^2\theta}{u_\tau} \frac{a(\omega\theta/U_e)^b}{[(\omega\theta)/U_e]^c + d]^e [f(\omega\theta)/U_e]^g} \quad (2.61)$$

and the constants are adjusted based on the APG measurements:

$$\begin{aligned} a &= (81.004d + 2.154) \times 10^{-7} & b &= 1.0 \\ c &= 1.5h^{1.6} & d &= 10^{-5.8 \times 10^{-5} Re_\theta H - 0.35} \\ e &= 1.13/h^{0.6} & f &= 7.645 Re_\tau^{-0.411} \\ g &= 6 & h &= 1.169 \ln(H) + 0.642 \end{aligned}$$

where H is the shape factor

Cross-correlation empirical models

Corcos

Corcos (1964) assumed that the loss of coherence between two spatially separated points is equal to the loss of coherence in the streamwise direction multiplied by the loss of coherence in the spanwise direction. From a curve fit for the narrow-band spatial correlation between wall pressures, Corcos obtained:

$$\Psi(x, z, \omega) = \Phi(\omega) \exp(i k_c x - |\alpha_{\omega x} x| - |\alpha_{\omega z} z|)$$

Corcos model in the wavenumber-frequency domain is found by applying the Fourier transform:

$$\Psi(k_x, k_z, \omega) = \Gamma(\omega) \Psi(k_x) \Psi(k_z) = \frac{2\Phi(\omega)}{\pi} \frac{\alpha_{\omega x} \alpha_{\omega z}}{(\alpha_{\omega x}^2 + (k_x - k_c)^2) (\alpha_{\omega z}^2 + k_z^2)}$$

Mellen (1990) gives a slightly modified version of the previous expression by dividing it by the area 2π :

$$\Psi(k_x, k_z, \omega) = \Gamma(\omega) \Psi(k_x) \Psi(k_z) = \frac{\Phi(\omega)}{\pi^2} \frac{\alpha_{\omega x} \alpha_{\omega z}}{(\alpha_{\omega x}^2 + (k_x - k_c)^2) (\alpha_{\omega z}^2 + k_z^2)}$$

with:

$$\alpha_{\omega x} = k_c \alpha_x = \frac{\omega}{U_c} \alpha_x \quad \alpha_{\omega z} = k_c \alpha_z = \frac{\omega}{U_c} \alpha_z$$

Graham (1997) normalizes the Corcos model:

$$\Phi(k_x, k_z, \omega) = \Psi(k_x, k_z, \omega) \frac{(2\pi)^2 \omega^2}{U_c^2 \Phi(\omega)} \quad (2.62)$$

and gives the following expression:

$$\Phi(k_x, k_z, \omega) = \frac{4\alpha_x \alpha_z}{\left[\alpha_z^2 + \left(\frac{U_c k_z}{\omega} \right)^2 \right] \left[\alpha_x^2 + \left(\frac{U_c k_x}{\omega} - 1 \right)^2 \right]} \quad (2.63)$$

where $\alpha_x = 0.10$ and $\alpha_z = 0.77$ based on measurement by Willmarth and Woolridge (1962). Blake (1986) recommends $\alpha_x = 0.116$ and $\alpha_z = 0.70$ for smooth walls. More recently, authors have observed that the correlation length coefficients are not constant over the entire frequency range (Cohen, 2015; Efimtsov, 1982; Finnveden et al., 2005; Hu and Herr, 2016).

Cockburn-Jolly

Cockburn and Jolly (1968) introduced a factor ϵ_{δ^*} to the Corcos model in order to take into account the limited thickness of the boundary layer:

$$\epsilon_{\delta^*} = \sqrt{1 + (3k_c\delta^*)^{-2}} \quad (2.64)$$

After applying the Graham normalization, the Cockburn-Jolly model is given by:

$$\Phi(k_x, k_z, \omega) = \frac{\alpha_x \alpha_z \epsilon_{\delta^*}}{[\alpha_z^2 \epsilon_{\delta^*}^2 + (k_x - k_c)^2] [\alpha_z^2 \epsilon_{\delta^*}^2 + k_z^2]} \quad (2.65)$$

Efimtsov

Efimtsov cross-correlation model (Efimtsov, 1982) is based on Corcos model but uses different correlation lengths α_x and α_z introducing boundary layer thickness dependence. Efimtsov's results are derived from an extensive series of measurements on aircraft, over a Mach number range $0.41 < M < 2.1$.

$$\frac{\Lambda_x}{\delta} = \left[\left(\frac{a_1 Sh}{U_c/u_\tau} \right)^2 + \frac{a_2^2}{Sh^2 + (a_2/a_3)^2} \right]^{-1/2} \quad (2.66a)$$

$$\frac{\Lambda_z}{\delta} = \left[\left(\frac{a_4 Sh}{U_c/u_\tau} \right)^2 + \frac{a_5^2}{Sh^2 + (a_5/a_6)^2} \right]^{-1/2} \quad M_\infty < 0.75 \quad (2.66b)$$

$$\frac{\Lambda_z}{\delta} = \left[\left(\frac{a_4 Sh}{U_c/u_\tau} \right)^2 + a_7^2 \right]^{-1/2} \quad M_\infty > 0.9 \quad (2.66c)$$

where the Strouhal number is defined as $Sh = \omega\delta/u_\tau$ and:

$$a_1 = 0.1 \quad a_2 = 72.8$$

$$a_3 = 1.54 \quad a_4 = 0.77$$

$$a_5 = 548 \quad a_6 = 13.5 \quad a_7 = 5.66$$

Chase

Chase (1980) developed his first model which gives better prediction for low wavenumbers compared to the Corcos model. Hereafter Graham's form of Chase's most popular wavenumber-frequency model is presented.

$$\Phi(k_x, k_z, \omega) = \frac{(2\pi)^3 \rho^2 \omega^2 u_\tau^2}{U_c^2 \Phi(\omega)} \left[\frac{C_M k_x^2}{[K_+^2 + (b_M \delta)^{-2}]^{5/2}} + \frac{C_T |\mathbf{k}|^2}{[K_+^2 + (b_T \delta)^{-2}]^{5/2}} \right] \quad (2.67)$$

with:

$$\begin{aligned}
 K_+^2 &= \frac{(\omega - U_c k_x)^2}{h^2 u_\tau^2} + |\mathbf{k}|^2 & \Phi(\omega) &= \frac{(2\pi)^2 h \rho^2 u_\tau^4}{3\omega(1+\mu^2)} (C_M F_M + C_T F_T) \\
 F_M &= \frac{1+\mu^2 \alpha_M^2 + \mu^4 (\alpha_M^2 - 1)}{[\alpha_T^2 + \mu^2 (\alpha_T^2 - 1)]^{3/2}} & F_T &= \frac{1+\alpha_T^2 + \mu(3\alpha_T^2 - 1) + 2\mu^4 (\alpha_T^2 - 1)}{[\alpha_M^2 + \mu^2 (\alpha_M^2 - 1)]^{3/2}} \\
 \alpha_M^2 &= 1 + \left(\frac{U_c}{b_M \omega \delta}\right)^2 & \alpha_T^2 &= 1 + \left(\frac{U_c}{b_T \omega \delta}\right)^2 & \mu &= \frac{h u_\tau}{U_c} & C_M &= 0.0745 \\
 C_T &= 0.0475 & b_M &= 0.756 & b_T &= 0.378 & h &= 3.0
 \end{aligned}$$

Chase attempted an extension of his model to the lower wavenumber regions in order to take into account the acoustic domain (Chase, 1987). A modified version of the Chase model was developed by Finnveden et al. (2005) by studying the vibration response of a structure excited by a turbulent boundary layer.

Smol'yakov and Tkachenko

Smol'Yakov et al. (1991) based their model on measured spatial correlations and fitted exponential curves to their experimental results.

$$\Psi(k_x, k_z, \omega) = 0.974 A(\omega) h(\omega) [F(\mathbf{k}, \omega) - \Delta F(\mathbf{k}, \omega)] \quad (2.68)$$

where

$$\begin{aligned}
 A(\omega) &= 0.124 \left[1 - \frac{U_c}{4\omega\delta^*} + \left(\frac{U_c}{4\omega\delta^*}\right)^2 \right]^{1/2} & h(\omega) &= \left(1 - \frac{m_1 A}{6.515\sqrt{G}} \right)^{-1} \\
 m_1 &= \frac{1+A^2}{1.025+A^2} & G &= 1 + A^2 - 1.005 m_1 \\
 F(\mathbf{k}, \omega) &= \left[A^2 + \left(1 - \frac{k_x U_c}{\omega} \right)^2 + \left(\frac{k_z U_c}{6.45\omega} \right)^2 \right]^{-3/2} \\
 \Delta F(\mathbf{k}, \omega) &= 0.995 \left[1 + A^2 + \frac{1.005}{m_1} \left(\left(m_1 - \frac{k_x U_c}{\omega} \right)^2 + \left(\frac{k_z U_c}{\omega} \right)^2 - m_1^2 \right) \right]^{-3/2}
 \end{aligned}$$

Mellen

Mellen (1990) built an elliptical model for wall pressure cross-spectrum derived from the Corcos model. Hereafter is the expression of the model as given by Miller (2002).

$$\Phi(k_x, k_z, \omega) = \frac{2\pi(\alpha_x \alpha_z)^2 k_c^3}{[(\alpha_x \alpha_z k_c)^2 + (\alpha_x k_z)^2 + \alpha_z^2 (k_x - k_c)^2]^{3/2}} \quad (2.69)$$

with $\alpha_x = 0.10$ and $\alpha_z = 0.77$.

Statistical models

In statistical models, the focus is the modelling of turbulent velocity cross-spectra across the TBL. Wall-pressure fluctuations are then computed from the velocity fluctuations through a Poisson equation in the incompressible limit, or a wave equation to include the acoustic part.

Panton and Linebarger

Panton and Linebarger (1974) reconstruct the flow direction wavenumber spectrum of wall-pressure fluctuations by solving the fluctuating pressure Poisson equation. A law of the wall

plus Coles (1956) wake function represents the mean velocity profile and a scale-anisotropic model was built (based on a curve-fitting process from Grant (1958) zero-pressure gradient boundary layer) to retrieve the normal velocity correlation R_{22} . They were able to compute wavenumber spectra for various Reynolds numbers and adverse pressure gradients.

Peltier and Hambric

Peltier and Hambric (2007) built a statistical model based on data from Reynolds-Averaged Navier-Stokes (RANS) solutions. The authors use Gavin (2002) Simplified Anisotropic Model (SAM) to reproduce the velocity correlations needed for the fluctuating pressure Poisson equation. Tuning the parameters of the velocity correlation model, Peltier and Hambric (2007) could predict wall-pressure spectrum for favorable, zero and adverse pressure gradient flows.

Monte

Monte (2013) studied the surface pressure fluctuations for cylinders with a high length to radius ratio. This work can find applications in the field of linear underwater sonar antennas where the hydrodynamic noise due to the boundary layer developing over the antenna is a major issue. Here again the pressure is obtained by solving the Poisson equation for an incompressible flow. The mean flow, the Reynolds stress tensor and the kinetic energy for an axisymmetric flow over a cylinder are obtained from a RANS calculation. The velocity correlations were obtained using the elliptic model of He and Zhang (2006) adapted to curved geometries.

Stochastic models

Another way of obtaining the pressure spectrum is to develop a model based on a synthesized turbulent velocity field. A stochastic model is then obtained by using this spatio-temporal realization of the TBL velocity field as an input for the Poisson equation for instance.

Ahn's horseshoe vortex model

Ahn et al. (2010) built a stochastic model where horseshoe/hairpin-like vortices are subjected to a mean flow to reproduce a standard instantaneous turbulent velocity field. As for the statistical models, a Poisson equation is solved in order to retrieve the induced pressure field at the wall. One is then able to compute the wavenumber wall-pressure spectrum using a Fast Fourier Transform (FFT) procedure. This model will be detailed in section 4.1.1.

Dhanak's streamwise vortex model

Dhanak et al. (1997) developed a coherent structure model to predict the wall-pressure fluctuations induced by the vortices in the near-wall region. Comparing the model predictions with exact solutions of the Navier-Stokes equations, they determined that the best candidates were pairs of counter-rotating streamwise vortices. The model could predict the high frequency and high spanwise wavenumber range quite well, as well as the probability density function of the surface pressure.

Hu model for frequency-wavenumber spectrum

Hu et al. (2016) developed a model for wall-pressure spectrum based on the Fast Random Particle-Mesh Method (FRPM) introduced by Ewert et al. (2011). The principle of this method is to generate a synthetic turbulent velocity field by using averaged turbulence statistics and mean flow description from RANS computations. This is then fed into the Poisson equation for pressure where both the mean-shear and turbulence-turbulence terms are considered. Comparing their results with experimental results for a ZPG and APG flow, they were able to obtain satisfactory results for the one-point spectra at low frequencies but faced considerable attenu-

2.3. TURBULENT BOUNDARY LAYER WALL-PRESSURE SPECTRUM

ation in the high frequency range since the FRPM was unable to reconstruct the correct levels of kinetic energy in the near-wall region. The cross spectra and the convective velocities were well determined and consistent with the measurements.

Chapter 3

Analysis of turbulent structures in flows subjected to zero and non-zero pressure gradients

3.1 Numerical database

Direct noise calculations consist in computing both the turbulent aerodynamic field and the associated acoustic fluctuations by solving the compressible flow equations (Gloerfelt and Berland, 2013). Such simulations are carried out for turbulent boundary layers at Mach 0.5 subjected to four different pressure gradients: a strong adverse pressure gradient (APGs), a weak adverse pressure gradient (APGw), a zero pressure gradient (ZPG) and a favorable pressure gradient (FPG). Inclined plates with different slopes are used to set the pressure gradients, which requires a curvilinear version of the flow solver as described hereafter.

3.1.1 Equations and numerical methods

The governing equations are the compressible Navier-Stokes equations written for a curvilinear domain by using a coordinate transform. The physical space (x_1, x_2) is mapped into a Cartesian regular computational space (ξ_1, ξ_2) , and the third direction, which corresponds to the spanwise direction z , is left unchanged. By noting ρ the density, u_i the velocity components ($u_3 \equiv w$ in the following) and E the total specific energy, the set of equations for the unknown vector $\mathbf{U} = (\rho, \rho u_1, \rho u_2, \rho u_3, \rho E)^T$ writes:

$$\frac{\partial \mathbf{U}}{\partial t} + \frac{\partial \mathbf{F}_c}{\partial \xi_1} + \frac{\partial \mathbf{G}_c}{\partial \xi_2} + \frac{\partial \mathbf{H}}{\partial z} = 0 \quad (3.1)$$

where the curvilinear fluxes are defined by:

$$\begin{cases} \mathbf{F}_c = \mathbf{F} \frac{\partial \xi_1}{\partial x_1} + \mathbf{G} \frac{\partial \xi_1}{\partial x_2} = \frac{1}{J} \left(\mathbf{F} \frac{\partial x_2}{\partial \xi_2} - \mathbf{G} \frac{\partial x_1}{\partial \xi_2} \right) \\ \mathbf{G}_c = \mathbf{F} \frac{\partial \xi_2}{\partial x_1} + \mathbf{G} \frac{\partial \xi_2}{\partial x_2} = \frac{1}{J} \left(-\mathbf{F} \frac{\partial x_2}{\partial \xi_1} + \mathbf{G} \frac{\partial x_1}{\partial \xi_1} \right) \end{cases} \quad (3.2)$$

with $J = x_{1,\xi_1} x_{2,\xi_2} - x_{1,\xi_2} x_{2,\xi_1}$ the Jacobian of the coordinate transformation. The fluxes $\mathbf{F} = \mathbf{F}_e - \mathbf{F}_v$, $\mathbf{G} = \mathbf{G}_e - \mathbf{G}_v$ and $\mathbf{H} = \mathbf{H}_e - \mathbf{H}_v$ are the sum of the inviscid (subscript **e**) and visco-thermal fluxes (subscript **v**) given by:

$$\mathbf{F}_e = (\rho u_1, \rho u_1^2 + p, \rho u_1 u_2, \rho u_1 u_3, (\rho E + p)u_1)^T \quad (3.3a)$$

$$\mathbf{G}_e = (\rho u_2, \rho u_1 u_2, \rho u_2^2 + p, \rho u_2 u_3, (\rho E + p)u_2)^T \quad (3.3b)$$

$$\mathbf{H}_e = (\rho u_3, \rho u_1 u_3, \rho u_2 u_3, \rho u_3^2 + p, (\rho E + p)u_3)^T \quad (3.3c)$$

$$\mathbf{F}_v = (0, \tau_{11}, \tau_{12}, \tau_{13}, u_1 \tau_{11} + u_2 \tau_{12} + u_3 \tau_{13} - q_1)^T \quad (3.3d)$$

$$\mathbf{G}_v = (0, \tau_{12}, \tau_{22}, \tau_{23}, u_1 \tau_{12} + u_2 \tau_{22} + u_3 \tau_{23} - q_2)^T \quad (3.3e)$$

$$\mathbf{H}_v = (0, \tau_{13}, \tau_{23}, \tau_{33}, u_1 \tau_{13} + u_2 \tau_{23} + u_3 \tau_{33} - q_3)^T \quad (3.3f)$$

The specific total energy is $E = p/[(\gamma - 1)\rho] + u_i^2/2$ for an ideal gas satisfying $p = \rho r T$, where p is the pressure, T the temperature, r the gas constant, and γ the ratio of specific heats. The viscous stress tensor τ_{ij} is modelled as a Newtonian fluid $\tau_{ij} = 2\mu S_{ij} - (2/3)\mu S_{kk}\delta_{ij}$, where $S_{ij} = (u_{i,j} + u_{j,i})/2$ is the strain rate tensor and μ is the dynamic molecular viscosity. The dynamic viscosity is approximated with Sutherland's law and the heat flux components q_i are modelled with Fourier's law as in Gloerfelt and Berland (2013).

Dispersion-relation preserving finite differences on an eleven-point stencil optimized by Bogey and Bailly (2004) are used for the derivatives of the convective fluxes, whereas standard fourth-order finite differences are used for the viscous-thermal fluxes. The equations are integrated in time using an explicit low-storage six-step Runge-Kutta scheme optimized in the wavenumber space by Bogey and Bailly (2004). At the last substep, a selective filtering on an eleven-point stencil (Bogey and Bailly, 2004) is applied in each direction with an amplitude of 0.2 to eliminate grid-to-grid unresolved oscillations. Since large enough computational domains are required for the wavenumber-frequency analysis, the grid resolutions correspond to wall-resolved large-eddy simulations (LES). The effects of unresolved scales are taken implicitly into account by the regularization term provided by the selective filter. The efficiency of this LES strategy has been previously demonstrated for TBL flows (Aubard et al., 2013; Gloerfelt and Berland, 2013).

Periodic boundary conditions are used in the spanwise direction. On the solid wall, the no-slip conditions $u_i = 0$ are imposed, with $\partial p/\partial n = 0$ for the inviscid part, where n is the direction normal to the solid surface. The finite-difference stencil for the convective terms is progressively reduced down to the second order. At the wall, the temperature is calculated with the adiabatic condition, and the density can be deduced using the ideal gas law. The viscous stress terms are evaluated from the interior points by using fourth-order backward differences.

Since the weak acoustic radiation from the TBLs is directly computed in the simulations, great care is required to select appropriate boundary conditions. At the upstream and upper boundaries of the computational domain, the radiation boundary conditions of Tam and Dong (1996), using a far-field solution of the sound waves, are applied. A large sponge zone (Gloerfelt and Lafon, 2008) is furthermore added at the downstream end of the domain so that unhindered passage of aerodynamic perturbations is possible without the generation of spurious acoustic waves.

A critical point is to design a silent inflow technique to introduce perturbations necessary to trigger laminar-to-turbulent transition of the boundary layer flows, without introducing spurious noise. To that aim, a strategy based on a controlled transition has been developed in Gloerfelt and Robinet (2013). A preliminary steady two-dimensional simulation with the same code is performed for the flow over a backward-facing step (see figure 3.1). At the inlet, a laminar Blasius boundary layer with a Reynolds number based on displacement thickness $Re_{\delta_n^*} \simeq 400$ is imposed ahead of the backward-facing step, whose height h yields a Reynolds number $Re_h \simeq 462$. A base flow is defined by extracting flow variables in a vertical plane located few points downstream of the step and a compressible linear stability analysis is conducted to find a resonant triad of

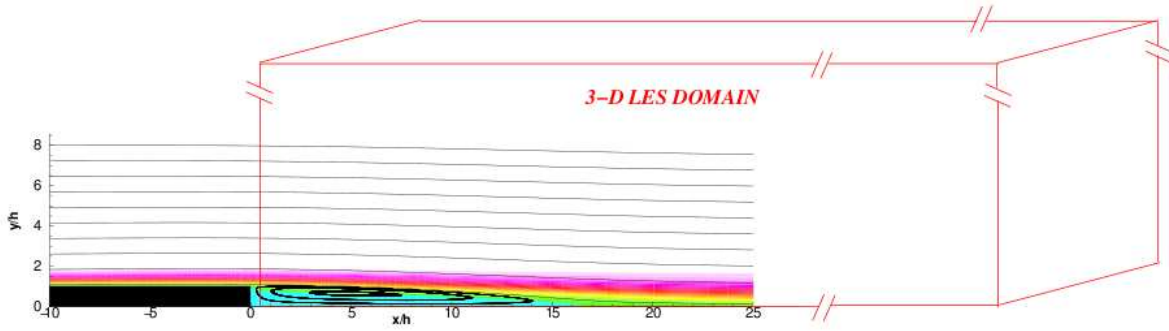


Figure 3.1 – Sketch of the computational domain for the non-zero-pressure-gradient computations - Mean streamwise velocity \bar{u} and streamlines from a 2D simulation with the backward-facing step of height h . The mean flow a few points after the step is used as inlet for the 3D domain - from Gloerfelt and Margnat (2014).

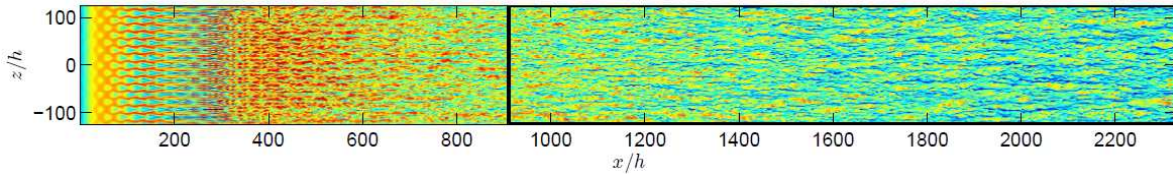


Figure 3.2 – Top view close to the wall ($y^+ \simeq 25$) of the streamwise velocity for the ZPG case showing the transition zone. A fully turbulent state is reached after the solid line for $x/h \simeq 900$.

unstable modes. Using the inlet freestream velocity U_∞ and step height h as reference velocity and length respectively, the triad is made up of one two-dimensional wave of frequency $0.2U_\infty/h$ and two oblique subharmonic waves of frequency $0.1U_\infty/h$ with opposite phase angles satisfying the resonant condition of Craik (1971). These values are close to those used in the work of Craik (1971) but here the velocity profile exhibits an inflexion point, leading to unstable modes with a greater amplification factor, which is favorable for developing instability waves from a low initial amplitude. The triad of unstable modes is superimposed on the base flow at the inlet of the three-dimensional simulations with equal amplitude of $6 \times 10^{-4}U_\infty/h$ for the fundamental and subharmonic waves. Details on the characteristics (frequency, wavenumber, amplitude) of the resonant triad are given in Gloerfelt and Robinet (2013), where it has been checked that the transition toward a turbulent state is smooth and acoustically quiet. Figure 3.2 illustrates the transition pattern for the ZPG case. A fully turbulent state with no trace of the initial disturbances is reached for $x/h \gtrsim 900$ and the zone of interest for the wall-pressure analyses starts downstream of this limit. As a consequence, details of the transition are not influential for the present study. The important point is that the strategy adopted to trigger turbulence is sufficiently silent so that the direct acoustic radiation can be investigated (Cohen, 2015; Cohen and Gloerfelt, 2015; Gloerfelt and Margnat, 2014).

3.1.2 Grid design

The data analyzed in the paper are obtained from a series of simulations, whose main parameters are summarized in table 3.2. Four values of the pressure gradient are considered by keeping a horizontal freestream and changing the angle α of the plate.

Side views of the grids are presented in figure 3.3. The ZPG mesh is the same as the simulations of Gloerfelt and Margnat (2014); Gloerfelt and Robinet (2013) and is discretized

with $1440 \times 400 \times 400$ points. Grid points are equally spaced in the spanwise direction and are clustered near the wall using a geometric progression of 2% for the 25 first points, then with a rate of 2.5% for the following 155 points. The distribution is then uniform for the next 120 points and a stretching is finally applied to the last 100 points up to the top boundary (visible in figure 3.3(c) for $y_2/h \gtrsim 600$). In the streamwise direction, the grid points are clustered near the inlet over a range of 200 points, so that small grid sizes are used for properly entering unstable modes. The grid spacing is then regular up to the exit zone where a grid stretching with a geometric progression of 3% is applied over the last 100 points to create a large sponge zone where the flow variables are progressively filtered with a Laplacian operator at each time step to minimize numerical reflections from the outlet.

	α	Δx^+	Δy_w^+	Δy_e^+	Δz^+	N_{x_1}	N_{x_2}	N_{x_3}
APGs	-11.49°	27.5	0.7	20.2	8.4	1600	400	400
APGw	-6.05°	32.3	0.8	23.7	9.9	1600	400	400
ZPG	0°	37.8	1.0	27.7	12.6	1440	400	400
FPG	10.19°	46.0	1.2	33.7	14.2	1600	400	400

Table 3.1 – Summary of meshes parameters for the simulated cases at Mach 0.5 with pressure gradients. The two values for Δy^+ indicate the mesh spacing at the wall (subscript w) and at the boundary layer edge (subscript e).

For the non-zero pressure-gradient cases, a curvilinear domain of 1600×400 points is defined and extruded in the third direction on $n_z = 400$ points. Along the x_1 -direction parallel to the external freestream, a first region of horizontal plate is defined in order to have the same inlet condition as the ZPG case. Note that the grid spacing is also refined on the 150 first points near the inlet boundary and is maintained constant for the 200 next points with a spacing slightly greater than in the zone of interest above the ramp. This second region corresponds to an inclined plate with an angle α from the horizontal, which is negative for the adverse-pressure-gradient cases and positive for the favorable-pressure-gradient cases. The values of α are reported in table 3.1 and are chosen to set the strength of the pressure gradient. The points are equally spaced on the ramp region with the nominal streamwise spacing. The third part of the mesh represents the exit zone where a horizontal plate is recovered with a severe stretching on the last 100 points. Note that the two transitions between the ramp and the flat portions are progressive and corresponds to a low radius of curvature set on approximately 30 grid points. The distribution of points in the wall-normal direction is the same as the ZPG case and the mesh is also regular in the spanwise direction.

The velocity fields and wall-pressure analyses are restricted to a zone of interest where a nearly equilibrium TBL flow is obtained. This area is defined between curvilinear abscissae x_{min} and x_{max} and is delimited with thick dashed lines in figure 3.3. These zones of interest for each cases exclude the transitional development zone, the exit sponge zone and the upper buffer region. For the non-zero pressure-gradient cases, the domain of interest in the (x_1, x_2) -plane in which the plate is inclined is transformed into a Cartesian (x, y) -plane where the plate is horizontal using a rotation and an interpolation of the variables. In the subsequent flow analyses, $u = \cos(\alpha)u_1 + \sin(\alpha)u_2$ and $v = -\sin(\alpha)u_1 + \cos(\alpha)u_2$ are the x -component parallel to the wall and y -component normal to the wall of the velocity respectively, where u_1, u_2 are the components defined in the (x_1, x_2) -plane and used in the governing equations (3.1). For the analyses of the database, the coordinate system (x, y, z) is used and the velocity components

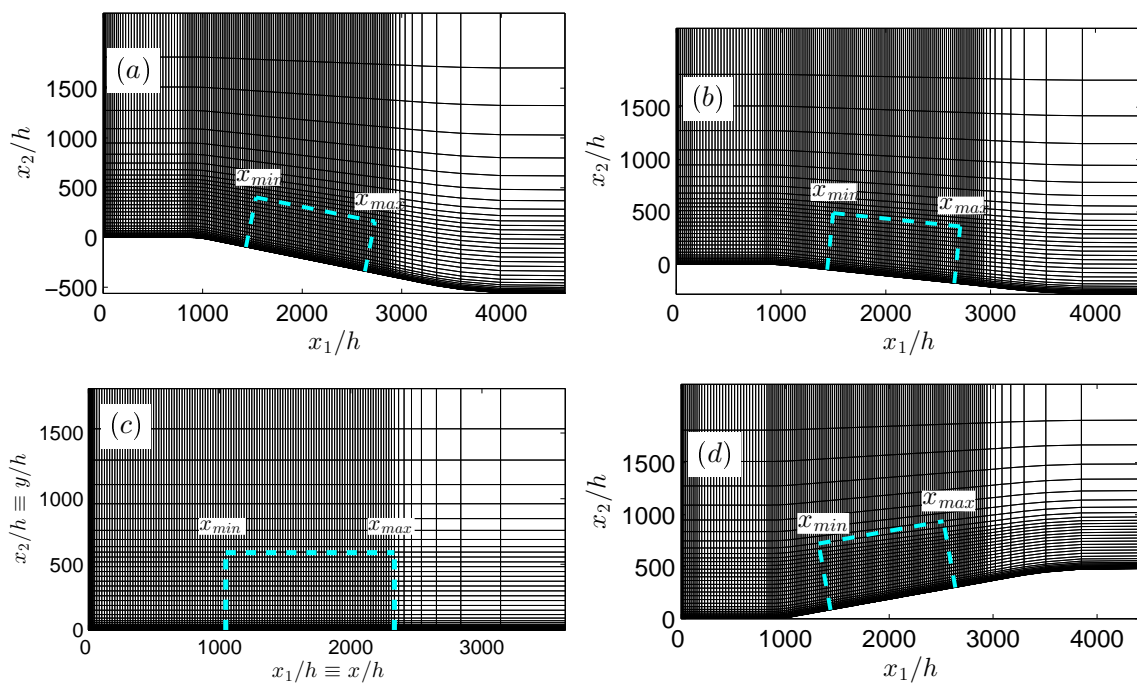


Figure 3.3 – Computation domain in the streamwise/wall-normal plane (x_1, x_2) : strong adverse APGs (a), weak adverse APGw (b), zero gradient ZPG (c), and favorable FPG (d). The zone of interest for the velocity and wall-pressure analyses is delimited with the dashed rectangle. Parameter h is the height of the backward-facing step located upstream of the domain involved in the turbulence transition process.

are denoted (u, v, w) . It is noteworthy that the grid spacing in this region is regular in the x - and z -directions, and that the physical values of the spacings Δx , Δz and Δy_{min} are the same for all simulations. They are given in table 3.1 in terms of wall units evaluated at the middle of the domain of interest (based on the friction velocity u_τ and the viscous length scale $\delta_v = \nu_w/u_\tau$). The subscript w is used to denote quantities evaluated at the wall and the subscript e quantities evaluated at the edge of the boundary layer. In the tables 3.3 and 3.4 the quantities representative of the different configurations are taken at the middle of the domain of interest $(x_{max} - x_{min})/2$, which are very close to the values averaged over $[x_{min}, x_{max}]$.

The time step for all simulations is $\Delta t = CFL \Delta y_{min} / (U_\infty + c_\infty) \simeq 0.025h/U_\infty$, corresponding to $CFL=1.5$. The total simulation time is roughly the same for the different cases, $t = 20\,000h/U_\infty$. Statistical quantities are averaged over time and the spanwise direction. Wall-pressure planes are stored every $30\Delta t$ during the last 240 000 iterations, corresponding to 8000 samples and a non-dimensional time of approximately $6\,000h/U_\infty$ or $4.9(x_{max} - x_{min})/U_\infty$.

3.1.3 Flow parameters

Computations are performed for a Mach 0.5 turbulent boundary layer subjected to zero (ZPG), adverse (APGw and APGs) and favorable (FPG) pressure gradients. The intensity of the pressure gradient is characterized by Clauser (1954) parameter β_C defined as:

$$\beta_C = \frac{\delta^*}{\tau_w} \frac{dp_e}{dx} \quad (3.4)$$

where δ^* , τ_w and dp/dx are respectively the TBL displacement thickness, the shear stress at the wall and the streamwise pressure gradient.

All parameters given in this section are measured at the middle of the zone of interest used for the study, which corresponds to a zone of 720 (ZPG) to 800 (pressure gradient cases) points in the streamwise direction centered around the middle of the inclined planes.

The 0.5 Mach number is lower than what is encountered in the field of aeronautics where the Mach numbers vary around Mach 0.8 in cruise flight conditions. It is believed that Mach number and compressibility (for flows ranging from Mach 0.5 to 0.9) have very low effect on the structure of turbulence as noticed by Gloerfelt and Margnat (2014). Calculations for the zero-pressure-gradient case were performed by Gloerfelt and Margnat (2014) and the non-zero-pressure-gradient cases were computed by Cohen and Gloerfelt (2015).

The general parameters of the fluid and the turbulent boundary layer flows are given in Tables 3.2 and 3.3 respectively.

M_∞	p_∞ (Pa)	T_∞ (K)	ν_∞ (m ² .s ⁻¹)
0.5	101300	298.15	1.5×10^{-5}

Table 3.2 – Free flow properties for the LES computation

One can notice the same value of Re_θ for both ZPG and FPG cases. This is due to the fact that the boundary layers thickens at the starting curvature of the inclined plane for the FPG case. Therefore, the initial TBL thickness δ_0 at the beginning of the inclined plane is greater than that of the ZPG case. Finally, table 3.4 provides the parameters characterizing the pressure gradient for each flow, i.e the inclination angle α of the wall, the Clauser parameter β_C , Clauser's defect shape factor G , the acceleration/deceleration parameter K , the viscous-scaled

	$\delta_{ref} \times 10^3$ (m)	$\delta_{ref}^* \times 10^4$ (m)	$\theta_{ref} \times 10^4$ (m)	$Re_{\theta_{ref}}$	Re_{ref}^+	$U_{e_{ref}}$ (m/s)	$u_{\tau_{ref}}$ (m/s)
APGs	1.83	4.53	2.77	3125	690	159	5.23
APGw	1.57	3.22	2.10	2462	694	166	6.09
ZPG	1.13	1.98	1.35	1693	610	173	7.17
FPG	1.24	1.62	1.17	1618	783	195	8.42

Table 3.3 – Boundary layer properties for the four pressure gradient cases. Subscript *ref* denotes values taken at the middle of the domain of interest.

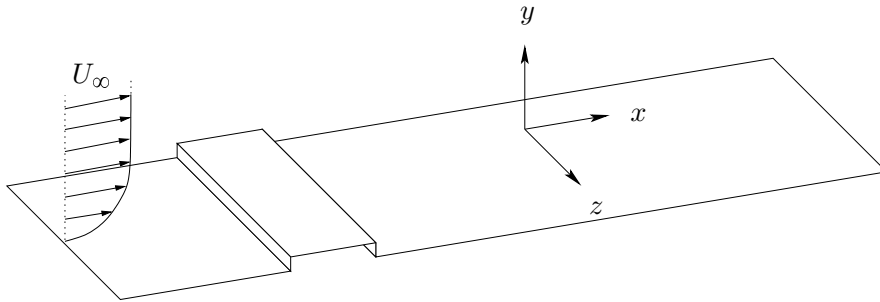


Figure 3.4 – Sketch of the computational setup and of the coordinate system (figure not to scale) for the 3D database. A small step lying in the spanwise direction is introduced downstream of the inlet boundary condition in order to ignite the transition to turbulence of the boundary layer flow - after Gloerfelt and Berland (2013)

pressure gradient Δ_p , Castillo and George (2001) parameter Λ , the shape factor H and Coles (1956) wake parameter Π .

	α	β_C	G	$K \times 10^7$	$\Delta_p \times 10^3$	Λ	H	Π
APGs	-11.49°	1.6	11.5	-3.4	9.8	0.24	1.63	1.8
APGw	-6.05°	0.51	9.2	-1.7	3.8	0.18	1.53	1.1
ZPG	0°	0	7.4	0	0	0	1.47	0.6
FPG	10.19°	-0.36	6.2	2.4	-3.8	-0.92	1.39	0.17

Table 3.4 – Parameters quantifying the pressure gradient for the different cases (α is the angle of the slanted wall used to impose a prescribed pressure gradient).

3D database

For the four other databases mentioned above, only two-dimensional planes were able to be saved due to data storage issues. Nonetheless, there is one three-dimensional database (ZPG3D) available from a previous computation of a Mach 0.5 zero pressure gradient turbulent boundary layer over a flat plate (see Gloerfelt and Berland (2013)). The free flow parameters are similar to those given in table 3.2. The grid and boundary layer parameters are given in tables 3.5 and 3.6 and a sketch of the computational domain is provided in figure 3.4. The main difference

3.1. NUMERICAL DATABASE

with the 2D databases is that the step used for the laminar-turbulent transition is within the computation domain. However, this difference has no impact on the fully turbulent velocity field.

	Δx^+	Δy_w^+	Δy_e^+	Δz^+	N_{x_1}	N_{x_2}	N_{x_3}
ZPG3D	37	0.98	27	14.7	1372	300	131

Table 3.5 – Summary of mesh parameters for the Mach 0.5 ZPG 3D database. The two values for Δy^+ indicate the mesh spacing at the wall (subscript w) and at the boundary layer edge (subscript e).

	$\delta_{ref} \times 10^3(\text{m})$	$\delta_{ref}^* \times 10^4(\text{m})$	$\theta_{ref} \times 10^4(\text{m})$	$Re_{\theta_{ref}}$	Re_{ref}^+	$U_{eref}(\text{m/s})$	$u_{\tau_{ref}}(\text{m/s})$
ZPG3D	1.13	1.97	1.36	1500	556	173	7.38

Table 3.6 – Boundary layer properties for the zero pressure gradient 3D database. Subscript ref denotes values taken at the middle of the domain of interest.

3.1.4 Available database summary

For the 2D databases, the following data is available:

- 8000 timesteps
- the three components of the velocity field (u, v, w)
- 8 regularly spaced streamwise/wall-normal (x, y) planes spanning the entire spanwise extent of the computational domain
- 11 wall-parallel (x, z) planes spanning the entire TBL thickness
- wall-pressure field $p(x, z, t)$
- wall-pressure frequency-wavenumber spectra $\Phi_{pp}(k_x, k_z, \omega)$.

For the ZPG3D database, the following data is available for the four pressure gradient cases:

- 4500 timesteps
- the three components of the velocity field (u, v, w) on 3D volume.

Table 3.7 summarizes which database is used for each step of the present study.

	FPG	ZPG	APGw	APGs	ZPG3D
Velocity field 3D analysis					X
Velocity field 2D analysis	X	X	X	X	
Pressure spectra analysis	X	X	X	X	

Table 3.7 – Use of the different databases for each step of the analysis.

3.1.5 Mean profiles and equilibrium state validation

The mean velocity profiles as well as the turbulent intensity u_{rms} are shown in figure 2.6. Concerning equilibrium of the different flows, the streamwise evolutions of the pressure gradient parameters mentioned in section 2.1.3 are plotted in figure 3.5. A constant character is more or less observed in the region of interest, however discrepancies are visible for the APGs case at the end of the domain.

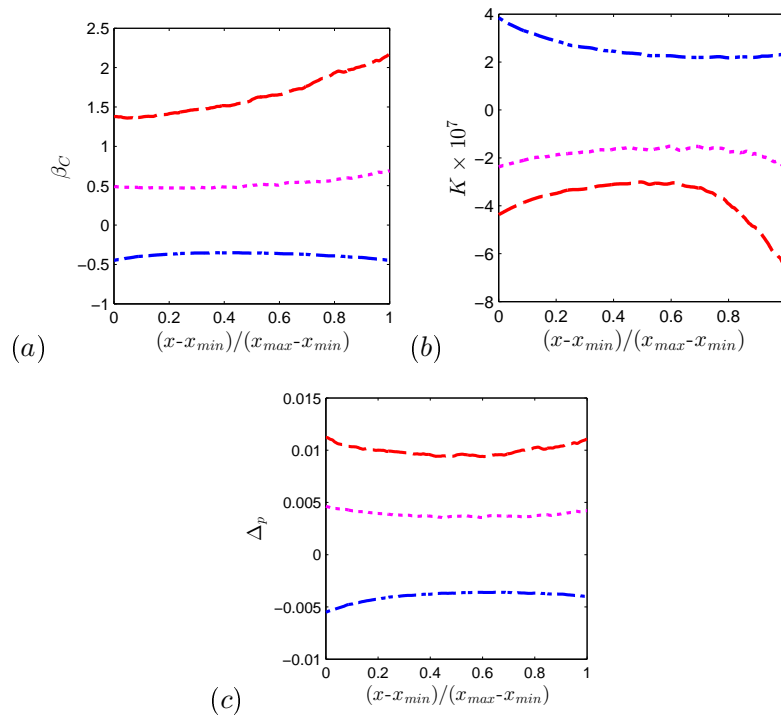


Figure 3.5 – (a) Clauser pressure gradient parameter β_C , (b) acceleration parameter K and (c) viscous scaled pressure parameter Δ_p for FPG (— — —), APGw (— — —) and APGs (— — —) - after Cohen (2015).

3.2 Instantaneous velocity fields analysis

In this part, instantaneous views of the flow field are presented. Velocity vector fields visualization as well as coherent structures identification are performed. The 3D structures identification is based on the old zero pressure gradient computation referred to as ZPG3D (Gloerfelt and Berland, 2013) since this is the only three-dimensional database available.

3.2. INSTANTANEOUS VELOCITY FIELDS ANALYSIS

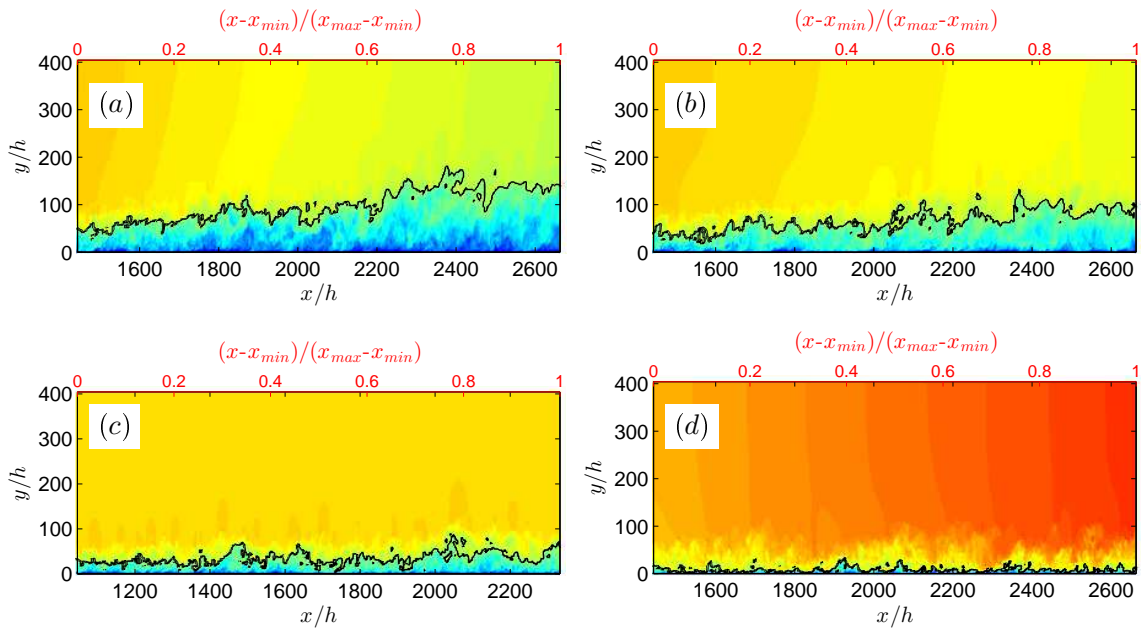


Figure 3.6 – Instantaneous streamwise velocity u in the streamwise/wall-normal plane for APGs (a), APGw (b), ZPG (c) and FPG (d). x_{min} and x_{max} denote the streamwise boundaries of the zone of interest. Black line corresponds to $u = 140\text{m/s}$ and highlights thickening of the boundary layer from FPG to APGs - scale is from 10 m/s (blue) to 260 m/s (red) - Provided by X. Gloerfelt.

3.2.1 Analysis and identification tools in two-dimensional planes

As it has been said in section 3.1.4, only two-dimensional planes were available due to storage issues. For this reason, a method is required to identify and analyse three-dimensional coherent structures out of two-dimensional velocity fields.

The hairpin-like vortex is the main structures in which we are interested. Mayam (2009) and Adrian et al. (2000) suggest identifying hairpin heads in streamwise/wall-normal planes by viewing the velocity-vector field in a reference frame moving with the structure. In this case, the following characteristics (illustrated in figure 3.7) are the signature of a hairpin-like vortex:

- a circular streamlines pattern is visible in the velocity-vector field rotating in the same direction as the mean velocity circulation (hairpin head)
- a second quadrant $Q2$ region ($u' < 0, v' > 0$) located beneath and upstream of the head
- a fourth quadrant $Q4$ region ($u' > 0, v' < 0$) facing the $Q2$ region, inducing a stagnation point at the frontier of the two events
- an inclined shear layer (ISL) between the $Q2$ and $Q4$ regions.

This method was applied to instantaneous velocity vector fields for the four pressure gradient cases as can be seen in figure 3.8. In this figure, the vector fields are represented in a reference frame moving at $U_c = 0.72U_e$ and the arrows and circles indicate the loci of stagnation points and hairpin heads. Multiple hairpins are aligned in the streamwise direction along a line with varying slope. This particular organization is the signature of hairpin packets.

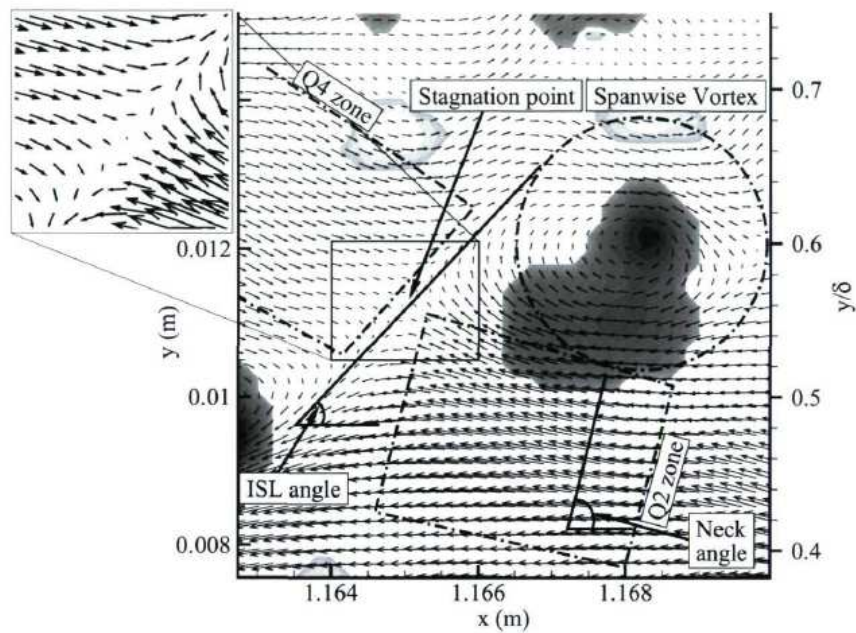


Figure 3.7 – Single hairpin-like vortex signature in streamwise/wall-normal plane - Velocity vector field in a frame of reference moving with the structure - after Mayam (2009).

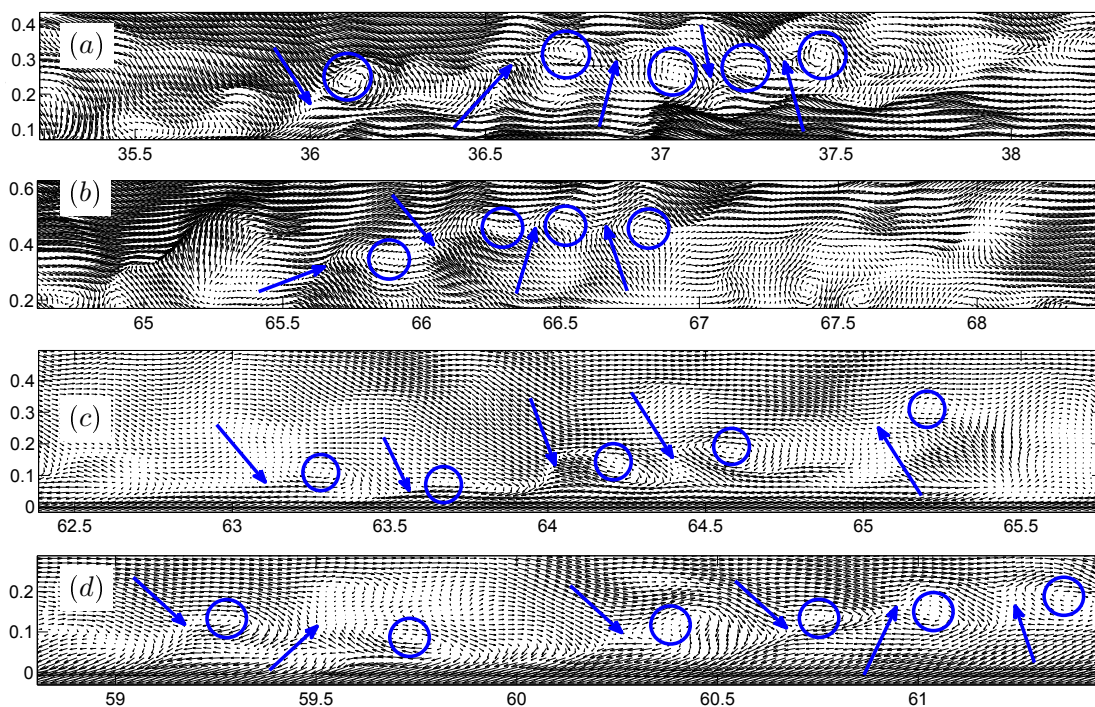


Figure 3.8 – Instantaneous views of streamwise/wall-normal vector fields showing hairpin vortex signatures, viewed in a frame of reference moving at $U_c = 0.72U_e$ for the APGs (a), APGw (b), ZPG (c) and FPG (d) configurations - Streamwise and wall normal axes (x, y) are made non-dimensional using the boundary layer thickness δ .

For the remainder of the study, the swirling strength criteria λ_{ci} (see equation (2.15)) will be used at multiple times for the coherent structures visualization and analyses. In order to eliminate background noise, which is of great importance for the statistical study of the velocity fields, the following threshold will be used:

$$|\lambda_{ci}| > 1.5\lambda_{ci}^{rms} \quad (3.5)$$

The root mean square value λ_{ci}^{rms} is computed as follows:

- 2D databases: since the hypothesis of equilibrium is well verified (see section 3.1.5), it is assumed that the root mean square of the swirling strength is only a function of the wall-normal coordinate $\lambda_{ci}^{rms} = \lambda_{ci}^{rms}(y)$. Therefore, for each case of pressure gradient, λ_{ci}^{rms} is computed at the middle of the domain of interest for all wall-normal positions and for each (x, y) plane. The final λ_{ci}^{rms} is the average over the 8 (x, y) planes.
- ZPG3D database: the method is the same as for the 2D cases but differs in the averaging process: the averaging is performed over the entire spanwise direction, i.e. 131 (x, y) planes.

The threshold based on the root mean square was depicted as a universal threshold by Wu and Christensen (2006), independent of the Reynolds number. The criterion $|\lambda_{ci}| > 1.5\lambda_{ci}^{rms}$ was found to effectively define the boundaries of vortex cores while minimizing the influence of the noise associated with the calculation of the velocity gradients. Natrajan et al. (2007) use the same threshold for PIV analysis of spanwise retrograde vortices. Mayam (2009) compares three thresholds: one based on the maximum value of $|\lambda_{ci}|_{max}$, one based on the number of mesh points within the λ_{ci} cluster and one based on the root mean square λ_{ci}^{rms} . He finally found that the threshold based on the root mean square was the best and chose $|\lambda_{ci}| > 1.45\lambda_{ci}^{rms}$ for his study. To compute the convection velocities of hairpin vortices and packets, Adrian et al. (2000) used a threshold based on the average value of the swirling strength $|\lambda_{ci}| > 30\lambda_{ci}^{avg}$.

3.2.2 Effect of pressure gradient on the coherent structures

Instantaneous views of the vortical motions in all flows are shown in Figure 3.9. Contours of the swirling strength λ_{ci} show that there are more vortical motions in the outer layer and that their size is greater in the case of the adverse pressure gradient. Indeed it has been demonstrated that the large scale structures emerge more predominantly in the outer region when the flow is subjected to an adverse pressure gradient (Bradshaw, 1967b; Harun et al., 2013; Lee and Sung, 2009).

In order to know in which a vortex is spinning, the following quantity is introduced:

$$\tilde{\lambda}_{ci} = \lambda_{ci} \frac{\omega_z}{\|\boldsymbol{\omega}\|} \quad (3.6)$$

Therefore,

- prograde vortex $\tilde{\lambda}_{ci} < 0$: vortex spinning in the same direction as the mean circulation
- retrograde vortex $\tilde{\lambda}_{ci} > 0$: vortex spinning in the direction opposite to the mean circulation.

For the remainder of the thesis, $\lambda_{ci} = \tilde{\lambda}_{ci}$. Figure 3.10 provides the number of prograde and retrograde spanwise vortices through the entire thickness of the boundary layer for the four pressure gradient cases. The method to do so consists in setting a probe in the middle of the domain (along the streamwise direction) which captures a spanwise vortex each time it

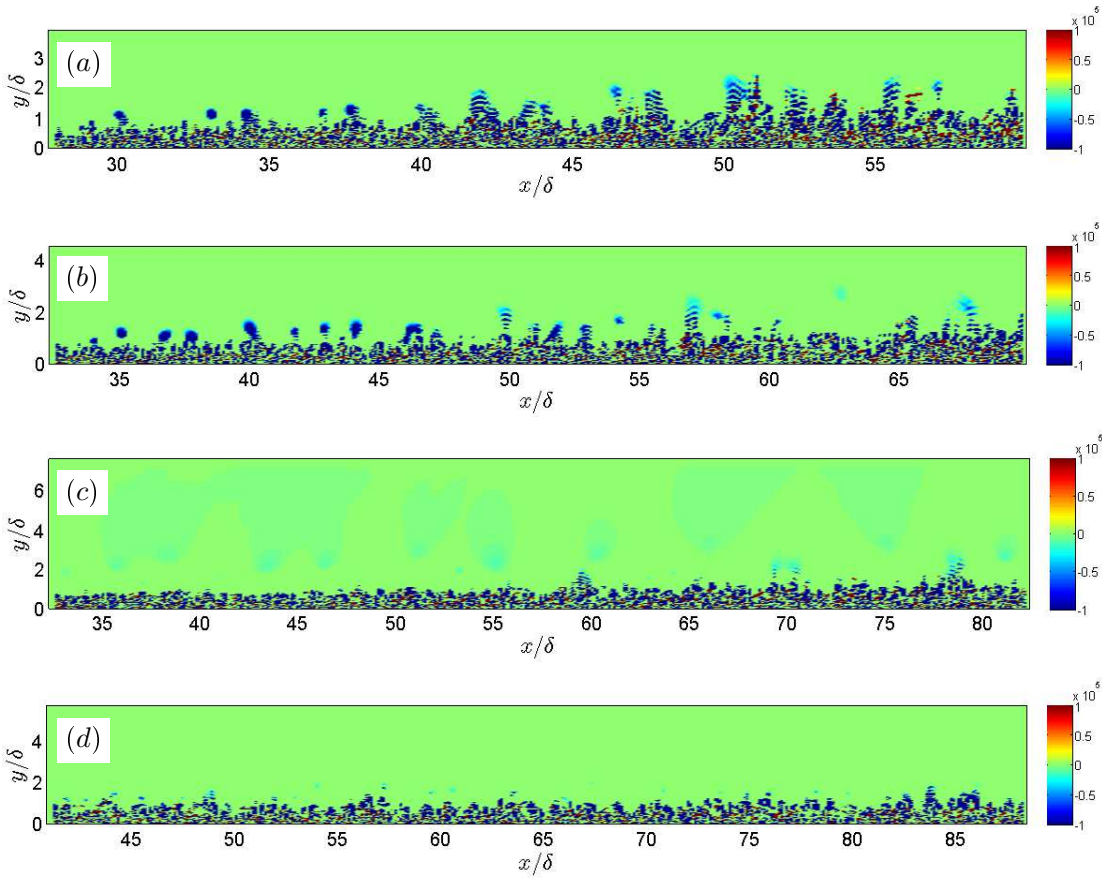


Figure 3.9 – Contours of swirling strength λ_{ci} for APGs (a), APGw (b), ZPG (c) and FPG (d).

3.2. INSTANTANEOUS VELOCITY FIELDS ANALYSIS

encounters a value $|\lambda_{ci}| > 1.5\lambda_{ci}^{rms}$. This operation is performed over the 8000 available timesteps at 19 wall-normal locations spanning from the inner layer to the edge of the boundary layer. The absolute number of vortices is not what is of interest here but rather the differences between the pressure gradient cases and the evolution along the wall-normal direction.

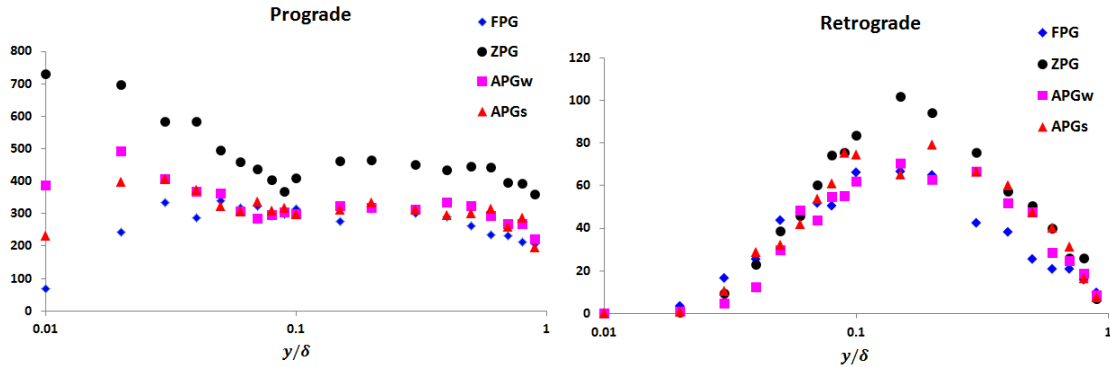


Figure 3.10 – Number of prograde and retrograde spanwise vortices for the four pressure gradient cases along the TBL thickness. The number of vortices is measured over 8000 snapshots with a threshold $|\lambda_{ci}| > 1.5\lambda_{ci}^{rms}$.

Looking at the prograde vortices distribution, the first remarkable result is that the number of spanwise vortices is higher for the ZPG flow through the entire TBL thickness with the highest values very close to the wall. In the inner layer, the favorable case shows the lowest values. There is a zone of convergence for all pressure gradient cases around $y/\delta \simeq 0.1$ which seems to be a local minimum. Beyond this point, the number of prograde vortices are quite similar for the non-zero pressure gradients with noticeable differences between APG and FPG for $y/\delta > 0.5$, confirming what has been said concerning the predominance of structures in the outer region for flows subjected to adverse pressure gradients.

For the retrograde vortices, the maximum is located near the end of the logarithmic region around $0.1 < y/\delta < 0.2$. Unlike the prograde case, there is not clear distinction for the ZPG case. The FPG flow shows the lowest number of retrograde vortices as the edge of the boundary layer is approached.

Comparing both prograde and retrograde vortices repartitions, it can be said that prograde vortices are encountered much more often throughout the boundary layer thickness (up to 14 times more often at some wall-normal locations than retrograde vortices). There seems to be a hierarchy for prograde vortices such as $N_{FPG}^p < N_{APG}^p < N_{ZPG}^p$ once again over the entire TBL whereas there are changing orders depending on the wall-normal distance for retrograde vortices. Finally, the evolution of prograde vortices looks very similar to the velocity intensities w_i^{rms} confirming the fact that these vortices, and particularly hairpin vortices, are correlated to the production of turbulent kinetic energy in the near-wall region.

3.2.3 Analysis of a three-dimensional database

The three-dimensional zero pressure gradient data base is analyzed in this section. The 3D velocity field is processed in order to visualize and provide some features of the three-dimensional characteristics of the turbulent structures.

Figure 3.11 reveals the presence of low-speed and high-speed streaks in the near-wall region up to $y^+ = 20$. The spanwise spacing between the streaks is around $\lambda_z^+ \simeq 100 - 200$ expressed in wall units, following the results in the literature whereas the streamwise extent goes up to

$\lambda_x^+ \simeq 2000 - 4000$ ($\lambda_x \simeq 3.5 - 7\delta$). Figure 3.12(a) shows the isosurface of swirling strength λ_{ci} and highlights the presence of numerous hairpin-like vortices in the outer region of the turbulent boundary layer. In some regions, hairpin vortices very close to each other and relatively arranged along a quasi-streamwise line reveal the hairpin packets organization. Figures 3.12(b) and 3.12(c) show an isolated hairpin-like structure with axes expressed in inner x_i^+ and outer x_i/δ variables respectively. As suggested by the literature, the hairpin vortices are most likely asymmetric. Here only the head and right leg are clearly distinguishable. The three parts of the structures, i.e. leg, neck and angle (refer to figures 2.14 and 2.15), are clearly visible. The neck angle is estimated at $\alpha_n = 53^\circ$ and the leg angle at $\alpha_l = 24^\circ$.

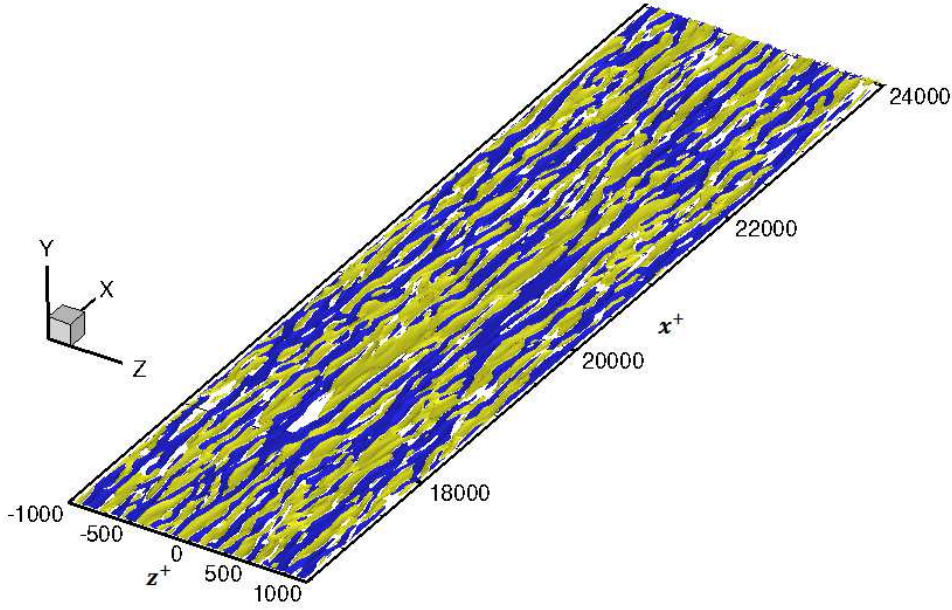


Figure 3.11 – Isosurface of instantaneous streamwise velocity u' revealing presence of low speed streaks $u'/U_e = -0.058$ (blue) and high speed streaks $u'/U_e = 0.058$ (yellow) in the near-wall region.

3.3 Statistical analysis of velocity fields

3.3.1 Conditionally averaged velocity fields

The conditionally averaged velocity field using the linear stochastic estimation method based on the swirling strength condition λ_{ci} is given by:

$$\hat{u}_j(\mathbf{x} + \mathbf{r}) = L_j \lambda_{ci}(\mathbf{x}), \quad L_j = \frac{\langle \lambda'_{ci}(\mathbf{x}) u'_j(\mathbf{x} + \mathbf{r}) \rangle}{\langle \lambda'^2_{ci}(\mathbf{x}) \rangle} \quad (3.7)$$

where $\langle \cdot \rangle$ denotes both time average and spatial average over the spanwise direction.

Figure 3.13 shows the estimated velocity vector fields from equation (3.7) for the four pressure gradient configurations. The vectors \hat{u}_i were set to unit in order to reveal more clearly the weak motions correlated to the event located at $(x/\delta = 0, y/\delta = 0.2)$; this wall normal distance is chosen for comparison with results from the literature. It can be seen that prograde vortices (indicated with black circles) align in the streamwise direction with a certain angle to the wall

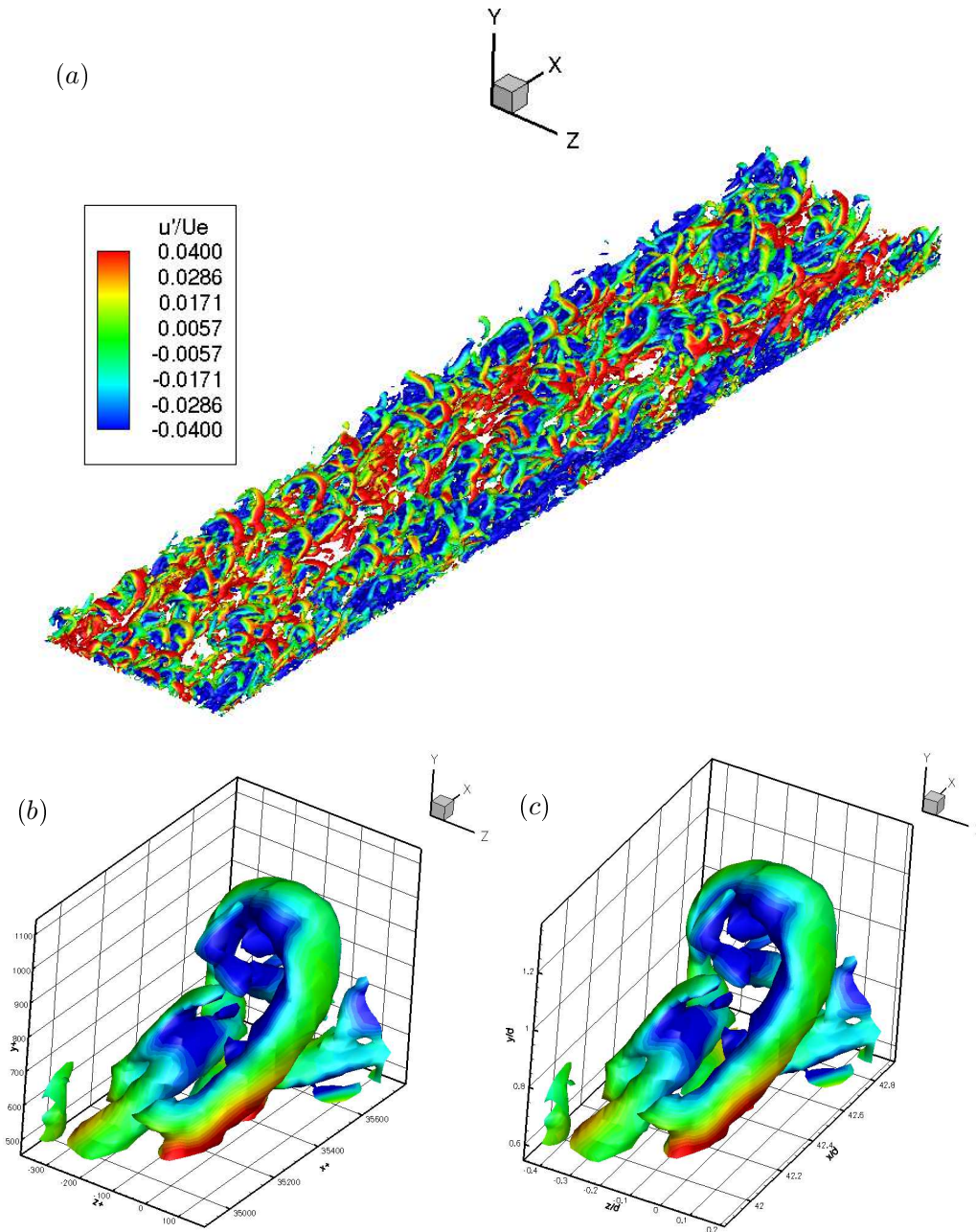


Figure 3.12 – Isosurface of swirling strength criterion $\lambda_{ci} = 4.2\lambda_{ci}^{rms}$ colored with fluctuating streamwise velocity u'/U_e showing (a) hairpin forest in the outer part of the boundary layer $y/\delta > 0.39$ and isolated hairpin with axes scaled with (b) inner variables x_i^+ and (c) outer variables x_i/δ .

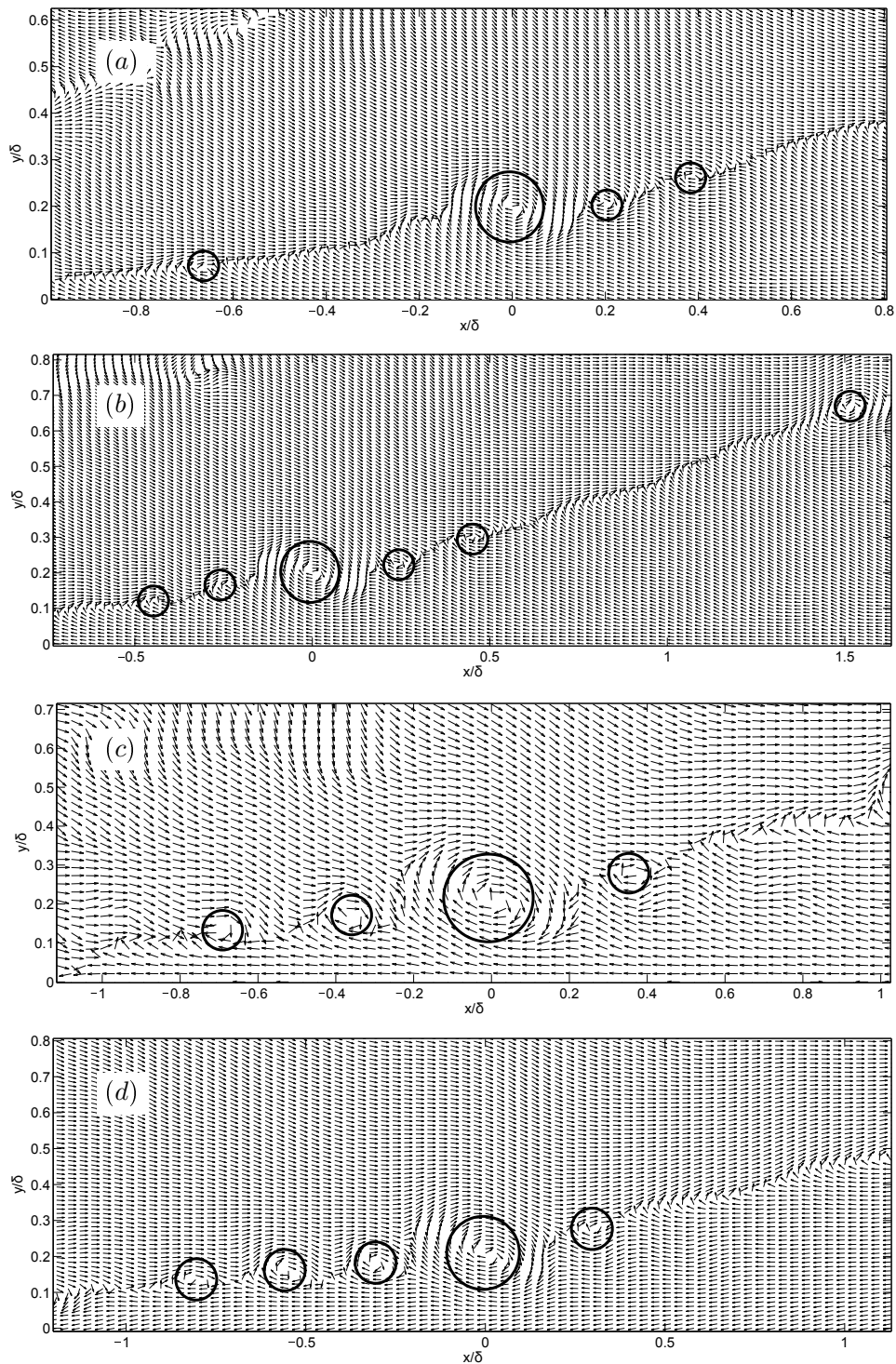


Figure 3.13 – Estimated velocity field \hat{u}_i using a negative swirling strength condition $\lambda_{ci} < 0$ for the APGs (a), APGw (b), ZPG (c) and FPG (d) configurations with reference point at $y/\delta = 0.2$ - Black circles indicate positions of prograde vortices (biggest circle indicates vortex at the reference point) - Streamwise and wall-normal axes (x, y) are made non-dimensional using δ .

(Adrian et al., 2000; Christensen and Adrian, 2001; Head and Bandyopadhyay, 1981; Lee and Sung, 2009; Mayam, 2009). These vortices gather the characteristics of hairpins as described in the previous section (upstream Q2 event, stagnation point, ISL, ...). Once again, this reveals that hairpin packets are dominant features of the turbulent boundary layer flow with and without presence of a pressure gradient. Streamwise separation distances between two successive vortices $\Delta_v x$ are (from left to right):

APGs	$\Delta_v x^+ = [434, 126, 112]$	$\Delta_v x/\delta = [0.68, 0.20, 0.18]$
APGw	$\Delta_v x^+ = [130, 163, 146, 130, 680]$	$\Delta_v x/\delta = [0.20, 0.26, 0.23, 0.20, 1.02]$
ZPG	$\Delta_v x^+ = [171, 201, 201]$	$\Delta_v x/\delta = [0.32, 0.37, 0.37]$
FPG	$\Delta_v x^+ = [180, 157, 225, 202]$	$\Delta_v x/\delta = [0.26, 0.23, 0.323, 0.29]$

where $\Delta_v x^+ = \Delta_v x u_\tau / \nu$ is the separation expressed in viscous wall units. It can be noticed that the secondary vortices surrounding the event vortex are closer to it for both adverse cases. Lee and Sung (2009) and Adrian et al. (2000) respectively reported $\Delta_v x^+ = 150$ (0.23δ) and $\Delta_v x^+ = 100 - 200$ streamwise separations for vortices near the event location.

When the estimated velocity fields are computed with event location at $y/\delta = 0.15$ (figure 3.14), a secondary inner packet configuration is revealed. It seems that subpackets of hairpin eddies exist within a same packet. This has been observed by Lee and Sung (2009) and Christensen and Adrian (2001) who suggest that the separation distance between vortices within a subpacket scales with inner variables whereas the separation between subpackets scales with outer variables. Moreover, it can be seen that the separation between eddies of the outer subpacket is greater than that of the near wall subpacket. These observations have also been noticed for the FPG, ZPG and APG cases with reference points at $y/\delta = 0.1$ and up to $y/\delta = 0.3$, but not at every wall-normal positions. Moreover it seems to vanish as the event locations are taken higher in the boundary layer.

Figure 3.15 shows the conditionally averaged velocity vector field based on the event $\lambda_{ci} < 0$ for all pressure gradient cases in planes (x, z) parallel to the wall around $y/\delta \simeq 0.10 - 0.16$. A clockwise vortex is visible at the event location $(x/\delta, z/\delta) = (0, 0)$, which indicates the presence of a vortical motion spinning positively along the wall-normal direction. Moreover, a second vortex spinning in the opposite direction is present approximately in the same transverse plane as the main vortex and a low-speed region $u' < 0$ is visible between the vortices. These velocity field characteristics are the signature, in the streamwise/transverse plane, of a hairpin-like structures, the two counter-rotating vortices corresponding to the imprints of the legs of the hairpin structure. Since the event has been chosen so that $\lambda_{ci} < 0$, the main vortex (at the event location indicated by the big circle) is the left leg of the hairpin and the secondary vortex (small circle) is the right leg of the vortex. The plain lines on figure 3.15 indicate the loci of zero velocity $u' = 0$. As for the linear stochastic estimated velocity fields in the streamwise/wall-normal plane (x, y) , these lines correspond to the locations of the hairpin vortices legs. Therefore, this provides evidence of the hairpin-packets average organization in the (x, z) plane. Looking at other planes, it can be noticed that the distance between the two $u' = 0$ contours increases downstream of the event location (this is visible on figure 3.15(a)). The conclusion is then that a hairpin packet grows in the spanwise direction, i.e. hairpin vortices at the "end" of a packet have a bigger extent in the transverse direction compared to those located at the "beginning" of the same packet.

Estimated velocity fields similar to those presented in figure 3.15 have been computed for all

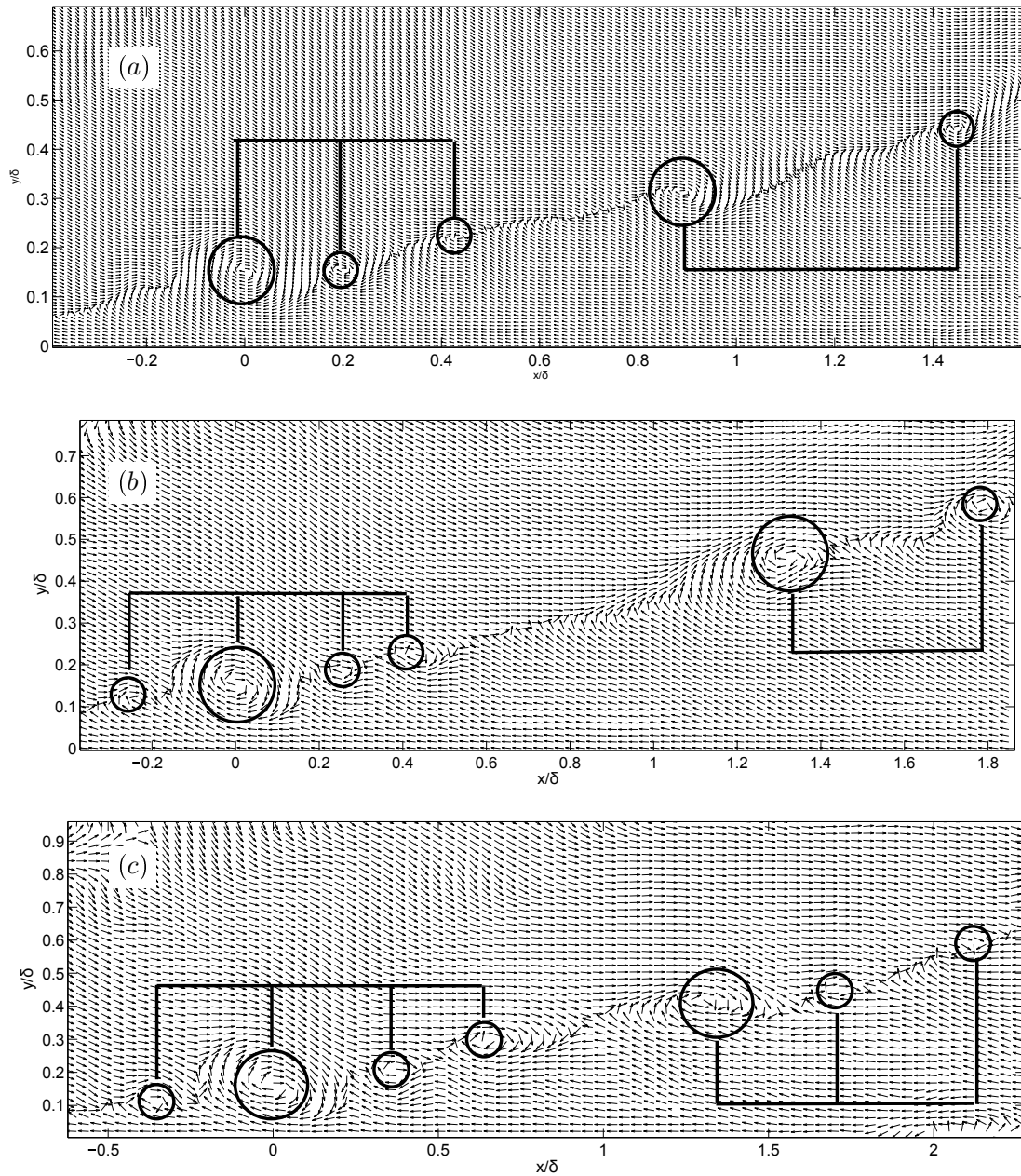


Figure 3.14 – Estimated velocity field using a negative swirling strength condition $\lambda_{ci} < 0$ for (a) APGs, (b) APGw and (c) ZPG configurations with reference point at $y/\delta = 0.15$ - Black circles indicate positions of prograde vortices. Horizontal lines are plotted to highlight hairpin structures within a same subpacket. Streamwise and wall-normal axes (x, y) are made non-dimensional using δ .

3.3. STATISTICAL ANALYSIS OF VELOCITY FIELDS

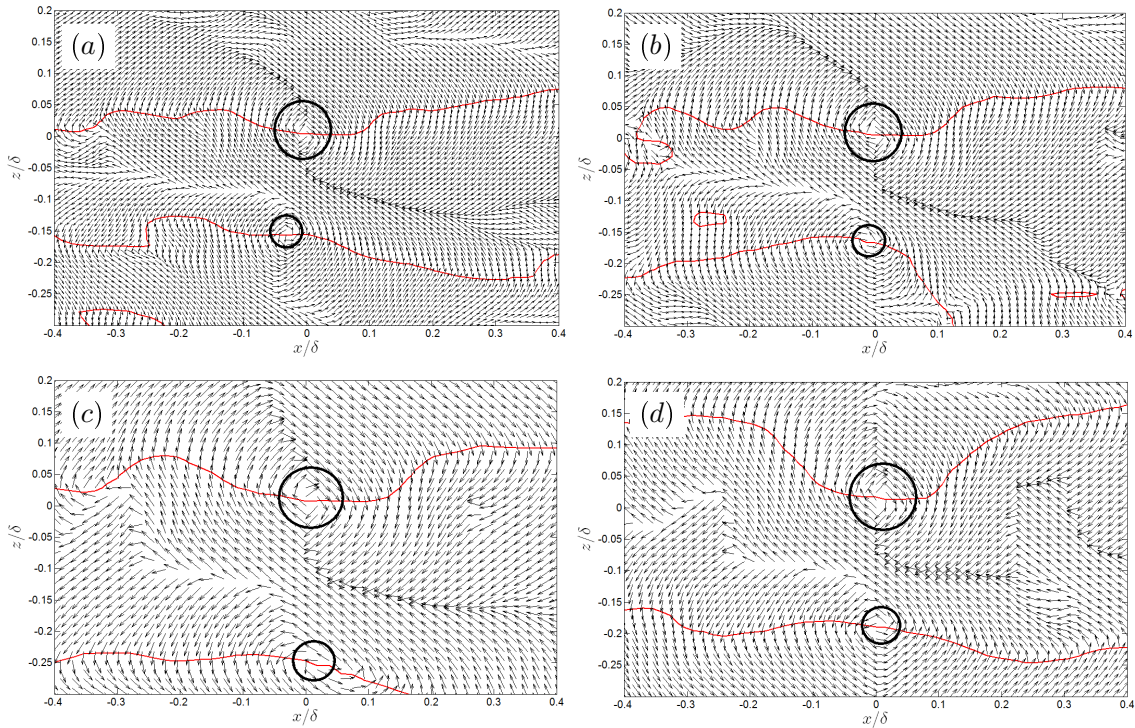


Figure 3.15 – Estimated velocity field in the streamwise/spanwise (x, z) plane using a negative swirling strength condition $\lambda_{ci} < 0$ for the (a) APGs $y/\delta = 0.10$, (b) APGw $y/\delta = 0.11$, (c) ZPG $y/\delta = 0.16$ and (d) FPG $y/\delta = 0.14$ - Circles indicate positions of vortices (biggest circle indicates vortex at the reference point) - Red line is the loci of $\bar{u} = 0$.

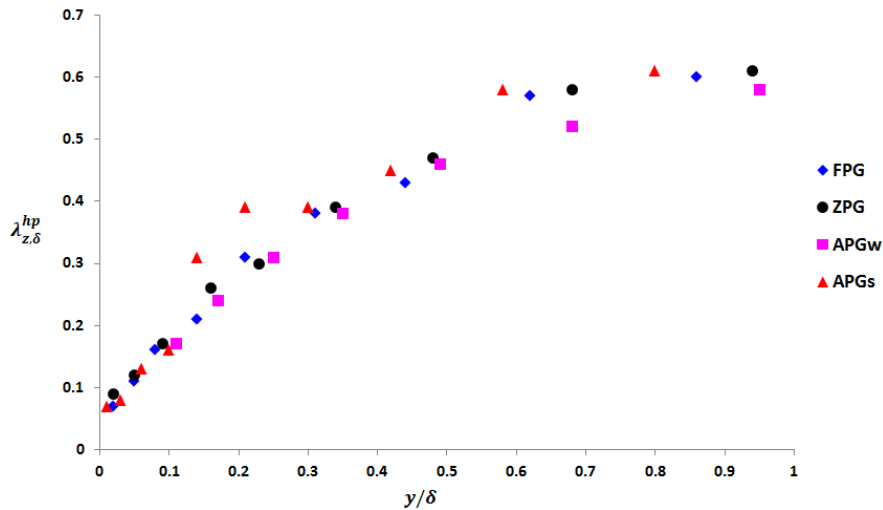


Figure 3.16 – Spanwise separation of hairpin vortices legs $\lambda_{z,\delta}^{hp}$ with respect to wall-normal distance.

pressure gradients and for the 11 wall-parallel planes available, except for the APGw case where some issues occurred on the first 4 planes closest to the wall. Based, on these velocity fields the average spanwise separation of hairpin legs $\lambda_{z,\delta}^{hp}$, i.e. hairpin spanwise length-scale could be measured. This result is shown in figure 3.16. The hairpin size increases when moving away from the wall, according to the attached-eddies hypothesis by Townsend (1976b), which states that the coherent structures grow proportionally to their distance from the wall. This behaviour is explicitly observable later in section 3.3.4 where the linear stochastic estimation method is applied to the three dimensional database ZPG3D. Obviously, this growth is not linear and tends towards an asymptote since the size of the structures is limited by the thickness of the boundary layer. All pressure gradient cases show a similar evolution, even though a sudden increase is visible for the APGs between $0.1 < y/\delta < 0.3$. This can be correlated with the beginning of the secondary peak of turbulent intensities which appears for the adverse pressure gradient flows (see figure 2.6). Surprisingly, the APGw shows values very similar to the favorable and zero pressure gradient flows, and is even lower for some wall-normal distances. Finally, the $\lambda_{z,\delta}^{hp}$ values in the very outer region of the turbulent boundary layer have to be looked at carefully since hairpin packets are believed to be absent this far from the wall. This point will be detailed in the next section with the analysis of two-point correlations of the streamwise velocity.

3.3.2 Two-points correlations

The two-point correlation of the streamwise velocity u is defined as:

$$R_{uu} = \frac{\langle u'(\mathbf{x})u'(\mathbf{x} + \mathbf{r}) \rangle}{u_{rms}(\mathbf{x})u_{rms}(\mathbf{x} + \mathbf{r})} \quad (3.8)$$

where $\langle \cdot \rangle$ denotes both time average and spatial average over the spanwise direction. The R_{uu} correlations are plotted in figure 3.17 along with the estimated velocity fields from Figure 3.13 for the three pressure gradients with reference point located at $y/\delta = 0.2$. The first observation that can be made is that the correlation has an elliptical shape elongated in the streamwise direction with a certain angle to the wall following that of the vortex packet.

Tay et al. (2009) looked at the streamwise extent of the correlation when studying the effect of surface roughness on turbulent boundary layers subjected to pressure gradients with Reynolds numbers $Re_\theta = 914$ for the ZPG case and $Re_\theta = 2182$ for the APG (deceleration parameter $K = -4.45 \times 10^{-7}$ stronger than the LES computation presented here). Their results are compared with those of the LES computation along with measurements by Volino et al. (2007) in figure 3.18. It can be seen that the levels are within a range varying from 0.1 to 1.15. For the present LES, both FPG and ZPG results exhibit a maximum correlation length around $y/\delta = 0.7$ and around $y/\delta = 0.6$ for the APG flows, whereas results from Tay et al. (2009) show maximum at $y/\delta = 0.43$ for both ZPG and APG cases. Ganapathisubramani et al. (2005) performed PIV measurements on a ZPG turbulent boundary layer at $Re_\tau = 1100$ and observed an increase in the correlation length through the log region between $y^+ = 92$ and $y^+ = 150$ and then a decreasing trend in the outer region between $y/\delta = 0.2$ and $y/\delta = 0.5$. For the LES, the favorable gradient provides the highest amplitude variation between $Lx_{uu}/\delta = 0.4$ and $Lx_{uu}/\delta = 0.9$ whereas the APG configurations provide the lowest amplitude variations. The streamwise extent of the correlation Lx_{uu} is estimated by measuring the distance between the most upstream and most downstream points of the ellipse. One can also notice that the results are quite similar to each other for all cases up to $y/\delta = 0.3$. Beyond this position, the favorable case shows a different trend. Results between ZPG and both APG flows separate around $y/\delta = 0.7$. Finally, it can be seen that both APG cases are very close to each other, with slightly higher correlation lengths for the APGw configuration. The results from Volino et al.

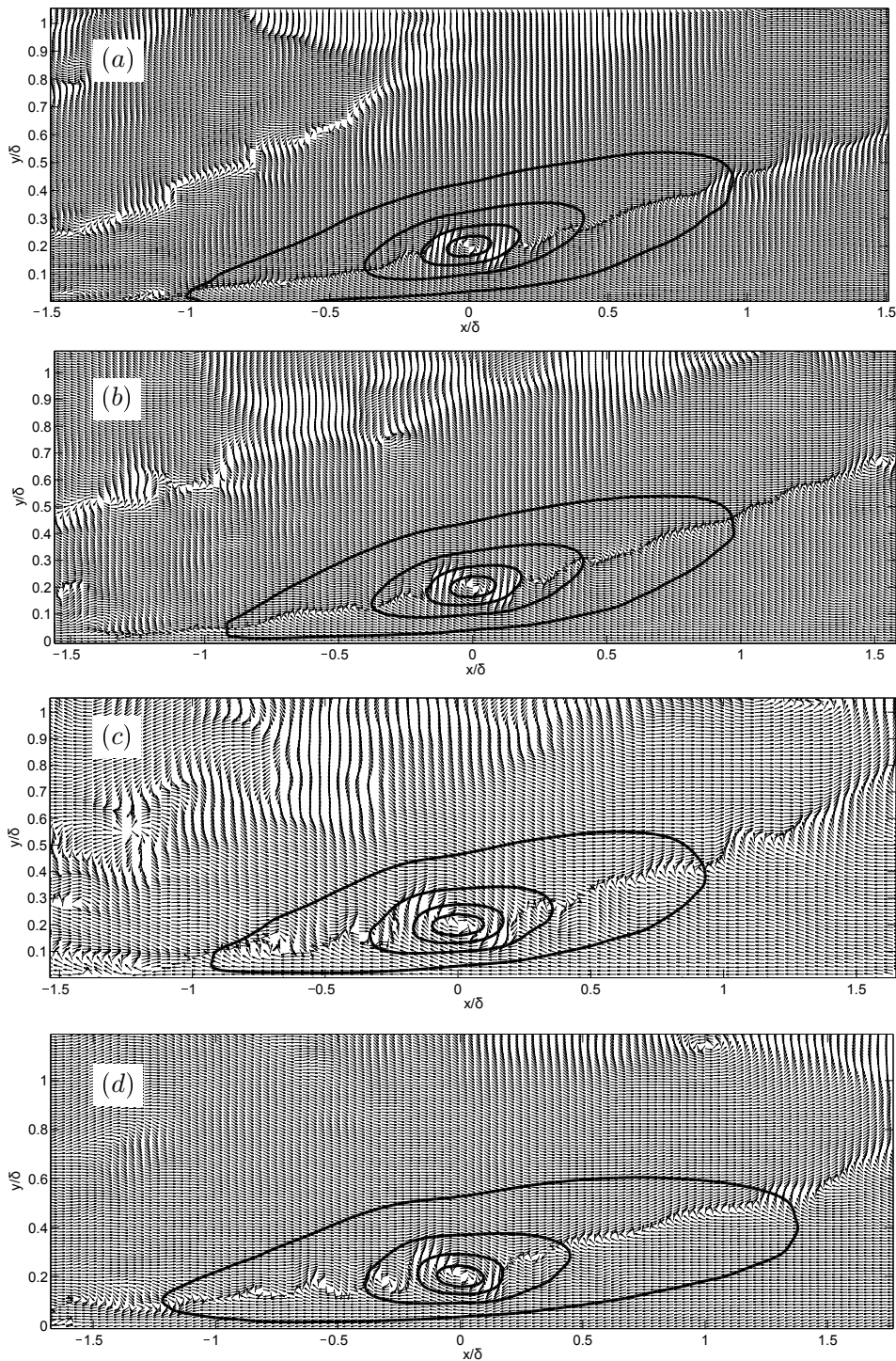


Figure 3.17 – Contours of R_{uu} correlation superimposed to estimated velocity field with reference point at $y/\delta = 0.2$ for the APGs (a), APGw (b), ZPG (c) and FPG (d) configurations - Contour levels range from 0.2 to 1.0 with a step of 0.2 - Streamwise and wall-normal axes (x, y) are made non-dimensional using δ .

(2007), who performed measurements in a water tunnel at $Re_\theta = 6069$, provide a more constant evolution between $Lx_{uu}/\delta = 0.6 - 0.7$.

When considering $R_{uu} = 0.6$ contour levels, the streamwise extent of the correlation is reduced by 20% to 36% compared to Lx_{uu} based on the $R_{uu} = 0.5$ contour. This value decreases as the reference point is located higher in boundary layer and the highest values correspond to the APG cases. Tay et al. (2009) observe a 50% reduction of the streamwise extent when doing so for the ZPG case.

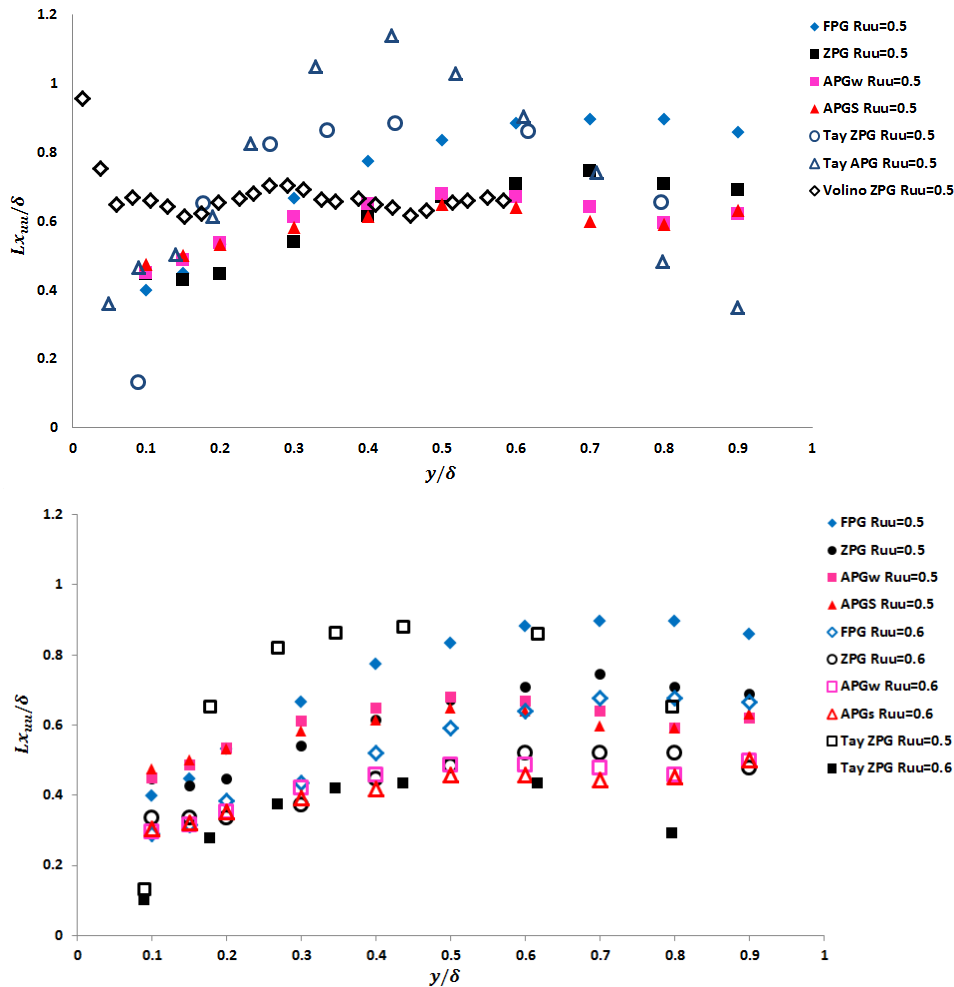


Figure 3.18 – Comparison of correlation R_{uu} streamwise extent Lx_{uu} - Based on $R_{uu} = 0.5$ contour level (top) and comparison between Lx_{uu} based on $R_{uu} = 0.5$ vs $R_{uu} = 0.6$ (bottom).

The elliptical shape of the correlation becomes more vague as the reference point is located higher in the boundary layer. This has also been observed by Tay et al. (2009) and Volino et al. (2007) who suggest that the reference point from which the correlation is calculated is above the hairpin packets producing the inclination (the LSE velocity fields also showed that the packet organization vanishes above a certain distance from the wall). This is shown in figure 3.19 where it can be seen that the elliptical shape vanishes at the upper limits of the outer region.

Figure 3.19 provides also an important information: the organization of hairpin-like eddies into packets remains higher in the boundary layer for the adverse pressure gradient cases. Indeed it can be seen that the correlation still follows a clear angle and an elliptical behaviour up to $y/\delta = 0.7$ for both APG cases, whereas these characteristics become unclear above $y/\delta = 0.6$ for

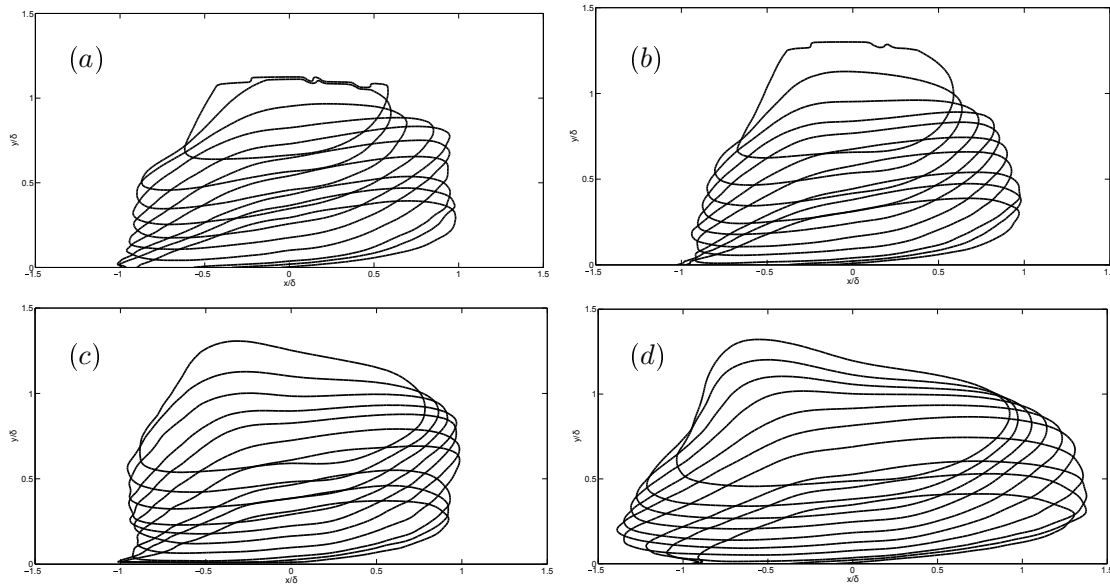


Figure 3.19 – Contours of $R_{uu} = 0.2$ correlation at all reference points $y/\delta = 0.1, 0.15, 0.2, 0.3, 0.4, 0.5, 0.6, 0.7, 0.8, 0.9$ for the APGs (a), APGw (b), ZPG (c) and FPG (d) configurations - Streamwise and wall-normal axes (x, y) are made non-dimensional using δ .

ZPG and FPG configurations. This result is consistent with what has been said in section 3.2.2 concerning large scale structures more likely to be present in the outer region when the flow is subjected to an adverse pressure gradient.

3.3.3 Angle of structures

Angle of hairpin packets

As it has also been mentioned, the correlation is aligned along the packet revealed by the conditional estimation (see figure 3.19), meaning that the correlation provides information on the hairpin packet angle, also referred to as the packet growth angle, given in figure 3.20. Before discussing the results, recall that the elliptical shape of the R_{uu} correlation vanishes far from the wall. Consequently it is more difficult to estimate the angle of the correlation for points near the edge of the boundary layer and therefore angles reported in figure 3.20 near the edge of the TBL should not be considered as growth angles.

The results from the LES show a clear hierarchy in levels depending on the pressure gradient: the favorable pressure gradient case provides the lowest angles whereas the adverse cases provide the highest levels through the entire boundary layer, with the strong adverse case APGs providing maximum values of the growth angle. It can also be seen that the evolution of the angles follows the same behaviour for the three pressure gradients with a maximum around $y/\delta = 0.4$ for the APG configurations and $y/\delta = 0.5$ for FPG and ZPG, whereas the results from Tay et al. (2009) exhibit a more "complex" evolution: indeed the ZPG case shows two maxima at $y/\delta = 0.08$ and $y/\delta = 0.61$ and the APG case shows a peak around $y/\delta = 0.26$. The results from the LES provide angles in the range $\alpha_p = [-2.1^\circ, 11.1^\circ]$ for FPG, $\alpha_p = [5.6^\circ, 14.5^\circ]$ for ZPG, $\alpha_p = [7.8^\circ, 18.6^\circ]$ for APGw and $\alpha_p = [9.6^\circ, 18.7^\circ]$ for APGs. The angles are estimated by measuring the angle of the line passing by the most upstream and most downstream points of the correlation $R_{uu} = 0.5$.

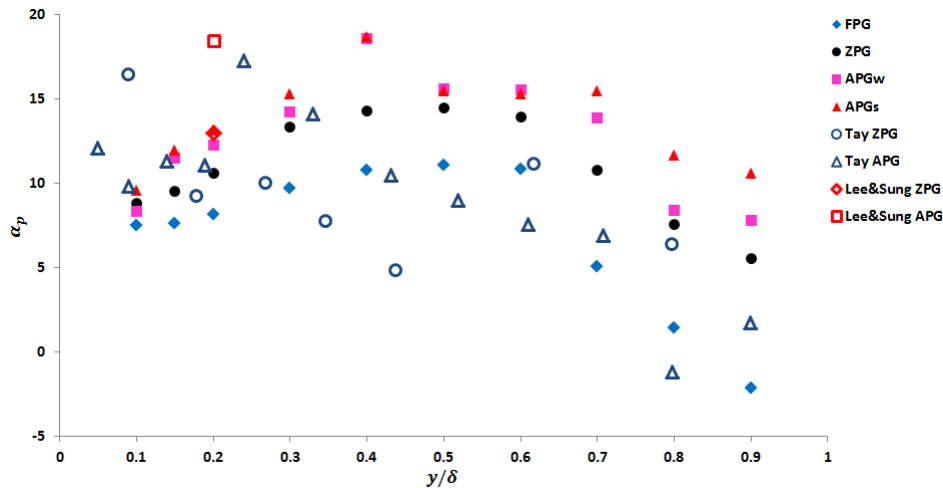


Figure 3.20 – Growth angle of hairpin packets given by the streamwise velocity correlation R_{uu} .

3.3.4 Statistical analysis of three-dimensional database

The linear stochastic estimation has been applied to the 3D zero pressure gradient database. In figure 3.21, the event $\lambda_{ci}^{xy} < 0$ is located at $y/\delta = 0.2$ and corresponds to a prograde vortex. Here, λ_{ci}^{xy} corresponds to the swirling strength based on the 2D velocity gradient tensor in the streamwise/wall-normal (x, y) plane. It is important to consider only the two-dimensional tensor in order to define the prograde vortex condition, even though it is a 3D velocity field. In other words, the 3D velocity field is estimated based on a 2D condition. The result provides a hairpin-like structure laying over a region of low momentum, with legs, neck and head clearly distinguishable. At this point, it is important recalling that this is a rather low Reynolds number turbulent boundary layer ($Re_\theta = 1500$). Therefore the shape of the estimated structures is a hairpin/horseshoe, rather than asymmetric cane-shaped structures which are abundant in higher Reynolds number flows. From a sideview of the estimated hairpin-like vortex, one can evaluate the leg angle $\alpha_l = 8.3^\circ$, the neck angle $\alpha_l = 50.7^\circ$ and the average hairpin angle $\alpha_{hp} = 20.9^\circ$. Figure 3.22 shows the corresponding velocity vector field in the (x, y) and (x, z) planes. In the side view 3.22(a), a strong hairpin head is visible surrounded by an upstream and a downstream vortex, which are the heads of the two secondary vortices shown in the 3D representation in figure 3.21. In the top view 3.22(b), two counter-rotating vortices are located slightly upstream of the hairpin head, and are the signature of the legs of the main hairpin structure. A clockwise rotating vortex (indicated by the small circle) is visible downstream of the reference point and corresponds to the left leg of the downstream secondary hairpin structure shown in the 3D representation (the λ_{ci} of the right leg as well as that of the upstream secondary hairpin legs are too low to be visible here).

A secondary hairpin vortex is visible downstream and the head of an upstream hairpin vortex is also distinguishable. Therefore, as for the 2D estimated velocity fields, the hairpin packet organization is retrieved here. The secondary vortices become less and less visible as the event location is taken further from the wall. This has been observed by Dennis and Nickels (2011) and is illustrated in figure 3.23. In this figure, event locations span wall-normal distances $0.2 < y/\delta < 0.9$ with a step of 0.1. The streamwise position of the event has no significance on the figure: it is simply translated towards higher streamwise positions in order to make the vortices distinguishable one from another. The first structure on the left ($y/\delta = 0.2$, green) exhibits a secondary vortex located downstream of the main one, as shown in figure 3.21, and this is the only structure showing this feature. As the reference point goes up, the leg/neck

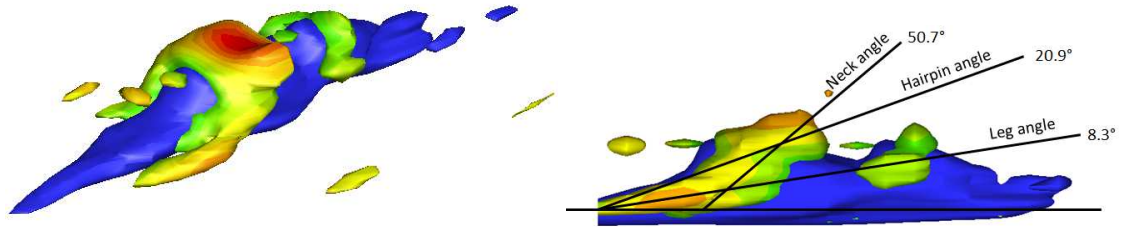


Figure 3.21 – Linear stochastic estimation of 3D velocity field reveals hairpin-like structure over a low momentum region - Isosurfaces of λ_{ci} colored with u' and isosurface of negative fluctuating velocity u' (blue) - condition location is $y/\delta = 0.2$.

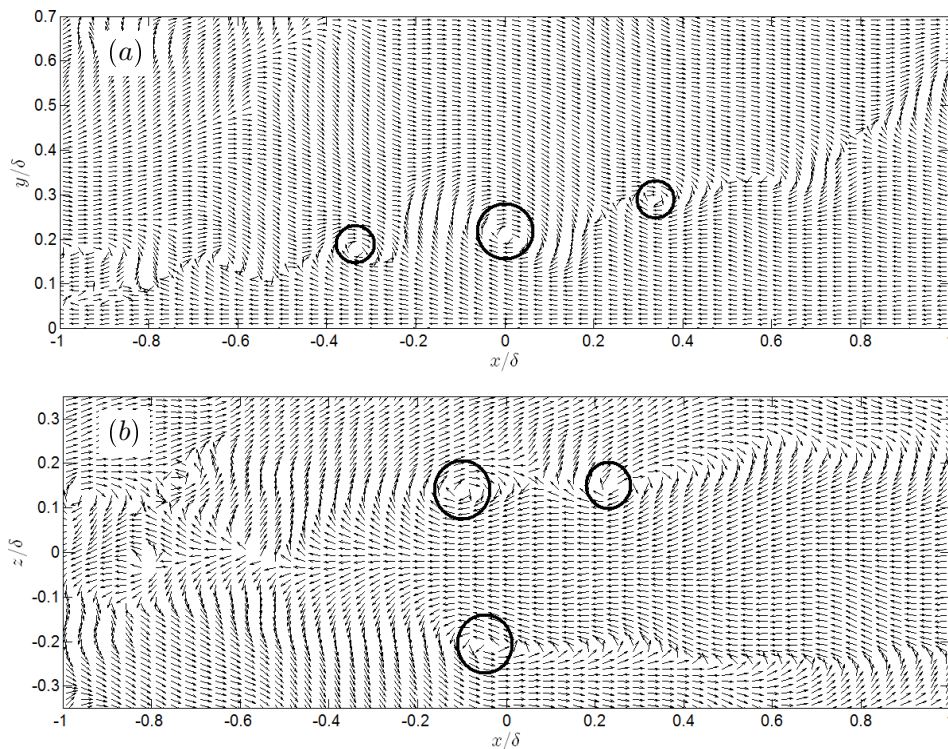


Figure 3.22 – Vector field of estimated velocity field shown in figure 3.21 in (a) the streamwise/wall-normal plane and (b) the streamwise/spanwise plane. Condition location is $y/\delta = 0.2$, big circles indicate vortices corresponding to the main hairpin structure and the small circles to the secondary structures.

geometry tends to vanish and the leg angle seems to increase. From this point, two options can be proposed:

- The hairpin-structures far from the wall are generated in the near wall region. As they are convected downstream, they rise away from the wall with a neck/leg geometry. Since the legs are bounded by the wall, their angle is much lower than that of the neck. At some point, the head of the hairpin is located so high in the boundary layer that the legs lift up from the wall. Since there is no limit beneath them anymore, the neck disappears.
- The hairpin-structures far from the wall are generated directly in the outer layer where the heads are so far from the wall that legs are free to develop without limitation from the wall. Under this hypothesis, the hairpin vortices do not develop the neck/leg geometry.

The front view (bottom figure) confirms that the structures have a larger transverse size the further they are located from the wall. The hairpin-structure for even at $y/\delta = 0.7$ is 1.5 times larger than that for event at $y/\delta = 0.2$. Very far from the wall, prograde vortex events located at $y/\delta = 0.8$ and $y/\delta = 0.9$ still generate hairpin-like structures but with very short legs and a rather asymmetric geometry (left leg is more developed than the right one). This suggests that even though hairpin packets are not likely to be found near the edge of the boundary layer (see two-points correlation analyses in section 3.3.2), individual hairpin vortices are still present. This is consistent with the typical eddy model by Falco (1977) and the hairpin vortex tips by Head and Bandyopadhyay (1981) observed at the upstream side of the large scale bulges.

In the 3D visualization, even though the threshold $|\lambda_{ci}| > 1.5\lambda_{ci}^{rms}$ was used, still a lot of background noise remained for the swirling strength field. In order to enhance the visualization of the coherent structures, a linear stochastic estimation (LSE) was performed based on the normalized velocity field $\mathbf{u}/\|\mathbf{u}\|$. The result is compared to the "regular" LSE in figure 3.24. It was observed that the normalized version of the LSE does not reduce the background noise but provides a finer resolution for the vortex motions. Therefore, this method might be more adequate to measure the angle of the structures for instance, however the angles remain the same compared to the classical LSE method.

Finally, the conditionally averaged velocity field was viewed in a transverse plane (y, z). In figure 3.25, a pair of counter-rotating vortices spinning "inwards" are clearly visible downstream and above the head of hairpin-like structure located at $y/\delta = 0.3$. This feature has also been observed for other wall-normal distance in the outer region of the boundary layer. By changing the value of the isosurface level λ_{ci} , an "inverse hairpin" was revealed, even though it is not sure whether the head of this structure exists or not. On the right view of figure 3.25, the two inward counter-rotating vortices seem to merge to form a head. The fact that this head is nearly visible can be simply explained by the fact that most of the swirling strength is concentrated around the event chosen for the estimation, i.e the main hairpin structure. It is then assumed that this inverse hairpin, with opposite spinning motions than that of the classical hairpin structure is a consequence of the conservation of local circulation in the flow.

The inverse hairpin lays at angle to the wall estimated between 30° and 40° . A model for the generation of such a structure is proposed in figure 3.26. In this concept, an inverse hairpin can exist only in presence of at least two streamwise aligned hairpin vortices (hairpins within a same packet for instance). The heads of both hairpins are rotating in the same direction, therefore they induce inverse vorticity in between them, which forms the head of the inverse hairpin. The head of the upstream hairpin generates a sweep event ($u' > 0, v' < 0$) whereas the legs and neck of the downstream hairpin generate an ejection ($u' > 0, v' > 0$). Since the downstream hairpin is larger than the upstream one (based on the analyses of LSE velocity field in wall-parallel planes, figure 3.15), the collision between sweep and ejection leads to the two inward-spinning quasi-streamwise vortices.

3.3. STATISTICAL ANALYSIS OF VELOCITY FIELDS

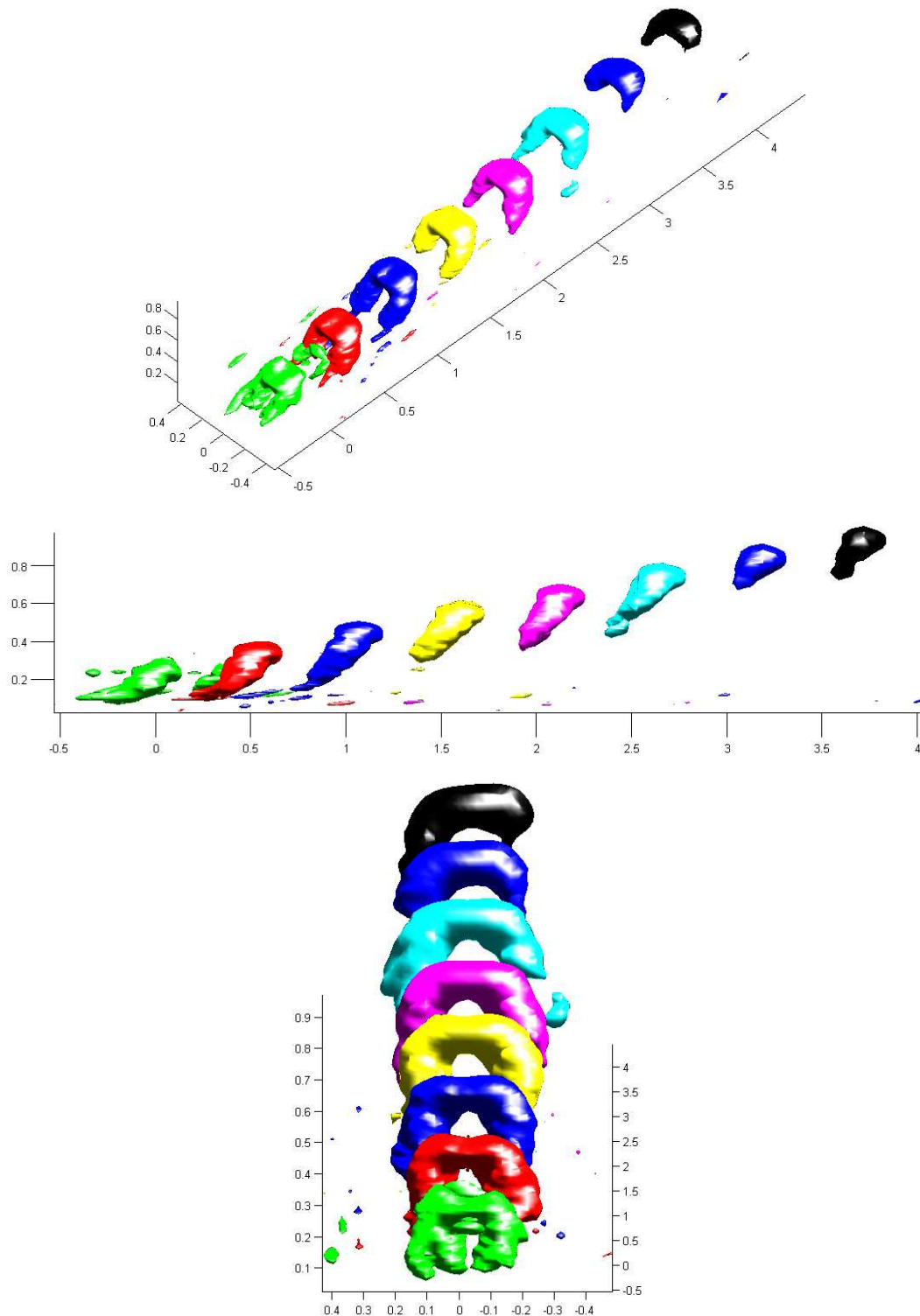


Figure 3.23 – Linear stochastic estimation of 3D velocity field with events locations between $0.2 < y/\delta < 0.9$ with a step of 0.1 - axes are made non-dimensional using δ .

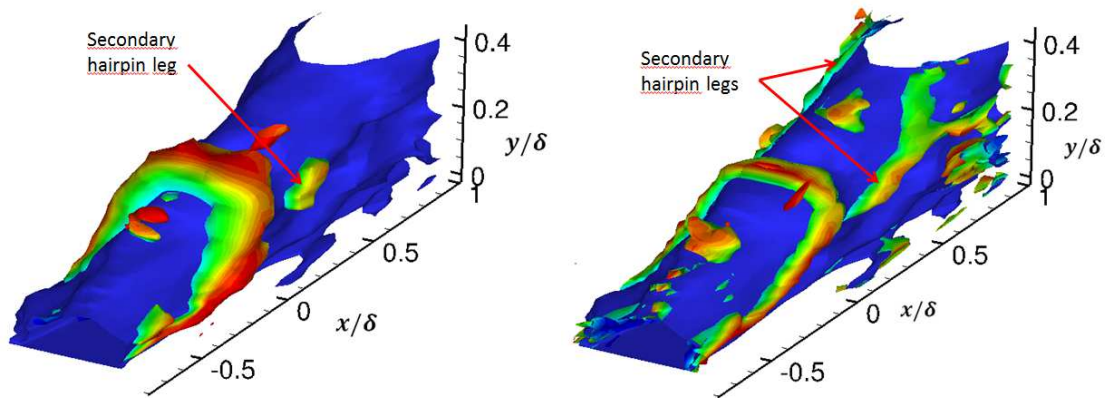


Figure 3.24 – Linear stochastic estimation of 3D velocity field with event located at $y/\delta = 0.3$ - Estimation based on (left) velocity field \mathbf{u} and (right) normalized velocity field $\mathbf{u}/\|\mathbf{u}\|$ - Isocontours of swirling strength λ_{ci} colored with streamwise velocity and negative streamwise velocity $u' < 0$.

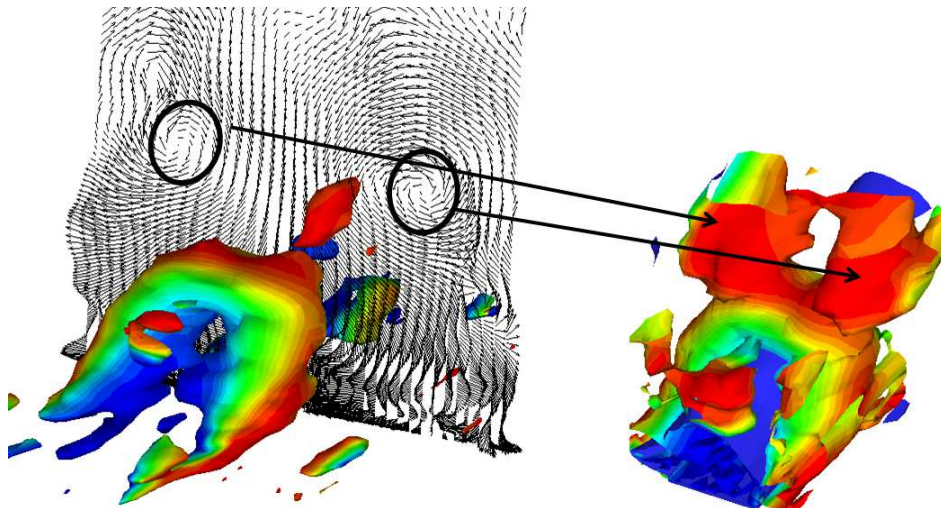


Figure 3.25 – Linear stochastic estimation of 3D velocity field with event located at $y/\delta = 0.3$ - Velocity vector field in plane (y, z) shows two counter-rotating vortices downstream and above main hairpin structure - Isocontours of λ_{ci} are different between left and right representations.

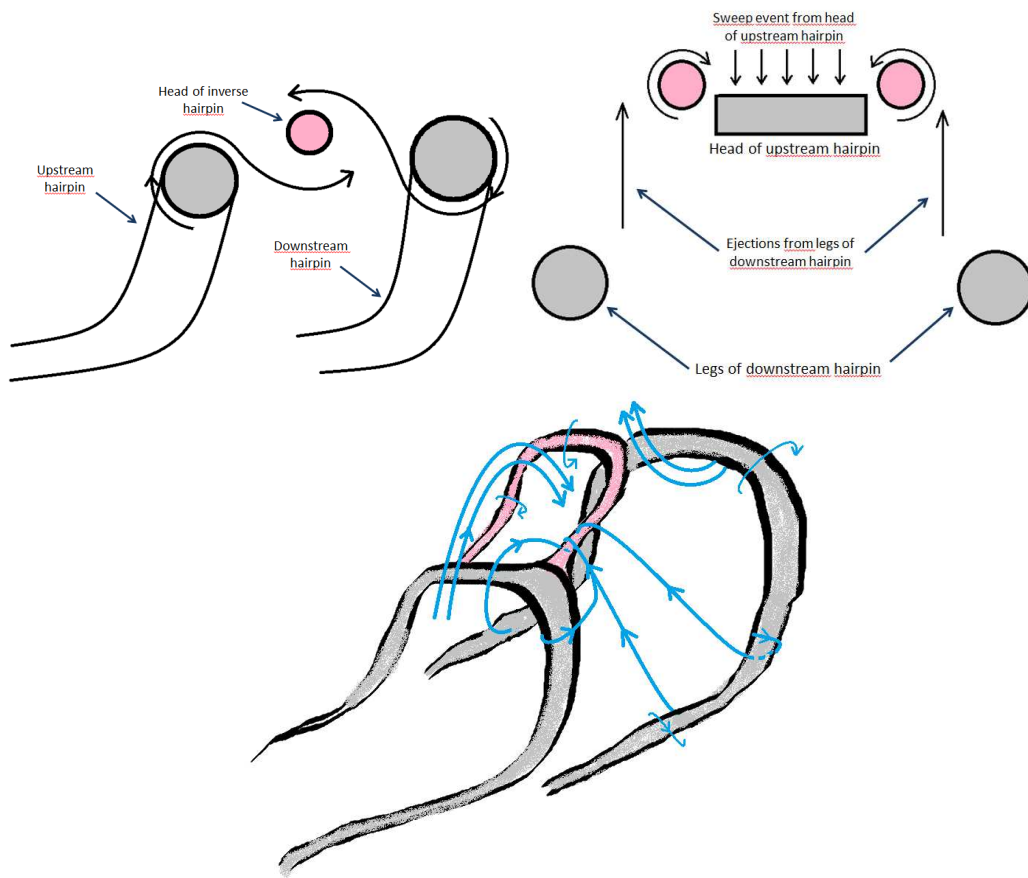


Figure 3.26 – Conceptual model for the generation of the inverse hairpin structure - side, front and 3D views.

Chapter 4

A stochastic model for wall-pressure spectrum

4.1 Definition of the model

4.1.1 Ahn's horseshoe model

Model's principle

Ahn et al. (2010) hairpin model is chosen as base model for this study. Hairpin vortices are represented by rectangular horseshoes at an angle of 45° to the wall (for the results presented in this chapter, the angle of the structure is 45° if nothing is mentioned). The hairpin legs and head have respective lengths L and λ and are modeled by a cylinder with a uniform vorticity distribution $\boldsymbol{\omega} = \Gamma/\pi r_c^2 \mathbf{e}_l$ along its axis, where Γ is the corresponding circulation as shown in Figure 4.1.

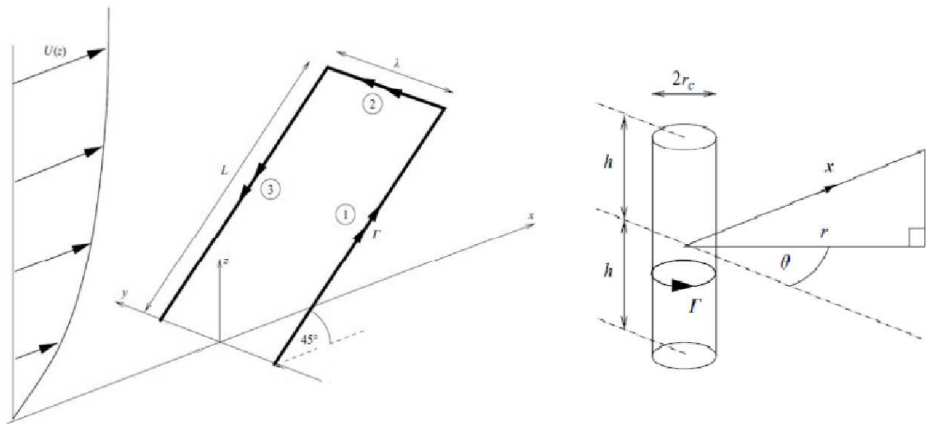


Figure 4.1 – Ahn's horseshoe-vortex representation. Each straight-line element has a constant circulation Γ and is modeled by a cylinder - after Ahn et al. (2010).

Figure 4.2 shows the steps to obtain the wall-pressure field. First the velocity field is calculated using a Biot-Savart integral, then the pressure field is obtained through a Poisson's equation.

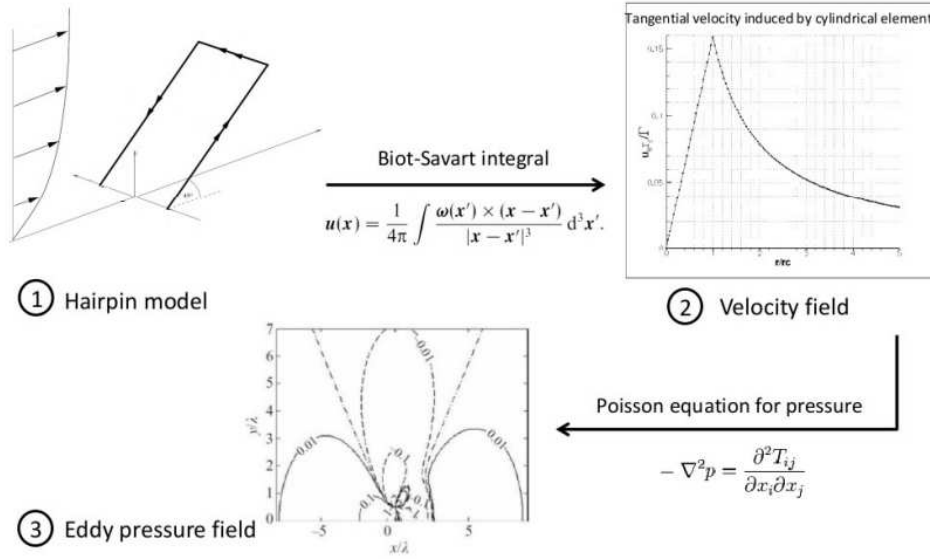


Figure 4.2 – Methodology to obtain the eddy pressure field - Figure 3 is extracted from Ahn et al. (2010).

Induced velocity field

The coordinate system is $\mathbf{x} = (x, y, z)$ and the components of the overall velocity field are $(U + u, v, w)$, where U is the mean streamwise velocity. The velocity field $\mathbf{u} = (u, v, w)$ induced by a horseshoe eddy is obtained from the vorticity field $\boldsymbol{\omega}$ using the Biot-Savart integral defined as:

$$\mathbf{u}(\mathbf{x}) = \frac{1}{4\pi} \int \frac{\boldsymbol{\omega}(\mathbf{x}') \times (\mathbf{x} - \mathbf{x}')}{|\mathbf{x} - \mathbf{x}'|^3} d^3\mathbf{x}' \quad (4.1)$$

The computation of such an integral is not straightforward since it is singular at the corners of the hairpin. Therefore, each linear element of the eddy is modeled using a method based on the exact two-dimensional Rankine vortex field given by:

$$\mathbf{u}_{2D} = \frac{\Gamma \mathbf{e}_\theta}{2\pi} \frac{r}{\max(r^2, r_c^2)} \quad (4.2)$$

where r is the radial coordinate in the cylindrical base ($\mathbf{e}_r, \mathbf{e}_\theta, \mathbf{e}_l$) and r_c is the vortex radius (see Figure 4.1). This expression is combined with a line element of length h as in Ahn et al. (2010) leading to the following expression of the 2D velocity field induced by a cylinder vortex:

$$\mathbf{u}(\mathbf{x}) = \frac{\mathbf{u}_{2D}}{2} \left[\frac{h-l}{\sqrt{(h-l)^2 + \max(r^2, r_c^2)}} + \frac{h+l}{\sqrt{(h+l)^2 + \max(r^2, r_c^2)}} \right] \quad (4.3)$$

where parameters h, l and r are introduced in figure 4.1. Ahn et al. (2010) calculate the induced velocity field for a cylinder aligned with the streamwise direction and adds a wall-normal velocity based on the fact that the eddies form an angle of 45° to the wall. In the present work, the induced velocity field is directly computed within the frame linked to the inclined eddy, so that the angle of the hairpins can be modified. To do so, distances r and l need to be calculated in the reference frame related to the hairpin structure as shown in figure 4.3, defined by:

$$\begin{pmatrix} x_{hp} \\ y_{hp} \\ z \end{pmatrix} = \begin{pmatrix} \cos(\alpha_{hp}) & \sin(\alpha_{hp}) & 0 \\ -\sin(\alpha_{hp}) & \cos(\alpha_{hp}) & 0 \\ 0 & 0 & 1 \end{pmatrix} \begin{pmatrix} x \\ y \\ z \end{pmatrix} + \overrightarrow{OO_{hp}} \quad (4.4)$$

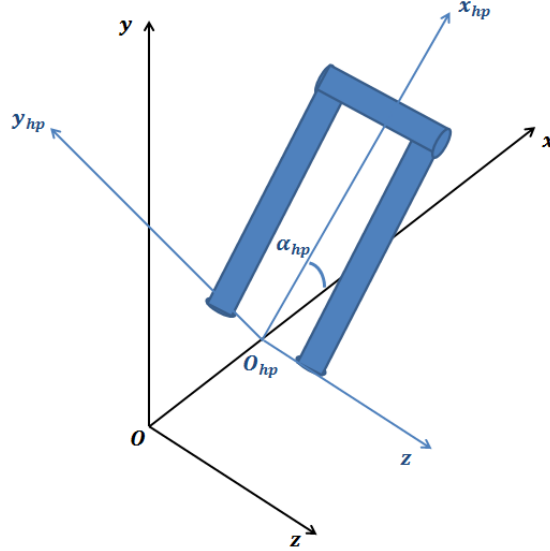


Figure 4.3 – Definition of local coordinate system attached to the hairpin structure. .

Once the velocity has been computed in this frame, it needs to be written in the original coordinate system aligned with the mean flow for the two legs of the hairpin vortex:

$$\begin{pmatrix} u \\ v \\ w \end{pmatrix} = \begin{pmatrix} U \\ 0 \\ 0 \end{pmatrix} + \begin{pmatrix} \cos(\alpha_{hp}) & -\sin(\alpha_{hp}) & 0 \\ \sin(\alpha_{hp}) & \cos(\alpha_{hp}) & 0 \\ 0 & 0 & 1 \end{pmatrix} \begin{pmatrix} u_{leg} \\ v_{leg} \\ w_{leg} \end{pmatrix} + \begin{pmatrix} u_{head} \\ v_{head} \\ w_{head} \end{pmatrix} \quad (4.5)$$

The velocity induced by the hairpin ($u_{leg}, v_{leg}, w_{leg}$) and ($u_{head}, v_{head}, w_{head}$) are calculated in the frame attached to the structure, so that $u_{leg} = 0$ and $w_{head} = 0$. Figure 4.4 shows the streamlines around a single hairpin-like structure subjected to a uniform mean flow. Since the legs of a hairpin are rotating outwards, the flow is accelerated around the eddy and decelerated between its legs. It is worth noting at this point that unlike the model from Ahn et al. (2010), the mirror image of the horseshoe vortex is not considered. The idea here is to use a hairpin-like vortex to provide a basic form of the wavenumber spectrum.

This preliminary calculation with a uniform mean flow has been undergone to verify that the velocity field induced by a single hairpin-like vortex is correctly computed.

Mean flow profile

There are several ways to introduce the mean velocity profile. One can retrieve profiles from LES or RANS computations and use these data as input for the eddy-based model. The most convenient way however (for industrialization and parametric study) is to work with analytical mean velocity models from the literature. Therefore, a composite profile that consists of Reichardt (1951) inner layer profile and Fernholz and Finley (1980) wake function given by equation (4.6) was implemented:

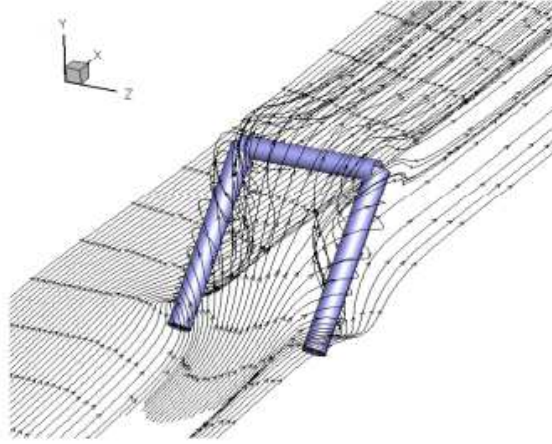


Figure 4.4 – Streamlines around a single hairpin in a uniform streamwise mean flow.

$$\frac{U}{u_\tau} = \frac{1}{\kappa} \ln \left(1 + \kappa \frac{yu_\tau}{\nu_w} \right) + C_1 \left[1 - e^{-yu_\tau/(\eta_1 \nu_w)} - \left(\frac{yu_\tau}{\eta_1 \nu_w} \right) e^{-yu_\tau/(\eta_1 \nu_w)} \right] + \frac{1}{\kappa} \left[\left(\frac{y}{\delta} \right)^2 - \left(\frac{y}{\delta} \right)^3 + 6\Pi \left(\frac{y}{\delta} \right)^2 - 4\Pi \left(\frac{y}{\delta} \right)^3 \right] \quad (4.6)$$

with

$$C_1 = \frac{-1}{\kappa} \ln(\kappa) + C$$

where Π is the wake parameter, κ the von Kármán constant and δ the TBL thickness. To evaluate the wake parameter Π according to the pressure gradient, three possibilities exist:

- by curve-fitting the wake-law to a mean velocity profile obtained from numerical computations or measurement data
- by solving the equation proposed by Coles (1956):

$$2\Pi - \ln(1 + \Pi) = \kappa \frac{U_e}{u_\tau} - \ln \left(\frac{\delta^* U_e}{\nu} \right) - \kappa C - \ln \kappa \quad (4.7)$$

where $C = 5.1$ is Coles (1956) notation for the logarithmic law constant.

- by using the following empirical formula proposed by Durbin and Reif (2002):

$$\Pi = 0.8(\beta_C + 0.5)^{3/4} \quad (4.8)$$

In order to know if the choice of the mean velocity profile has no influence on the final result, a second profile was tested. The inner part of the boundary layer profile was computed using Musker (1979) law given by:

$$U_{inner}^+ = 5.424 \tan^{-1} \left[\frac{(2y^+ - 8.15)}{16.7} \right] + \log_{10} \left[\frac{(y^+ + 10.6)^{9.6}}{(y^{+2} - 8.15y^+ + 86)^2} \right] - 3.52 \quad (4.9)$$

and the wake region was modeled using Coles (1956) law:

$$W(\eta) = \sin^2\left(\frac{\eta\pi}{2}\right) \quad (4.10)$$

leading to the overall mean velocity profile given by:

$$U^+ = U_{inner}^+ + \frac{2\Pi}{\kappa} W\left(\frac{y}{\delta}\right) \quad (4.11)$$

No difference was observed on the wall-pressure spectra induced using both velocity profiles and the Reichardt-Fernholz-Finley model was retained.

Pressure field

The equation governing the pressure is obtained by taking the divergence of the Navier-Stokes equations for incompressible flow. Under the assumption that the mean shear dominates as postulated by Townsend (1976b), the source term in the Poisson equation can be linearized:

$$\nabla^2 p = -2\rho \frac{dU}{dy} \frac{\partial v}{\partial x} \quad (4.12)$$

The Green's function approach is used to find the solution for the wall-pressure, leading to:

$$p(\mathbf{x}) = -2\rho \int_{y'>0} G(\mathbf{x}'; \mathbf{x}) \frac{dU(y')}{dy'} \frac{\partial v(\mathbf{x}')}{\partial x'} d^3 \mathbf{x}' \quad (4.13)$$

with $G(\mathbf{x}'; \mathbf{x})$ being the Green's function defined by:

$$G(\mathbf{x}'; \mathbf{x}) = -\frac{1}{4\pi} \left(\frac{1}{|\mathbf{x}' - \mathbf{x}|} + \frac{1}{|\mathbf{x}' - \mathbf{x}_l|} \right) \quad (4.14)$$

where $\mathbf{x}_l = (x, -y, z)$ is the image of \mathbf{x} associated with the wall plane. By restricting the calculation only to points on the wall located at \mathbf{x}_w , integrating equation (4.13) by part gives the final expression of the wall-pressure field:

$$p(\mathbf{x}_w) = \frac{\rho}{\pi} \int_{y'>0} \frac{x' - x_w}{|\mathbf{x}' - \mathbf{x}_w|^3} \frac{dU(y')}{dy'} v(\mathbf{x}') d^3 \mathbf{x}' \quad (4.15)$$

For more details on the procedure to obtain equation (4.15), one can refer to Ahn et al. (2010). The results presented hereafter then correspond to the non-dimensional wall-pressure field $\tilde{p}(\mathbf{x}_w)$ given by:

$$\tilde{p}(\mathbf{x}_w) = \frac{p(\mathbf{x}_w)}{\frac{1}{2}\rho u_\tau \Gamma} \quad (4.16)$$

where u_τ is the friction velocity, Γ the eddy circulation and λ the width of an eddy.

The objective is to build a model for the spectrum of surface-pressure fluctuations. The wavenumber spectrum is given by the scale integral:

$$S(k_x, k_z) = \int_{\lambda_{min}}^{\lambda_{max}} n_e(\lambda) \tilde{P}(k_x, k_z, \lambda) \tilde{P}^*(k_x, k_z, \lambda) d\lambda \quad (4.17)$$

with $\tilde{P}(k_x, k_z, \lambda)$ being the Fourier transform of the pressure field induced by the eddy having a breadth λ , which determines its lengthscale, and $\tilde{P}^*(k_x, k_z, \lambda)$ is complex conjugate. λ_{min} and λ_{max} are the lengthscales of the smallest and largest hairpin eddy. The function $n_e(\lambda)$ is the density number such as the number of eddies in the size range $\lambda_1 < \lambda < \lambda_2$ is $\int_{\lambda_1}^{\lambda_2} n_e(\lambda) d\lambda$

4.1. DEFINITION OF THE MODEL

per unit of wall area. Ahn et al. (2010) determine the expression of this function using circulation conservation and the shape of the velocity profile in the logarithmic region. The final wavenumber spectrum (non-dimensional) is given by:

$$S(k_x, k_z) = \int_{\lambda_{min}}^{\lambda_{max}} \lambda |\tilde{P}(k_x \lambda, k_z \lambda)|^2 d\lambda \quad (4.18)$$

For more details on this procedure, refer to Ahn et al. (2010). In the absence of self-similarity of the eddies, this integral needs to be evaluated for every value of lengthscale λ , through the entire thickness of the boundary layer, which is numerically very costly. Therefore, the boundary layer is divided into six sublayers within which the pressure spectrum can be considered quasi-universal. This way, only six velocity fields induced by hairpin vortices having their heads in the middle of each sublayer need to be computed. The lower limit of the near-wall sublayer is chosen so that it matches the beginning of the logarithmic region $y^+ = 30$. For the upper limit, Ahn et al. (2010) chose $y/\delta = 0.4$ based on the fact that experiments by Hutchins et al. (2005) and Hambleton et al. (2006) support that above this distance the structures are detached, whereas here, only attached eddies are considered. Moreover, the largest observed convection velocities correspond to the mean velocity at about 0.4δ .

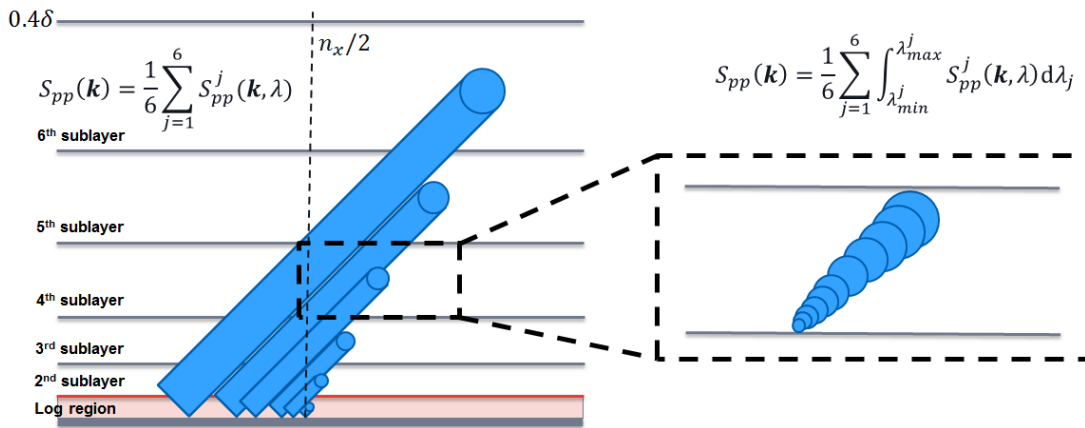


Figure 4.5 – Scheme of the integration of the wavenumber spectrum method through each sublayer to model a continuous distribution of hairpin eddies.

By summing the six spectra from the six sublayers, one obtains a wavenumber spectrum with interference lobes in the spanwise direction. These are the consequence of the spacing between the legs of the hairpins of discrete sizes. Therefore, for each sublayer, the corresponding spectrum is interpolated over the entire range of eddy lengthscales within that sublayer in order to take into account a continuous distribution of horseshoe structures (this procedure is illustrated in figure 4.5). By doing so, the interference lobes are smoothed as shown in figure 4.6 where the (k_x, k_z) is plotted for the lowest sublayer which corresponds to the logarithmic region. In this figure, and for the rest of the manuscript, the calculated spectrum is not the raw spectrum provided by equation 4.18 as this provides a wavenumber spectrum which is not continuous around $k_x = 0$ (see figures 6 and 8 in Ahn et al. (2010)). As the wall-pressure model described here will be implemented for fluid-structure coupling, the wavenumber spectrum is made continuous by "shifting" the spectrum peak to $k_x = 0$.

The outer region of the boundary layer is divided into 5 regions. Following Ahn et al. (2010), the spacing for these regions follows an exponential law so that their boundaries are set to $y/\delta = 0.1, 0.132, 0.174, 0.230, 0.303$ and 0.4 . As a reminder, the lower limit of the first

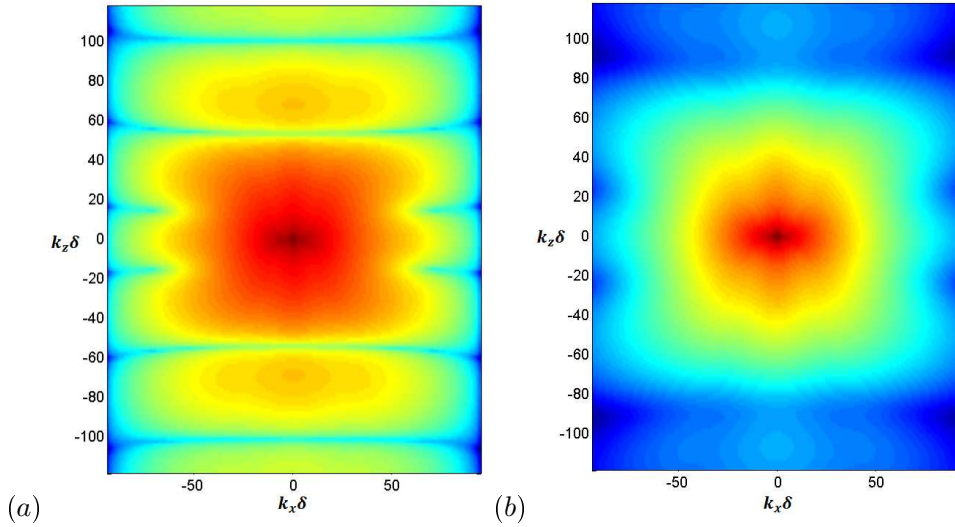


Figure 4.6 – Wavenumber spectrum in the (k_x, k_z) plane (a) without continuous distribution and (b) with continuous distribution of hairpin eddies - only the first sublayer (logarithmic region) is considered here.

sublayer corresponds to the beginning of the logarithmic layer $y^+ = 30$. The heads of each hairpin structure lays in the middle of each sublayer which determines the length of the hairpin legs. The breadth λ of each eddy is then set to $L/\lambda = \sqrt{2}, 1.412, 1.391, 1.330, 1.203$ and 0.992 . Ahn et al. (2010) have demonstrated that only the aspect ratio of the structure L/λ has an influence on the wavenumber spectrum. Under the hypothesis that the radius r_c of the vortices is proportional to the scale of the structure, they chose $r_c = 0.05\lambda$.

Figure 4.7 shows the streamwise wavenumber spectra for each of the six sublayers. The hairpin structures lay at an angle of 45° to the wall and are subjected to a mean flow corresponding to a zero pressure gradient turbulent boundary layer. The logarithmic region shows the lowest levels in the low wavenumber range but high contribution for high wavenumbers. For the outer region $y/\delta > 0.1$, on the one hand increasing levels are observed in the low wavenumber range as the eddies increase in size while on the other hand, the biggest eddies have less contribution to the high wavenumbers. This result follows observation made from measurements and numerical simulations.

Influence of the upper limit

The results shown previously correspond to wavenumber spectra for a single sublayer. It is interesting to evaluate the influence of the upper limit of the eddy distribution when considering the contribution from all sublayers. Figure 4.8 shows the wavenumber spectra for a continuous distribution of eddies laying within 3 sublayers up to 9 sublayers. For sublayers 7,8 and 9 the aspect ratios of the structures are respectively $L/\lambda = 0.6866, 0.4904$ and 0.3269 . As predicted by Ahn et al. (2010), it can be seen that eddies above $y/\delta = 0.4$ (6 sublayers) have negligible contribution to the overall spectrum. Based on this observation, the following results will correspond to an upper limit of $y/\delta = 0.4$ for the largest eddy head location.

Influence of velocity field calculation method

In the model proposed by Ahn et al. (2010), the velocity field induced by the hairpin structure is given by equation (4.3) which is obtained after simplifications and hypothesis for the Biot-

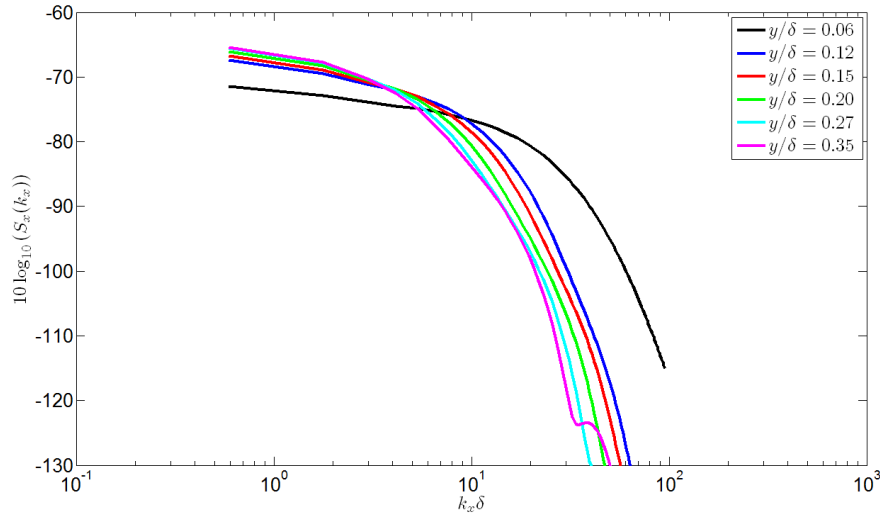


Figure 4.7 – Streamwise wavenumber spectrum for each of the six hairpin sublayers. Legend indicates the wall-normal position y/δ of the heads of the hairpin eddies.

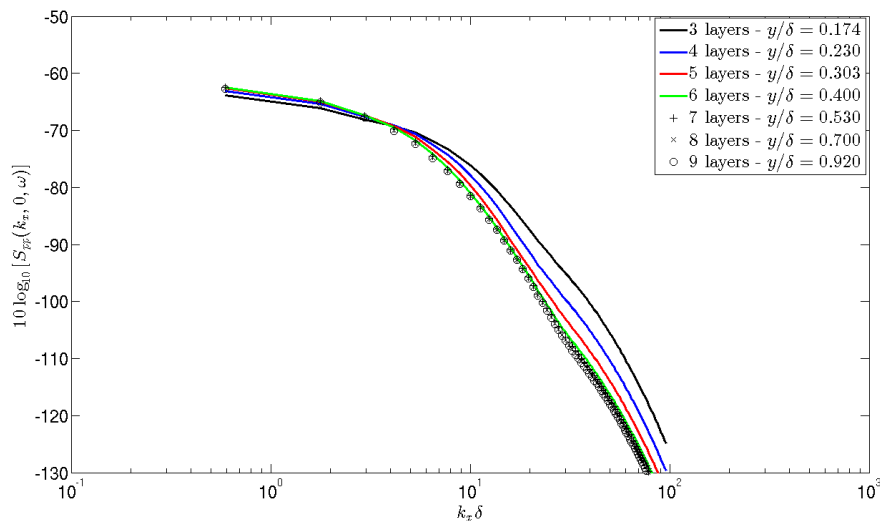


Figure 4.8 – Influence of the upper limit position of the hairpin eddy field to the wavenumber spectrum. For each case, the legend indicates the upper limit y/δ of the highest sublayer.

Savart integral. The pressure spectrum has been calculated for both these methods and the result is shown in figure 4.9. It can be seen that the difference for a spectrum obtained using the analytical expression of the induced velocity field and the direct evaluation of the Biot-Savart equation is negligible. Therefore, the remainder of the study corresponds to results from the analytical version for computation time issues.

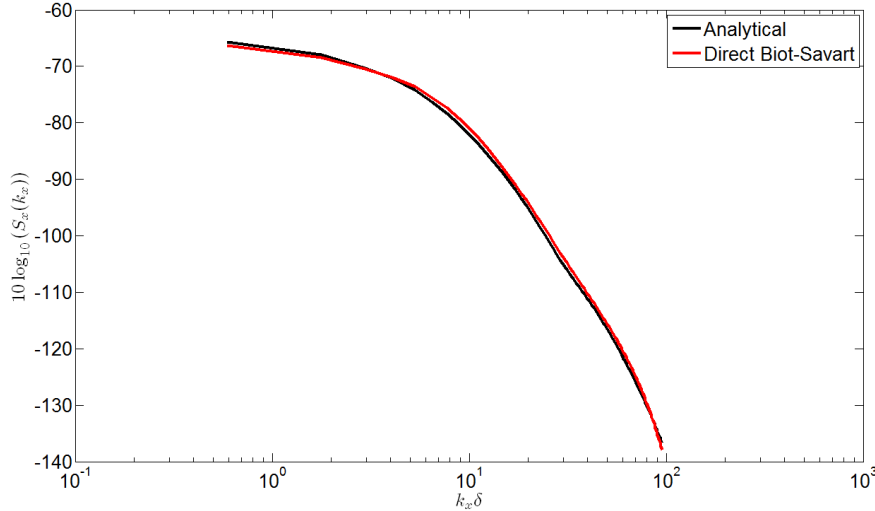


Figure 4.9 – Influence of the velocity induced field calculation method on the wavenumber spectrum.

Influence of the eddy shape

In the model developed by Ahn et al. (2010), the hairpin structures are idealized rectangular horseshoes. Chang (1998) and Chang et al. (1999) have reported that the source terms T_{ij} in the Poisson equation that have a major contribution to the wall-pressure spectrum are those related to the spinning motion of the legs in the spanwise/wall-normal plane. Moreover, Dhanak et al. (1997) were able to retrieve satisfactory results for the high frequency and high wavenumber ranges of the pressure spectrum using a model based on pairs of counter-rotating vortices in the near-wall region.

The idea here is to quantify whether the rectangular horseshoe structure is the best candidate for wall-pressure spectrum modeling. The first test consists of vortices with the complete hairpin structure geometry as described by Robinson (1991a) and Head and Bandyopadhyay (1981), i.e. two legs, a neck and a head. This is shown in figure 4.10 (left) where the isosurface of fluctuating wall-normal velocity v' reveals the shape of the eddy. In the second test the pressure spectrum resulting from a pair of counter-rotating vortices located in the near-wall region (figure 4.10 right) was computed. The counter rotating vortices have a length of $L^+ = 430$ in wall units. Based on the observations by Johansson et al. (1987) and Johansson et al. (1991), they are placed at an angle of 5° to the wall. Finally the influence of the head of the hairpin was investigated as shown in figure 4.11. This has been performed in order to measure the relative weights of the legs of the hairpin eddy versus that of the head. It is worth noting that the use of the Biot-Savart integral is based on the hypothesis that the vorticity field is solenoidal. This is violated here since we consider isolated contributions. Therefore, even if the decomposition is possible mathematically, it has no real physical signification.

The streamwise wavenumber spectra for the different shaped hairpin structures are shown in figure 4.12. The counter-rotating (CR) vortices are located in the near-wall region whereas for the

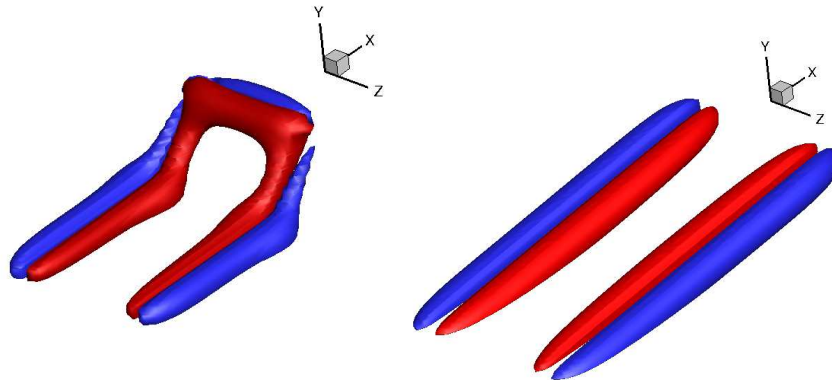


Figure 4.10 – Local velocity field around a hairpin-like vortex with neck/legs geometry located in the logarithmic region (left) and a pair of outward-spinning counter rotating quasi-streamwise vortices at an angle of 5° to the wall located in the buffer region (right) - Isosurfaces of wall-normal velocity $v' < 0$ (blue) and $v' > 0$ (red).

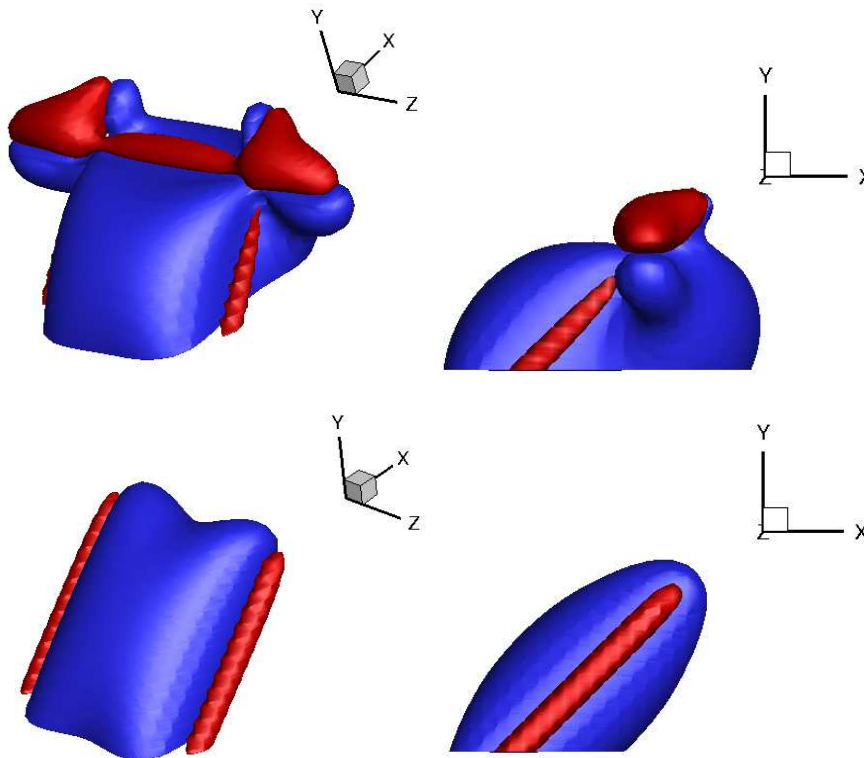


Figure 4.11 – Local velocity field around a horseshoe-like vortex with head (top) and without head (bottom) located in the logarithmic region - Isosurfaces of fluctuating streamwise velocity $u' < 0$ (blue) and $u' > 0$ (red).

other cases, the structures span the boundary layer thickness up to 0.4δ . At low wavenumbers, the rectangular and leg/neck shaped hairpin structures show the same and highest levels of energy, while the no head structure provides the lowest levels. In the high wavenumbers range, the no head and CR structures have similar levels and the rectangular hairpin eddy provides highest levels once more. The biggest discrepancies are visible for mid wavenumbers $0.3 < k_x\delta < 20$. The no head eddy shows highest levels whereas the CR vortices show the lowest. In contrast to these cases, the rectangular and leg/neck shapes have a rather constant slope in this region. Finally, the oscillations for the CR vortices are due to the presence of a single pair of vortices with a unique lengthscale $L^+ = 430$. Therefore the continuous distribution modeling described in figure 4.5 is not applied for this case.

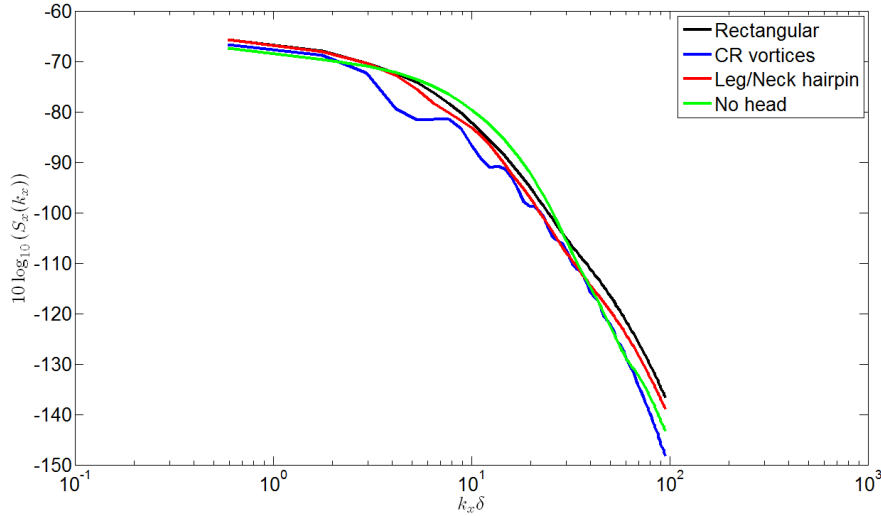


Figure 4.12 – Streamwise wavenumber spectra predicted by the model for different shapes of the coherent structures.

4.1.2 Introducing large-scale structures

It has been said that hairpin-like structures tend to group in the stream direction to form hairpin packets. This type of arrangement has been observed in multiple wall-bounded flows. The idea here is to reproduce this large-scale structure in the hairpin model. Figure 4.13 shows a packet of 5 hairpin vortices. For now, the hairpin vortices are perfectly aligned along the streamwise direction, whereas it has been seen through the analysis of the three-dimensional database in section 3.2.3, that the packets have rather a meandering path. The separation between two hairpin structures of a same packet is constant and is set to the average of the vortex separations Δ_ν/δ estimated in section 3.3.1, considering only the vortices near the event location. Therefore, hairpin vortices within a packet are separated by 0.19δ for APGs, 0.22δ for APGw, 0.35δ for ZPG and 0.28δ for FPG.

The hairpin packet in the model generates a low momentum region beneath it. The "intensity" of this low-speed region depends on the number of hairpin vortices within the packet and the distance between each individual structure. For the model, the average separation distance is based on the analyses of conditionally averaged velocity fields as shown in figures 3.13 and 3.14.

Figure 4.14 shows the wavenumber spectrum predicted by the model in the (k_x, k_z) plane with and without the hairpin packets configuration. In this example, all hairpin structures

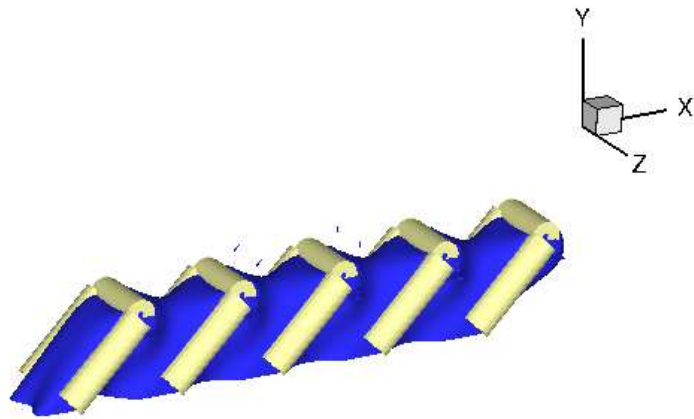


Figure 4.13 – Low-momentum region developing under a packet of five hairpin-like eddies - Isosurface of negative fluctuating velocity $u' < 0$ in blue.

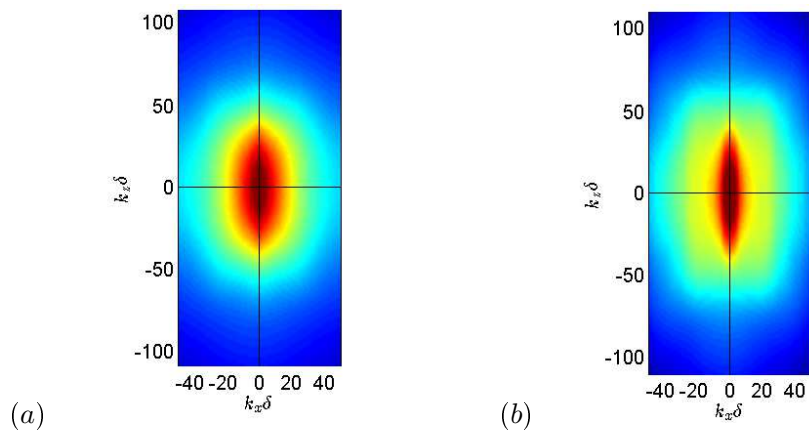


Figure 4.14 – Model prediction of wavenumber-frequency spectrum in the (k_x, k_z) plane for (a) single hairpin and (b) for packets of five hairpin structures. The black cross indicates the position of the peak.

have the same size so that the packet is aligned with the wall. It can be seen that the packets introduce anisotropy in the shape of the peak with a smaller extent in the k_x direction. This behaviour is similar to what is found in experiments and numerical results (see figure 2.25) and is a direct proof of coherent structures having a bigger extent in the direction of the stream. This result is crucial since it shows that hairpin packets are mandatory to build a reliable model by taking into account the anisotropy of the turbulent motions; i.e. the hairpin packet model provides better prediction of the wavenumber spectrum compared to the single hairpin model.

4.1.3 Introducing pressure gradient effect

As it has already been mentioned, one of the main challenges is to build a model capable of predicting wall-pressure spectra for flows subjected to pressure gradients. Based on what has been learned from the literature and the analyses of the LES velocity fields above, there are three main means of taking into account the influence of a pressure gradient in the model.

- Mean flow: it has been showed that the pressure gradient has a direct impact on the wake region of the mean velocity profile and the dimensionless turbulent boundary layer thickness $\delta u_\tau/\nu$ which gives an indication on how the TBL thickness evolves with respect to the pressure gradient. The first observation can be modeled by modifying the wake parameter Π in the analytical expression of the velocity profile.
- Hairpin-eddy angle: it has been demonstrated in the previous chapter, as well as in the literature (Lee and Sung, 2009; Mayam, 2009), that the angle of the individual eddies is modified depending on the pressure gradient.
- Hairpin packet angle: as for the individual hairpin-like vortices, the hairpin packets have different angles depending on the pressure gradient: low angles to the wall for favorable pressure gradients and higher angles for adverse pressure gradients.

Concerning the first point, table 4.1 gives the values of Π and the dimensionless parameter $\delta u_\tau/\nu$ through which the TBL thickness is imposed for each pressure-gradient. These values correspond to the LES cases since it is our first case of validation for the model. Figure 4.15 shows the mean velocity profiles computed out of equation (4.11).

	FPG	ZPG	APG _w	APG _s
Π	0.17	0.6	1.1	1.8
$\delta u_\tau/\nu$	696	540	637	638

Table 4.1 – Parameters for the mean velocity profiles extracted from the LES computations.

The effect of the angle of the single eddies is shown in figure 4.16. The mean flow as well as the size of the eddies are similar for each configuration. There are two noticeable results as the angle of the structure increases: 1) the levels in the low wavenumber domain are higher; this can be linked to the increasing levels of energy for adverse pressure gradients where the coherent structures (single hairpins and hairpin packets) have higher angles and 2) lower energy for the high wavenumbers. This last result suggests that near-wall structures have a higher contribution to the pressure spectrum at high wavenumbers.

4.1. DEFINITION OF THE MODEL

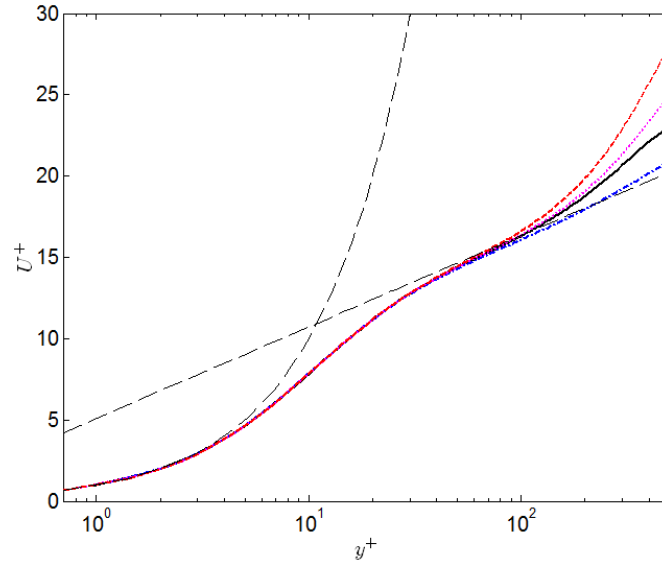


Figure 4.15 – Mean velocity profiles for favorable (— — —), zero (—) , adverse weak (— — —) and adverse strong (— — —) pressure gradients. Dashed black lines correspond to the theoretical linear law $U^+ = y^+$ and logarithmic law $U^+ = \ln(y^+)/0.41 + 5.1$.

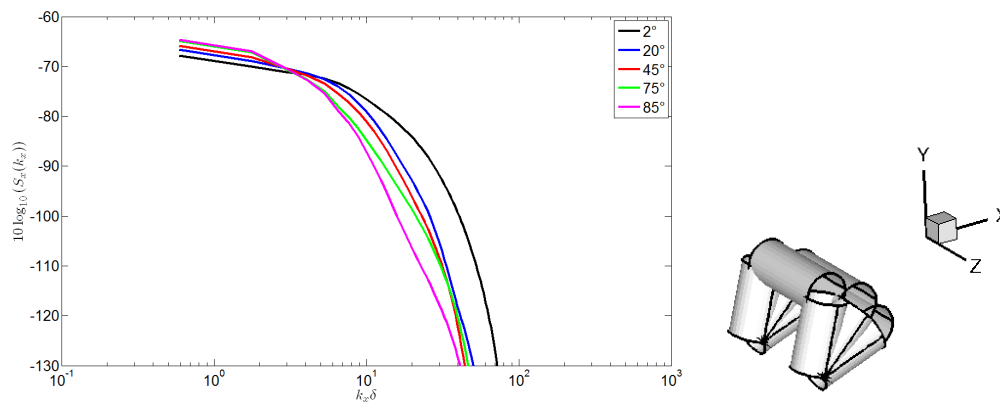


Figure 4.16 – Streamwise wavenumber spectrum for hairpin structures at different angles to the wall. Hairpin structures at 20°, 45° and 75° are illustrated on the right.

4.1.4 Coupling with autospectrum model and frequency dependency

For now, the (k_x, k_z) spectrum is the spatial Fourier transform of the space-time pressure correlation at "zero time delay". This means that it represents the integral of all frequency components in the wavenumber-frequency domain.

In order to perform coupling with an aircraft structure, the 3D wavenumber-frequency spectrum is necessary. Since there is no frequency dependence for the spectrum in the hairpin model, this needs to be modeled. There are three effects of the frequency on the convective peak which are visible in figure 4.17:

- since the maximum of energy is located around the convective wavenumber $k_c = \omega/U_c$, the convective peak is shifted towards higher wavenumber as the frequency increases.
- the slope of the spectrum along the streamwise wavenumber k_x is steeper for low frequencies
- the maximum levels of energy decrease as the frequency increases.

The methods used to take into account each of these effects are detailed below.

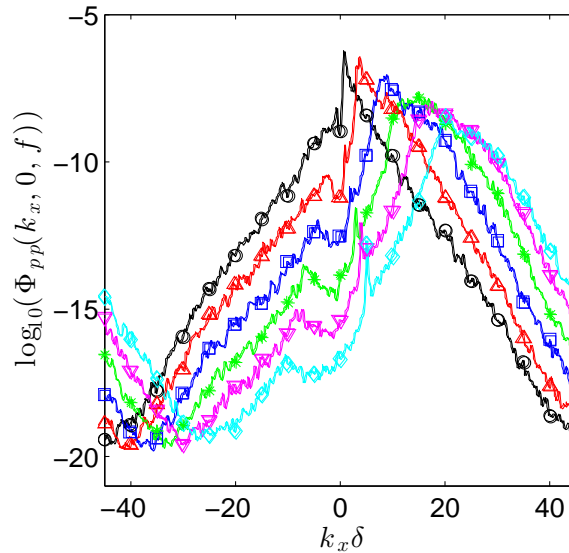


Figure 4.17 – Streamwise wavenumber spectra $S_{pp}(k_x, k_z = 0, \omega)$ for the ZPG case of the LES computation for different frequencies $\omega \delta_{ref}^*/U_e$ \circ — 1.1, \triangle — 5.2, \square — 10.4, $*$ — 12, ∇ — 20.9, and \diamond — 31.1 - after Cohen (2015).

Shifting of the convective ridge

This is done by the knowledge of the convective wavenumber. The modelling of the convection velocity follows the method used by Panton and Linebarger (1974). At low wavenumbers, the surface pressure spectrum is dominated by the contribution of large structures, i.e. of the wake region. Therefore, the convective velocity should be related to the mean velocity in this region:

$$\frac{U_c - U}{u_\tau} = F(k_x \delta, \Pi) \quad (4.19)$$

where Π is the wake parameter linked to the intensity of the pressure gradient. The high wavenumber region is believed to be dominated by contribution of small-scale structures and the convection velocity should then scale with inner variables:

4.1. DEFINITION OF THE MODEL

$$\frac{U_c}{u_\tau} = f\left(\frac{k_x \nu}{u_\tau}\right) \quad (4.20)$$

By differentiating and equating both these expressions, this leads to the overlap laws:

$$F = \beta \ln(k_x \delta) + A_1(\Pi) \quad (4.21a)$$

$$f = \beta \ln\left(\frac{k_x \nu}{u_\tau}\right) + A_2 \quad (4.21b)$$

Equating the expressions again yields the friction law:

$$\frac{U_c}{u_\tau} = -\beta \ln\left(\frac{u_\tau \delta}{\nu}\right) + A_2 - A_1(\Pi) \quad (4.22)$$

Comparing this to the mean velocity profile, one can establish the coefficients $\beta = 1/\kappa$, κ being the Von Kármán constant, $A_1 = -2\Pi/\kappa$ and $A_2 = 5.0$. Based on convective velocity data by Bradshaw (1967a,a), Panton and Linebarger (1974) were able to determine the form of the 'wake' function W . The full convection velocity profile with respect to the streamwise wavenumber is then given by:

$$\frac{U_c}{u_\tau} = f\left(k_x \delta; \frac{u_\tau \delta}{\nu}\right) + W(k_x \delta, \Pi) \quad (4.23a)$$

$$f = -\frac{1}{\kappa} \ln(k_x \delta) + \frac{1}{\kappa} \left(\frac{u_\tau \delta}{\nu}\right) + 5.0 \quad (4.23b)$$

$$W = \frac{2}{K} \sqrt{\Pi} (k_x \delta - 1) e^{\frac{2}{3}(k_x \delta - 1)} \quad \text{for} \quad k_x \delta < 1 \quad (4.23c)$$

Decreasing levels of maximum energy

The pressure spectrum provided by equation (4.18) is a non-dimensional quantity. In order to retrieve the real levels of energy, the wavenumber spectrum is coupled with an autospectrum model for wall-pressure fluctuations. The model chosen for this is the Klabas et al. (2016) model given by equation (2.60) provided in the wall-pressure models review in section 2.3.4. Therefore, the expression of the wavenumber-frequency spectrum for wall-pressure is given by:

$$\Phi_{pp}(k_x, k_z, \omega) = \Phi(\omega) \times S_{pp}(k_x, k_z, \omega) \quad (4.24)$$

Note that now $S_{pp}(k_x, k_z, \omega)$ is frequency dependent due to the convection velocity that has been introduced in the model. In addition to retrieving the real levels of energy, the one-point spectrum will contribute to the decreasing levels at high frequencies (see figure 2.24 for one-point spectrum behaviour for example).

Slope change

According to the wavenumber spectra shown in figure 4.17, the slope is weaker as the frequency increases, meaning that small scales have an increasing contribution to the energy for high frequencies. For now, the model is built in a way that all hairpin structures have the same weight when summing each spectrum of each sublayer. The idea is then to introduce a function that gives more or less importance to the eddies based on their size. The wavenumber spectrum from equation (4.18) becomes:

$$S(k_x, k_z, \omega) = \int_{\lambda_{min}}^{\lambda_{max}} \mathcal{A}(\lambda, \Pi, \omega) |\tilde{P}(k_x \lambda, k_z \lambda)|^2 d\lambda \quad (4.25)$$

where $0 < \mathcal{A}(\lambda, \Pi, \omega) < 1$ is a ponderation function of the eddy size λ , the pressure gradient Π and the frequency:

$$\mathcal{A}(\lambda, \Pi, \omega) = \frac{1}{\pi} \arctan \left[\text{sign} \left(\frac{\omega}{\omega_c} - 1 \right) g \left(\frac{\lambda}{\delta}, \Pi \right) \right] + B \quad (4.26)$$

with $B = 0.5$ and $g \left(\frac{\lambda}{\delta}, \Pi \right) = \lambda/\delta - \frac{\lambda_{max} + \lambda_{min}}{\delta \Pi}$ a function controlling the slope of the arctan function as well as the "cut-off" lengthscale depending on the pressure gradient.

4.2 Comparison with SONOBL database

The LES numerical database used for the velocity fields analyses was performed within the SONOBL (Sources of Noise from Boundary Layers over vehicles) project. The main objectives were to provide new databases for turbulent boundary layers with non-zero pressure gradients, in particular to help enhancing the wall-pressure spectrum models and to evaluate both direct and indirect acoustic contributions, respectively the acoustic radiation into the free stream and the contribution due to the wall-pressure fluctuations.

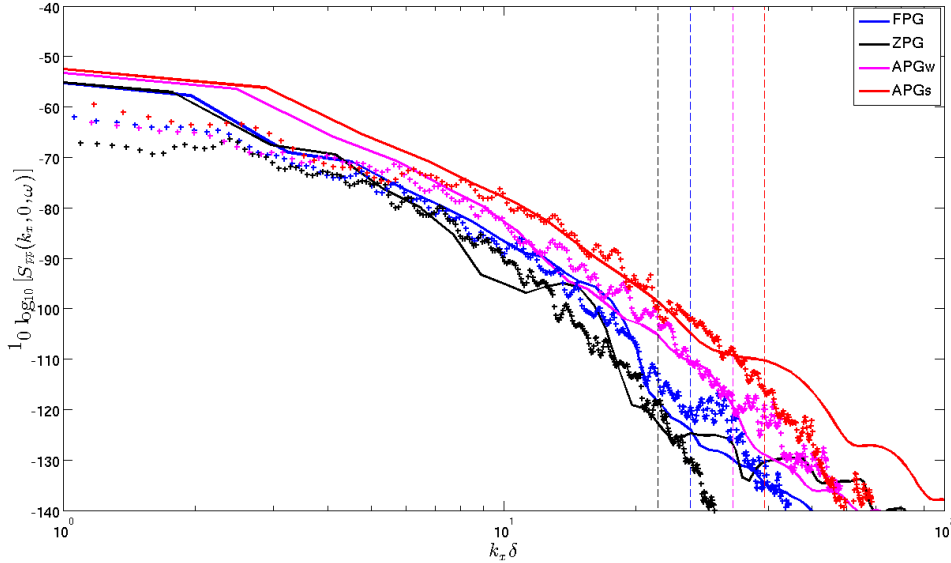


Figure 4.18 – Comparison of streamwise wavenumber spectra between (+) LES database and (—) the hairpin packet model for first frequency $\omega\delta/U_e = 0.06$ (FPG), 0.09 (APGw) and 0.10 (APGs). Dashed vertical lines indicate the cut-off wavenumbers for the LES computations.

Figure 4.18 shows the streamwise wavenumber spectra from the LES computations compared with the hairpin packet model predictions for the lowest frequency. The dashed vertical lines correspond to the cut-off wavenumbers for the LES cases which is estimated to be $k_x^{co} = 2\pi/4\Delta x$, meaning that eddies with a lengthscale smaller than four times the mesh resolution in the streamwise direction are not resolved. For the ZPG case, the hairpin structures are set at an angle of 45° to the wall, following the model by Ahn et al. (2010). Mayam (2009) and Lee and Sung (2009) found that the average angle of hairpin eddies is 18% higher for APG flows compared to ZPG cases. Based on this observation, the angles of the hairpin eddies for the hairpin packet

4.3. COUPLING WITH VIBRO-ACOUSTICS CODE

model here are set to 53° and 60° for the APGw and APGs cases respectively. For FPG case, the angle is 37° . It can be seen that the model predicts the correct hierarchy in term of energy levels, i.e. lowest levels for the favorable and zero pressure gradient case and highest levels for the strong adverse pressure gradient case. However, the levels at very low wavenumbers $k_x \delta < 3$ are over-predicted by the model. It can also be noticed that the model provides satisfactory slopes as well for each flow. In order to evaluate the modeling of the frequency dependence, the streamwise wavenumber spectra for APGw and APGs are shown for example at three different frequencies in figure 4.19.

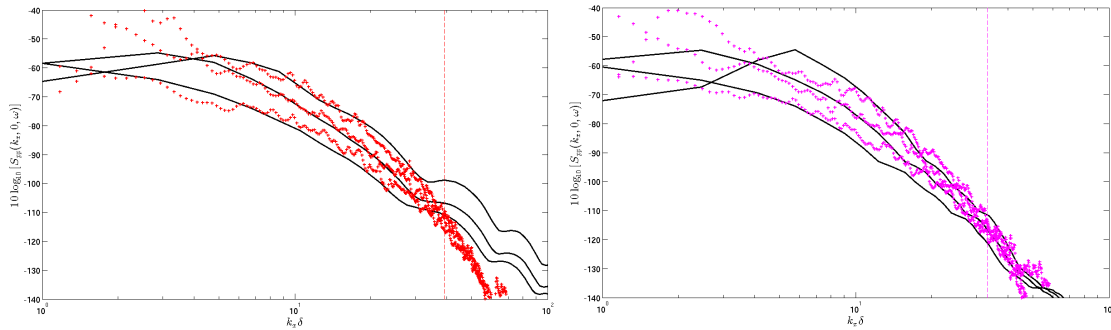


Figure 4.19 – Comparison of streamwise wavenumber spectra between (+) LES database and (—) the hairpin packet model at three frequencies for (left) APGw [0.09, 0.86, 1.72] and (right) APGs [0.10, 1.04, 2.08]. Frequencies $\omega \delta / U_e$ are given inside brackets.

4.3 Coupling with vibro-acoustics code

Measurements of panels vibrations on three regions of the Advanced Technology Research Aircraft (ATRA) have been carried out by the Deutsches Zentrum für Luft und Raumfahrt (DLR). This was done by placing accelerometers against the inside skin of the aircraft in the front, mid and aft cabin as shown in figure 4.20. Data for cruise flight conditions, i.e Mach number $M = 0.78$ and flight level 35000ft, are available.



Figure 4.20 – ATRA aircraft from the DLR. The colors indicate the areas where measurements of panels accelerations have been performed: front cabin (blue), mid cabin (red) and aft cabin (green) - after Klabes et al. (2015).

In parallel, a Statistical Energy Analysis (SEA) (Fahy, 1994; Le Bot, 2015; Lyon, 1975; Lyon and Maidanik, 1962) model was developed within Airbus for the front cabin area for acoustic and vibration predictions (see figure 4.21). For the present study, the turbulent boundary layer is the

only source of excitation of the structure. The results are computed using the vibro-acoustics software VA-One. For the models, the turbulent boundary layer parameters are given in table 4.2.

$\delta \times 10^3$ (m)	u_τ (m/s)	U_e (m/s)	β_C
60.2	7.122	239.9	0

Table 4.2 – Boundary layer parameters for front cabin region - A. Klages personal communication.

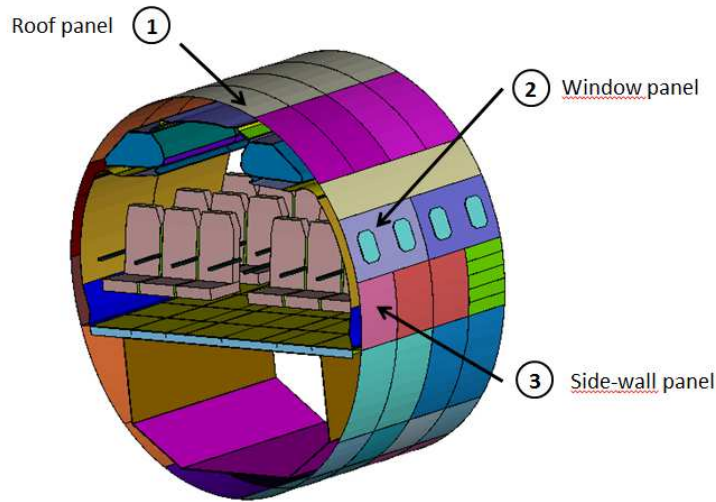


Figure 4.21 – SEA model for the front cabin area. The panels mentioned here are used for SEA computation using the TBL models.

Figure 4.22 shows the predictions of the Corcos model, Cockburn-Jolly model, a modified Efimtsov model, hairpin (HP) model, hairpin packet (HPP) model and Ewert’s FRPM model (see section 2.3.4) applied by Amador Medeiros et al. (2016) for a roof panel in the front area of the fuselage. The modified Efimtsov model is built using measurement fitted parameters from flight tests on the ATRA. The predictions are compared to the in-flight measurements from accelerometers. The Corcos excitation is the default TBL model implemented in the VA-One software. All wavenumber-frequency models are made non-dimensional and coupled with the same autospectrum model from Klages et al. (2016). The overall trend is that the Corcos and Cockburn-Jolly models over-predict the levels at low frequencies below $f < 400\text{Hz}$. The Cockburn-Jolly model provides however better results over the entire frequency range than the Corcos model which shows low levels at high frequencies. The Efimtsov and hairpin models have similar behaviours. They are quite satisfactory below 500Hz and at high frequencies $f > 2000\text{Hz}$. They under-predict the levels between $630 < f < 1600$ up to 13dB less than those measured. Overall, the Efimtsov and HPP model provide better results than the HP model. Finally, the LES spectrum for the ZPG case is also shown. The non-dimensional frequency $\omega\delta/U_e$ and wavenumbers $(k_x\delta, k_z\delta)$ were used to rescale the spectrum to frequencies and wavenumbers adapted to aircraft panels. The results from the LES provided very low levels, about 30dB

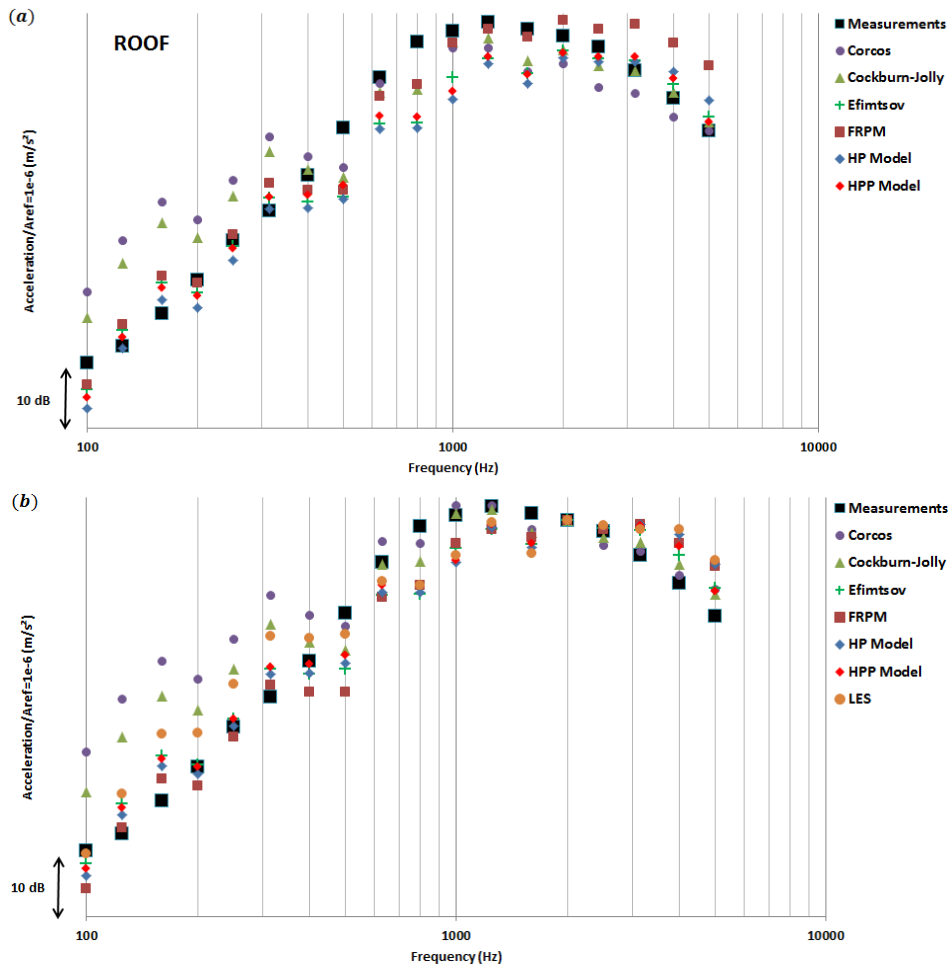


Figure 4.22 – Comparison between the SEA predictions submitted to the hairpin model and the flight test measurements on roof panel of the front cabin - acceleration vs 1/3 octave band frequencies - (a) Direct predictions, (b) predictions are rescaled to match measurement point at 2000Hz. Measurements, Cockburn-Jolly, Efimtsov and FRPM data have been communicated by A. Klabas.

below measurements. Therefore, in order to compare them to the models, all levels in figure 4.22(b) are rescaled to match measurements at 2000Hz (the SEA model provides the best results around this frequency).

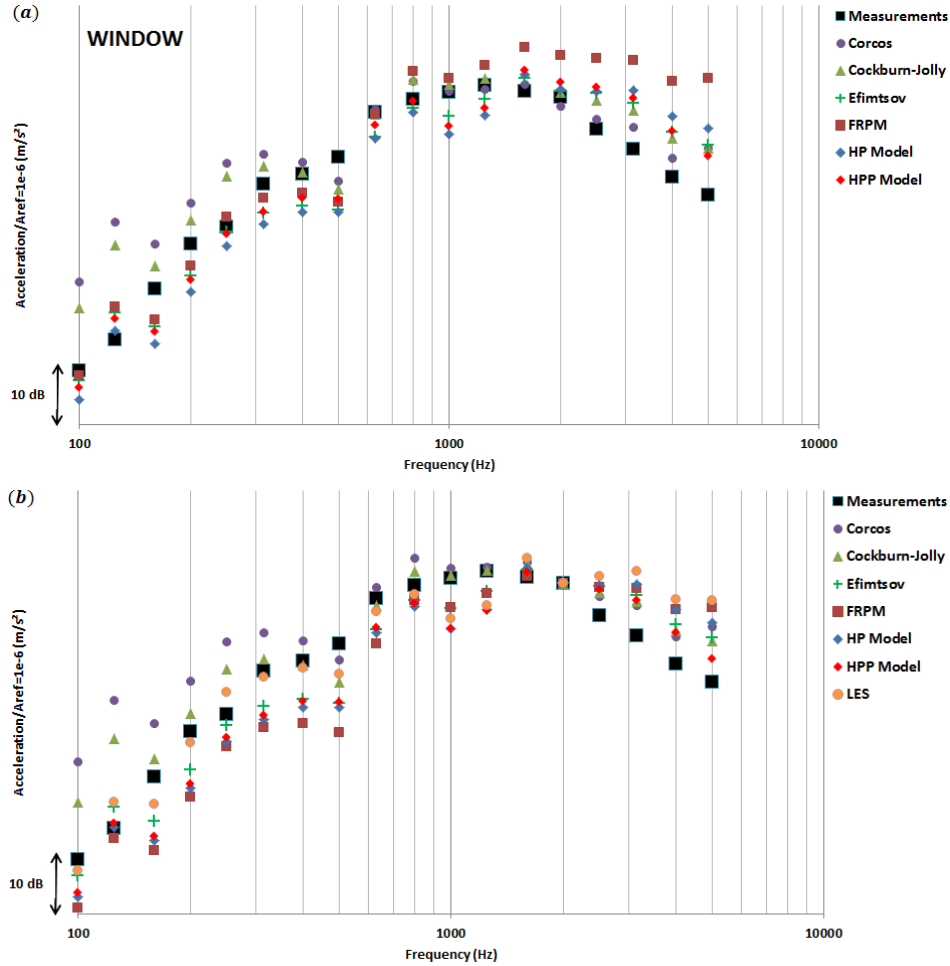


Figure 4.23 – Comparison between the SEA predictions submitted to the hairpin model and the flight test measurements on window panel of the front cabin - acceleration vs 1/3 octave band frequencies - (a) Direct predictions, (b) predictions are rescaled to match measurement point at 2000Hz. Measurements, Cockburn-Jolly, Efimtsov and FRPM data have been communicated by A. Klabas.

The same analysis is performed for a window panel in figure 4.23 and a lower side-wall panel at floor level in figure 4.24. For the window panel, the same conclusions can be drawn, except that the FRPM model provides highest discrepancies for $f > 1600\text{Hz}$ (these results need to be regarded as preliminary as developments are still ongoing for the FRPM model). On the other hand, the Corcos model seems very promising for this frequency range. For the lower side-wall panel, similar observations can be made. Finally, for the window and lower side-wall panels, all models predict maximum level at 1600Hz, whereas it varies in the range $1250\text{Hz} < f < 2000\text{Hz}$ for the roof panel. The bending wavenumber k_b for flat plates is given by

$$k_b = \omega^{1/2} \sqrt[4]{\frac{12\rho_p(1-\nu_p^2)}{Eh_p^2}} \quad (4.27)$$

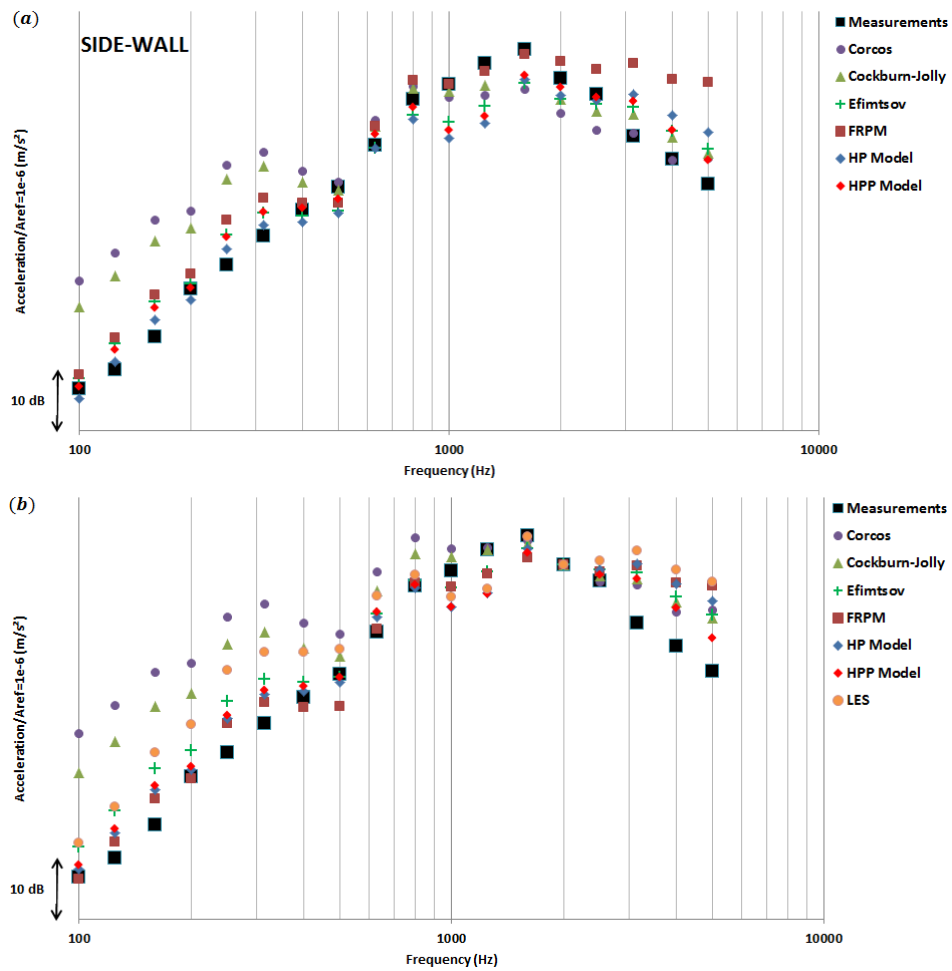


Figure 4.24 – Comparison between the SEA predictions submitted to the hairpin model and the flight test measurements on lower side-wall panel of the front cabin - acceleration vs 1/3 octave band frequencies - (a) Direct predictions, (b) predictions are rescaled to match measurement point at 2000Hz. Measurements, Cockburn-Jolly, Efimtsov and FRPM data have been communicated by A. Klabes.

where ρ_p , E , ν_p and h_p are respectively the density, the Young modulus, the Poisson coefficient, and the thickness of the plate. For aluminum fuselage panels, $k_b(f = 1600\text{Hz}) \simeq 67\text{m}^{-1}$. Under the approximation that the convection velocity is $U_c = 0.7U_e$, the convective wavenumber is $k_c(f = 1600\text{Hz}) = 61\text{m}^{-1}$, and therefore the aerodynamic coincidence is fairly well predicted.

This being said, it is important to keep in mind the limitations of the SEA method. In the SEA model used here, the fuselage vibration pattern is deduced from analytical model of reduced ribbed panel. The validity of the fuselage vibration modeling varies with frequency. At low frequencies $f < 400\text{Hz}$, the confidence is low. In this range, the SEA hypothesis requiring energy gaps between panels is certainly not fulfilled since the structure is strongly influenced by global modes. Between 400Hz and 800Hz, the so-called mid-frequency range for aircraft fuselage, the confidence in the structure modeling is medium. The validity of the modeling should be studied carefully as it corresponds to the transition from global to local structure modes which generally results in a very sensitive and uncertain modeling. Above 800Hz, SEA hypotheses for aircraft fuselage structure are surely fulfilled, the variability is low and the confidence level is the highest. To tackle the low confidence level at low-medium frequencies for aircraft structure, Airbus uses finite-element models. However, the coupling of the different TBL models with such models could not be done yet. For these reasons, the TBL models comparison should be done by highlighting the slopes (from 100 to 1000Hz and from 2000 to 5000Hz) of the predicted spectra for the panels. Moreover, the aerodynamic coincidence frequency depends highly on the accuracy of the structure dynamic and variability with theoretical results is not necessarily due to the modeling of the frequency-wavenumber spectrum for wall-pressure. The oscillations of the vibration at low and medium frequencies are clearly due to the structure modeling. Rarely observed in measurements, it comes from limitations of the reduced ribbed panel modeling which amplifies modal density variations (it is a consequence of the TBL/structure coupling).

Chapter 5

Conclusions and perspectives

Summary

This thesis was performed in the context of flow-induced noise over aircraft. The turbulent boundary layer induces pressure fluctuations at the wall that make the panels of the fuselage vibrate. These vibrations are then transmitted through the structure and radiate noise inside the cabin and cockpit. The levels of interior noise increase with the speed of the vehicle and for this reason, aircraft manufacturers have demonstrated an increasing interest in this topic over the past years in order to provide passengers and crew members with the best acoustic comfort possible. To do so, predictions of interior noise levels need to be performed at the early development stages of a new aircraft using wall-pressure models and vibro-acoustics computations. Several models for the wall-pressure fluctuations exist in the literature, but a great majority of them are limited to canonical flows which lack precision in regions subjected to pressure gradients such as the aircraft flight deck or the wing/fuselage junction.

The objective here was to understand the physical mechanisms responsible for the turbulent boundary layer excitation and the effect of pressure gradients on the wall-pressure fluctuations. A wall-pressure model was then developed based on these results. The analysis was performed using an available Large Eddy Simulation (LES) database of turbulent boundary layer flows at Mach 0.5 subjected to four different pressure gradients: favorable, zero, adverse weak and adverse strong (weak and strong characterize the intensity of the pressure gradient which can be measured with Clauser's pressure parameter β_C for instance). For these four databases, only two-dimensional planes (8 streamwise/wall-normal and 12 streamwise/spanwise) were available due to storage issues. The three components of velocity (u, v, w) were available for each of these planes as well as the pressure field on the plane of the wall. In addition, an older three-dimensional database (complete 3D domain) of a Mach 0.5 zero-pressure-gradient turbulent boundary layer was available, with the three components of the velocity field and the wall-pressure. For the five flows, great care has been taken to obtain turbulent boundary layers in equilibrium in order to have spatially homogeneous and statistically stationary quantities in the streamwise direction.

The pressure fluctuations at the wall are the imprint of the turbulent velocity field, and more specifically of the coherent motions or turbulent structures which have multiple length- and time-scales. In this work, a vortex identification method based on the swirling strength λ_{ci} (Zhou et al., 1999) was used. This quantity reveals regions of high vorticity where the velocity field is characterized by a swirling motion and has been widely used recently by authors interested in coherent structures in turbulent flows. The identification method has revealed

that the boundary layer flow is predominantly populated by so-called hairpin vortices for all pressure gradient cases. These structures tend to group in larger scale structures referred to as hairpin packets which correspond to multiple hairpin vortices aligned along the streamwise direction laying over regions of low momentum. Statistical analysis tools such as two-point correlations and linear stochastic estimation showed that these packets have a certain angle to the wall which depends on the pressure gradient: low angle for a favorable pressure gradient flow which increases as the pressure gradient becomes more and more adverse. This analysis also revealed that the hairpin vortices and hairpin packets are the most common structures related to swirling spanwise vorticity (spanwise vorticity induced by a swirling/spinning motions and not mean shear). The effect of the pressure gradient on the streamwise spacing between hairpin vortices within a same packet were quantified. Subpacket organization, which corresponds to smaller-scale hairpin packets within a same packet was also observed. The angle of the hairpin packets was measured based on the pressure gradient and the distance of the packets to the wall. This showed that the hairpin packets organization tends to vanish beyond 0.6δ for the favorable and zero-pressure-gradient cases and beyond 0.7δ for the adverse pressure gradients (here δ denotes the boundary layer thickness). The influence of the pressure gradient as well as the wall-normal distance on the streamwise extent of hairpin packets was also assessed. Similar analysis in the streamwise/transverse planes provided results on the spanwise lengthscale of the hairpin structures and hairpin packets, according to the pressure gradient and their wall-normal position in the boundary layer. It was observed that the effect of the pressure gradient depends on the distance of the structures from the wall and that a particular behaviour for the strong adverse pressure case existed around 0.1δ which can be correlated to the secondary peak of turbulent intensities u_i^{rms} for adverse pressure gradient flows.

The statistical analysis of the three-dimensional zero-pressure-gradient database provided a three-dimensional estimation of the structures with respect to their distance from the wall. The increasing size of hairpin-like vortices could be explicitly observed and the leg-neck-head geometry seemed to vanish, replaced by a leg-head geometry when moving away from the wall. This also showed that even if hairpin packets tend to vanish beyond 0.6δ , individual hairpin vortices still exist at these distances. Moreover, a pair of counter-rotating quasi-streamwise vortices was identified laying over hairpin packet at several wall-normal positions. These vortices have a positive angle to the wall and a circulation opposite to that of the hairpin structures. To the authors knowledge, this has never been observed before and an "inverse hairpin" model was proposed.

Following the work of Ahn et al. (2010), a stochastic model for wall-pressure spectrum was developed. The idea is to build a stochastic velocity field using hairpin packets which are subjected to a turbulent mean flow. The results from the LES databases analysis are used to characterize the hairpin packets depending on the pressure gradient case that needs to be simulated. The pressure field at the wall is obtained by solving a Poisson equation. It has been demonstrated that a model based on hairpin packets rather than single hairpins retrieves the anisotropic character of the wavenumber spectrum more accurately. A frequency dependence as well as coupling with an autospectrum model was introduced to build the complete wavenumber-frequency wall-pressure spectrum which is necessary for vibro-acoustics simulations. The frequency dependence is modeled using a pressure-gradient-dependent convection velocity and a function which weights the contribution of the different eddy scales. The model shows good agreement with numerical results of flows subjected to pressure gradients. Finally, the model was used as input for a Statistical Energy Analysis (SEA) simulation in order to predict the levels of vibration of panels submitted to a turbulent boundary layer flow over a portion of an aircraft cabin. The computation was performed using the vibro-acoustic software VA-One. Comparison with in

flight measurements using accelerometers showed good agreement in the low and high frequency regions but provided low levels in the mid frequency range. First results from the hairpin packet model look promising compared to other models from the literature when considering the entire frequency range that is solved. However, the SEA modeling of the structure of the aircraft has its limitations and the confidence in the SEA vibro-acoustic model needs to be assessed, independently of the wall-pressure model.

Perspectives

The first task to conduct as future work is to perform additional comparison of the hairpin packet model with numerical and experimental databases of turbulent boundary layer flows subjected to pressure gradients, as well as using the model for SEA simulations over regions of the aircraft with non-zero pressure gradients (cockpit or wing/fuselage junction for instance). An LES computation of a Mach 0.7 zero-pressure gradient turbulent boundary layer with a domain four times longer and twice wider those analyzed in the current study was recently performed at the DynFluid Laboratory. For this case, Reynolds numbers $Re_\theta = O(10^4)$ (an order of magnitude higher than what is presented here) were achieved. An analysis of the coherent structures would provide interesting results on the Reynolds number effect on hairpin vortices and hairpin packets (density, geometry, angles, ...). This would also help improving the the hairpin packet model when considering high Reynolds numbers flows and fulfill the validation needs to ensure the robustness of the model.

In terms of potential improvements, the following paths could be pursued. The measurement of the angle of single hairpin structures would be very interesting in order to characterize the influence of the pressure gradient on this quantity. This can be done by measuring the angle of the $Q2$ event laying between the legs of hairpin vortices in the streamwise/wall-normal planes. Another solution, which is more straightforward, is to store three-dimensional databases for the non-zero pressure gradient cases and perform a statistical reconstruction of the vortices. This will provide directly the angles of the structures as well as their geometry depending the pressure gradient.

Results from the literature are contradictory regarding the contribution of the mean-shear and the turbulent-turbulent source terms in Lighthill's equation for pressure. As study similar to that of Chang et al. (1999) would provide additional results for discussion. It would also characterize the contribution of the different layers (near-wall, logarithmic, outer-region) and coherent structures (hairpin packets, bulges, quasi-streamwise vortices, ...) to the wall-pressure spectrum and its dependence on the pressure gradient. Once again, this is only possible if three-dimensional databases are available.

In the hairpin packet model, the source for the pressure field is the mean-shear term. A calculation including the turbulence-turbulence term would be interesting. This could help evaluate the importance of each term to the wall-pressure spectrum without applying Lighthill's analogy to a three-dimensional velocity field which is numerically costly. For now, all hairpin structures within a packet are the same whereas the analysis of the LES databases has revealed that the eddies downstream of a packet are larger than those upstream of the packet. This aspect would then need to be taken into account in the model. Finally, work still needs to be done concerning the frequency dependence. More accurate knowledge on how the pressure gradient influences the slope of the wavenumber spectrum with increasing frequencies is needed in order to improve the weighting function that has been introduced in the model.

Bibliography

- R.J. Adrian. On the role of conditional averages in turbulence theory. In G. Zakin, J. & Patterson, editor, *Fourth Biennial Symposium on Turbulence in Liquids*, pages 323–332. Science Press, 1975.
- R.J. Adrian. Stochastic estimation of conditional structure: a review. *Applied Scientific Research*, 53:291–303, 1994.
- R.J. Adrian, C.D. Meinhart, and C.D. Tomkins. Vortex organization in the outer region of the turbulent boundary layer. *J. Fluid Mech.*, 422:1–54, 2000.
- B.-K. Ahn, W.R. Graham, and S.A. Rizzi. A structure-based model for turbulent-boundary-layer wall pressures. *J. Fluid Mech.*, 650:443–478, 2010.
- A. Amador Medeiros, L. Alimonti, B. Gardner, S. Callsen, and A. Klages. An SEA modeling of general surface pressure excitations based on their wavenumber-frequency spectrum. *Inter-Noise, Hamburg, Germany*, 2016.
- R.K. Amiet. Noise due to turbulent flow past a trailing edge. *J. Sound Vib.*, 47(3):387–393, 1976.
- R.A. Antonia and L. Fulachier. Topology of a turbulent boundary layer with and without wall suction. *J. Fluid Mech.*, 198:429–451, 1989.
- R.A. Antonia, D.K. Bisset, and L.W.B. Browne. Effect of Reynolds number on the organized motion in a turbulent boundary layer. *J. Fluid Mech.*, 213:267–286, 1990.
- G. Aubard, P. Stefanin Volpiani, X. Gloerfelt, and J.-C. Robinet. Comparison of subgrid-scale viscosity models and selective filtering strategy for large-eddy simulations. *Flow, Turbulence and Combustion*, 91(3):497–518, 2013.
- J.R. Baltzer, R.J. Adrian, and X. Wu. Turbulent boundary layer structure identification via POD. *Center for Turbulence Research*, 2010.
- W.V. Bhat. Flight test measurement of the exterior turbulent boundary layer pressure fluctuations on boeing model 737 airplane. *J. Sound Vib.*, 14:439–457, 1971.
- H. Blackwelder, R.F. and Eckelmann. Streamwise vortices associated with the bursting phenomenon. *J. Fluid Mech.*, 94(03):577–594, 1979.
- R.F. Blackwelder and R.E. Kaplan. On the wall structure of the turbulent boundary layer. *J. Fluid Mech.*, 76:89–112, 1976.
- R.F. Blackwelder and L.S.G. Kovasznay. Time scales and correlations in a turbulent boundary layer. *Phys. Fluids*, 15:1545–1554, 1972.

- W.K. Blake. *Mechanics of flow-induced sound and vibration*, volume 1: General concepts and elementary sources, pages 130–149. Academic Press, Inc, 1986.
- H. Blasius. Grenzsichten in flüssigkeiten mit kleiner reibung. *Z. Math. Phys.*, 56:1–37, 1908.
- C. Bogey and C. Bailly. A family of low dispersive and low dissipative explicit schemes for noise computation. *J. Comput. Phys.*, 194:194–214, 2004.
- J.P. Bonnet, D.R. Cole, J. Delville, M.N. Glauser, and L.S. Ukeiley. Stochastic estimation and proper orthogonal decomposition: complementary techniques for identifying structure. *Experiments in Fluids*, 17:307–314, 1994.
- P. Bradshaw. Inactive motion and pressure fluctuations in turbulent boundary layers. *J. Fluid Mech.*, 30:241–258, 1967a.
- P. Bradshaw. The turbulent structure of equilibrium boundary layers. *J. Fluid Mech.*, 29:625–645, 1967b.
- T.F. Brooks and T.H. Hodgson. Trailing edge noise prediction from measured surface pressures. *J. Sound Vib.*, 78(1):69–117, 1981.
- T.E. Burton. Wall pressure fluctuations at smooth and rough surfaces under turbulent boundary layers with favorable and adverse pressure gradients. Tech. Report 70208-9, Massachusetts Institute of Technology, 1973.
- T.E. Burton. The connection between intermittent turbulent activity near the wall of a turbulent boundary layer with pressure fluctuations at the wall. *Massachusetts Inst. of Tech. Report*, 1, 1974.
- B.J. Cantwell. Organized motion in turbulent flow. *Annual review of fluid mechanics*, 13(1):457–515, 1981.
- L. Castillo and W.K. George. Similarity analysis for turbulent boundary layer with pressure gradient: outer flow. *AIAA Journal*, 39(1):41–47, 2001.
- M.R. Catlett, J.B. Forest, J.M. Anderson, and D.O. Stewart. Empirical spectral model of surface pressure fluctuations beneath adverse pressure gradients. *20th AIAA/CEAS AeroAcoustics Conference*, 16-20 June, Atlanta, GA, USA, AIAA Paper 2014-2910, 2014.
- P. Chakraborty, S. Balachandar, and R.J. Adrian. On the relationships between local vortex identification schemes. *J. Fluid Mech.*, 535:189–214, 2005.
- P. Chang, U. Piomelli, and W. Blake. Relationship between wall pressure and velocity sources. *Phys. Fluids*, 11(11):3434–3448, 1999.
- P.A. Chang. *Relationship between turbulent wall pressure and velocity field sources*. PhD thesis, University of Maryland, College Park, MA, 1998.
- D.M. Chase. Modeling the wavevector-frequency spectrum of turbulent boundary layer wall pressure. *J. Sound Vib.*, 70:29–67, 1980.
- D.M. Chase. The character of the turbulent wall pressure spectrum at subconvective wavenumbers and a suggested comprehensive model. *J. Sound Vib.*, 112(1):125–147, 1987.
- M.S. Chong, A.E. Perry, and B.J. Cantwell. A general classification of three-dimensional flow fields. *Phys. Fluids*, A2:765, 1990.

- K.T. Christensen and R.J. Adrian. Statistical evidence of hairpin vortex packets in wall turbulence. *J. Fluid Mech.*, 431:433–443, 2001.
- F.H Clauser. Turbulent boundary layers in adverse pressure gradients. *Journal of the Aeronautical Sciences*, 21:91–108, 1954.
- J.A. Cockburn and A.C. Jolly. Structural-acoustic response, noise transmission losses and interior noise levels of an aircraft fuselage excited by random pressure fields. Technical report, Air Force Flight Dynamics Laboratory, Air Force Systems Command, AFFDL-TR; 68-2, 1968.
- E. Cohen. *Etude de la pression pariétale et du bruit de couches limites turbulentes avec gradient de pression*. PhD thesis, Ecole Nationale Supérieure des Arts et Métiers, Paris, France, 2015.
- E. Cohen and X. Gloerfelt. Effect of pressure gradients on turbulent boundary layer noise and wall-pressure fluctuations. *21th AIAA/CEAS AeroAcoustics Conference*, 22-26 June, Dallas, TX, USA, AIAA Paper 2015-3117, 2015.
- D. Coles. The law of the wake in the turbulent boundary layer. *J. Fluid Mech.*, 1:191–226, 1956.
- O. Collery. Comparison of turbulent boundary layer auto-spectral models with flight tests results. In *Inter-Noise 2010*, Lisbon, Portugal, 2010.
- O. Collery, M. Etchessahar, and M. Alaoui. Flight deck shape effect on turbulent boundary layer auto-spectrum. In *21st International Congress on Acoustics*, Montreal, Canada, 2013.
- G. Comte-Bellot, J. Sabot, and I. Saleh. Detection of intermittent events maintaining Reynolds stress. In *Proceedings of the Dynamic Flow Conference 1978 on Dynamic Measurements in Unsteady Flows*, pages 213–229. Springer, 1978.
- G.M. Corcos. The structure of the turbulent pressure field in boundary layer flows. *J. Fluid Mech.*, 18:353–378, 1964.
- E.R. Corino and R.S. Brodkey. A visual investigation of the wall region in turbulent flow. *J. Fluid Mech.*, 37(01):1–30, 1969.
- S. Corrsin. Investigation of flow in an axially symmetrical heated jet of air. 1943.
- S. Corrsin and A.L. Kistler. The free-stream boundaries of turbulent flows. *NACA Tech Notes*, (3133), 1954.
- A.D.D. Craik. Non-linear resonant instability in boundary layers. *J. Fluid Mech.*, 50(2):393–413, 1971.
- R. Cucitore, M. Quadrio, and A. Baron. On the effectiveness and limitations of local criteria for the identification of a vortex. *European Journal of Mechanics*, B/F 18:261–282, 1999.
- J. Delery. Effet de la viscosité et couche limite. support de cours : ENSTA-INSTN. 2007.
- D.J.C. Dennis and D.B. Nickels. Experimental measurement of large-scale three-dimensional structures in a turbulent boundary layer. part 1. vortex packets. *J. Fluid Mech.*, 673:180–217, 2011.
- D.M. Dhanak, A.P. Dowling, and C. Si. Coherent vortex model for surface pressure fluctuations induced by the wall region of a turbulent boundary layer. *Phys. Fluids*, 9(2716), 1997.

- S.A. Dixit and O.N. Ramesh. Large-scale structures in turbulent and reverse-transitional sink flow boundary layers. *J. Fluid Mech.*, 649:233–273, 2010.
- P. Druault, X. Gloerfelt, and T. Mervant. Investigation of flow structures involved in sound generation by two- and three-dimensional cavity flows. *Computers and Fluids*, 48:54–67, 2011.
- P.A. Durbin and B.A.P. Reif. Statistical theory and modeling for turbulent flows, 2002.
- H.U. Eckert. Simplified treatment of the turbulent boundary layer along a cylinder in compressible flow. *Journal of the Aeronautical Sciences*, 19(1):23–28, 1952.
- B.M. Efimtsov. Characteristics of the field of turbulent wall pressure fluctuations at large Reynolds numbers. *Soviet Physics - Acoustics*, 28(4):289–292, 1982.
- B.M. Efimtsov, N.M. Kozlov, S.V. Kravchenko, and A.O. Andersson. Wall pressure fluctuation spectra at small forward-facing steps. *AIAA-99-1964*, 1999.
- H.A. Einstein and H. Li. The viscous sublayer along a smooth boundary. *J. Eng. Mech. Div. ASCE*, 82(1), 1956.
- G.E. Elsinga, R.J. Adrian, B.W. Van Oudheusden, and F. Scarano. Three-dimensional vortex organization in a high-Reynolds-number supersonic turbulent boundary layer. *J. Fluid Mech.*, 644:35–60, 2010.
- R. Ewert, M. Meinke, and W. Schröder. Aeroacoustic source terms for the linearized Euler equations. *AIAA Paper 2000-2046*, 2000.
- R. Ewert, J. Dierke, J. Siebert, A. Neifeld, C. Appel, M. Siefert, and O. Kornow. CAA broadband noise prediction for aeroacoustic design. *J. Sound Vib.*, 330(17):4139–4160, 2011.
- F.J. Fahy. Statistical energy analysis: a critical overview. *Philosophical Transactions of the Royal Society of London A: Mathematical, Physical and Engineering Sciences*, 346(1681):431–447, 1994.
- R.E. Falco. Coherent motions in the outer region of turbulent boundary layers. *Physics of Fluids*, 20(10):S124–S132, 1977.
- A.J. Favre, J.J. Gaviglio, and R. Dumas. Space-time double correlations and spectra in a turbulent boundary layer. *J. Fluid Mech.*, 2(04):313–342, 1957.
- H.H. Fernholz and P.J. Finley. A critical commentary on mean flow data for two-dimensional compressible boundary layers. *AGARD-AG-253*, 1980.
- S. Finnveden, F. Birgersson, U. Ross, and T. Kremer. A model of wall pressure correlation for prediction of turbulence-induced vibration. *Journal of Fluids and Structures*, 20(8):1127–1143, 2005.
- B. Ganapathisubramani, N. Hutchins, W.T. Hambleton, E.K. Longmire, and I. Marusic. Investigation of large-scale coherence in turbulent boundary layer using two-point correlations. *J. Fluid Mech.*, 524:57–80, 2005.
- J.R. Gavin. *Unsteady forces and sound caused by boundary layer turbulence entering a turbomachinery rotor*. PhD thesis, The Pennsylvania State University, University Park, PA, 2002.

- X. Gloerfelt and J. Berland. Turbulent boundary-layer noise: direct radiation at Mach number 0.5. *J. Fluid Mech.*, 723:318–351, 2013.
- X. Gloerfelt and P. Lafon. Direct computation of the noise induced by a turbulent flow through a diaphragm in a duct at low Mach number. *Computers and Fluids*, 37:388–401, 2008.
- X. Gloerfelt and F. Margnat. Effect of Mach number on boundary layer noise. *20th AIAA/CEAS AeroAcoustics Conference*, 16-20 June, Atlanta, GA, USA, AIAA Paper 2014-3291, 2014.
- X. Gloerfelt and J.-C. Robinet. A silent inflow condition for the study of boundary layer noise. *19th AIAA/CEAS AeroAcoustics Conference*, 27-29 May, Berlin, Germany, AIAA Paper 2013-2247, 2013.
- P.W. Goodwin. An in-flight supersonic TBL surface pressure fluctuation model. *Contract No. NAS1-20013, Boeing Document*, (D6-81571), 1994.
- M. Goody. Empirical spectral model of surface pressure fluctuations. *AIAA Journal*, 42(9):1788–1794, 2004.
- S.V. Gordeyev and F.O Thomas. A temporal proper decomposition (TPOD) for closed-loop flow control. *Experiments in Fluids*, 54(3), 2013.
- L. Graftieaux, M. Michard, and N. Grosjean. Combining PIV, POD and vortex identification algorithms for the study of unsteady turbulent swirling flows. *Measurement Science and Technology*, 12(9):1422, 2001.
- W.R. Graham. A comparison of models for the wavenumber-frequency spectrum of turbulent boundary layer pressures. *J. Sound Vib.*, 206(4):541–565, 1997.
- H.L. Grant. The large eddies of turbulent motion. *J. Fluid Mech.*, 4(02):149–190, 1958.
- E.J. Gutmark, S. Verfaillie, J-P. Bonnet, and F. Grinstein. Linear stochastic estimation of a swirling jet. *AIAA Journal*, 44(3):457–468, 2006.
- G. Haller. Lagrangian coherent structures from approximate velocity data. *Physics of Fluids (1994-present)*, 14(6):1851–1861, 2002.
- G. Haller. An objective definition of a vortex. *J. Fluid Mech.*, 525:1–26, 2005.
- G. Haller and F.J. Beron-Vera. Coherent Lagrangian vortices: the black holes of turbulence. *J. Fluid Mech.*, 731:R4, 2013.
- W.T. Hambleton, N. Hutchins, and I. Marusic. Simultaneous orthogonal-plane particle image velocimetry measurements in a turbulent boundary layer. *J. Fluid Mech.*, 560:53–64, 2006.
- Z. Harun, J.P. Monty, R. Mathis, and I. Marusic. Pressure gradient effects in the large-scale structure of turbulent boundary layers. *J. Fluid Mech.*, 715:477–498, 2013.
- G-S. He, C. Pan, L-H. Feng, Q. Gao, and J-J. Wang. Evolution of Lagrangian coherent structures in a cylinder-wake disturbed flat plate boundary layer. *J. Fluid Mech.*, 792:274–306, 2016.
- G-W. He and J-B. Zhang. Elliptic model for space-time correlations in turbulent shear flows. *Physical Review E*, 73(5):055303, 2006.
- M.R. Head and P. Bandyopadhyay. New aspects of turbulent boundary layer structures. *J. Fluid Mech.*, 107:297–338, 1981.

- P.H. Hoffmann, K.C. Muck, and P. Bradshaw. The effect of concave surface curvature on turbulent boundary layers. *J. Fluid Mech.*, 161:371–403, 1985.
- P.J. Holmes, J.L. Lumley, and G. Berkooz. *Turbulence, coherent structures, symmetry and dynamical systems*. Cambridge University Press, 1996.
- M.S. Howe. *Acoustics of fluid-structures interactions*, chapter 3, Sound generation in a fluid with rigid boundaries, pages 164–166. Cambridge University Press, 1998.
- N. Hu and M. Herr. Characteristics of wall pressure fluctuations for a plate turbulent boundary layer with pressure gradients. *22nd AIAA/CEAS AeroAcoustics Conference*, 30 May - 1 June, Lyon, USA, AIAA Paper 2016-2749, 2016.
- N. Hu, C. Appel, M. Herr, N. Reiche, and R. Ewert. Numerical study of wall pressure fluctuations for zero and non-zero pressure gradient turbulent boundary layers. *22nd AIAA/CEAS AeroAcoustics Conference*, 30 May - 1 June, Lyon, USA, AIAA Paper 2016-2911, 2016.
- J.C.R. Hunt, A.A. Wray, and P. Moin. Eddies, stream, and convergence zones in turbulent flows. Tech. Report CTRS88, Center for Turbulence Research, 1988.
- A.K.M.F. Hussain. Coherent structures and turbulence. *J. Fluid Mech.*, 173:303–356, 1986.
- N. Hutchins, W.T. Hambleton, and I. Marusic. Inclined cross-stream stereo particle image velocimetry measurements in turbulent boundary layers. *J. Fluid Mech.*, 541:21–54, 2005.
- T. Hyhlík and H. Netrebská. Evaluation of travelling vortex speed by means of dynamic mode decomposition and residual vorticity. *EPJ Web of Conferences*, 114, 2016.
- A.J Izzo. An experimental investigation of the turbulent characteristics of a boundary layer flow over a vibrating plate. Technical Report U417-69-049, DTIC Document, 1969.
- J. Jeong and F. Hussain. On the identification of a vortex. *J. Fluid Mech.*, 285:69–94, 1995.
- A.V. Johansson, P.H. Alfredsson, and H. Eckelmann. On the evolution of shear-layer structures in near-wall turbulence. In *Advances in turbulence*, pages 383–390. Springer, 1987.
- A.V. Johansson, P.H. Alfredsson, and J. Kim. Evolution and dynamics of shear-layer structures in near-wall turbulence. *J. Fluid Mech.*, 224:579–599, 1991.
- M.B. Jones, I. Marusic, and A.E. Perry. Evolution and structure of sink-flow turbulent boundary layers. *J. Fluid Mech.*, 428:1–27, 2001.
- C. Juan, D. Álamo, J. Jiménez, P. Zandonade, and R.D. Moser. Self-similar vortex clusters in the turbulent logarithmic region. *J. Fluid Mech.*, 561:329–358, 2006.
- M.C. Junger and D. Feit. *Sound, structures, and their interaction*, volume 225. MIT press Cambridge, MA, 1986.
- T. Kameda, M. Shinsuke, and H. Osaka. Non-equilibrium and equilibrium boundary layers without pressure gradient. In *IUTAM Symposium on Computational Physics and New Perspectives in Turbulence*, pages 197–202. Springer, 2008.
- Y-C Kan, I. Beckman, and M.P. Martín. Turbulence structure and wall signature in hypersonic boundary layer. *43rd AIAA Fluid Dynamics Conference*, 24-27 June, San Diego, CA, USA, AIAA Paper 2013-3119, 2013.

- T. Kármán. Mechanische Ähnlichkeit und Turbulenz. *Nachrichten von der Gesellschaft der Wissenschaften zu Göttingen, Fachgruppe 1*, 5:58–76, 1930.
- S. Kida and H. Miura. Identification and analysis of vortical structures. *European Journal of Mechanics*, B/F 17:471–488, 1998.
- H. Kim, S.J. Kline, and W.C. Reynolds. The production of turbulence near a smooth wall in a turbulent boundary layer. *J. Fluid Mech.*, 50(01):133–160, 1971.
- Y.N. Kim and A.R. George. Trailing edge noise from hovering rotors. *AIAA Journal*, 20(9): 1167–1174, 2005.
- A. Klages, C. Appel, and M. Herr. Fuselage excitation during cruise flight conditions: Measurement and prediction of pressure point spectra. *21st AIAA/CEAS AeroAcoustics Conference*, 22-26 June, Dallas, TX, USA, AIAA Paper 2015-3115, 2015.
- A. Klages, C. Appel, M. Herr, and S. Callsen. Fuselage excitation during cruise flight conditions: a new CFD based pressure point spectra model. *Inter-Noise, Hamburg, Germany*, 2016.
- P.S. Klebanoff. Characteristics of turbulence in boundary layer with zero pressure gradient. *NACA TN-3178*, Report 1247:1135–1153, 1954.
- S.J. Kline. The role of visualization in the study of the structure of the turbulent boundary layer. *Coherent Structure of Turbulent Boundary Layers*, pages 1–26, 1978.
- S.J. Kline and R.E. Falco. Summary of the AFOSR. In *MSU research specialists workshop on coherent structure in turbulent boundary layers*, pages 1–56, 1979.
- S.J. Kline and P.W. Runstadler. Some preliminary results of visual studies of the flow model of the wall layers of the turbulent boundary layer. *Trans. ASME*, pages 166–70, 1959.
- S.J. Kline, W.C. Reynolds, F.A. Schraub, and P.W. Runstadler. The structure of turbulent boundary layers. *J. Fluid Mech.*, 30(04):741–773, 1967.
- A.N. Kolmogorov. The local structure of turbulence in incompressible viscous fluid for very large Reynolds numbers. *Proceedings of the USSR Academy of Sciences*, 30:299–303, 1941a.
- A.N. Kolmogorov. Dissipation of energy in the locally isotropic turbulence. *Proceedings of the USSR Academy of Sciences*, 32:16–18, 1941b.
- B.O. Koopman. Hamiltonian systems and transformations in Hilbert space. *P. Natl. Acad. Sci. USA*, 17:315–318, 1931.
- L.S.G. Kovaszny. Structure of the turbulent boundary layer. *Physics of Fluids (1958-1988)*, 10(9):S25–S30, 1967.
- L.S.G. Kovaszny, V. Kibens, and R.F. Blackwelder. Large-scale motion in the intermittent region of a turbulent boundary layer. *J. Fluid Mech.*, 41(02):283–325, 1970.
- R.H. Kraichnan. Pressure fluctuations in a turbulent flow over a flat plate. *J. Acoust. Soc. Am.*, 28(3):378–390, 1956.
- P.-A. Krogstad and R.A. Antonia. Structure of turbulent boundary layers on smooth and rough walls. *J. Fluid Mech.*, 277:1–21, 1994.

BIBLIOGRAPHY

- A.L. Laganelli and H.F. Wolfe. Prediction of fluctuating pressure in attached and separated turbulent boundary-layer flow. *Journal of Aircraft*, 30(6):962–970, 1993.
- L. Landweber. Effect of transverse curvature on frictional resistance. Technical report, DTIC Document, 1949.
- J. Laufer. The structure of turbulence in fully developed pipe flow. 1954.
- A. Le Bot. *Foundation of statistical energy analysis in vibroacoustics*. OUP Oxford, 2015.
- J.-H. Lee and H.J. Sung. Structures in turbulent boundary layers subjected to adverse pressure gradients. *J. Fluid Mech.*, 639:101–131, 2009.
- M.J. Lighthill. On sound generated aerodynamically I. General theory. *Proc. of the Royal Society of London*, A 211:564–587, 1952.
- M.J. Lighthill. On sound generated aerodynamically II. Turbulence as a source of sound. *Proc. of the Royal Society of London*, A 222:1–32, 1954.
- Z. Liu, R.J. Adrian, and T.J. Hanratty. Large-scale modes of turbulent channel flow: transport and structure. *J. Fluid Mech.*, 448:53–80, 2001.
- M.V. Lowson. Prediction of boundary layer pressure fluctuations. Technical report, DTIC Document, 1968.
- H.J. Lugt. The dilemma of defining a vortex. In B. Schmidt V. Muller, K. G. Roesner, editor, *Recent Developments in Theoretical and Experimental Fluid Mechanics*, pages 309–321, berlin, Springer-Verlag, 1979.
- J.L. Lumley. Coherent structures in turbulence. In R. E. Meyer, editor, *Transition and Turbulence*, pages 215–241, 1981.
- R.H. Lyon. *Statistical energy analysis of dynamical systems: theory and applications*. MIT Press, 1975.
- R.H. Lyon and G. Maidanik. Power flow between linearly coupled oscillators. *The Journal of the Acoustical Society of America*, 34(5):623–639, 1962.
- M.H.S. Mayam. *Experimental study of the turbulence structures in a boundary layer subjected to a strong adverse pressure gradient*. PhD thesis, Faculté des Sciences et de Génie de l’Université de Laval, Québec, Canada, 2009.
- B.E. McGrath and R.L. Simpson. Some features of surface pressure fluctuations in turbulent boundary layers with zero and favorable pressure gradients. Tech. Report CR-4051, NASA, 1988.
- W.C. Meecham and M.T. Travis. Theoretical pressure correlation functions in turbulent boundary layers. *Phys. Fluids*, 23:1119–1131, 1980.
- M.V. Melander and F. Hussain. Polarized vorticity dynamics on a vortex column. *Phys. Fluids*, A 5:1992, 1993.
- R.H. Mellen. On modeling convective turbulence. *Journal of the Acoustical Society of America*, 88(6):2991–2893, 1990.

- A.G. Mercer. Turbulent boundary layer flow over a flat plate vibrating with transverse standing waves. Tech. Report 41, series B, St. Anthony Falls Hydraulic Laboratory, 1962.
- R.N. Meroney and P. Bradshaw. Turbulent boundary-layer growth over a longitudinally curved surface. *AIAA Journal*, 13(11):1448–1453, 1975.
- S.T. Miller. Turbulent boundary layer models for acoustic analysis. Master’s thesis, Wichita State University, 2002.
- P. Moin, R.J. Adrian, and J. Kim. Stochastic estimation of organized structures in turbulent channel flow. In *Symposium of Turbulent Shear Flow*, Toulouse, France, September 1987.
- S. Monte. *Evaluation du bruit hydrodynamique sur une antenne linéaire remorquée*. PhD thesis, Université Pierre et Marie Curie, Paris VI, Paris, France, 2013.
- J.F. Morrison, H.M. Tsai, and P. Bradshaw. Conditional-sampling schemes for turbulent flows, based on the variable-interval time averaging (VITA) algorithm. *Experiments in Fluids*, 7: 173, 1988.
- R.D. Moser. *Statistical analysis of near-wall structures in turbulent channel flow*, chapter 5, Fundamentals of flow-induced vibration and noise, pages 45–62. New York: Hemisphere Publ., 1990.
- K.C. Muck, P.H. Hoffmann, and P. Bradshaw. The effect of convex surface curvature on turbulent boundary layers. *J. Fluid Mech.*, 161:347–369, 1985.
- D. Musker. Explicit expression for the smooth wall velocity distribution in a turbulent boundary layer. *AIAA Journal*, 17:655–657, 1979.
- S. Nakagawa and T.J. Hanratty. Particle image velocimetry measurements of flow over a wavy wall. *Phys. Fluids*, 13(11):3504–3507, 2001.
- V.K. Natrajan, Y. Wu, and K.T. Christensen. Spatial signatures of retrograde spanwise vortices in wall turbulence. *J. Fluid Mech.*, 574:155–167, 2007.
- L.R. Panton and J.H. Linebarger. Wall pressure spectra calculations for equilibrium boundary layers. *J. Fluid Mech.*, 65(Part. 2):261–287, 1974.
- L.J. Peltier and S.A. Hambric. Estimating turbulent boundary layer wall pressure spectra from CFD RANS solutions. *J. Fluids Struct.*, 23:920–937, 2007.
- S.B. Pope. *Turbulent flows*. Cambridge University Press, 2000.
- A. Powell. Aerodynamic noise and the plane boundary. *J. Acoust. Soc. Am.*, 32(8):982–990, 1960.
- L. Prandtl. Über Flüssigkeits bewegung bei sehr kleiner Reibung. *Verhaldlg III Int. Math. Kong.*, pages 484–491, 1904.
- A.K. Praturi and R.S. Brodkey. A stereoscopic visual study of coherent structures in turbulent shear flow. *J. Fluid Mech.*, 89(02):251–272, 1978.
- R.G. Rackl and A. Weston. Modeling of turbulent boundary layer surface pressure fluctuations auto and cross spectra - verification and adjustments based on TU-144LL data. *NASA/TM*, (209858), 2005.

- H. Reichardt. Complete representation of the turbulent velocity distribution in smooth pipes. *Z. Angew Math. Mech.*, (31):208–219, 1951.
- D. Rempfer and H.F. Fasel. Evolution of three-dimensional coherent structures in a flat-plate boundary layer. *J. Fluid Mech.*, 260:351–375, 1994.
- S.A. Rizzi, R.G. Rackl, and E.V. Andrianov. Flight test measurement from the TU-144LL structure/cabin noise experiment. *NASA/CR*, (213938), 2000.
- J.E. Robertson. Prediction of in-flight fluctuating pressure environments including protuberance induced flow. Tech. Report CR-119947, NASA, 1971.
- S.K. Robinson. Coherent motions in the turbulent boundary layer. *Annual Review of Fluid Mechanics*, 23:601–639, 1991a.
- S.K. Robinson. The kinematics of turbulent boundary layer structure. *NASA STI/Recon Technical Report N*, 91:26465, 1991b.
- J.C. Rotta. Über die Theorie der turbulenten Grenzschichten. *Mitteilungen aus dem Max-Planck-Institut für Strömungsforschung*, (1), 1950.
- C.W. Rowley, I. Mezic, S. Bagheri, P. Schlatter, and D.S. Henningson. Spectral analysis of nonlinear flows. *J. Fluid Mech.*, 641:115–127, 2009.
- Y. Rozenberg. *Modélisation analytique du bruit aérodynamique à large bande des machines tournantes : utilisation de calculs moyennés de mécanique des fluides*. PhD thesis, Ecole Centrale de Lyon, Lyon, France, 2007.
- E. Salze, C. Bailly, O. Marsden, E. Jondeau, and D. Juvé. An experimental characterisation of wall pressure wavevector-frequency spectra in the presence of pressure gradients. *20th AIAA/CEAS AeroAcoustics Conference*, 16-20 June, Atlanta, GA, USA, AIAA Paper 2014-2909, 2014.
- P. Schlatter and R. Örlü. Assessment of direct numerical simulation data of turbulent boundary layers. *J. Fluid Mech.*, 659:116–126, 2010.
- M. Schlegel, B.R. Noack, P. Jordan, A. Dillmann, E. Gröeschel, W. Schröder, M. Wei, J.B. Freund, O. Lehmann, and G. Tadmor. On least-order flow representations for aerodynamics and aeroacoustics. *J. Fluid Mech.*, 697:367–398, 2012.
- H. Schlichting and K. Gersten. *Boundary Layer Theory*. Springer, 8th revised and enlarged edition edition, 2000.
- H.H. Schloemer. Effects of pressure gradients on turbulent-boundary-layer wall-pressure fluctuations. *J. Acoust. Soc. Am.*, 42(1):93–113, 1967.
- P.J. Schmid and J. Sesterhenn. Dynamic mode decomposition of numerical and experimental data. In *61st Annual Meeting of the APS Division of Fluid Dynamics*, San Antonio, TX, USA, November 2008.
- A. H. Shapiro. Film notes for vorticity. In *National Committee for Fluid Mechanics Films*, MIT, Cambridge, Massachusetts, 1969.
- M. Sieber, C.O. Paschereit, and K. Oberleithner. Spectral proper orthogonal decomposition. *J. Fluid Mech.*, 792:798–828, 2016.

- M. Siefert and R. Ewert. Sweeping sound generation in jets realized with a Random Particle-Mesh method. *AIAA Paper*, (2009-3369), 2009.
- S.G Siegel, J. Seidel, C. Fagley, D.M. Luchtenburg, K. Cohen, and T. McLaughlin. Low-dimensional modelling of a transient cylinder wake using double proper orthogonal decomposition. *J. Fluid Mech.*, 610:1–42, 2008.
- R. Simpson, M. Ghodbane, and B. McGrath. Surface pressure fluctuations in a separating turbulent boundary layer. *J. Fluid Mech.*, 177:167–186, 1987.
- C.R. Smith and S.P. Metzler. The characteristics of low-speed streaks in the near-wall region of a turbulent boundary layer. *J. Fluid Mech.*, 129:27–54, 1983.
- A.V. Smol'yakov. Calculation of the spectra of pseudosound wall-pressure fluctuations in turbulent boundary layers. *Acoustical Physics*, 46(3):342–347, 2000.
- A.V. Smol'Yakov, V.M. Tkachenko, and J.S. Wood. Model of a field of pseudosonic turbulent wall pressures and experimental data. *Soviet physics. Acoustics*, 37(6):627–631, 1991.
- P.R. Spalart and J.H. Watmuff. Experimental and numerical study of a turbulent boundary layer with pressure gradients. *J. Fluid Mech.*, 249:337–371, 1993.
- C.K.W. Tam and Z. Dong. Radiation and outflow boundary conditions for direct computation of acoustic and flow disturbances in a nonuniform mean flow. *J. Comput. Acous.*, 4(2):175–201, 1996.
- Z. Tang and N. Jiang. Dynamic mode decomposition of hairpin vortices generated by a hemisphere protuberance. *Science China: Physic, Mechanics & Astronomy*, 55(1):118–124, 2012.
- G.F.K. Tay, D.C.S. Kuhn, and M.F.. Tachie. Adverse and favourable pressure gradient turbulent flows over smooth and rough surfaces. *39th AIAA Fluid Dynamics Conference*, 22-25 June, San Antonio, TX, USA, AIAA Paper 2009-4046, 2009.
- T. Theodorsen. Mechanisms of turbulence. pages 1–19, Ohio State University, 1952.
- S.P. Timoshenko and S. Woinowsky-Krieger. *Theory of plates and shells*. McGraw-hill, 1959.
- A.A. Townsend. On the fine-scale structure of turbulence. In *Proceedings of the Royal Society of London A: Mathematical, Physical and Engineering Sciences*, volume 208, pages 534–542. The Royal Society, 1951.
- A.A. Townsend. The structure of turbulent shear flow. *Cambridge University Press*, 1st ed., 1976a.
- A.A. Townsend. The structure of turbulent shear flow. *Cambridge University Press*, 2nd ed., 1976b.
- C. Truesdell. The kinematics of vorticity. Indiana University, 1953.
- F. Tubino and G. Solari. Double proper orthogonal decomposition for representing and simulating turbulence fields. *J. Eng. Mech.-ASCE*, 131(12):1302–1312, 2005.
- R.J. Volino, M.P. Schultz, and K.A. Flack. Turbulent structure in rough and smooth wall boundary layers. *J. Fluid Mech.*, 592:263–293, 2007.

BIBLIOGRAPHY

- H. Vollmers. Detection of vortices and quantitative evaluation of their main parameters from experimental velocity data. *Measurement Science and Technology*, 12(8):1199, 2001.
- J.M. Wallace, H. Eckelmann, and R.S. Brodkey. The wall region in turbulent shear flow. *J. Fluid Mech.*, 54(01):39–48, 1972.
- F.M. White. *Viscous fluid flow*. McGraw-Hill, Mechanical Engineering Series, second edition edition, 1991.
- W.W. Willmarth. Pressure fluctuations beneath turbulent boundary layers. *Ann. Rev. Fluid Mech.*, 7:13–38, 1975.
- W.W. Willmarth and S.S. Lu. Structure of the Reynolds stress near the wall. *J. Fluid Mech.*, 55(01):65–92, 1972.
- W.W. Willmarth and F.W. Roos. Resolution and structure of the wall pressure field beneath a turbulent boundary layer. *J. Fluid Mech.*, 22:81–94, 1965.
- W.W. Willmarth and C.E. Woolridge. Measurements of the fluctuating pressure at the wall beneath a thick turbulent boundary layer. *J. Fluid Mech.*, 14:187–210, 1962.
- Y. Wu and K.T. Christensen. Population trends of spanwise vortices in wall turbulence. *J. Fluid Mech.*, 568:55–76, 2006.
- A.D. Young. *Boundary Layers*. AIAA Education Series, 1989.
- J.C. Yu and M.C. Joshi. On sound radiation from the trailing edge of an isolated airfoil in a uniform flow. *AIAA Paper*, (79-0603):1979, 1979.
- Y.S. Yu. Effects of transverse curvature on turbulent boundary layer characteristics. *J. Ship Res*, 3:33–41, 1958.
- Q. Zhang, L. Yingzheng, and S. Wang. The identification of coherent structures using proper orthogonal decomposition and dynamic mode decomposition. *Journal of Fluid and Structures*, 49, 2014.
- C.D. Zhou, R.J. Adrian, S. Balachandar, and T.M Kendall. Mechanisms for generating coherent packets of hairpin vortices in channel flow. *J. Fluid Mech.*, 388:353–396, 1999.

Résumé long en français

Structures turbulentes et modélisation de la pression pariétale pour une couche limite turbulente en présence de gradients de pression

Thèse de doctorat de l'École Nationale Supérieure des Arts et Métiers, Spécialité "Mécanique et Matériaux"

Soutenue par Miloud ALAOUI le 19 décembre 2016 devant le jury :

- Pr. Christophe BAILLY, Professeur, LMFA, École Centrale de Lyon, France Examineur
- Pr. Jan DELFS, Professeur, DLR Braunschweig, Germany Rapporteur
- Pr. Jean-Marc FOUCAULT, Professeur, École Centrale de Lille, France Président
- Pr. Xavier GLOERFELT, Professeur, DynFluid, Art et Métiers ParisTech, Paris, France Directeur de thèse
- Pr. William GRAHAM, Professeur, Cambridge University, UK Rapporteur
- Pr. Laurent JOLY, Professeur, ISAE Toulouse, France Examineur
- Dr. Alois SENGISSSEN, Ingénieur de recherche, Airbus Operations, Toulouse, France Tuteur industriel

1. INTRODUCTION

Cette étude se concentre sur le rôle des structures turbulentes, dites aussi structures cohérentes, dans l'excitation de panneaux d'avion soumis à un écoulement de couche limite turbulente en présence de gradients de pression longitudinaux. Le bruit généré par des écoulements autour de véhicules est devenu un enjeu majeur pour l'industrie du transport depuis que les niveaux de bruits liés aux éléments propulsifs ont considérablement été réduits. Il s'agit d'une thèse Cly□Ry□ lancée par Airbus, en partenariat avec le laboratoire DynFluid de l'École Nationale Supérieure d'Arts et Métiers de Paris.

2. CONTEXTE ET MOTIVATIONS

Depuis plus d'un demi-siècle, les constructeurs aéronautiques s'efforcent de réduire le bruit des turboréacteurs qui constitue une forte gêne à l'intérieur de l'appareil mais également autour des aéroports. Ainsi, la couche limite turbulente, à savoir la région de l'écoulement sur la peau d'un véhicule ayant un caractère turbulent, est devenue la principale source de bruit et d'inconfort sonore pour les passagers et les membres d'équipage en régime de croisière (voir Figure 1). Par conséquent, de nombreuses études ont été menées, à travers des mesures en soufflerie mais aussi des essais en vol, pour caractériser et modéliser le bruit de couche limite dans le but d'améliorer les méthodes d'isolation phonique des avions.

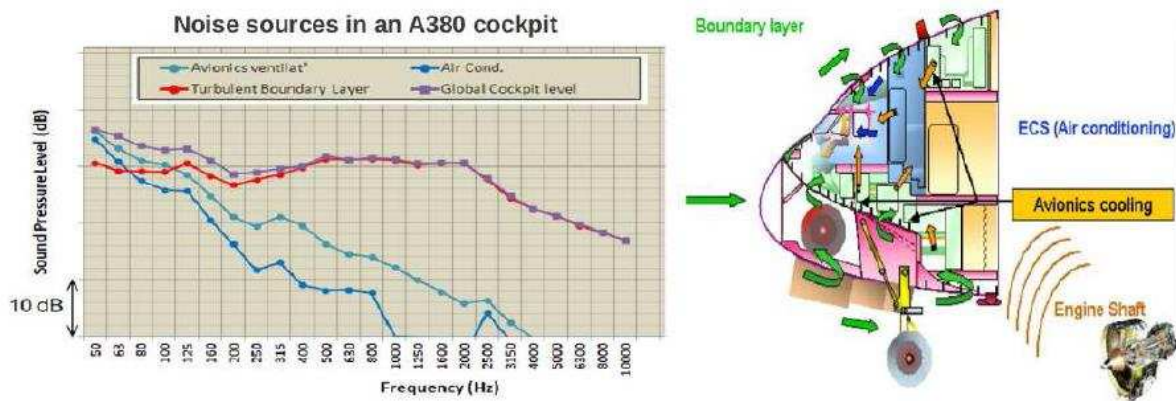


Figure 1 - Niveaux et sources de bruit dans un cockpit d'Airbus A380

Le mécanisme de génération de bruit intérieur par un écoulement externe est assez simple (voir Figure 2). Le caractère turbulent de la couche limite induit des fluctuations de pression instationnaires sur les panneaux du fuselage qui se mettent alors à vibrer. Ces vibrations sont transmises à travers la structure de l'avion et rayonnent (rayonnement acoustique) dans la cabine et le cockpit.

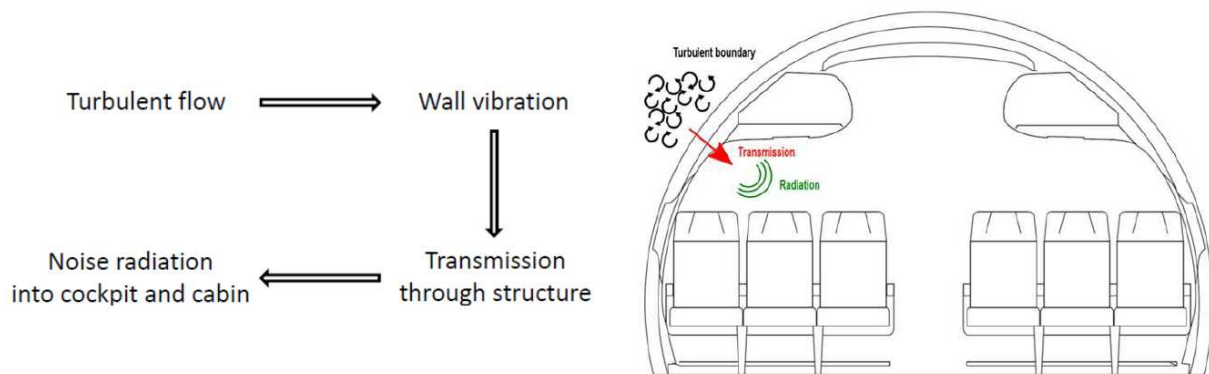


Figure 2 - Mécanisme de transmission du bruit de couche limite

Les modèles de pression pariétale sous une couche limite turbulente qui existent aujourd'hui ne sont pas adaptés pour les régions de l'avion soumises à des gradients de pression, tels que la pointe avant et la jonction aile/fuselage. Grâce aux avancées en terme d'algorithme, de puissance de calcul et des méthodes numériques ces dernières années, de nouveaux moyens d'investigation des écoulements pariétaux ont pu être développés afin de caractériser plus précisément les structures turbulentes existantes dans la couche limite à des nombres de Mach représentatifs des applications industrielles.

En effet, les fluctuations de pression qui excitent la peau de l'appareil ne sont que l'empreinte des structures turbulentes. Il est alors primordial d'étudier ces structures afin d'appréhender au mieux le bruit lié aux écoulements et de construire des modèles de prédiction plus robustes.

La très grande majorité des études s'intéressent à l'écoulement canonique d'une couche limite turbulente sur plaque plane et sans gradient de pression. De nombreuses études ont également été menées sur des couches limites soumises à un gradient de pression adverse (gradient de pression positif dans la direction de l'écoulement) puisque ce type de gradient peut être critique dans des applications industrielles ; un gradient adverse fort peut par exemple entraîner une séparation de la couche limite au-dessus des ailes d'un avion conduisant à une perte soudaine de la portée ou encore induire un effet de pompage dans les turbomachines. Le dernier type de gradient, dit gradient favorable (gradient de pression négatif dans la direction de l'écoulement) arrive quant à lui en dernière position en terme de quantité d'études.

Toutefois, malgré une littérature prépondérante sur la couche limite, les structures cohérentes ont été assez peu regardées, en particulier lorsque l'écoulement est soumis à un gradient de pression. De plus, le rôle de ces structures dans la production de la turbulence et au transport de masse et de quantité de mouvement est un élément bien connu depuis plusieurs années, mais peu d'éléments existent quant à leur contribution aux fluctuations de pression pariétale.

3. OBJECTIFS

Aujourd'hui, les constructeurs aéronautiques montrent un intérêt croissant pour le bruit généré par l'écoulement autour du fuselage et du cockpit. Ils utilisent des moyens de prédiction du bruit intérieur basé sur des modèles analytiques de pression pariétale qui manquent de robustesse, notamment dans les régions à géométries non canoniques. Par conséquent, deux objectifs principaux ont été fixés pour cette étude :

1. D'un point de vue phénoménologique, comprendre l'effet d'un gradient de pression sur l'excitation de couche limite en s'intéressant aux structures cohérentes qui existent dans un tel écoulement. De nombreux auteurs ont identifié le « hairpin » (tourbillon en forme d'épingle à cheveux), comme étant l'une des structures la plus fréquemment observée dans l'écoulement de couche limite et on suppose qu'il a un rôle majeur sur la pression pariétale.
2. De construire un modèle stochastique de prédiction du spectre de pression pariétale. Ce modèle aura cette propriété peu commune de prendre en compte les caractéristiques turbulentes de l'écoulement, contrairement à la grande majorité des modèles qui ne se basent principalement que sur des grandeurs moyennes. Malgré un degré de complexité plus élevé, il conviendra de bâtir un modèle adapté à des applications industrielles, notamment en terme de ressources et de temps de calcul.

Cette étude a été menée en parallèle du projet SONOBL (Source of Noise from Boundary Layer over vehicles) et coordonnée par le laboratoire de mécanique des fluides DynFluid de l'Ecole Nationale Supérieure d'Arts et Métiers (ENSAM) de Paris, en collaboration avec le Laboratoire de Mécanique des Fluides et d'Acoustique (LMFA) de l'Ecole Centrale de Lyon (ECL), Airbus, Renault et Dassault. Dans le cadre de ce projet, une importante base de données numérique issue de Simulation aux Grandes Echelles (Large Eddy Simulation LES) de couches limites turbulentes soumises à des gradients de pression nul et non-nuls a été produite. Les résultats de ces calculs ont pu être comparés à des mesures d'écoulements équivalents effectués en soufflerie au LMFA. Le travail mené dans cette thèse a consisté à post-traiter les bases numériques LES en se concentrant tout particulièrement sur l'étude des structures cohérentes de type hairpin.

4. ORGANISATION DE LA THÈSE

Cette thèse s'articule autour de trois axes majeurs.

1. Une revue bibliographique des écoulements de couches limites turbulentes soumises à des gradients de pression en se focalisant particulièrement sur les structures cohérentes, notamment les tourbillons de type hairpin. L'étude de ces structures repose sur des méthodes de visualisations et d'identifications d'évènements présentant une certaine cohérence spatiale et/ou temporelle. Ces outils d'analyse, qui peuvent être instantanés ou statistiques, constituent une part essentielle de l'étude bibliographique. Enfin, une bonne connaissance des travaux liés aux fluctuations de pression pariétale sous une couche limite et des modèles de prédiction d'une structure mécanique par un écoulement turbulent constituent également une base nécessaire pour atteindre les objectifs de ce travail de recherche.
2. La majeure partie de cette thèse correspond au post traitement de bases de données numériques de champs de vitesses de couches limites turbulentes issus de calcul LES. Quatre types d'écoulement étaient disponibles : gradient de pression nul, favorable et deux adverses. Un gradient de pression adverse introduit un véritable changement dans l'écoulement, comparativement à un écoulement canonique ; il était donc intéressant d'étudier deux cas de gradients de pression adverses, un faible et un plus intense. Au vu des objectifs fixés, cette étude s'est concentrée sur les tourbillons de type hairpin et la manière dont ils sont affectés par la présence d'un gradient de pression.

- Les résultats de l'étude des structures cohérentes ont alors servi de point d'entrée à la construction d'un modèle stochastique de spectre de la pression pariétale. Ce modèle, inspiré du modèle de Ahn et al. (JFM 2010), repose sur les tourbillons hairpin pour créer un champ de pression instantanée à la paroi qui prend en compte les effets d'un gradient de pression. Le point final de cette thèse a consisté à appliquer ce modèle à une portion d'un fuselage d'avion afin de prédire l'accélération des panneaux de la peau de l'appareil soumis à un écoulement dans des conditions de croisière.

5. PRINCIPAUX RÉSULTATS

En présence d'un obstacle, la vitesse d'un écoulement à sa paroi est nulle dû à la viscosité du fluide. La couche limite est alors la région de l'écoulement où la vitesse du fluide passe de zéro $u = 0$ à la vitesse de l'écoulement libre loin de l'obstacle U_∞ comme le montre la Figure 3. Dans une majorité d'applications industrielles, les vitesses importantes des écoulements, les contraintes mécaniques et géométriques induisent un régime turbulent.

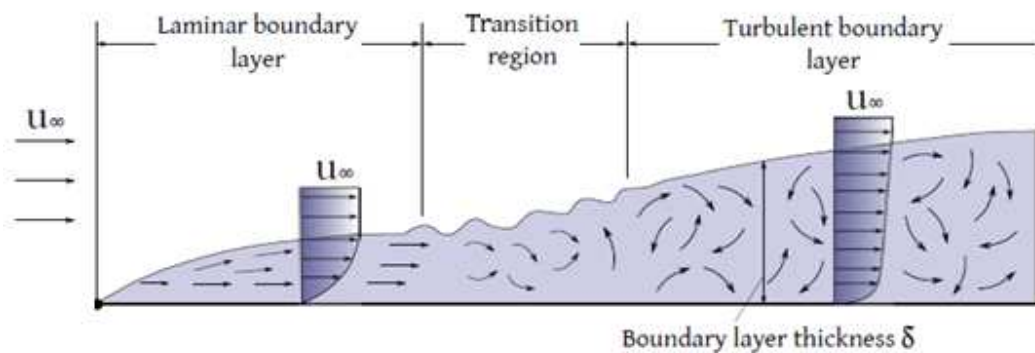


Figure 3 - La couche limite turbulente

Le caractère désordonné d'un écoulement turbulent est relatif. En effet, depuis la fin des années 1950, il a été montré qu'il existe des régions de l'écoulement où des grandeurs telles que le champ de vitesse ou de pression présentent une certaine cohérence spatiale et/ou temporelle. Ces régions sont nommées structures turbulentes, structures cohérentes, évènements turbulents ou encore évènement cohérents. Parmi les plus connus dans les écoulements de couche limite turbulente, on peut citer :

- les sweeps et ejections, qui sont respectivement des mouvements rapides proches paroi de fluides projetés en direction de la paroi et de fluides éjectés loin de la paroi.
- les low et high-speed streaks, qui sont des structures longitudinales proche paroi de faible et grande quantité de mouvement respectivement (voir Figure 4).
- les bulges qui sont des structures grandes échelles dans la partie externe de la couche limite séparées par des « vallées » de fluide non turbulent (voir Figure 5).
- les tourbillons qui sont des régions où le fluide présente un mouvement de rotation.

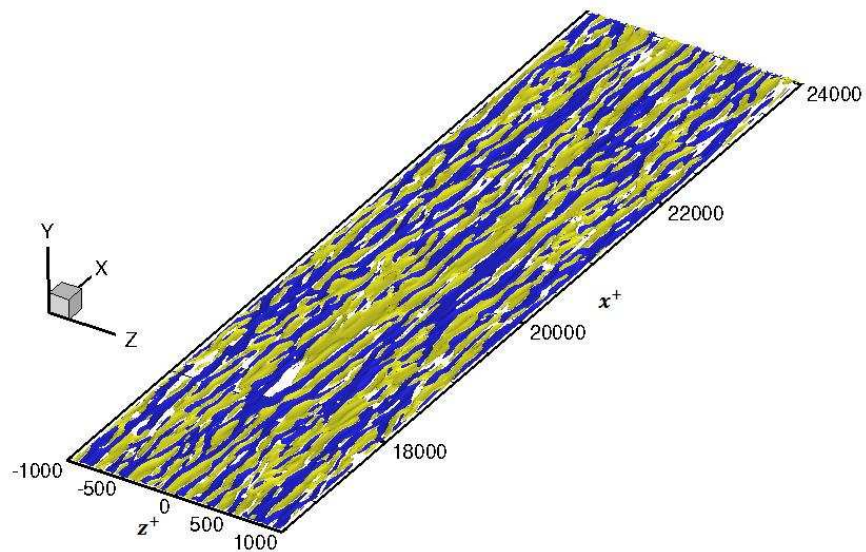


Figure 4 - Isocontours de la vitesse proche de la paroi révélant les structures low-speed streaks (bleu) et high-speed streaks (jaune).

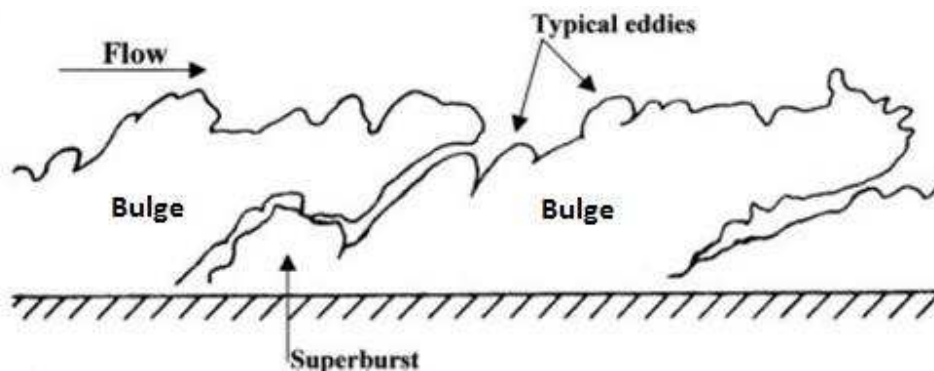


Figure 5 - Schéma de couche limite turbulente montrant les structures grande échelle « bulges » séparées par des « vallées » d'écoulement non turbulent.

Dans cette étude, nous nous intéressons particulièrement aux structures tourbillonnaires dites « hairpin ». Il s'agit de structures présentant une forme d'épingle à cheveux ou de fer à cheval, caractérisées par deux jambes, un cou, et une tête transversale à la direction de l'écoulement tel que le montre la Figure 6. On peut également y voir une organisation en paquet, i.e un groupement de plusieurs hairpins alignés avec l'écoulement. Cette structure grande échelle a été observée dans tous les écoulements de couche limite où l'auteur s'intéressait à l'étude des hairpins.

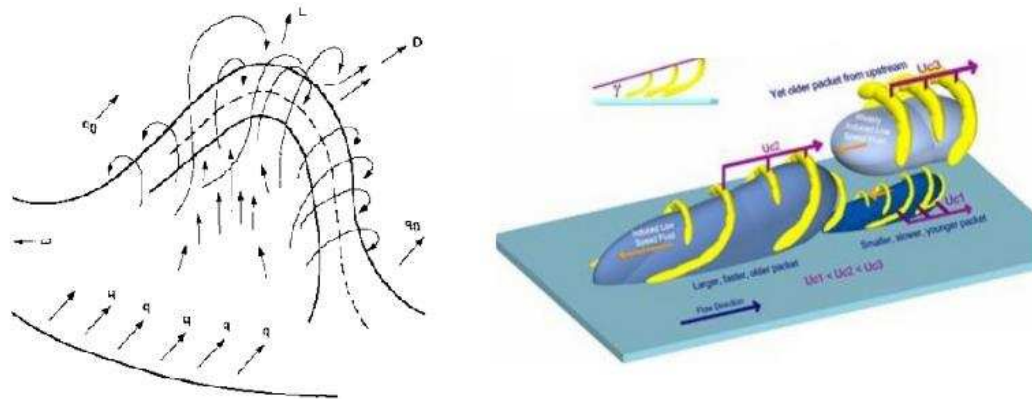


Figure 6 - Modèle de tourbillon de type hairpin (gauche) et organisation en paquets de hairpins (droite)

Un caractère important des paquets de hairpins est qu'ils forment un angle, en général plus faible que celui des hairpins individuels, avec la paroi. L'une des premières estimations de cette inclinaison fut réalisée au début des années 1980 en utilisant une méthode de visualisation d'écoulement. Les auteurs ont relevé un angle d'environ 20° comme le montre la Figure 7. Plus récemment, d'autres auteurs ont mesuré des angles de paquets entre 8° et 35° en utilisant des moyens similaires ou basés sur des méthodes statistiques appliquées à des mesures en soufflerie ou à des bases de données numériques. Il a également été démontré que la présence d'un gradient de pression adverse conduit à une augmentation de l'angle d'inclinaison des paquets, mais aussi à celui des hairpins.

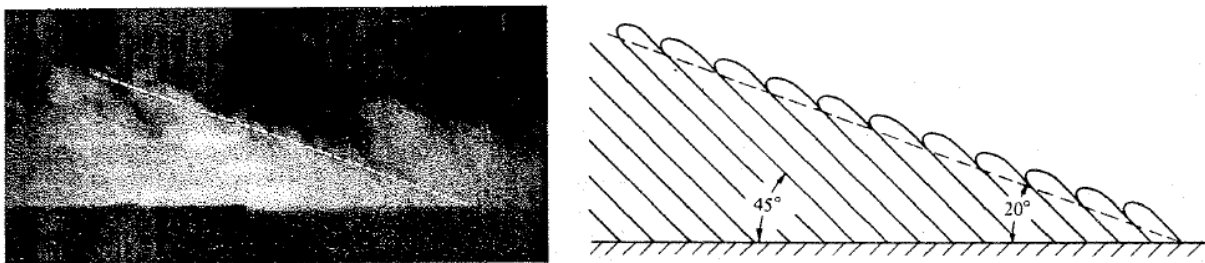


Figure 7 - Mise en évidence d'alignements de hairpins selon un angle de 20° à la paroi - l'écoulement est de la droite vers la gauche.

Pour cette étude, une base de données de calculs LES a été post-traitée pour quatre écoulements de couche limite turbulente à Mach 0.5 et à nombres de Reynolds basés sur l'épaisseur de quantité de mouvement $Re_\theta = 1.5 - 3 \times 10^3$:

1. Gradient de pression favorable (FPG)
2. Gradient de pression nul (ZPG)
3. Gradient de pression adverse faible (APGw, « w » pour weak)
4. Gradient de pression adverse fort (APGs, « s » pour strong)

La Figure 8 montre les domaines de maillage pour ces quatre calculs. La méthode pour introduire un gradient de pression est d'incliner la paroi. La valeur de l'angle d'inclinaison contrôle l'intensité du gradient de pression. Les analyses des champs de vitesse ont été réalisées sur un sous-domaine du domaine de calcul, appelé zone d'intérêt et représentée par

un rectangle en pointillés sur la figure. Dans cette région, on considère que la couche limite est en quasi-équilibre.

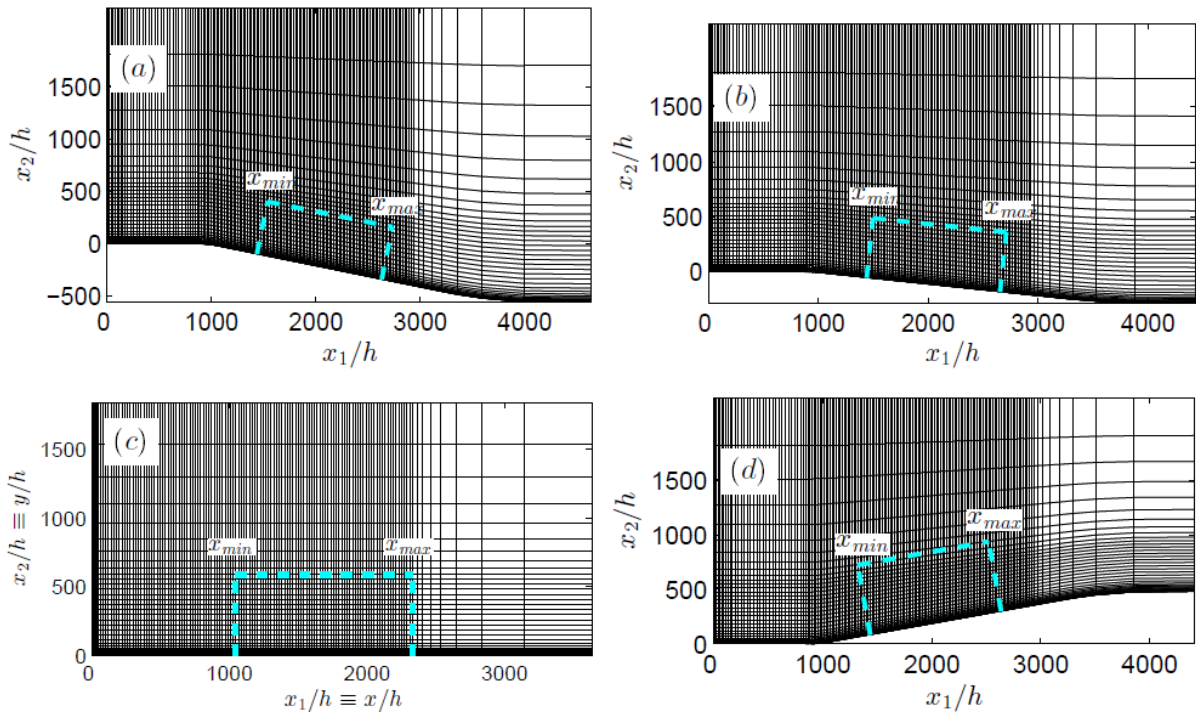


Figure 8 - Maillages dans le plan longitudinale/normale à la paroi pour les calculs (a) APGs, (b) APGw, (c) ZPG et (d) FPG. Les rectangles en pointillés montrent les zones d'intérêt utilisées pour l'analyse.

Sur la Figure 9, un critère de visualisation des structures tourbillonnaires a été appliqué et révèle la prédominance des harpins ainsi que l'arrangement en paquet. Sur cette figure, l'écoulement correspond à une couche limite turbulente sur plaque plane sans gradient de pression. L'arrangement en paquet existe également dans les écoulements soumis à un gradient de pression, ce que montre la Figure 10. Ici, les champs de vitesse sont visualisés dans un système de référence se déplaçant à une vitesse de convection $U_c = 0.72U_\infty$. Dans ce cadre, des mouvements de rotation (cercles) ainsi que des points de stagnation (flèches) sont visibles et sont représentatifs des structures hairpins ; les mouvements de rotation, dans le sens horaire, sont la signature des têtes de hairpins. On remarque ainsi un enchaînement de plusieurs hairpins dans la direction de l'écoulement qui forment un paquet de hairpin. On peut enfin ajouter que les paquets présentent une inclinaison variable par rapport à la paroi.

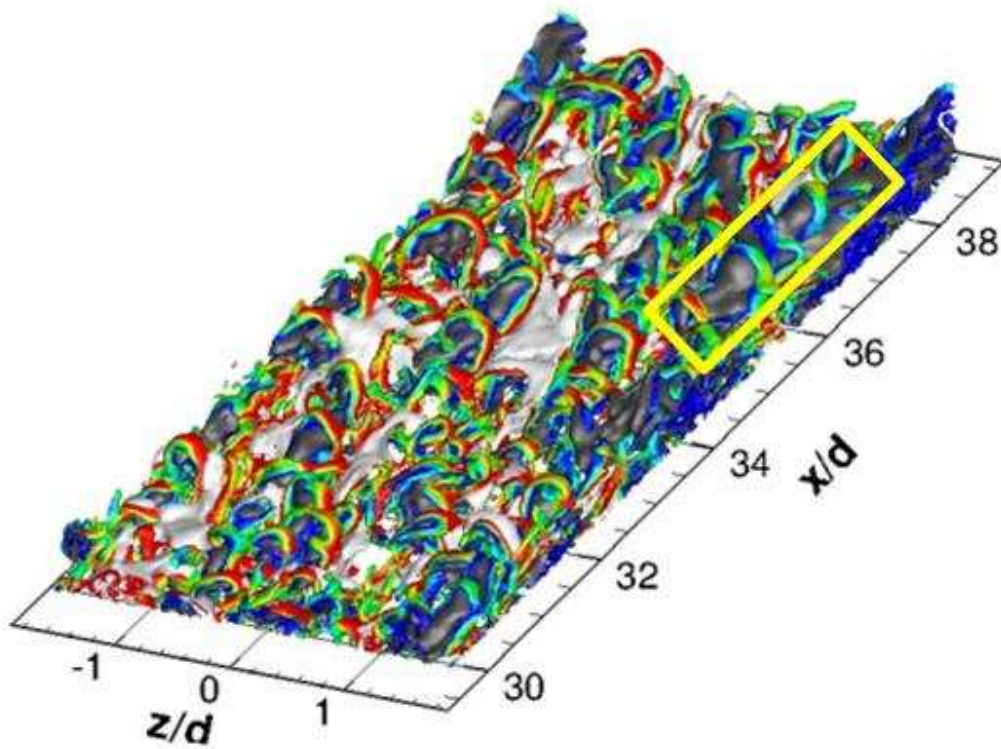


Figure 9 - Mise en évidence de tourbillons de type hairpins et organisation en paquet (rectangle jaune) dans une couche limite sans gradient de pression.

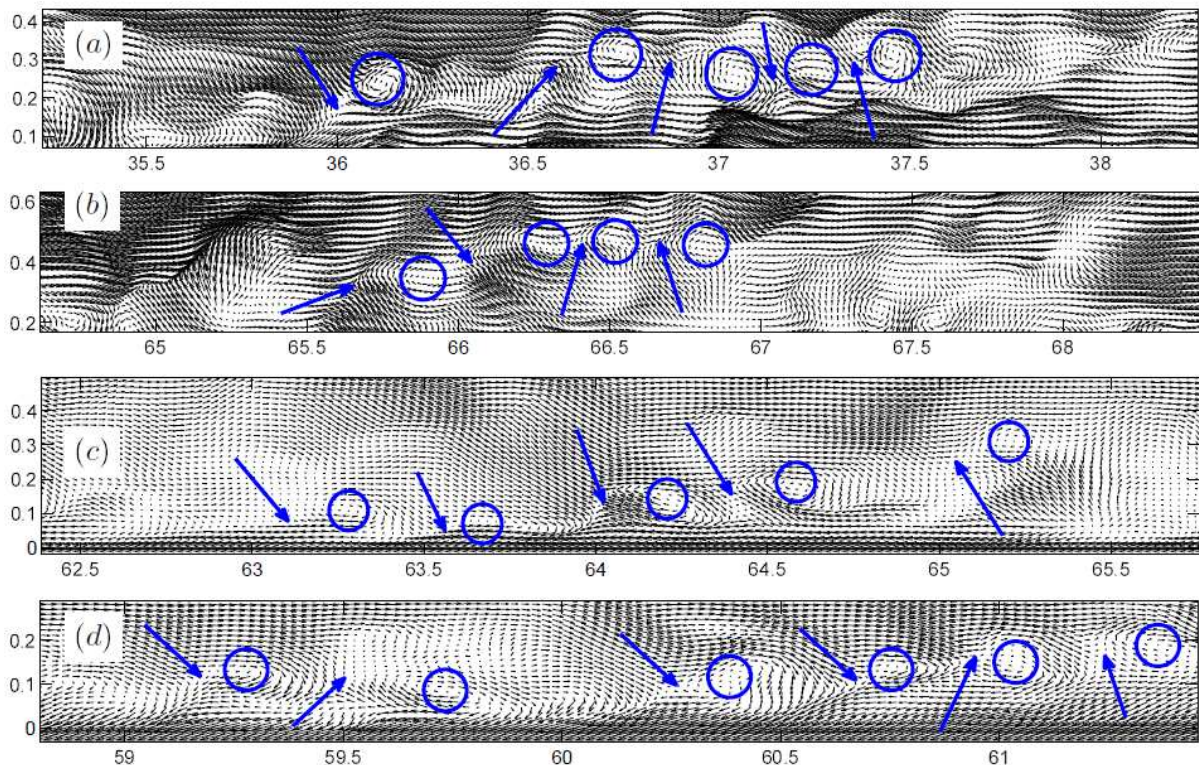


Figure 10 - Champs de vecteurs de vitesse instantanée dans un plan longitudinal/normal à la paroi, représentés dans un système de référence se déplaçant à $U_c = 0.72U_\infty$ pour les écoulements (a) APGs, (b) APGw, (c) ZPG et (d) FPG.

Les Figure 9 - Mise en évidence de tourbillons de type hairpins et organisation en paquet (rectangle jaune) dans une couche limite sans gradient de pression. et Figure 10 - Champs de vecteurs de vitesse instantanée dans un plan longitudinal/normal à la paroi, représentés dans un système de référence se déplaçant à $U_c = 0.72U_\infty$ pour les écoulements (a) APGs, (b) APGw, (c) ZPG et (d) FPG. donnent une vue instantanée du champ de vitesse pris à un temps aléatoire au cours du calcul. Afin de mieux caractériser les tourbillons, une méthode statistique, dite Estimation Stochastique Linéaire, est introduite. Cette méthode consiste à reconstruire, de manière stochastique, un champ de vitesse conditionnel, i.e. un champ de vitesse contraint par une certaine condition. La condition, ou événement, choisie ici est le tourbillon prograde. Il s'agit d'un tourbillon transverse (perpendiculaire à l'écoulement et parallèle à la paroi) dont la circulation est dans la même direction que la circulation moyenne de l'écoulement. Dans notre cas, il s'agit d'un tourbillon avec un mouvement de rotation horaire.

Le résultat de cette outil d'analyse est montré dans la Figure 11 - Estimation stochastique du champ de vitesse basée sur une condition de tourbillon prograde situé à $y/\delta = 0.2$ pour les écoulements (a) APGs, (b) APGw, (c) ZPG et (d) FPG. pour les quatre cas de gradient de pression et pour un point de référence (point où se situe l'évènement) à $y/\delta = 0.2$, δ étant l'épaisseur de la couche limite. On retrouve ainsi une organisation des tourbillons hairpins (repérés par des cercles) en paquet possédant un angle positif à la paroi. Cet angle a été estimé en fonction de la distance à la paroi et du gradient de pression. Les résultats sont montrés dans la Figure 12 dans laquelle sont également notés des résultats de littérature sur le sujet. On observe que les angles les plus élevés correspondent aux écoulements soumis à un gradient de pression adverse et que le cas favorable correspond aux angles les plus faibles. Une remarque

intéressante est que cet angle croît avec la distance à la paroi puis chute brutalement lorsqu'on approche du bord de la couche limite. Ceci s'explique par le fait que l'organisation en paquet disparaît au-delà d'une certaine distance par rapport à la paroi ; au-delà de $y/\delta = 0.6$ pour les cas FPG et ZPG et $y/\delta = 0.7$ pour les cas APG. Autrement dit, les paquets de hairpins persistent plus haut dans la couche limite pour les écoulements avec gradient de pression adverse.

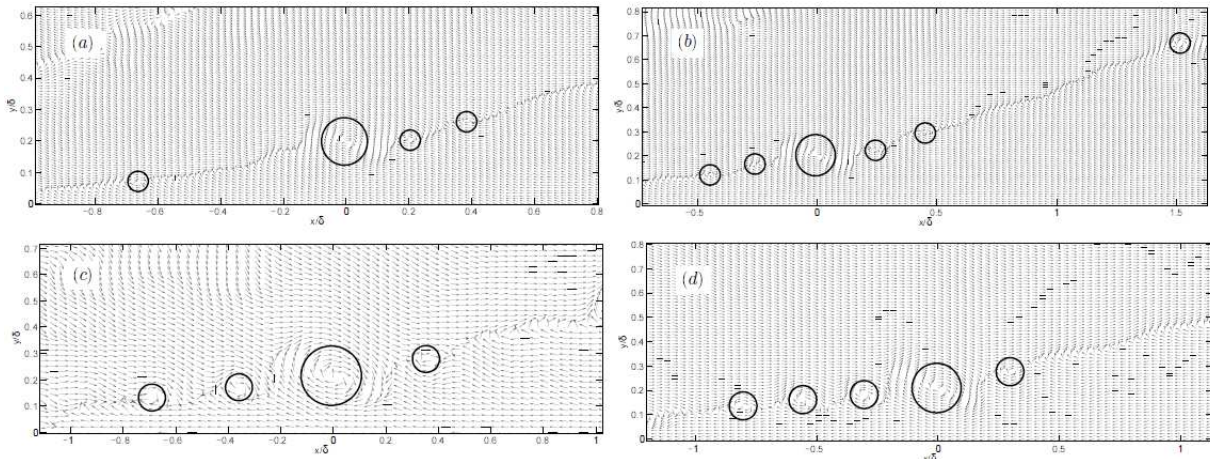


Figure 11 - Estimation stochastique du champ de vitesse basée sur une condition de tourbillon prograde situé à $y/\delta = 0.2$ pour les écoulements (a) APGs, (b) APGw, (c) ZPG et (d) FPG.

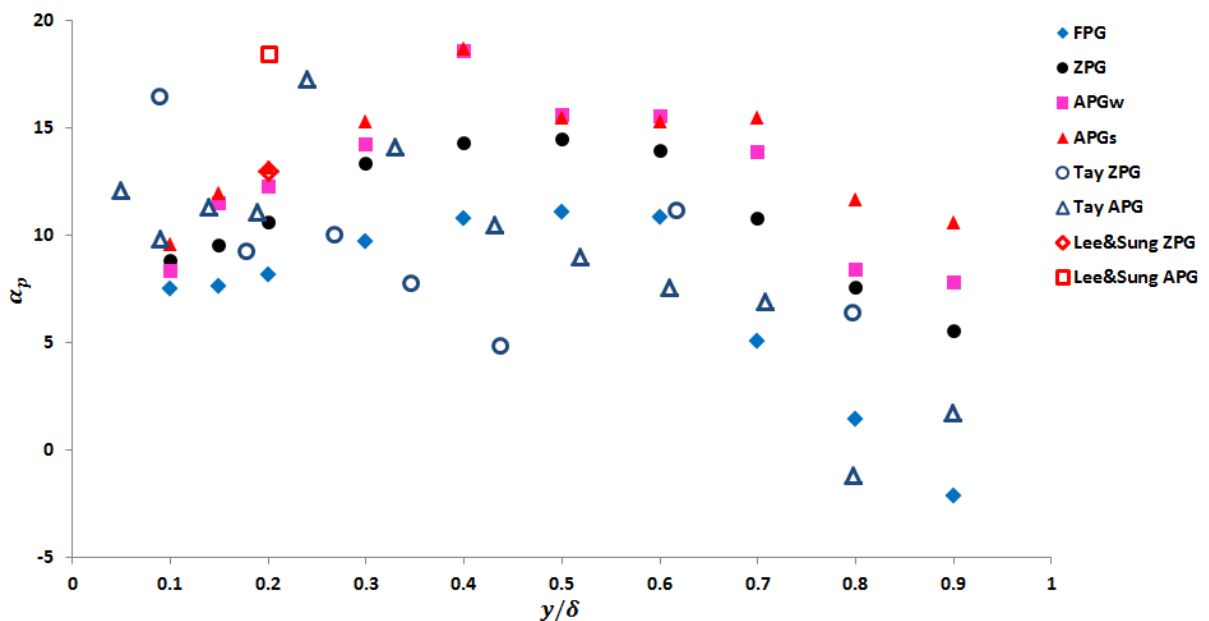


Figure 12 - Angles des paquets de hairpins en fonction de la distance des paquets à la paroi.

Une estimation stochastique similaire à celle présentée dans la Figure 11 a été réalisée sur un volume pour un écoulement sans gradient de pression. La Figure 13 montre le résultat de cette estimation. On observe un hairpin principal autour du point de référence de l'estimation ainsi qu'un hairpin secondaire en aval de celui-ci. De nouveau, ceci est caractéristique d'une organisation en paquet des tourbillons de type hairpins. Les résultats de la littérature ainsi que

les champs instantanés révèlent que les paquets de hairpins reposent sur des structures longitudinales basse vitesse dites Low Momentum Region (LMR). Ici, on retrouve ce type de structure qui est représentée en bleu. On remarque également qu'il est possible d'estimer les angles des jambes et du cou d'un hairpin grâce à ce genre de calcul.

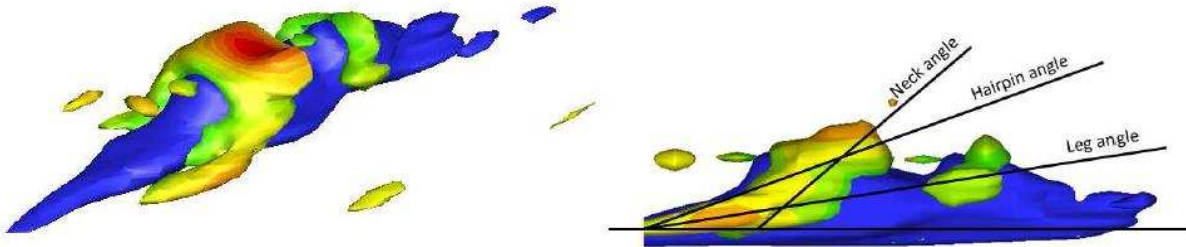


Figure 13 - Estimation stochastique du champ de vitesse pour une condition de type tourbillon prograde à $y/\delta = 0.2$ pour une couche limite sans gradient de pression. En bleu est représenté une structure basse vitesse dite Low Momentum Region (LMR).

Il était alors intéressant de regarder l'évolution de la topologie des tourbillons de type hairpins en fonction de leur distance à la paroi. Sur la Figure 14 on représente le résultat d'un calcul similaire à celui décrit précédemment pour un point de référence de l'évènement variant entre $y/\delta = 0.2$ et $y/\delta = 0.9$. Deux points sont alors remarquables :

- L'échelle spatiale des hairpins dépend de leur distance à la paroi ; les structures les plus grandes se trouvent en bordure de couche limite
- Les hairpins persistent très haut dans la couche limite, jusqu'à $y/\delta = 0.9$, alors que nous avons vu que les paquets ne sont pas présents à des distances à la paroi supérieures à $y/\delta = 0.7$.

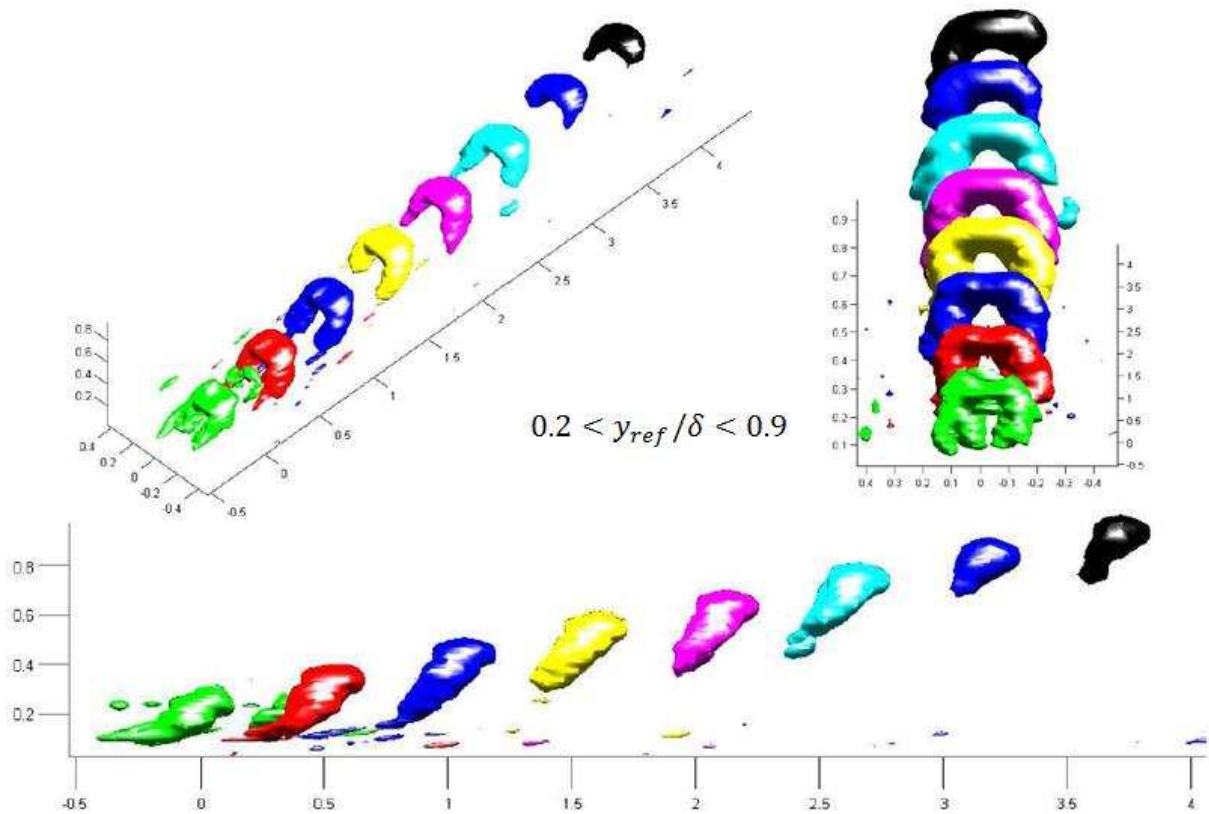


Figure 14 - Reconstruction de structures hairpins par estimation stochastique linéaire basée sur une condition de type tourbillon prograde pour différentes distances à la paroi.

Cette analyse permet alors de construire un modèle stochastique de spectre de pression pariétale basé sur des structures de type hairpin. Ce modèle est inspiré des travaux de Ahn et al. (JFM 2010) dont le principe est illustré dans la Figure 15

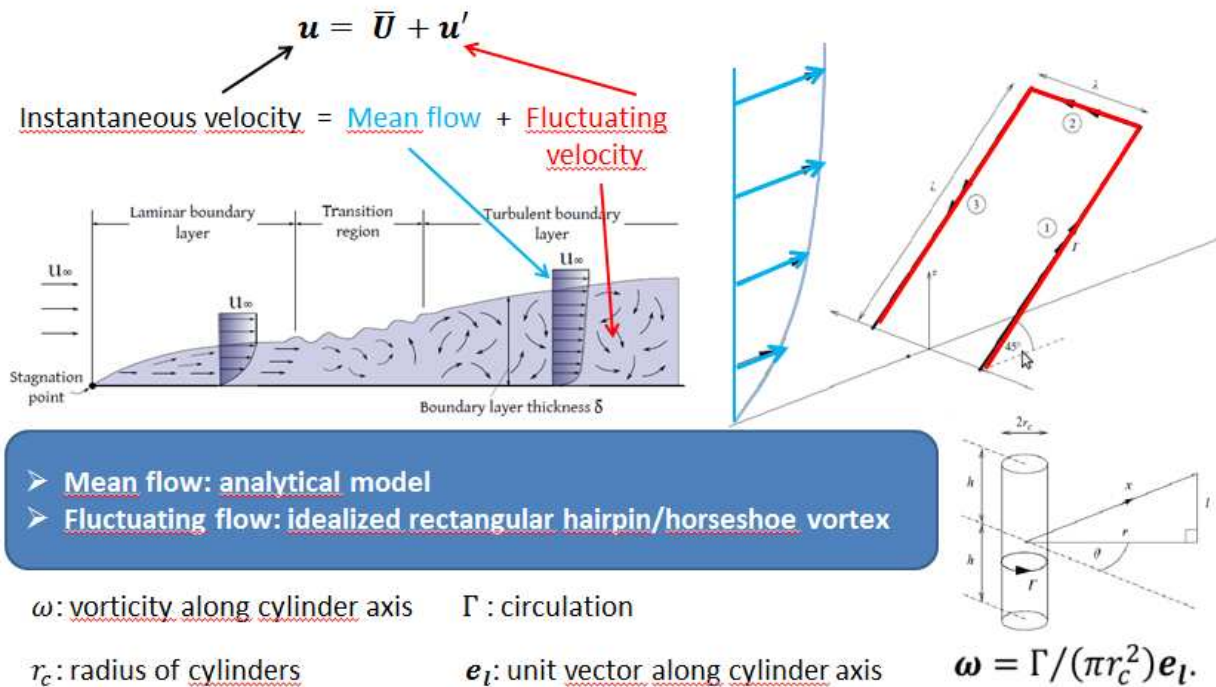


Figure 15 - Principe du modèle stochastique de hairpin de Ahn et al. (JFM 2010)

En turbulence, la décomposition de Reynolds suggère que le champ de vitesse instantanée \mathbf{u} peut être décomposé en un champ moyen de vitesse $\bar{\mathbf{U}}$ et un champ fluctuant de vitesse \mathbf{u}' , soit $\mathbf{u} = \bar{\mathbf{U}} + \mathbf{u}'$. L'idée de Ahn et al. est alors de construire un champ stochastique de vitesse instantanée en utilisant un tourbillon de type hairpin pour modéliser le champ fluctuant. Les structures ont une forme simplifiée de portique. Chaque élément du portique est modélisé par un cylindre avec une distribution uniforme de vorticité $\boldsymbol{\omega}$ le long de son axe. Le champ de vitesse induit par la combinaison champ moyen + hairpin est calculé en utilisant une intégrale de Biot-Savart. Comme cela a déjà été dit, nous sommes intéressés par le spectre de pression pariétale. Pour ce faire, on utilise une équation de Poisson avec un terme source ne prenant en compte que la contribution du terme linéaire (ou rapide). Enfin, on applique une transformée de Fourier spatiale sur le champ de pression pariétale afin d'obtenir le spectre nombre d'onde qui est adimensionné. Cette démarche est résumée sur la Figure 16.

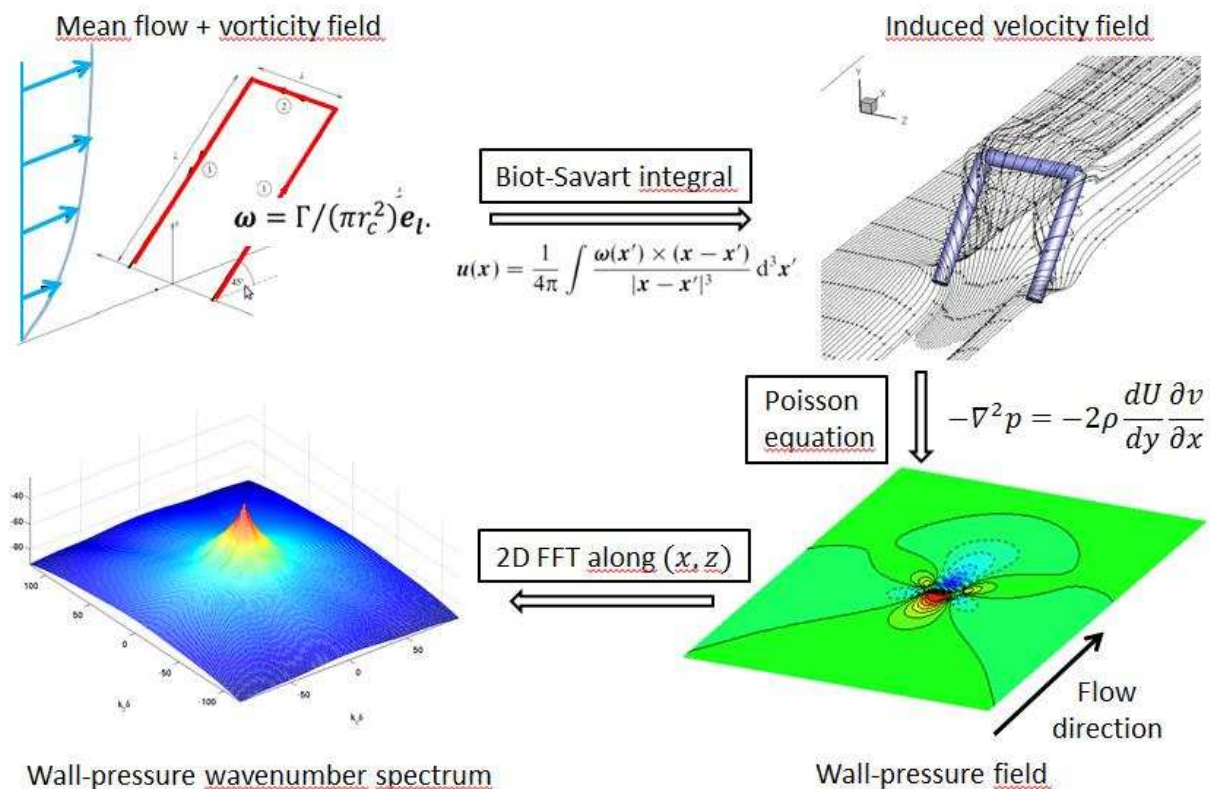


Figure 16 - Schéma d'obtention du spectre de pression pariétale à partir du modèle de hairpin.

A ce stade, le spectre calculé ne contient pas de dépendance fréquentielle ; il peut être considéré comme un spectre intégré sur l'ensemble des fréquences. En effet, le spectre de pression pariétale est un spectre fréquence-nombre d'onde que l'on peut noter $S_{pp}(k_x, k_z, \omega)$, où k_x , k_z et ω sont respectivement le nombre d'onde longitudinal, le nombre d'onde transversal et la fréquence (on trouve le terme fréquence par abus de langage mais il s'agit en réalité de la pulsation $2\pi f$). Trois « ingrédients » sont alors implémentés afin de reconstruire l'intégralité du spectre :

1. Le spectre nombre d'onde est multiplié par un auto-spectre de pression pariétale (modèle analytique de la littérature). Ceci permet d'introduire une première dépendance fréquentielle ainsi que de retrouver les bons niveaux d'énergie.
2. L'introduction d'une vitesse de convection U_c (inspirée du modèle de Panton et Linebarger JFM 1974) afin de modéliser la convection des structures en fonction de leur échelle spatiale.
3. Une fonction de pondération empirique qui pilote la contribution de chaque échelle de structure en fonction de la bande fréquentielle considérée.

L'étude des bases numériques nous a appris que les hairpins s'organisent en paquet. Par conséquent, dans notre modèle le hairpin individuel est remplacé par un paquet. En procédant ainsi, on peut de plus générer une structure basse vitesse de type LMR tel que le montre la Figure 17 - Paquet de cinq portiques au-dessus d'une région basse vitesse. En enrichissant ainsi le modèle, on introduit un caractère anisotropique au spectre de pression pariétale (voir Figure 18), ce qui est conforme aux résultats de la littérature.

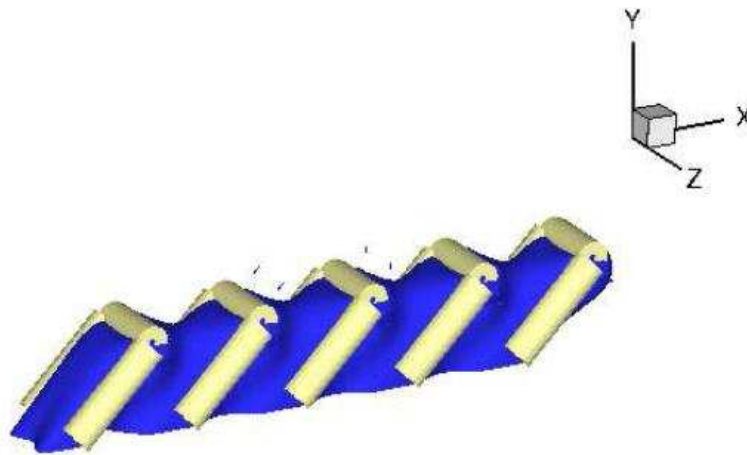


Figure 17 - Paquet de cinq portiques au-dessus d'une région basse vitesse.

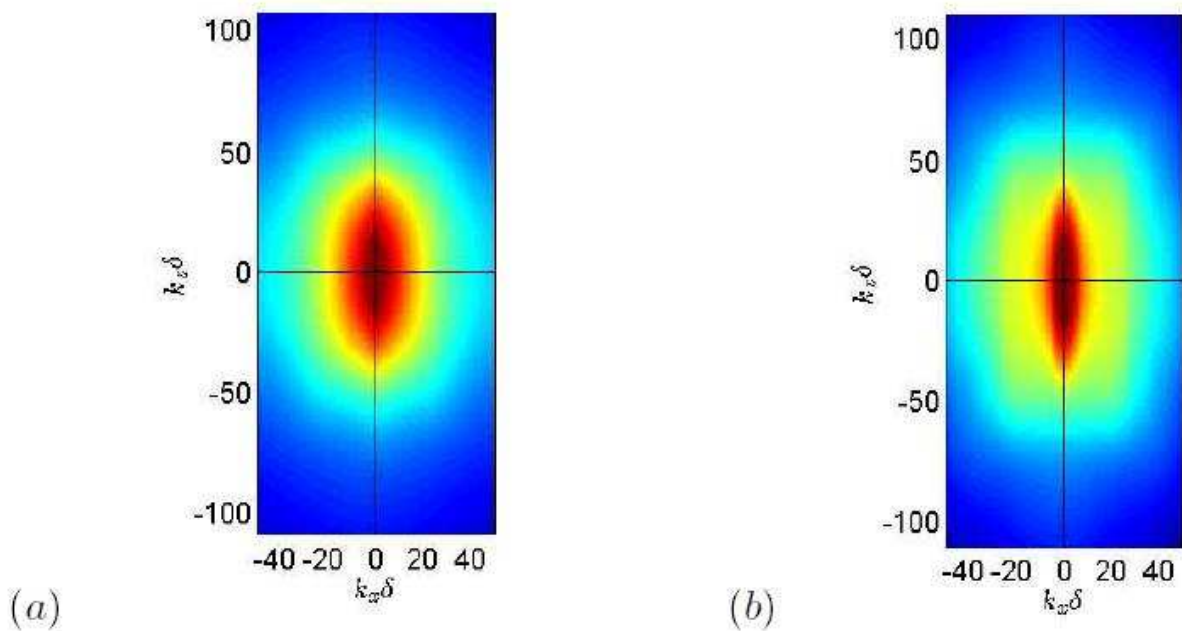


Figure 18 - Spectre de pression pariétale pour (a) un hairpin individuel et (b) un paquet de cinq hairpins.

La dernière étape de construction du modèle est l'influence d'un gradient de pression. Pour ce faire, deux paramètres sont considérés :

1. Prise en compte de la forme du sillage dans le profil moyen de vitesse à travers la valeur du paramètre de sillage de Coles qui dépend du gradient de pression à modéliser
2. Modification de l'angle des structures hairpins ; nous avons mentionné en effet que le gradient de pression a une influence directe sur l'inclinaison des structures par rapport à la paroi.

Un calcul du spectre de pression pariétale a été réalisé à partir du modèle de paquets de hairpins correspondant aux écoulements des simulations LES. Ceci est montré sur la Figure 19. Ici, les lignes verticales repèrent la position de l'échelle de coupe des calculs LES, estimée à $2\pi/4\Delta x$, où Δx est le pas de maillage dans la direction de l'écoulement. Ceci signifie que les échelles inférieures $4\Delta x$ ne sont pas résolues. Les structures hairpins sont placées à 45° par rapport à la paroi pour le cas ZPG, 37° pour le cas FPG, 53° pour le cas APGw et 60° pour le cas APGs. On remarque alors que le modèle prédit la bonne hiérarchie en terme de niveaux et une bonne estimation des pentes des spectres pour les nombres d'ondes moyens. Toutefois, le modèle surestime les niveaux pour les faibles nombres d'ondes $k_x\delta < 3$.

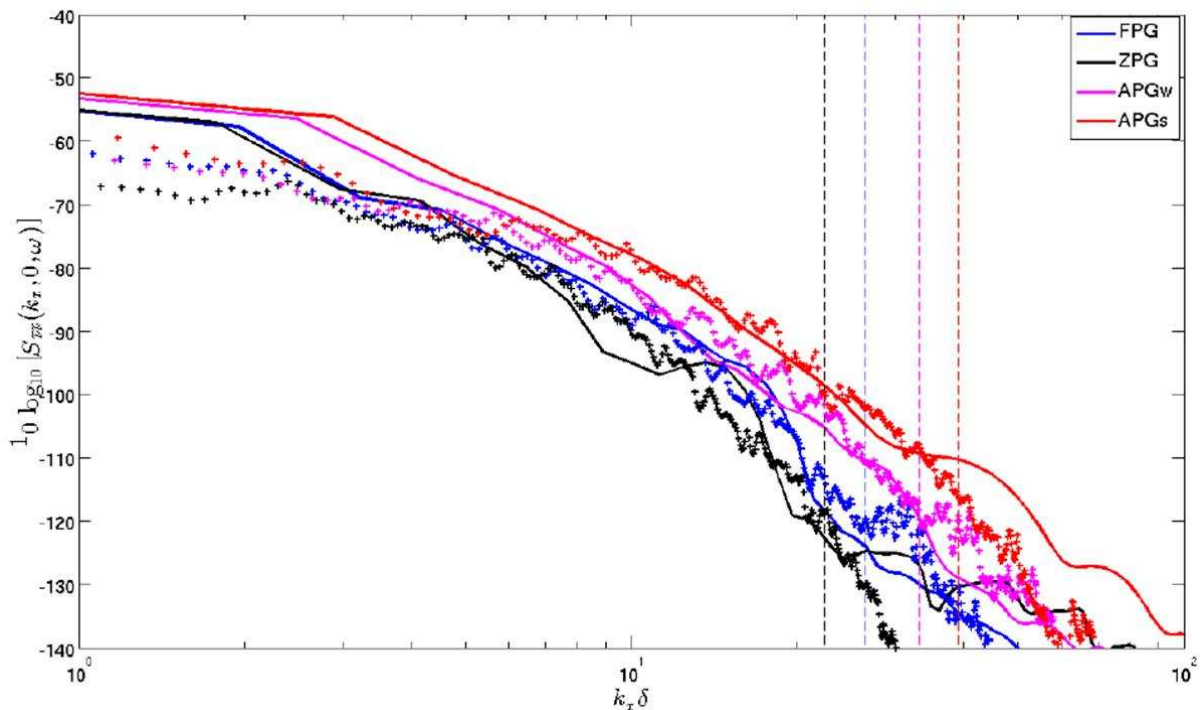


Figure 19 - Spectre de pression pariétale en fonction du nombre d'onde longitudinal pour les quatre cas de gradients de pression à la première fréquence- Prédiction du modèle de paquets de hairpins comparé aux calculs LES (++).

Pour finir, le modèle de paquet de hairpins a été appliqué à un cas industriel concret . Des mesures d'accélération de panneaux de fuselage ont été réalisées sur l'avion A320 d'essai ATRA (Advanced Technology Research Aircraft) du DLR (Deutsches Zentrum für Luft und Raumfahrt). En parallèle, Airbus a réalisé un modèle vibroacoustique de type SEA (Statistical Energy analysis) d'une portion avant de cabine d'un avion A320, présenté sur la Figure 20.

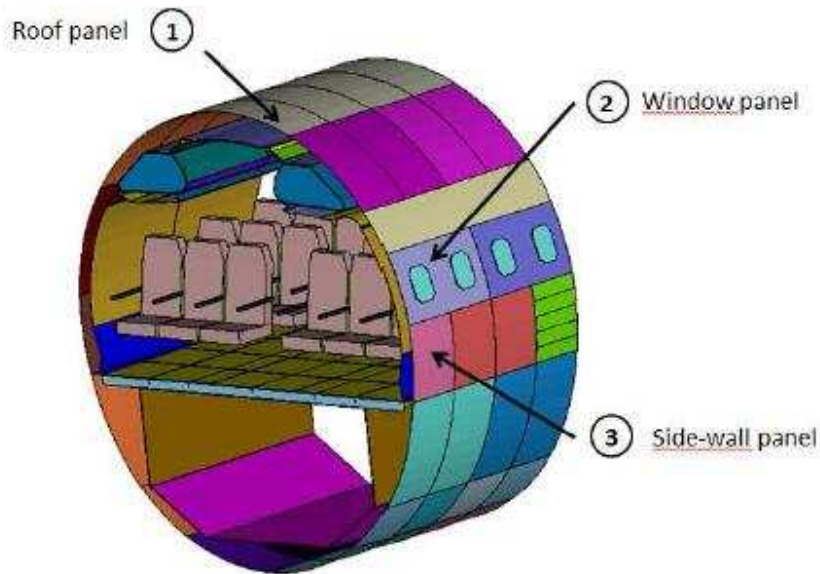


Figure 20 - Modèle SEA de la portion avant d'une cabine d'avion de type A320.

Le modèle SEA permet de simuler l'accélération des panneaux de fuselage lorsqu'il sont soumis à une excitation de type couche limite. La comparaison de l'accélération prédite par le modèle SEA soumis à différents modèles de couche limite et l'accélération mesurée en vol dans des conditions de croisière est montrée sur la Figure 21 pour le panneau supérieur de la cabine (Roof panel).

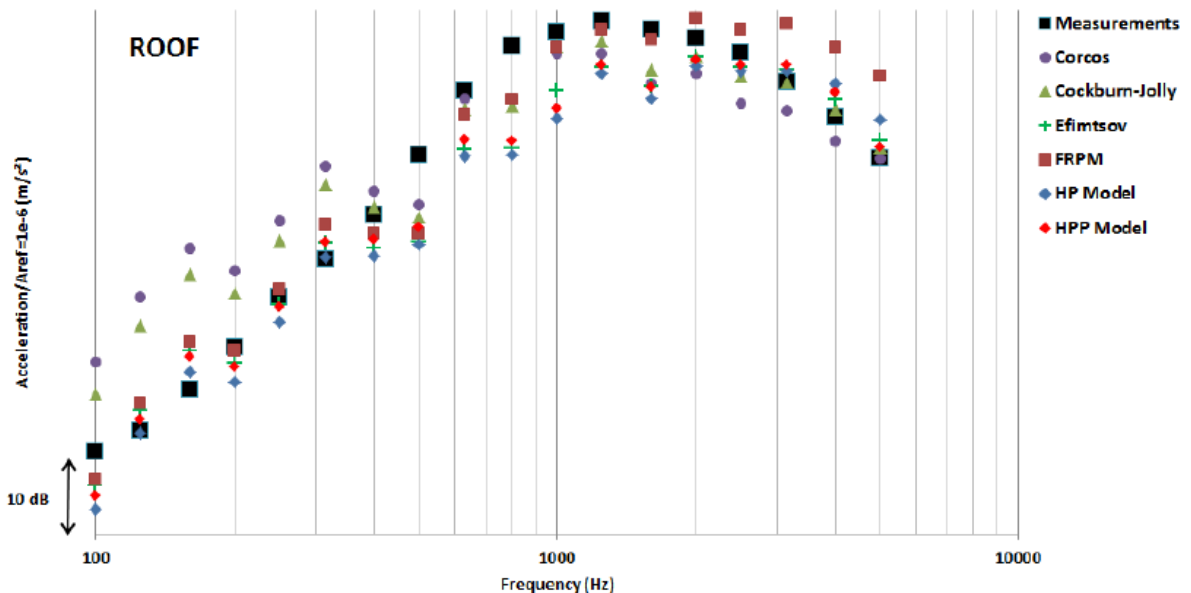


Figure 21 - Accélération du panneau supérieur (Roof panel) mesurée en vol et prédite par le modèle SEA sous différents types d'excitations de couche limite.

Les modèles HP et HPP correspondent au modèle de hairpin individuel (de type Ahn et al. JFM 2010) et modèle de paquet de hairpins respectivement. Les modèles de Corcos, Cockburn-Jolly, Efimtsov et FRPM (Fast Random Particle Mesh) sont issus de la littérature. Les données de ses deux derniers modèles, les résultats des mesures en vol ainsi que les paramètres de couche limite des conditions de croisière de l'avion ont été communiqués par A. Klages, dans le cadre de sa thèse sur un sujet similaire. On remarque alors que ce sont les modèles HPP et Efimtsov qui donnent les meilleurs résultats. Il faut préciser qu'ici, les constantes du modèle d'Efimtsov ont été calibrées à partir des mesures en vol sur l'avion ATRA.

6. PERSPECTIVES

Ce type de travaux et de modèle ouvrent de nombreuses possibilités. Une des premières tâches à effectuer est de réaliser davantage d'études comparatives du modèle de paquet de hairpins avec des données expérimentales et numériques d'écoulement de couches limites soumises à des gradients de pression. Il convient également d'appliquer ce modèle à un calcul SEA sur des régions d'avion avec un gradient de pression, tel que la pointe avant et la jonction voilure/fuselage.

Un calcul LES d'une couche limite sans gradient de pression à Mach 0.7 et avec un nombre de Reynolds plus élevé $Re_\theta = O(10^4)$ a également été réalisé plus récemment au laboratoire Dynfluid. Une analyse des structures cohérentes pour un tel écoulement donnerait des résultats intéressants sur l'effet du nombre de Reynolds sur les tourbillons de type hairpin (densité, angle, topologie, etc.). Ceci fournirait également des éléments d'amélioration du modèle de paquet de hairpins pour des écoulements à hauts nombres de Reynolds.

Dans cette étude, nous avons mesuré l'angle des paquets de hairpins. Il est également intéressant de mesurer l'angle des hairpins individuels afin d'évaluer l'effet du gradient de pression sur cet angle. Ceci peut être réalisé en mesurant l'angle de l'évènement $Q2$ (ejection) entre les jambes des hairpins. Un autre moyen serait de réaliser une estimation stochastique du champ de vitesse sur une base de données 3D comme cela a été fait pour le cas ZPG ici. Pour cela, il est nécessaire de stocker des volumes, ce qui demande des capacités de stockage de données très importantes. Cette méthode est toutefois la plus robuste puisqu'elle donne directement l'angle des structures de type hairpin.

Le modèle de paquet de hairpin tel qu'il a été construit repose sur l'hypothèse que seul le terme source rapide contribue à la pression pariétale. Il semble important de confirmer, ou non, cette hypothèse en intégrant dans l'équation de Poisson de calcul du champ de pression pariétale le terme lent (turbulent-turbulent). Cette hypothèse peut également être vérifiée directement à partir des bases de données LES en résolvant un problème d'analogie de Lighthill, mais là encore, une base volumique est nécessaire. Enfin, une telle base permettrait aussi d'estimer la contribution de chaque couche de l'écoulement à la pression pariétale. En effet, les conclusions de la littérature sont contradictoires à ce sujet ; certains résultats suggèrent que les couches loin de la paroi ont une contribution négligeable à la pression pariétale alors que d'autres montrent que ceci n'est pas vrai.

STRUCTURES TURBULENTES ET MODELISATION DE LA PRESSION PARIETALE POUR UNE COUCHE LIMITE TURBULENTE EN PRESENCE DE GRADIENT DE PRESSION

RESUME : L'écoulement autour des véhicules produit une couche limite turbulente très proche de la paroi. Le caractère turbulent induit des fluctuations de pression pariétale qui font vibrer les panneaux du véhicule. Ces vibrations sont alors transmises à travers la structure et rayonnent du bruit dans l'habitacle. Les niveaux sonores dus à l'écoulement augmentent avec la vitesse du véhicule. Pour cette raison, cette problématique connaît un intérêt croissant dans le secteur aéronautique.

Le but de cette thèse est double : comprendre les mécanismes à l'origine de ces fluctuations de pression à la paroi et prédire l'excitation de la structure avion due à l'écoulement turbulent.

Pour ce faire, des calculs Large Eddy Simulation (LES) sont disponibles. Il s'agit de bases de données numériques d'écoulements de couches limites turbulentes en présence de gradients de pression favorable, adverse et nul. Ceci permet de caractériser l'écoulement sur des géométries courbes telles que la pointe avant d'un avion. L'effet du gradient de pression sur des structures cohérentes de type « hairpins » et paquets de « hairpins » a pu être identifié et quantifié à travers des méthodes de visualisation et d'analyse statistique. Une méthode d'estimation stochastique du champ de vitesse a révélé la présence de tourbillons contra-rotatifs au-dessus des paquets de hairpins. Ces tourbillons ont une vorticité opposée à celle des hairpins et un modèle de « hairpins inversé » a été proposé.

En s'inspirant du travail de Ahn et al. (2010), un modèle stochastique de spectre de la pression pariétale a été développé. Il s'agit de reconstruire un champ stochastique de vitesse instantanée et d'en déduire le champ de pression à la paroi en résolvant une équation de Poisson sur la pression. Le champ de vitesse est obtenu en soumettant des structures de type paquets de hairpins à un écoulement moyen. Les caractéristiques des paquets de hairpins en fonction du gradient de pression sont basées sur l'analyse des bases LES. Les résultats de ce modèle sont comparés à ceux issues de bases de données numériques. Enfin, ce modèle est utilisé pour caractériser l'écoulement de couche limite turbulente dans une simulation de Statistical Energy Analysis (SEA) afin de prédire les niveaux de vibration des panneaux d'une portion de fuselage d'avion.

Mots clés : couche limite turbulente, simulation, gradient de pression, pression pariétale, structures cohérentes.

COHERENT STRUCTURES AND WALL-PRESSURE FLUCTUATIONS MODELING IN TURBULENT BOUNDARY LAYERS SUBJECTED TO PRESSURE GRADIENTS

ABSTRACT: The flow around vehicles creates a turbulent boundary layer in the vicinity of the wall. The turbulent behavior induces pressure fluctuations that make the panels vibrate. These vibrations are then transmitted through the structure of the vehicle and radiate noise inside the cabin. The flow-induced noise levels increase with the speed of the vehicle. For this reason, aircraft manufacturers show a great interest in this topic.

There are two objectives for this thesis: understand the mechanisms responsible for the wall-pressure fluctuations and predict this source of aircraft panel excitation.

A study of available Large Eddy Simulation (LES) computations was performed. The database consists in simulations of turbulent boundary layer flows submitted to favorable, adverse and zero pressure gradients. This is necessary to understand the nature of the flow over curved geometries such as the aircraft flight deck. The effect of pressure gradients on coherent hairpin structures and hairpin packets could be identified and quantified based on visualization and statistical analysis methods. Linear stochastic estimation of the velocity fields revealed a pair of counter-rotating streamwise vortices above hairpin packets. These vortices have a vorticity opposite to that of the hairpins and an "inverse hairpin" model was proposed.

Following the work of Ahn et al. (2010), a stochastic model for wall-pressure spectrum was developed. The idea is to build a stochastic turbulent velocity field using hairpin packets which are subjected to a mean flow. The characteristics of the packets depending on the pressure gradient are based on the analyses of the LES database. The pressure field at the wall is obtained by solving a Poisson equation. The results of the hairpin packet model are compared to numerical data. Finally, the model is used as input for a Statistical Energy Analysis (SEA) simulation in order to predict the levels of vibrations of panels submitted to a turbulent boundary layer flow over a portion of an aircraft cabin.

Keywords: boundary layer, turbulence, compressible, adverse and favorable pressure gradient, wall pressure fluctuations, frequency-wavenumber spectrum, aeroacoustic.

